Modelling spreading, vaporisation and dissolution of multi-component pools

A thesis submitted to University College London for the degree of
Doctor of Philosophy

By

MARIA ISABEL FERNANDEZ

Department of Chemical Engineering
University College London
Torrington Place
London WC1E 7JE

February 2013

ABSTRACT

The present work describes the fundamental extension of an integral pool spreading, vaporisation and dissolution model, part of the Process Hazard Assessment Tool (Phast) software. The base model accounts for spills on land and water surfaces. For pools spreading on water, the model includes three successive regimes, gravity-resistive, viscous-resistive and viscous-surface tension. For the case of pool spreading on land, it accounts for the hold-up of liquid within the surface's rough elements. Pool vaporisation considers two limiting cases: evaporation and boiling. The heat transfer mechanisms accounted for include conduction from the ground, convection from water and air, conduction from ice and solar incidence.

The extended multi-component model tracks the transient pool inventory at each step. While the pool is boiling the liquid and vapour phases are in equilibrium. For evaporation, the model accounts for the diffusion of multiple components into air. The dissolution of water-soluble chemicals present in the mixture, a novel feature amongst existing multi-component pool models, is introduced by the present work. The application of the model to mixtures highlighted the drawbacks of approximating such systems by a single component evaporating pool.

The implementation of a numerical algorithm based on Backward Differentiation Formula (BDF) showed improved numerical stability when compared to a widely used pool model (LPOOL by HGSYSTEM (Post, 1994)). The improvements were most noticeable when the model behaved as a stiff problem.

The validation of the multi-component pool model against published experimental data shows good agreement for pool spreading and boiling on land and water surfaces. The pool evaporation model is in good agreement with the experimental data for low to medium volatility chemicals. Suggestions for further work include an extension to non-ideal mixtures; incorporate the modelling of chemical reactions and a stratified pool model.

ACKNOWLEDGEMENTS

I wish to thank the following people and organisations who have contributed so much in many ways to facilitate the completion of this thesis.

My supervisor, Prof. Haroun Mahgerefteh for giving me the opportunity to undertake this project and for his advice and guidance through the completion of my studies

To Henk Witlox and Dr. Michael Harper from DNV Software for the continuous support during my PhD

To the Dorothy Hodgkin Postgraduate Awards (DHPA), the UCL Graduate School and DNV Software for the financial assistance which made this project possible

To the technical and administrative staff of the Department of Chemical engineering, UCL

To my family, and especially to my brother Luis, for their patience, love and encouragement

To my friends and colleagues at UCL for enriching my experience of this four years. It was great to meet you all

To Alex Collard, for being a great support and always being there when I needed

To my office mates: Aisha, Garfield, Navid, Peng, Sergey, Shirin and Solomon

A mis padrinos

TABLE OF CONTENTS

CHAPTER 1. INTRODUCTION

Liquid fuels are handled and transported by sea and land in increasingly larger amounts to meet the mounting world energy demand. From 2008 to 2035 the world energy demand is estimated to increase by 53%, of which liquid fuels are predicted to supply a third of the total (US Energy Information Administration, 2011).

The accidental release of a liquid fuel represents a major safety hazard as depending on its boiling point, it may evaporate upon contact with a surface forming a vapour cloud that can disperse into the atmosphere and reach population centres. The vapour cloud evolved could ignite, leading to fire or explosion with catastrophic consequences.

In 2005, a major accident that took place in the Buncefield oil storage terminal in Hertfordshire, has been the largest explosion in the United Kingdom in over three decades (Office of Public Sector Information, 2008). The explosion was preceded by the ignition of a vapour cloud formed after the overfilling of a depot tank which caused unleaded petrol to accumulate in the surrounding bund. Fortunately no fatalities or major injuries resulted from the accident yet the financial losses for the operating company were of the order of £1 billion.

An accidental release of oil from tankers and offshore platforms can lead to large scale environmental pollution as the spill forms a slick that spreads and drifts by the action of the sea currents (Hoult, 1972a). One of the most notorious hydrocarbon spills was the Exxon Valdez in 1989 where 42,000 m^3 of crude oil were released into the sea when the oil tanker ran aground in Prince William Sound’s Bligh Reef (Skinner and Reilly, 1989). The spill covered a total area of 7,770 km^2 along the coast of Alaska and resulted in financial losses totalling US $3.8 billion from fines, compensation and clean-up costs. More recently, an explosion which sank the offshore platform Deep Water Horizon caused the release of an estimate of 780,000 m^3 of crude oil into the Gulf of Mexico (McNutt et al., 2011). The oil spill covered an area of 10,000 km^2 within 10 days. The financial cost of the incident is estimated to be in the region of US $35 billion covering the cost of the spill response, containment, clean-up operation, relief well drilling and compensation to the states bordering the Gulf of Mexico.

Following public concern due to major industrial accidents occurred between 1970 and 1980, see for example Flixborough in the UK in 1974 (Parker et al., 1975) and Seveso in Italy in 1976 (Sambeth, 1983), the European Parliament adopted a directive on major accident hazards of certain industrial activities known as Seveso I Directive in 1982. This was replaced in 1996 by the Seveso II Directive (European Commission, 2012), which stipulated that all European Union member states should bring into force national laws, regulations and administrative provisions to prevent and limit the consequences of major industrial accidents. In the UK, the Control of Major Accident Hazard (COMAH) regulations were introduced in 1999 to meet the Seveso II Directive (European Commission, 2012). The COMAH regulations require that "businesses take all necessary measures to prevent major accidents involving dangerous substances" and "limit the consequences to people and the environment of any major accidents which do occur" (Control of Major Accident Hazard, 2010).

To comply with these regulations, the relevant industries are required to present and update a Safety Report of their operations (COMAH-Safety Reports, 2010). The main purpose of the Safety Report is to provide evidence that suitable and sufficient consequence assessments for each major accident scenario has been carried out with respect to people and the environment. In the case of a loss of containment and consequent liquid spillage, the formation of a vapour cloud from a pool is one of the major accident scenarios which need to be investigated as part of the consequence assessment (COMAH-Safety Reports, 2010). An essential component in this assessment is the prediction of the area covered by the evaporating pool, the evaporation rate and the total inventory vaporised. As such, the development of modelling tools for the accurate prediction of the consequences associated with such accidents is of paramount importance.

Most existing models for estimating the spreading and vaporisation rate from a liquid pool fall into two main categories. These are integral and Computational Fluid Dynamics (CFD) models. CFD models capture the pool details such as, thickness, speed and local friction at every location by solving the shallow water equations in one or two dimensions. CFD models can reproduce pool features such as hydraulic jumps resulting from the contact of the pool edge with an obstacle or bund (Ponchaut et al. 2011) and account for the effect of terrain slopes and trenches (Ivings and Webber, 2007). On the other hand, integral models are based on the assumption that the pool has a prescribed thickness profile along its length and time invariant shape which allows for analytical expressions of the pool spreading velocity derived from shallow water theory.

Despite their higher level of accuracy, CFD based models are however computationally very expensive. This causes significant practical difficulties in developing hazard assessment tools, as pool evaporation models are usually applied in conjunction with discharge and dispersion models. Other challenges faced by CFD pool modelling are uncertainties in the pool behaviour undergoing turbulent boiling/bubbly spreading (as it can be argued to be the case of LNG spreading on water (Fay, 2007)), droplet breakup and vaporisation (Ivings et al., 2009).

Many integral models (e.g. SPILL (Shaw and Briscoe, 1980); GASP (Webber, 1990); LSM90/LPOOL (Cavanaugh et al., 1994); Phast (Witlox, 2008); Fay, 2003 and 2007) are reported in the literature for estimating the vaporisation rate from a liquid pool under different scenarios and with different levels of accuracy with respect to experimental data. The models differ primarily on the assumptions made for the determination of the spreading rate, the calculation of the heat transfer from the ground, the correlations used for the vaporisation rate, the numerical solution of the differential equations and the release mechanism considered (Ivings et al., 2009).

For example, the Process Hazard Analysis Software Tool (Phast) integral pool model predicts pool spreading, evaporation and dissolution, with good agreement against real data for cryogenic spills such as liquefied Methane on land and water surfaces (Witlox, 2008). Further verification of the Phast pool model against CFD based models (Ponchaut et al., 2011) has shown good agreement in its prediction of the cumulative amount of vapour generation. However, Phast pool model is limited to the modelling of pure component releases and cannot account for the vaporisation and dissolution of mixtures.

This thesis describes the further theoretical development and validation of Phast (Witlox, 2008) integral model for the prediction of the spreading, vaporisation and dissolution from pools. The objectives are to:

- ☐ Extend the single-component pool model to multi-component mixtures
- ☐ Improve the numerical robustness of the model solution
- ☐ Validate/verify the model's predictions against published real data

The thesis is divided into seven chapters.

In chapter 2, a review of the theoretical background of integral models that have found widespread use in industry and academia for predicting pool spreading and vaporisation is presented. The chapter is divided into two sections, one describing pure component models and the other for models capable of handling mixtures. Where possible, the validation and verification of their predictions as well as their shortcomings are presented and discussed.

Chapter 3 describes the Phast integral pool model, which serve as the basis for the present work. The general assumptions of the model are also given. The chapter is divided into the four sections; the first three sections respectively describe the theoretical formulation of pool spreading, mass transfer and heat transfer mechanisms. The last section presents the numerical algorithm used to solve the model equations.

Chapter 4 presents the extension of the Phast pool evaporation model to multi-component mixtures. To account for the mixture behaviour, the multi-component pool model keeps track of the transient pool inventory through the deployment of established mixing rules to estimate overall pool properties. The formulation of the multi-component model and the main assumptions embodied are presented first. A series of hypothetical studies are next developed to assess the model efficacy.

Chapter 5 focuses on the development of a stable and efficient numerical algorithm for the multi-component pool model. The chapter is divided into two sections; the first, describes the implementation of the new numerical algorithm. A series of case studies are next presented to exemplify the model's improvement in terms of numerical stability and range of application.

In chapter 6, the multi-component pool model is validated against real data published in the open literature. The validation tests cover a wide range of conditions including different materials (e.g. low and high volatility, pure substances and mixtures); different surfaces (e.g. soil, concrete and water) in the presence or absence of bunds, as well as instantaneous and continuous releases The results of the validation tests are then used to determine the accuracy and the range of applicability of the model.

Chapter 7 presents the conclusions and suggestions for future work.

CHAPTER 2. LITERATURE REVIEW OF POOL SPREADING AND VAPORISATION MODELS

2.1 Introduction

Historically, the mathematical modelling of pool spreading and vaporisation can be traced back to the 1970s. The first studies focused on the modelling of two types of accidental scenarios: oil releases on the sea (Fay, 1969; Hoult, 1972a; Blokker, 1964) and spills from LNG tankers (Burgess et al., 1970 and 1972; Lind, 1974). Assumptions based on the properties of the material spilled and empirical correlations applied to heat and mass transfer processes render these models limited in their range of applicability. Since then, pool spreading and vaporisation models have been extended to handle pure components, multi-component mixtures and various release scenarios.

In this chapter, a review of the Integral models that have found widespread use in industry and academia for predicting pool spreading and vaporisation is presented. The theoretical background of the models as well as the validation and verification of their simulation results are presented where available. Pool spreading and evaporation models capable of handling pure liquids are first reviewed; next, models which also consider ideal and non-ideal mixtures are addressed.

2.2 Raj and Kalelkar (1974)

Raj and Kalellkar’s (1974) pool model was developed as part of a US Coast Guard project that looked into the hazards of accidental fluid releases into the atmosphere and spills on water. The model takes into consideration many of the physical aspects of liquid pool behaviour such as spreading, vaporisation and dispersion in water, as well as including a sub-model for pool fires. It predicts the spreading rate as a function of time, the time for complete vaporisation and the maximum extent of the pool area. However, the model considers only catastrophic failure scenarios where the total amount of the material is released instantaneously, and is also only applicable to pure substances.

2.2.1 Theoretical background

Raj and Kalelkar's (1974) spreading model is based on the previous work of Fay (1969) on the spreading of crude oil on water. Crude oil is a mixture of a very large number of components. When this mixture is modelled as a single-component fluid of constant properties, a number of approximations are made. For example, the effects of evaporation and dissolution of lighter components as well as bio-degradation are ignored. Fay (1969) assumed a bulk model with constant properties as a first step in developing and understanding the spreading process.

Fay's (1969) spreading model divides the phenomenon into three successive regimes in which the effect of gravity, water resistance, viscosity and surface tension are considered.

Raj and Kalelkar (1974) presented the following expression, first presented by Fay (1969), for the pool radius as a function of time in the regime where gravity and resistance forces are predominant.

$$r(t) = K\left[\left(\frac{\rho_w - \rho}{\rho_w}\right) g V\right]^{1/4} t^{1/2} \tag{2.1}$$

where,

r = radius of the pool (m) at time, t (s)

ρ = density of the chemical (kg/m^3)

ρ_w = density of water (kg/m^3)

g = gravitational constant (m/s^2)

V = volume of the spill (m^3)

K = empirical constant (=1.14)

The value of 1.14 for the proportionality constant K in equation (2.1) was originally proposed by Fay (1969) after comparison against the oil slick experiments of Liang (1971). Other authors (Webber and Jones, 1987) have reported slightly different values for K (1.28 and 1.7) when comparing this model against Chang and Reid's (1982)

Liquefied Petroleum Gas (LPG) experiments and Dodge et al.'s (1983) tests with heavier hydrocarbons, such as n-Pentane and n-Octane.

Raj and Kalelkar (1974) extended Fay's (1969) pool spreading model to account for the spreading of chemicals less viscous than water. This extension only applies to the later stages of the spill when the viscous and surface tension forces are prevalent.

Regarding pool vaporisation, Raj and Kalelkar's (1974) model makes a distinction between pools formed from releases of cryogenic or pressurised gases and pools formed from volatile liquid spills. For the first type of pools, a constant heat influx from the water body, determined from experimental evidence of LNG boiling on water (see Burgess et al., 1970 and 1972), provides the energy necessary for the liquid to vaporise. Additionally, the model accounts for ice formation beneath the cryogenic liquid as the extremely low pool temperatures cause a thin sheet of ice to form between the pool and the water. The phenomenon of ice formation was observed in a series of laboratory scale tests later performed by Reid and Smith (1978) for LNG. For volatile pools the model uses the heat-mass transfer analogy for flat plates to obtain the rate of evaporation from the pool surface.

Dissolution effects are also taken into account on two different conditions: with and without currents. For calm water with no currents, the dissolution is modelled by a diffusion mechanism; for rivers, channels or open sea, diffusion is replaced by forced convection.

2.2.2 Validation of results

No validation of Raj and Kalelkar's (1974) model against real data has been reported in the published literature. Nevertheless, Raj and Kalelkar (1974) presented the results of their spreading model for a hypothetical spill of a chemical of density 800 kg/m3 and viscosity greater than that of water.

Raj and Kalelkar's (1974) graphically showed the variation of the pool radius, χ, against time, τ, (non-dimensional quantities) obtained from Raj and Kalelkar's (1974) model for different values of the chemical's dimensionless surface tension, Σ_l, and viscosity, Γ_l, where,

$$\chi = \frac{r}{V^{1/3}} \tag{2.2}$$

$$\tau = \left(\left(\frac{\rho_w - \rho}{\rho_w} \right) \frac{g}{V^{1/3}} \right)^{0.5} t \tag{2.3}$$

$$\Sigma_l = \frac{\sigma}{\mu_l \left(\left(\frac{\rho_w - \rho}{\rho_w} \right) g V^{1/3} \right)^{0.5}} \tag{2.4}$$

$$\Gamma_l = \left(\frac{V}{\nu_l} \left(\frac{\rho_w - \rho}{\rho_w} \right) g \right)^{1/4} \tag{2.5}$$

and,

σ = surface tension of the chemical (N/m)

ν_l = kinematic viscosity of the chemical (m^2/s)

Raj and Kalelkar's (1974) concluded that the variations in viscosity and surface tension (non-dimensional quantities) do not have a marked effect on the value of the maximum radius of the pool. However, it also shows that small changes in these parameters affect to great extent the times at which the spill makes a transition from one spreading regime to the next.

2.3 SPILL (Shaw and Briscoe, 1980)

The SPILL model was developed by the Safety and Reliability Directorate (SRD) for the Health and Safety Executive (HSE) in the UK. The authors (Shaw and Briscoe, 1980) indicate that the model is limited to single-component liquid pools formed from releases of cryogenic or pressurised gases on land and water. Both catastrophic releases (e.g. vessel failure, ship collision) and minor containment failures (e.g. vessel inlet/outlet pipe rupture) are considered when modelling the source terms for the model. The model predicts transient pool spreading and vaporisation rates.

2.3.1 Theoretical background

SPILL's spreading on water model uses Fay's (1969) equation for the pool radius as a function of time in the gravity-water resistance regime. Shaw and Briscoe (1980) argued that due to the speed with which cryogenic pools boil-off, the subsequent spreading regimes where viscosity and surface tension forces prevail are rarely encountered.

The spreading of pools on land follows a similar approach to the spreading on water. The resulting equations for spills on land and water are as follows.

For instantaneous spills the radius of the pool is given by:

$$r = \left[{r_0}^2 + \left(\frac{8g\Delta V_0}{\pi} \right)^{0.5} t \right]^{0.5} \tag{2.6}$$

where,

r_0 = the radius of the pool at the previous time step (m)

V_0 = the volume initially spilled assumed to remain constant (m^3)

$$\Delta \begin{cases} = 1 & \text{for pools spreading on land} \\ = \dfrac{\rho_w - \rho}{\rho_w} & \text{for pools spreading on water} \end{cases}$$

The rest of the symbols are as previously defined.

For a continuous spill of volumetric rate, $\dot{V}_c$, Shaw and Briscoe (1980) express the pool radius as:

$$r = \left(\frac{32 g \Delta \dot{V}_c}{9\pi} \right)^{1/4} t^{3/4} \tag{2.7}$$

It should be noted that the value $(8/\pi)^{0.25} = 1.263$ which appears in equation (2.7), is close to the value of 1.14 in equation (2.1) originally proposed by Fay (1969) (see also the discussion in section 2.2.1).

The vaporisation rate from the cryogenic pool per unit area is obtained directly from the heat flux from the surface by (Shaw and Briscoe, 1980):

$$\dot{m}''_{vap} = \frac{Q''_{surf}}{\Delta H_{vap}} \tag{2.8}$$

where,

$\dot{m}''_{vap}$ = pool vaporisation rate per unit area (kg/m^{2}s)
Q''_{surf} = the heat flux from the surface (W/m^2)
ΔH_{vap} = heat of vaporisation at the pool temperature (J/kg)

In the case of water surfaces, a constant heat flux is considered, based on field observations (Burgess et al., 1970, 1972; Boyle and Kneebone, 1973). For pools on land, the heat transferred from the surface is modelled as a transient 1-D problem (Incropera and DeWitt, 1996). This model takes into account the gradual decrease in the rate at which heat enters the pool due to the cooling of the ground in contact with the cryogenic liquid. When the heat influx decreases to a level such that more heat than that provided is required for the pool to keep boiling, the pool temperature is expected to drop below the normal boiling point of the liquid. However, Shaw and Briscoe (1980) conservatively assume that the pool remains at the normal boiling point of the material until complete vaporisation.

2.3.2 Validation of results

Shaw and Briscoe (1980) verified their model by comparison against various empirical and theoretical models including those by Burgess et al. (1972), Lind (1974), Fay (1973) and Raj and Kalelkar (1974). The case study was based on an instantaneous 1000 m^3 LNG spill at 112 K on calm water.

The good agreement observed between the predictions of Shaw and Briscoe (1980), Fay (1973) and Raj and Kalelkar (1974) follows from the fact that these models use similar spreading laws. However, significant differences are observed in the results obtained using Burgess et al. (1972) and Lind (1974) models. These last two models predict a linear instead of power relation between the pool radius and time (figure 2.2). Shaw and Briscoe (1980) credited this discrepancy to the limitations of the Burgess et al. (1972) and Lind (1974) empirical models. These models were based on experiments carried out by the U.S. Coast Guard (Burgess et al., 1972) and ESSO Research and Engineering Company (Feldbauer et al., 1973), respectively, where between 0.1 and 10 m^3 of LNG were released on a water basin.

2.4 GASP (Webber, 1990)

Gas Accumulation over a Spreading Pool (GASP) was developed by the Safety and Reliability Directorate (SRD) for the Health and Safety Executive (HSE). The model describes the simultaneous spreading and vaporisation of an instantaneous or continuous release on land and water surfaces.

2.4.1 Theoretical background

GASP’s spreading model is based on the analytical solution of the shallow water equations generalised to include turbulent or laminar frictional effects on land surfaces. The spreading model distinguishes between three different types of surfaces: smooth ground, rough ground and water. The distinction between smooth and rough surfaces is made aiming to account for the ability of the latter to hold liquid in large puddles. On a rough surface, the pool will spread until it reaches a minimum thickness which is dependent on the average surface roughness of the ground. Typically, the minimum thickness is set equal to the average surface roughness length.

GASP accounts for non-uniform pool heights by incorporating an effective shape factor, ***s***, defined as the ratio between the height at the pool's edge and the mean pool height (Webber, 1990). The mean pool height is the ratio of the volume to the surface area of the pool.

GASP's heat transfer model accounts for heat contributions from the surface, atmosphere, mass added to the pool (for continuous releases only), as well as solar radiation heating (for spills taking place during daylight) (Webber, 1990).

Spills of cryogenic liquids on water are given a more detailed treatment than previous models. Film boiling is incorporated into the model using Klimenko's (1981) correlation and is applicable when the heat flux into the pool exceeds a critical heat flux, defined as the transition point between nucleate and film boiling. For spills on water where no film boiling occurs, an experimentally determined heat transfer coefficient is used in line with previous models (see for example, Shaw and Briscoe (1980)).

GASP's vaporisation model uses the equation for the mass transfer coefficient developed by Brighton (1985), an improvement on previous works on evaporation (for example, Sutton (1934)), to give a more accurate treatment of the velocity and concentration profiles above the pool. According to Brighton (1985), the mass transfer from the liquid to the air is only limited by molecular diffusion across a stagnant boundary layer above the pool surface. The underlying assumption to this approach is that the surroundings provide the required heat input for the pool to be in thermal equilibrium with the air above it. Additionally, GASP allows the unified treatment of boiling and evaporating pools (Webber, 1990) by incorporating an interpolation function.

The computer implementation of GASP uses a variable step variable order Gear's method (Gear, 1971) for the solution of the system of ordinary differential equations. This numerical method was chosen by Webber (1990) for its ability to cope with the rapid numerical changes in the model solution during the transition between evaporating and boiling pools.

2.4.2 Validation of results

Webber and Jones (1987) used the experimental results from Moorhouse and Carpenter (1986) to validate GASP for the spreading and vaporisation of LNG on concrete. Brighton (1990) also validated GASP's evaporation model against Hakinson and Murphy (1987) experiments of n-Butane on land.

2.4.2.1 Moorhouse and Carpenter (1986)

Webber and Jones (1987) compared the variation of pool radius, *r*, with time, *t*, obtained by GASP with the experimental results obtained by Moorhouse and Carpenter (1986) for the simultaneous spreading and vaporisation of a continuous LNG spill on concrete. The LNG was released at 112 K at a rate of 64.5 kg/s. Additionally, a minimum thickness of 10^{-2} m was used to obtain GASP's predictions.

Webber and Jones (1987) found excellent agreement can be observed between GASP and the experimental data. This is believed to be partially related to the use of a value for the minimum thickness (10^{-2} m) employed in the GASP's simulation. For spreading on rough surfaces, GASP assumes a layer of fluid of height equivalent to the surface roughness length is held-up by the irregularities of the surface (Webber, 1990). This is denoted in GASP as the minimum thickness. The minimum thickness was set to 10^{-2} m, which seems rather high for a concrete surface (a value of $5 \cdot 10^{-3}$ m for concrete is usually found in the literature (van den Bosch, 2005a; Napier and Roopchand, 1986)). However, Moorhouse and Carpenter (1986) used the same value of 10^{-2} m for obtaining good agreement between their own model and the experimental data.

Webber and Jones (1987) attributed the oscillations in the predicted pool radius, observed in figure 2.5, to the dynamic aspects of the spreading model and considered them to represent small gravity waves. The authors also highlighted the impact of the oscillations on the computational workload as the calculation algorithm is forced to decrease the step size in order to maintain accuracy.

2.4.2.2 Hakinson and Murphy (1987)

Hakinson and Murphy (1987) carried out a set of eight tests in which an insulated square pan of side equal to 1.22 m containing 100% n-Butane was allowed to evaporate under the influence of wind and sun as summarised in table 2.1. Wind speed was sampled at a height of 0.3 m from the ground at the side of the pool, which is a more reliable measurement than at heights of 10 m previously reported in similar experiments. Additionally, the evaporation pan was recessed into the ground to avoid distortion of the wind speed profile above the pool by protrusion of the edges of the pan. The evaporation rate was determined by the change in level of n-Butane in the pan measured over regular time periods.

The tests were carried out under a wide range of ambient conditions, e.g. wind speeds ranges between 0.5 to 5.5 m/s and ambient temperatures were between 275 and 290 K. Also, the atmospheric stability varied greatly between the tests as some were carried out during the day and others at night time.

Brighton (1985) compared the Hakinson and Murphy (1987) experimental data and model for the variation of the average mass transfer coefficient, denoted as j, with the dimensionless number $\mathrm{Re}_0^{1/2}\cdot\mathrm{Sc}$ where,

Re_0 = roughness Reynolds number $\left(\frac{u^* z_0}{\nu_a}\right)$

u^* = friction velocity (m/s)

z_0 = roughness length (m)

ν_a = kinematic viscosity of air (m^2/s)

Sc = Schmidt number (ν_a / D and D is diffusivity).

A roughness length of 2.28 x 10^{-4} m and wind speed ranging from 1.0 to 6.9 m/s were used as inputs to Brighton's (1985) model. The average mass transfer coefficient is a function of the ratio of the pan length to the roughness length, the roughness Reynolds number and the Schmidt number (Brighton, 1990).

Brighton (1990) found that his evaporation model over predicts the mass transfer coefficient with an average difference of 60%. The largest difference was observed for test 2 for which the model predicted an average evaporation rate three times higher than the measured rate. Test 2 was carried out during the night were the atmosphere is very stable and with a very low wind speed (0.5 m/s). For this test Brighton (1990) found that the Richardson number was very close to unity, indicating that the air flow above the pool was driven by density differences and not by the kinetic energy of the wind.

Brighton (1990) summarised the following as the possible causes of lack of agreement between the model and the experimental data:

- The validity of the gradient-transport hypothesis for turbulent diffusion: the gradient-transport assumption considers that turbulent diffusion can be modelled analogous to molecular diffusion.
- The mathematical approximation made to achieve an analytical result

- The validity of the assumption of passive vapour behaviour: by considering that the evolution of vapour from the pool won’t have an effect wind profile above the pool
- The failure of experimental conditions to match the idealised assumptions (e.g. developing boundary layer, change of surface roughness, etc.)

2.5 Phast (Witlox, 2008)

Phast (Witlox, 2008) was developed as commercially available software by Det Norske Veritas (DNV) for the purposes of risk assessment in the process industry. Phast includes a single-component pool model that accounts for spreading, vaporisation and dissolution, for both continuous (constant or variable rate) and instantaneous releases.

2.5.1 Theoretical background

Phast’s model for pool spreading on land follows on the work of Shaw and Briscoe (1980) (see section 2.3.1) by implementing a spreading law where the velocity at the leading edge of the pool is proportional to the square root of the pool depth. For spreading on water, Phast uses Dodge et al.’s (1983) spreading equations for instantaneous and continuous releases for the three successive regimes which consider the effects of gravity, water resistance, viscosity and surface tension in the same way as Fay (1969) model (see sections 2.2.1 and 2.3.1).

Phast pool model predicts the variation of the pool temperature over time by performing an energy balance over the control volume of the pool. Phast pool model accounts for heat transfer from the surface, atmosphere and solar radiation incidence. For spills on water two parallel mechanisms for heat transfer between the pool and the surface are used; the first, accounts for heat transfer due to convection and the second, accounts for heat loss or gain from the dissolution of soluble chemicals in water. For spills of cryogenic chemicals on water a model for ice formation based on Reid and Smith (1978) is implemented. Validation of the ice formation model is also presented in Reid and Smith (1978) for small scale spills of LNG.

The vaporisation model distinguishes between two limiting cases; a cryogenic release that boils violently upon release and a volatile pool that evaporates at a temperature lower than its boiling point. For a boiling pool, the vaporisation is driven by the rate of heat entering the pool that provides the necessary energy for the phase change to occur. In an evaporating pool, the vaporisation rate is controlled by the rate of mass transfer across a boundary layer formed above the pool surface, similarly to other models (see for example, GASP (Webber, 1990)). For evaporating pools, Phast's expression for the mass transfer coefficient is based on MacKay and Matsugu's (1973) model, modified to account for high mass transfer rates.

Phast pool model also considers mass losses by dissolution of water-soluble chemicals on rivers, channels or open sea spills. The model follows on equations first presented by Dodge et al. (1983) that consider the effects of waves and surface roughness, dependent on the wind velocity.

2.5.2 Validation of results

Witlox (2008) validated Phast pool model against experimental data for spills on land and water. Three sets of experimental results were used:

- Dodge et al. (1983) – spreading of n-Pentane on calm water
- Reid and Wang (1978) – vaporisation of LNG on concrete
- Kawamura and MacKay (1987) – evaporation of various hydrocarbons on sand

2.5.2.1 Dodge et al. (1983)

Witlox (2008) compared the variation of the pool radius with time obtained by Phast pool model with the experiments of Dodge et al. (1983) for the instantaneous release of 0.04 m^3 of n-Pentane on calm water. The wind speed during the test was 1.83 m/s measured at 10 m above the water basin and the pool had an initial temperature of 293 K.

Witlox (2008) found that Phast pool model generally shows good agreement with the experimental data despite the minor over-prediction (by ~ 5s) of the time for the pool to reach its maximum area. Similar to the other models already presented in this review, the pool spreading on water equations in Phast are semi-empirically derived. Consequently, the over-prediction of the time for the pool to reach its maximum area may be due to the range of validity of the empirical constants used in this model.

2.5.2.2 Reid and Wang (1978)

Witlox (2008) compares the variation of cumulative mass vaporised with the square root of time obtained by Phast pool model with the experimental results from Reid and Wang (1978) for the instantaneous release of 20 kg of LNG on a confined concrete surface. The initial temperature of the LNG was 112 K and the surface temperature of the concrete was in the range 280 – 290 K. Good agreement is found between the model and experimental data.

2.5.2.3 Kawamura and MacKay (1987)

Phast's pool evaporation model was validated by Witlox (2008) using experimental data obtained by Kawamura and MacKay (1987) for the evaporation of confined pools of hydrocarbons on sand. The results of the validation are given in table 2.2.

From the table it can be seen that Phast pool model produces more accurate predictions for higher vapour pressure chemicals such as n-Pentane and Hexane as compared to the less volatile substances such as Toluene and Freon 11. The maximum error reported by the authors is close to 50%.

Table 2.1. Comparison of the average evaporation rate obtained using Phast and the experimental results obtained by Kawamura and MacKay (1987) for the evaporation of confined pools of hydrocarbons on sand (Witlox, 2008)

Test number	**18**	**19**	**20**	**21**	**22**	**23**
Chemical	Toluene	Cyclo-hexane	Hexane	n-Pentane	n-Pentane	Freon 11
Experimental evaporation rate (g/m^2.s)	1.08	2.61	2.02	6.39	7.53	9.69
Model evaporation rate (g/m^2.s)	0.56	2.09	1.74	6.37	8.07	13.85
% difference	-48	-20	-14	0.3	7	43

2.6 Brambilla and Manca (2009)

Brambilla and Manca’s (2009) single-component pool spreading and vaporisation model is based on GASP (Webber, 1990), with various modifications to account for the following effects:

- Friction in the presence of film boiling
- Turbulent mixing on water
- The estimation of the friction velocity at the pool surface

2.6.1 Theoretical background

Brambilla and Manca’s (2009) spreading model incorporates Webber’s (1990) solution for shallow water equations with friction. Additionally, Brambilla and Manca’s (2009) model introduces a friction estimation in the presence of film boiling which accounts for a reduction on the drag between the pool and the water surface.

For spills on water when no film boiling occurs, Brambilla and Manca’s (2009) model propose a turbulence factor to account for an increase in the heat transfer between the surface and the pool due to turbulent mixing. According to a previous study of Hissong (2007), the turbulence factor can be affected by:

- The velocity of the released substance when it hits the water surface
- The interfacial area between water and the spilled substance and their relative motion
- The scale of the release

Unfortunately, there is a little knowledge at present regarding some of the parameters of the proposed correlation for the turbulence factor. Consequently, further experiments are needed to validate the correlation and to determine the values of the involved constants.

Brambilla and Manca (2009) also proposed a correlation to evaluate the friction velocity on the pool surface. The friction velocity is a required input for Brighton's (1985) evaporation model implemented into GASP. Following the implementation of a rigorous method for estimating the friction velocity (van Ulden and Holstlag, 1985), Brambilla and Manca (2009) suggest the percentage values shown in table 2.3 for various wind speeds at 10 m above the pool, at day-time and night-time conditions, for smooth and rough land and sea surfaces.

Table 2.2. Summary of the friction velocity estimates based on the wind speed at day-time and night-time conditions for smooth and rough land and sea surfaces

	Smooth land surface	Rough land surface	Smooth sea surface[*]	Rough sea surface[**]
Day-time	8% of the wind speed at 10 m	14% of the wind speed at 10 m	3.5% of the wind speed at 10 m	8.5% of the wind speed at 10 m
Night-time	5.5% of the wind speed at 10 m	11% of the wind speed at 10 m	3.5% of the wind speed at 10 m	8.5% of the wind speed at 10 m

[*] Sea surface considered smooth at wind speeds less than 7 m/s

[**] Sea surface considered rough at wind speeds greater or equal to 7 m/s

The computer implementation of Brambilla and Manca's (2009) model adopted a variable coefficient and variable time step numerical algorithm to solve ordinary differential equations called VODE (Brown et al., 1989). This routine is capable of integrating both stiff and non-stiff problems. It uses a variable-coefficient Adams-Moulton method for non-stiff cases and Backward Differentiation Formula (BDF) for stiff problems.

2.6.2 Validation of results

Brambilla and Manca (2009) tested the correlation developed to predict the friction velocities given in table 2.3 against experimental data. Table 2.4 present the comparison data for LNG spills on water carried out at China Lake, California, US in the 1980s, namely the Coyote series (Goldwire et al., 1983).

As can be observed, in most cases, relatively good agreement between model and test data is obtained.

Table 2.3. Validation of van Ulden and Holstlag (1985) model with Coyote series (Goldwire et al., 1983) data (Brambilla and Manca, 2009)

Test number	Friction velocity (m/s)		Monin-Obukhov length (m)	
	Measured	Evaluated	Measured	Evaluated
3	0.280	0.310	-6.35	-14.06
4a	0.280	0.298	-24.2	-15.46
4b	0.269	0.285	-33.3	-26.2
4c	0.328	0.380	-79.4	-63.4
5	0.439	0.459	-16.5	∞

In order to validate the spreading model, Brambilla and Manca (2009) compared the experimental data of Cronin and Evans (2002) with simulated results. Cronin and Evans (2002) experiments involved the spreading of water over a concrete surface using different bund arrangements. Brambilla and Manca (2009) observed that the spreading model is in good agreement with the experimental data, especially in terms of the time at which the water reaches the bund.

2.7 Drivas (1982)

Drivas' (1982) model was one of the first developed to simulate the evaporation of individual components in a mixture of volatile chemicals. The model can determine the total evaporation rate, liquid composition and vapour composition as a function of time.

It focuses solely on the vaporisation of confined spills, excluding the applicability of the model to cases where both spreading and vaporisation take place.

2.7.1 Theoretical background

Drivas' (1982) formulation of the vaporisation rate for volatile multi-component pools assumes an ideal solution, and is only valid for non-boiling pool. The composition of the vapour leaving the pool is determined by Raoult's Law. The pool is also assumed to be well-mixed with uniform concentration and temperature.

Applying the mass transfer rate equation for each component in the mixture and under the above assumptions yields:

$$\frac{dn_i}{dt} = -k\ A\frac{n_i}{n_T}P_{vap\,i} \tag{2.9}$$

where,

$\frac{dn_i}{dt}$ = rate of moles of component i in the pool per unit time (kmole/s)

k = mass transfer coefficient (m/s)

A = area of the pool (m)

$\frac{n_i}{n_T}P_{vap\,i}$ = is the partial pressure of component i (Pa)

Assuming that the ratio n_T/A remains constant with respect to time, integrating the above equation and summing over all the components i in the mixture (where i = 1,.., n, n being the total number of components in the mixture) results in:

$$n_T = \sum_{i=1}^{n} n_i^{\,0} \exp(-kAP_{vap\,i}t) \tag{2.10}$$

where, n_i^0 is the initial number of moles of component i in the pool and n_T is the total number of moles in the pool.

Taking the derivative of equation (2.10) the following expression is obtained for the rate of moles loss from the pool:

$$\frac{dn_T}{dt} = -k\sum_{i=1}^{n} n_i^{\,0} P_{vap\,i}\,\exp(-kAP_{vap\,i}t) \tag{2.11}$$

Substituting n_i^0 for $x_{pooli}^0.n_T^0$ and expressing equation (2.11) in terms of mass instead of moles gives the following expression:

$$\frac{dM_{pool}}{dt} = -k\cdot M^0{}_{pool}\sum_{i=1}^{N}\frac{P_{vap\ i}\cdot x^0{}_{pool\ i}\cdot M_{w\ i}\cdot\exp\left(-k\cdot P_{vap\ i}\cdot t\right)}{\sum_{i=1}^{N} x^0{}_{pool\ i}\cdot M_{w\ i}} \tag{2.12}$$

where,

M_{pool} = total mass in the pool (kg)

k = mass transfer coefficient (m/s)

$M^0{}_{pool}$ = total mass in the pool at the previous time step (kg)

$P_{vap\ i}$ = vapour pressure of component i (Pa)

$M_{w\ i}$ = molecular weight of component i (kg/kmol)

$x^0{}_{pool\ i}$ = mass fraction of component i in the pool at the previous time step (kg/kg)

N = total number of components in the mixture

The mass transfer coefficient in equation (2.9), k, which represents the resistance to mass transfer in the gas phase, is expressed by MacKay and Matsugu's (1973) equation:

$$k = \left(\frac{\pi\cdot r^2}{n_{pool}\cdot R\cdot T}\right)\left(0.0292u^{0.78}(2r)^{-0.11}Sc^{-0.67}\right) \tag{2.13}$$

where,

n_{pool} = number of moles in the pool (kmol)

R = universal gas constant (=8.3144 J/K.kmol)

T = temperature of the pool (K)

u = wind speed at the reference height of 10 m (m/s)

2.7.2 Validation of results

Drivas (1982) validated the multi-component evaporation model against experimental data for crude oil weathering in a wind tunnel from Matsugu (1973).

Drivas (1982) found relative good agreement between the model and the experiment can be observed. Drivas' (1982) model is found to under predict the evaporation of the pool at early times and over predicts it after a few days. Drivas (1982) attributed the over prediction of evaporation, probably because the remaining oil becomes too viscous for the well-mixed assumption to apply. However, differences between theoretical and experimental values may also be due to simplifications made in the modelling of the actual composition of the crude oil.

2.8 LSM90 (Cavanaugh et al., 1994)

LSM90 model was developed by Exxon to model simultaneous spreading and vaporisation of multi-component spills on water and land surfaces. The model is able to account for transient changes in the composition of the remaining liquid and vapour leaving the pool. LSM90 only considers ideal mixtures.

2.8.1 Theoretical background

LSM90 uses Shaw and Briscoe (1980) model for the spreading of unconfined spills on land and water. For spills on land in the presence of bunds, LSM90 introduces a correction to account for the slightly more complex geometry of a concentric tank.

Heat transfer from the atmosphere, ground, bund, mass spill rate (for continuous releases), and the effect of solar incidence are accounted for in the model.

LSM90 treats boiling and evaporating pools independently, but allows transitions to take place between these two scenarios. An example of a transition could be a cryogenic spilled at a temperature lower than its saturation temperature, or a spill of a chemical that boils close to ambient temperature such as n-butane (i.e., normal boiling point -0.5 ^{o}C).

The vaporisation rate for evaporating pools follows on the work of Drivas (1982) (see section 2.7.1), also applying the well-mixed assumption. On the other hand, in a boiling pool, a flash calculation allows the calculation of the necessary amount of heat to be removed from the pool in order to maintain its temperature at the mixture's bubble point.

The numerical solution of the ordinary differential equations in the computer implementation of LSM90 is given by a first order finite differences method with a variable step size. The step size is adjusted based on the criteria that the pool mass should not change by more than 1% or the pool temperature should not vary by more than 1 K during a time step. The purpose of these criteria is to maintain the accuracy of the solution without significantly increasing the computational workload. However, the different time scales involved in the simultaneous solution of the spreading and vaporisation problems make the system stiff, posing numerical problems that may not be efficiently countered by an explicit first order method.

2.8.2 Validation of results

Cavanaugh et al. (1994) model was validated against Burro (Koopman et al., 1980) and Esso Matagorda Bay (Feldbauer et al., 1972) series of LNG experiments on unconfined water.

Cavanaugh et al. (1994) found the maximum deviation between predicted and measured evaporation rate to be close to 50%, agreement within 14% between model and field data was observed in eight out of ten experiments. Better agreement was found at lower than at higher evaporation rates. However, the lack of further detail in the presentation of the validation does not allow concluding on a possible trend for the accuracy of the model predictions.

2.9 Leonelli et al. (1994)

Leonelli et al.'s (1994) multi-component pool model accounts for ideal and non-ideal liquid mixtures. In this publication, the authors present and compare two pool models; the first of them assumes a well mixed pool with a uniform temperature; the second model introduces the concept of a pool formed by two parts a well-mixed bulk and a very thin surface layer. The models account for simultaneous spreading and vaporisation on confined and unconfined land surfaces, and can handle instantaneous or continuous releases.

2.9.1 Theoretical background

Leonelli et al.'s (1994) spreading model follows on the work of Shaw and Briscoe (1980) for pools on land. Equations for the pool radius as a function of time are presented for both instantaneous and continuous spills. Heat contributions from the surroundings to the pool include conductive heat transfer from the ground, convective heat from the atmosphere and solar incidence.

The vaporisation model can consider non-ideal or ideal liquids. In the case of ideal mixtures, Leonelli et al. (1994) use Raoult's Law. For non-ideal mixtures, activity coefficients are introduced to the model.

As with models previously reviewed here (see for example, LSM90 and Phast), boiling and evaporating pools are given a separate treatment and allowances are made for the pool to make a transition between one vaporisation regime and the other. For boiling pools, a flash calculation using Rachford-Rice relation combined with an energy balance is performed to determine the amount of vapour generated and the temperature increment in the pool at the time step. For evaporating pools, Leonelli et al. (1994) carried out a comparative analysis between the following models:

- MacKay and Matsugu (1973)
- Pasquill (1943)
- Heat-mass transfer analogy for a flat plate in laminar flow

In the stratified pool model, separate heat balances are carried out for the bulk and surface layers. The heat required for vaporisation at the pool surface is provided by solar radiation and convection from the atmosphere and from the bulk layer. The energy balance for the bulk includes conduction from the soil and heat contributions from new mass added to the pool.

2.9.2 Validation of results

Leonelli et al. (1994) presented the validation of their model against experiments carried out by Mikesell et al. (1991) with solutions of ammonia and water over an insulated pan. In figure 2.14, the cumulative mass vaporised vs. time for a solution of initially 28.8% w/w ammonia, 71.2% w/w water is presented. Leonelli et al. (1994) compared the temperature variation over time for the well-mixed and stratified pool model against the experimental data.

The results of the comparison between model and experimental data showed a better fit for MacKay and Matsugu's (1973) model as compared to the others. Even though the pool dimensions are small (diameter 26 cm), and full turbulent flow may not develop along the length of the pool, the correlation for laminar flow predicted low values for the evaporation rate in comparison to observations.

When comparing the pool temperature predicted by the stratified and well-mixed pool models Leonelli et al. (1994) found that the former agrees better with the measured data. Although, as far as the evaporation rate is concerned, the authors reported that there were practically no differences between the results obtained with the stratified and the well-mixed model.

2.10 CHEMMAP (French and Isaji, 2004)

CHEMMAP (French and Isaji, 2004) is a chemical spill model designed to predict the trajectory, fate, impacts and biological effects of chemicals and product mixtures accidentally released on water. The model has been used, under contract by the Minerals Management Service (MMS) of the US Department of Interior to analyse environmental risks associated with chemical products used in deepwater oil and gas operations in the Gulf of Mexico. CHEMMAP incorporates a number of modules which simulate the following conditions:

- Initial release for surface and subsurface spills
- Slick spreading, transport and entrainment of floating materials
- Evaporation and volatilisation
- Dissolution and adsorption
- Sedimentation and resuspension
- Degradation

For the present purposes the phenomena included in this review will be the spreading, transport, evaporation and dissolution of floating materials on water.

2.10.1 Theoretical background

CHEMMAP estimates the spreading rate of the slick using the algorithm of Fay (1971), which considers three successive regimes where the effects of gravity, water resistance, viscosity and surface tension are accounted for (see also section 2.2.1).

CHEMMAP only considers the evaporation of volatile liquid pools and does not account for the behaviour of cryogenic spills. Pool evaporation is modelled following the approach of MacKay and Matsugu (1973). Conceptually, this model assumes that the mass transfer from liquid to the air is only limited by molecular diffusion across a stagnant boundary layer above the pool surface. As was mentioned in section 2.5.1, the underlying assumption to this approach is that the surroundings provide the required heat input for the pool to be in thermal equilibrium with the air above it.

Dissolution of a chemical of interest from an insoluble solvent (such as naphtha, for example) is modelled following on the work of MacKay and Leinonen (1977). The slick is treated as a flat plate, with a mass flux related to solubility and temperature. It assumes a well-mixed layer with most of the resistance to mass transfer lying in the hypothetically stagnant region close to the slick. The dissolution rate of pure chemicals is expressed as a function of solubility by a first-order constant rate equation.

2.10.2 Validation of results

French et al. (2006) presented the validation of the model against experiments carried out by Kawamura and MacKay (1987) who measured the evaporation rate of various chemicals from a galvanized sheet-metal pan using toluene, cyclohexane, hexane and dichloromethane.

French et al., (2006) state that the closeness of the best fit curve (linear regression) of their results to the ideal 1:1 line points towards good correspondence between predicted and real data. However, the low value of the regression coefficient ($R^2 = 0.421$) indicates that the best fit curve does not represent the actual trend of the data points, thus higher differences between model and experiments are expected.

2.11 Concluding remarks

Based on the above review, it is clear that there is still significant scope for improving Integral pool models reported in the open literature.

The review showed that while current multi-component pool models are able to predict spreading and vaporisation in different types of surfaces (Cavanaugh et al., 1994 and Leonelli et al., 1994), they fail to account for the dissolution of water-soluble chemicals in spills on rivers, bays or in open sea. Of the models presented in this review, dissolution has only been considered for pure components in Phast (Witlox, 2008) and Raj and Kalelkar (1974) models.

There is still uncertainty in some parameters used in integral models, such as the constant K for spreading on water, the minimum thickness for spreading on land and the heat transfer coefficient between the pool and water surface. This is partly due to the fact that these parameters are based on the available experimental data which is mostly old and at small scale.

Webber (1990) and Brambilla and Manca (2009) highlighted the numerical difficulties intrinsic to the simultaneous solution of the spreading and vaporisation equations. Both use in their computer implementation a variable step numerical algorithm to avoid the pitfalls of a stiff problem. Still, further improvement in the robustness of the solution of the pool model can be achieved by implementing a more efficient numerical routine.

CHAPTER 3. BACKGROUND THEORY FOR THE MODELLING OF POOL SPREADING, VAPORISATION AND DISSOLUTION

3.1 Introduction

In the previous chapter, a comprehensive review of the state of the art in evaporating pool modelling was presented. The review highlighted the limitations of the existing models in terms of range of application, accuracy and computational efficiency. In this chapter the background theory for the modelling of pool spreading, vaporisation and dissolution based on the published literature is presented. This theoretical background summarises the assumptions and model approximations incorporated in the Phast pool model, reviewed in the previous chapter. The chapter then concludes with the motivation for the present study.

In this chapter, the derivation of the model equations governing spreading, evaporation and dissolution of cryogenic and volatile pools is presented. This includes:

- The general assumptions made in developing the model
- Derivation of the equations that describe the spreading of the pool on land and water surfaces
- Derivation of the equations that describe the rate of mass transfer between the pool and the surroundings due to vaporisation and dissolution
- Derivation of the equations that describe the transient heat transfer between the pool and the surroundings

3.2 Modelling assumptions

The major assumptions made in the development of the pool spreading and vaporisation model employed in this study are (Witlox, 2008):

1. The fluid properties of the pool including density, specific heat capacity and vapour pressure are assumed to be constant over the entire volume of the pool at each time step. This is the underlying assumption in all integral pool models which handle average properties across the pool volume

2. The pool is cylindrical in shape. This assumption is applied to unconfined pools spreading over flat surfaces such as flat ground or water basins and to confined pools spreading inside a bund. In the case of a confined pool, the maximum radius of the pool is equal to the radius of the bund. Once the pool has reached its maximum radius, variations in the volume of the pool due to evaporation and spill rate are accounted for by changing the height of the pool

3. The pool is axis-symmetric with the spill source located in the centre of the pool

4. Only fluid flow in the radial direction is considered

5. The height of the pool is uniform along its length. In reality, the pool will have a height profile depending on the topography of the surface (e.g., if the surface is inclined, rough or smooth). Except at early stages of spreading, the pool height is very small with respect to the pool radius, so the variation on the pool height is small with respect to the horizontal spreading distance. Average uniform pool height is therefore a common approximation in Integral pool models
6. The pool is well-mixed. The pool is assumed to be sufficiently thin so that its temperature is constant in the vertical direction. For volatile pools, a temperature gradient in the vertical direction exists if the ground and air above the pool are at different temperatures. However, some authors (see for example Leonelli et al., 1994) have reported little impact on the prediction of the vaporisation rate when

accounting for a vertical temperature gradient in the pool. Experimental confirmation of this phenomenon is however not available

7. The vapour above the pool behaves as an ideal gas. This is a reasonable simplification given that the pool is subject to low pressures (1 atm)

3.3 Pool spreading

In this section, the derivation of spreading laws for spills on land and water surfaces for instantaneous and continuous releases, following studies by Dodge et al. (1983), is presented. For the spreading of pools on water, the radius of the pool is expressed as an explicit function of time. For the spreading of pools on land, the radius of the pool is determined from the radial velocity at the edge of the pool.

3.3.1 Pool spreading on water

The spreading of a pool on water can be divided into three consecutive regimes: gravity-resistive, resistive-viscous and viscous-surface tension (Fay, 1969). In each regime one or more of the forces that cause or retard the spreading of the pool (gravitational, resistive, viscous and surface tension forces) is dominant and subsequently governs the velocity at the edge of the pool.

3.3.1.1 Gravity-resistive regime

Figure 3.1 shows the idealised spreading of a pool on water. In this regime, the transient spreading of the pool is driven by the gravitational potential energy associated with the elevated and the submerged part of the pool and is turned into kinetic energy associated with the outward radial motion of the pool (Ponchaut et al., 2009).

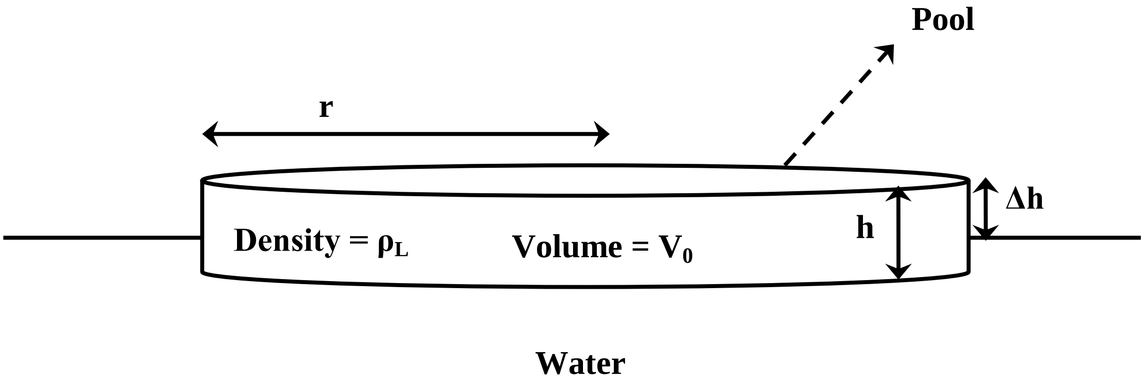

Figure 3.1 Schematic representation of a pool spreading on water. r, h and Δh, are respectively, the pool radius, the pool height and the height of the elevated portion of the pool due to buoyancy

For the spreading of a pool on water, the continuity equation can be written as (Hoult, 1972a):

$$\frac{\partial h}{\partial t}+\frac{1}{r}\frac{\partial}{\partial r}\left(rUh\right)=0 \tag{3.1}$$

where,

t = time (s)
U = radial velocity of the pool (m/s)

For a pool with low depth, at any given time, the variation of height in the radial direction is very small. Consequently, the pool is assumed to be in hydrostatic equilibrium in the vertical direction. A simple hydrostatic calculation shows that the horizontal force due to the fact that the oil floats on the water is (Hoult, 1972a):

$$F_{res}=\left(\frac{1}{2}\rho_w\, g\, r\, \Delta h^2\right) \tag{3.2}$$

The resistive force, $F_{res,}$ balances the acceleration of the oil slick. Thus, the momentum balance around the pool can be expressed as (Hoult, 1972a):

$$\rho_w\left(\frac{\partial hU}{\partial t}+\frac{1}{r}\frac{\partial}{\partial r}\left(rhU^2\right)\right)=-\rho_w g\Delta h\frac{\partial h}{\partial r} \tag{3.3}$$

The above expression can be further simplified using equation (3.1) resulting in:

$$\frac{\partial U}{\partial t} + U\frac{\partial U}{\partial r} + g\Delta\frac{\partial h}{\partial r} = 0 \tag{3.4}$$

Equations (3.1) and (3.4) describing the conservation of mass and momentum are comparable to the equations of a compressible polytropic gas, in which the wave speed, c, (m/s) is given by (Hoult, 1972a):

$$c = \sqrt{g\,\Delta h} \tag{3.5}$$

Thus, from equation (3.5), Hoult (1972a) gave the radial velocity at the leading edge of the pool, U_{LE}, as:

$$U_{LE} = (\lambda g\,\Delta h)^{1/2} \tag{3.6}$$

where, λ is an empirical constant.

Dodge et al. (1983) determined the radius of the pool in the gravity resistive regime for an instantaneous pool by assuming U_{LE} to be equal to r/t and substituting h as a function of the initial volume released V_0:

$$r = K_1 (V_0 g\Delta)^{1/4} t^{1/2} \tag{3.7}$$

where, K_1 is an empirical constant (=1.53) derived from Dodge et al. (1983) experiments.

For continuous spills of constant rate, $\dot{m}_{spill}$, the radius of the pool in the gravity resistive regime is obtained by substituting the term V_0 in equation (3.7) for the volume spilled up to the current time, $(\dot{m}_{spill}\ t)/\rho$, (Dodge et al., 1983):

$$r = K_2 \left(g\Delta\frac{\dot{m}_{spill}}{\rho} \right)^{1/4} t^{3/4} \tag{3.8}$$

where, K_2 is an empirical constant (=1.24) derived from Dodge et al. (1983) experiments

3.3.1.2 Viscous-resistive regime

As the pool height decreases due to spreading, the gravitational acceleration of the spill will reduce and the viscous drag between the pool and the water surface will become the predominant force. A viscous boundary layer of a given thickness will be formed below the pool as shown in figure 3.2.

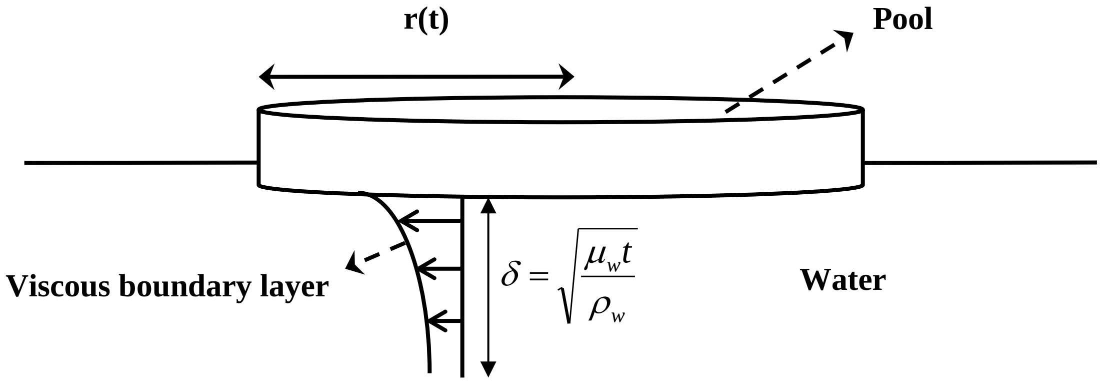

Figure 3.2. Schematic representation of the pool spreading in the viscous-resistive regime (Dodge et al., 1983)

Hoult (1972a) stated that the thickness of the viscous boundary layer can be approximated to:

$$\delta = \sqrt{\frac{\mu_w t}{\rho_w}} \tag{3.9}$$

where,

δ = thickness of the viscous boundary layer (m)

μ_w = water dynamic viscosity at the surface temperature (Pa.s)

The retarding force exerted on the pool by the viscous drag, F_{vis}, is proportional to (Hoult, 1972a):

$$F_{vis} = r^2 \frac{\mu_w}{\delta}\left(\frac{r}{t}\right) \tag{3.10}$$

Equating the retarding viscous force in equation (3.10) to equation (3.2), the following is obtained:

$$r\left(\frac{1}{2}\Delta g h^2\right) = K_v\, r^2\left(\frac{\mu_w}{\delta}\right)\left(\frac{r}{t}\right) \tag{3.11}$$

where, K_v is a proportionality constant.

By substituting *h* in the above equation for $V_0 / \left(\pi r^2\right)$ and solving for the pool radius, the following expression for an instantaneous spill is found (Dodge et al., 1983):

$$r = K_3\left(\frac{{V_0}^2 g\Delta}{\sqrt{\nu_w}}\right)^{1/6} t^{1/4} \tag{3.12}$$

where,

K_3 = empirical constant (= 1.21) derived from Dodge et al. (1983) experiments

ν_w = kinematic viscosity (m^2/s), given by:

$$\nu_w = \frac{\mu_w}{\rho_w} \tag{3.13}$$

For continuous spills of constant spill rate, analogously to the gravity-resistive regime, the pool radius in the viscous-resistive regime is obtained by substitution of V_0 (Dodge et al., 1983):

$$r = K_4\left(\frac{g\,\Delta \dot{m}_{spill}{}^2}{\rho_L \sqrt{\nu_w}}\right)^{1/6} t^{7/12} \tag{3.14}$$

where, K_4 is empirically derived (= 1.09) from Dodge et al. (1983) experiments

3.3.1.3 Viscous-surface tension regime

As vaporisation progresses the height of the pool further reduces and the resistive force at the edge of the pool (a function of the pool height, see equation (3.2)) becomes negligible. Surface tension effects become the dominant force opposing viscous drag when the pool height is of the order of 10^{-5} to 10^{-4} m (Dodge et al., 1983). The net surface tension (σ_{net}) is a sum of the interfacial tension effects between air (σ_{la}), pool and water (σ_{lw}), as shown in figure 3.3.

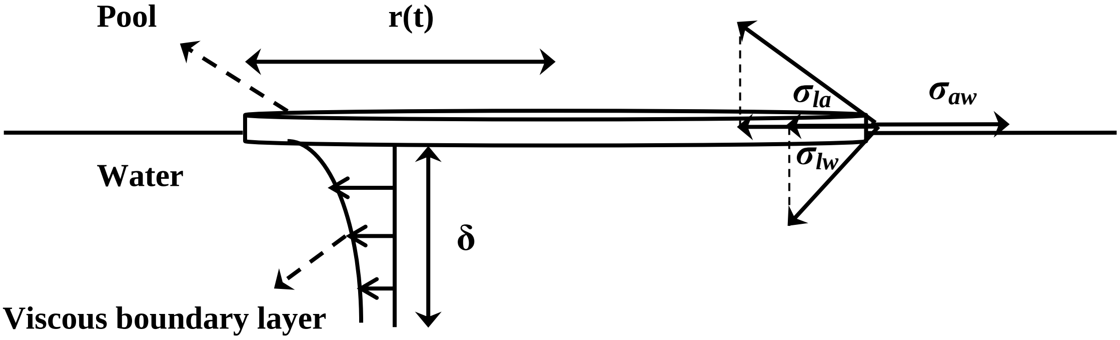

$$\sigma_{net} = \sigma_{aw} - \sigma_{la} - \sigma_{lw}$$

Figure 3.3. Schematic representation of the pool spreading in the viscous-surface tension regime (Dodge et al., 1983)

The balance of the viscous and surface tension forces is given by (Dodge et al., 1983):

$$2\pi r\sigma_{net} = \pi r^2\left(\frac{\mu_w U}{\delta}\right) \tag{3.15}$$

where,

σ_{net} = net surface tension (N/m) given by:

$$\sigma_{net} = \sigma_{wa} - \sigma_{la} - \sigma_{lw} \tag{3.16}$$

For instantaneous spills, the pool radius in the viscous-surface tension regime as a function of time is given by (Dodge et al., 1983):

$$r = \left(\frac{4\sigma_{net}^{2}}{\rho_w \mu_w} \right)^{1/4} t^{3/4} \tag{3.17}$$

For continuous spills, the viscous-surface tension regime occurs simultaneously with the viscous-resistive regime. Therefore, the pool radius for continuous spills at later vaporisation stages is determined from equation (3.14).

3.3.1.4 Transition time between spreading regimes

The transition between spreading regimes takes place when the equations for the pool radius as a function of time intersect (i.e., the predicted radii are equal).

Instantaneous spills

For instantaneous spills, the transition time, t_1 , from gravity-resistive to gravity-viscous spreading regime is calculated by equating equations (3.7) and (3.12):

$$1.53(V_0 g\Delta)^{1/4} t_1^{1/2} = 1.21 \left(\frac{V_0^{2} g\Delta}{\sqrt{\nu_w}} \right)^{1/6} t_1^{1/4} \tag{3.18}$$

$$t_1 = 0.378 \left(\frac{V_0}{g\, \nu_w \Delta} \right)^{1/3} \tag{3.19}$$

Similarly, the transition time, t_2 , between the gravity-viscous and viscous-surface tension regimes for instantaneous spills is calculated by equating equations (3.12) and (3.17):

$$t_2 = 1.464 \left(\frac{V_0^2 g\, \mu_w \Delta}{\rho_w} \right)^{1/3} \left(\frac{\rho_w}{2\sigma_{net}} \right) \tag{3.20}$$

Continuous spills

For continuous spills the transition time, t_3 , between the gravity-resistive and resistive-viscous regimes is calculated by equating equations (3.8) and (3.14):

$$t_3 = 0.773\left(\frac{\dot{m}_{spill}\rho_w}{\rho_L g\Delta\,\mu_w}\right)^{1/2} \tag{3.21}$$

As mentioned in section 3.3.1.3, both the viscous-resistive and viscous-surface tension regimes occur simultaneously for a continuous spill, therefore there is no transition time between them.

3.3.2 Pool spreading on land

Shaw and Briscoe (1980) derived a spreading law for pools on land similar to the gravity-resistive model for pools spreading on water. The viscous-resistive regime does not take place as the pool is spreading over a solid surface (i.e., no viscous boundary layer is formed between the pool and the surface). Additionally, land surfaces usually present a roughness of the order of 10^{-2} to 10^{-4} m which causes the pool to stop spreading before the surface tension effects become predominant.

The pool is modelled as a collapsing cylinder spreading over a thin film of height, h_{min}, equal to the average surface roughness length as shown in figure 3.4. This represents the liquid held by the roughness of the surface.

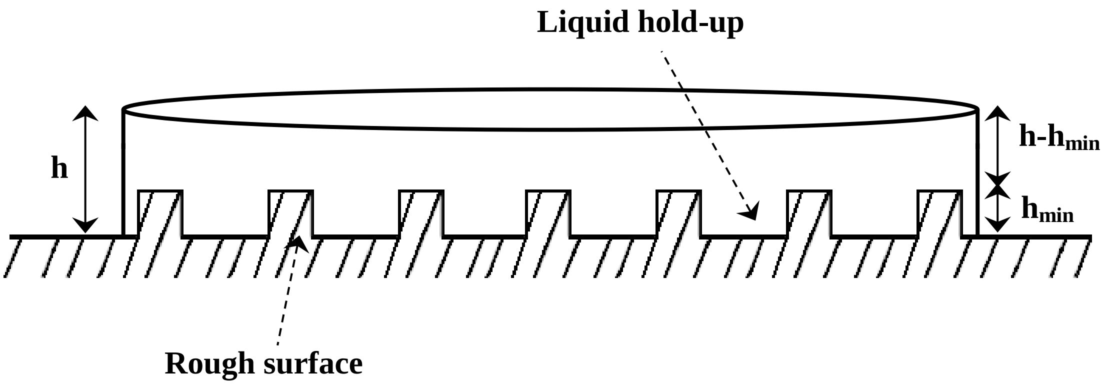

Figure 3.4. Schematic representation of a pool spreading on land

The spreading law used in this model for pools on rough land surfaces is given by (Shaw and Briscoe, 1980):

$$\frac{dr}{dt} = \sqrt{2g(h - h_{\min})} \tag{3.22}$$

where, $h_{\min}$ is the minimum pool depth (m) set equal to the roughness length of the surface.

3.4 Mass transfer

Figure 3.5 shows the flow of mass into (mass spill rate, $\dot{m}_{spill}$) and out of (due to vaporisation, $\dot{m}''_{vap}$, and dissolution, $\dot{m}''_{sol}$) a spreading pool following a continuous or instantaneous spill.

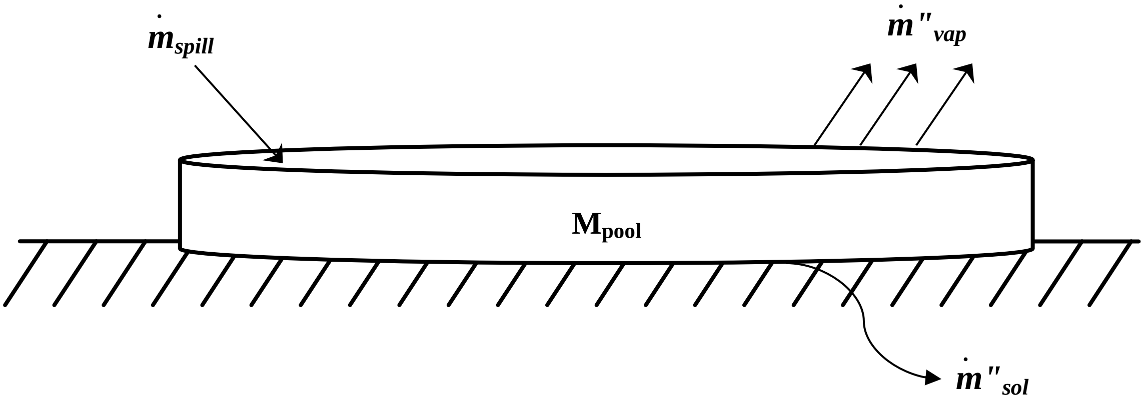

Figure 3.5. Schematic representation of the mass transfer taking place in the pool

A general mass balance over the control volume of the pool can be written as:

$$\frac{dM_{pool}}{dt} = \dot{m}_{spill} - \pi r^2 \left(\dot{m}''_{vap} + \dot{m}''_{sol}\right) \tag{3.23}$$

where,

M_{pool} = mass of the pool (kg)

$\dot{m}''_{vap}$ = mass vaporisation flux (kg/m^{2}s)

$\dot{m}''_{sol}$ = mass flux of the chemical dissolved in water (kg/m^{2}s)

Depending on the source term, the mass spill rate, $\dot{m}_{spill}$, can be equal to zero for instantaneous releases or a function of time for continuous releases. In this model, variable spill rates are approximated as average spill rates over specified time intervals. For spills on land and non-soluble chemical pools on water, the mass dissolved flux, $\dot{m}''_{sol}$, is equal to zero.

The vaporisation flux of the pool, $\dot{m}''_{vap}$, is dependent on whether the spill boils violently upon release or whether the resulting volatile pool evaporates at a temperature lower than its boiling point. For a boiling pool, the vaporisation rate is driven by the rate of heat entering the pool that provides the necessary energy for the phase change to occur. In an evaporating pool, the vaporisation rate is driven by the mass diffusion across a stagnant boundary layer above the pool surface.

3.4.1 Evaporating pools

The vaporisation flux, $\dot{m}''_{vap}$, from an evaporating pool can be expressed in the general form (Brighton, 1985):

$$\dot{m}''_{vap} = \left(C_s - C_\infty\right)u_a^* k_L^* \tag{3.24}$$

where,

C_s = vapour concentration at the pool surface (kg/m^3)

C_∞ = vapour concentration in the air bulk (kg/m^3)

u_a^* = wind friction velocity at the surface of the pool (m/s)

k_L^* = overall mass transfer coefficient corrected for high mass transfer rate, given by:

$$k_L^* = \theta \cdot k_L \tag{3.25}$$

where,

θ = correction factor applied for high mass transfer rate (–)

k_L = uncorrected mass transfer coefficient (–)

The vapour concentration in the air bulk is negligible (C_∞ = 0). Hence equation (3.24) becomes:

$$\dot{m}''_{vap} = C_s u_a^* \theta k_L \tag{3.26}$$

The vapour concentration at the pool surface, C_s, is calculated by assuming the vapour is saturated behaving as an ideal gas:

$$C_s = \frac{M_w P_v}{RT_L} \tag{3.27}$$

where,

M_w = molecular weight of the chemical (kg/kmol)
P_v = vapour pressure of the chemical (Pa)
R = universal gas constant (=8.3144 J/K.kmol)
T_L = temperature of the pool (K)

3.4.1.1 Estimation of the mass transfer coefficient

An expression for the uncorrected mass transfer coefficient, k_L, (see equation 3.25) can be derived from the solution of the advection-diffusion equation (Socolofsky and Jirka, 2004):

$$\frac{\partial C}{\partial t} + \nabla(uC) = D\nabla^2 C \tag{3.28}$$

where,

C = vapour concentration (kg/m^3)
u = velocity vector (m/s)
D = diffusion coefficient (m^2/s)
∇ = vector derivative

Assuming that air flows only in the horizontal direction, steady state conditions have been reached and C is the average concentration along the length of the pool, the above equation can be rewritten as:

$$u(z)\frac{\partial C}{\partial x} = D\frac{\partial^2 C}{\partial z^2} \tag{3.29}$$

where,

x = horizontal coordinate (m)
z = vertical coordinate (m)
$u(z)$ = velocity in the horizontal direction (m/s)

Defining a dimensionless concentration, χ, as the mass fraction of vapour to saturated vapour and replacing the diffusion coefficient by the turbulent eddy diffusivity, $K^{'}(z)$, the following equation is obtained:

$$u(z)\frac{\partial \chi}{\partial x} = \frac{\partial}{\partial z}\left(K^{'}(z)\frac{\partial \chi}{\partial z} \right) \tag{3.30}$$

$$K^{'}(z) = \frac{1}{\sigma}\kappa u^{*} z \tag{3.31}$$

where,

σ = turbulent Schmidt number
κ = von Karman constant (=0.41) (Brighton, 1985)

The solution of equation (3.30) requires an equation for the velocity profile, $u(z)$, and the implementation of boundary conditions at the pool surface and in the air bulk.

Kunsch (1998) following on the work of Brighton (1985) for evaporation from a liquid surface into a turbulent atmosphere introduced a wind velocity profile of the form:

$$u(z) = u_1\left(\frac{z}{z_1} \right)^{n/2-n} \tag{3.32}$$

where,

u_1 = wind speed at the height z_1 (m/s)
z_1 = height of the boundary layer over the pool diameter, *D* (m)

$$n = \left(Ln\left(\frac{z_1}{z_0} \right) \right)^{-1} \tag{3.33}$$

z_0 = the roughness length of the pool surface (m)

And the boundary conditions:

$$1-\chi = k_L\left[\frac{\sigma}{\kappa}Ln\frac{zu_a^{\;*}}{v_a}+\beta(Sc)\right] \text{ at } z=0 \text{ and } 0<x<D \tag{3.34}$$

$$\chi = 0 \text{ at } z=\infty \text{ and } 0<x<D \tag{3.35}$$

$$\chi = 0 \text{ at } x=0 \text{ and } z>0 \tag{3.36}$$

where,

v_a = kinematic viscosity of air (Pa.s)

$\beta(Sc)$ = semi-empirical correlation dependent on the Schmidt number

Sc = Schmidt number

The boundary condition at the pool surface (equation 3.34) accounts for the presence of a laminar sub-layer where mass transfer is dominated by diffusion. This boundary condition was first presented by Brighton (1985).

Kunsch (1998) solved equation (3.30), integrating over the thickness of the laminar layer above the pool, assuming a constant average vaporisation flux in the layer.

$$\begin{cases} k_L = \dfrac{C_2}{\beta(Sc)+\dfrac{\sigma}{\kappa n}\left(C_1C_2\dfrac{D}{z_0}\right)^{\frac{n}{1+2n}}} & (3.37) \\ C_1 = \dfrac{\kappa^2 n(1+n)(1+2n)}{\sigma e^{1/n}} & (3.38) \\ C_2 = 1+\dfrac{1}{2}\left(\dfrac{n}{1+n}\right) & (3.39) \end{cases}$$

where, e is the Napier constant (= 2.7183)

3.4.1.2 Mass transfer coefficients at high mass transfer rates

Mass transfer from an evaporating pool involves the bulk flow of material across the liquid-vapour interface. At low evaporation rates the bulk flow is only important in the calculation of the vapour flux across the interface. However, at higher mass transfer

rates the additional transfer of momentum and energy by the fluid vaporising liquid may be significant (Bird et al., 1960).
Several authors (Opschoor, 1979; Brighton, 1985; Kunsch, 1998) have adopted a correction factor, θ, (see equation (3.26)) for the mass transfer coefficient at high mass transfer rates derived from film theory. This is based on one-dimensional mass transfer in the vertical direction where the thickness of the laminar layer above the pool is constant along its length. However, Opschoor (1979) indicates that a correction factor derived from boundary layer theory gives a more accurate correction than the film theory.

The correction factor derived using boundary layer theory takes into account the effect of the variation in velocity and concentration in both the vertical and horizontal directions (Bird et al., 1960) and is given by:

$$\theta = \frac{\prod'(0, Sc, K)}{\prod'(0, Sc, 0)} \tag{3.40}$$

where, $\prod'(0, Sc, K)$ is the dimensionless concentration gradient at the pool surface and $\prod'(0, Sc, 0)$ is the dimensionless concentration gradient at the pool surface at negligible mass transfer rates.

Values for θ as a function of the rate factor, ϕ, are shown in table 3.1.

Table 3.1 Values for the correction factor for mass transfer coefficients calculated using the boundary layer theory (Bird et al., 1960)

Rate factor (ϕ)	θ
0.01	1.006
0.02	1.011
0.05	1.029
0.1	1.057
0.2	1.117
0.5	1.304
1.0	1.646
2.0	2.421
3.0	3.282
5.0	5.140
∞	∞

The values in table 3.1 show that θ approaches unity as the vapour pressure approaches zero. θ also increases with increasing vapour pressure, up to infinity when the vapour pressure is equal to the atmospheric pressure. At this point the pool makes a transition from evaporation to a boiling regime. The behaviour of equation (3.40) at variable vapour pressures makes it a general solution at low and high mass transfer rates.

The rate factor, ϕ , is determined by the Schmidt number and the ratio of molar bulk flow to , *R*, given by:

$$R = \frac{P_v}{\left(P_{atn} - P_v\right)} \tag{3.41}$$

as shown in figure 3.6.

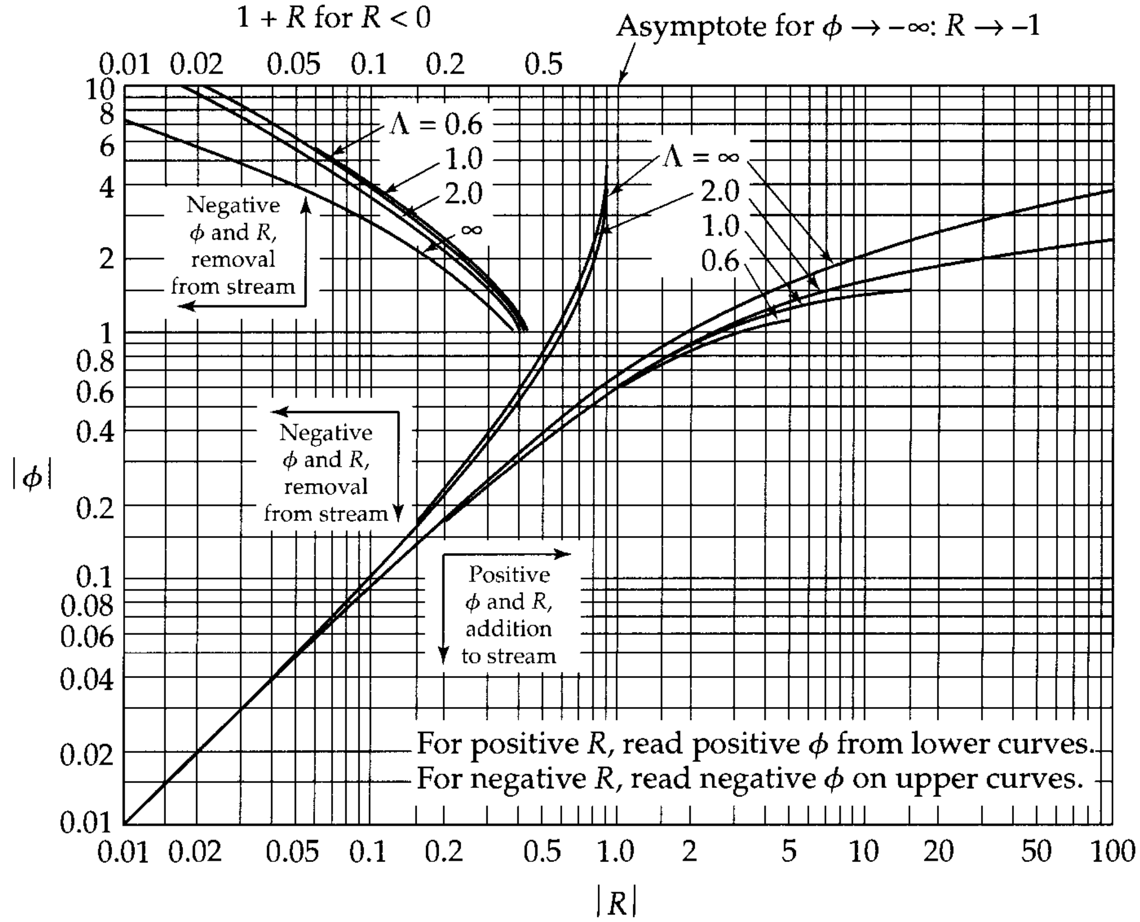

Figure 3.6. Mass fluxes between a flat plate and a laminar boundary layer as a function of parameter R (Bird et al., 1960)

3.4.2 Boiling Pools

When the pool is boiling, the liquid is in equilibrium with the vapour above the pool. The temperature of the liquid remains constant, as the heat that enters the pool provides the energy necessary for the phase change. The vaporisation flux, $\dot{m}''_{vap}$, is calculated using:

$$\dot{m}''_{vap} = \frac{Q''_{net}}{H_{vap}} \tag{3.42}$$

where,

Q''_{net} = net heat transfer flux between the pool and the surroundings, which also includes the heat added to the pool from a continuous spill (W/m^2)

H_{vap} = heat of vaporisation at the pool temperature (J/kg)

3.4.3 Dissolution in water

Water-soluble chemicals spilled on water can dissolve as well as boil or evaporate. Dodge et al. (1983) developed a model to estimate the flux of dissolved chemical as a function of the solubility of the chemical and the water surface properties. The overall mass transfer coefficient between the pool and water, k_w, is defined as (Dodge et al., 1983):

$$k_w = \frac{\dot{m}''_{sol}}{\rho_w \left(w_s - w_\infty\right)} \tag{3.43}$$

where,

k_w = overall mass transfer coefficient across the pool-water interface (m/s)

w_s = mass fraction of the chemical in water at the pool-water interface

w_∞ = mass fraction of the chemical in the water bulk (= 0)

Analogous to an evaporating pool (see section 3.4.1.2), a correction factor for high mass transfer rates, θ, is introduced (Witlox, 2008):

$$\theta = \frac{1}{w_s} Ln\left(\frac{1}{1 - w_s}\right) \tag{3.44}$$

Therefore, the expression for the pool dissolution flux of a water-soluble chemical in both rivers and open water surfaces is given by:

$$\dot{m}''_{sol}(t) = k_w \rho_w Ln\left(\frac{1}{1 - w_s}\right) \tag{3.45}$$

The dissolution model distinguishes between two types of surfaces:

- Rivers or channels
- Open or coastal water surfaces

3.4.3.1 Dissolution on rivers and channels

Experimental studies carried out by Hibbs and Gulliver (1999) and Herbes et al. (1983) in stirred tanks have found that the presence of the pool does not affect the interfacial turbulence at the water surface when it is caused by the turbulence generated in the water bulk. This observation makes it possible to compare the mass transfer across the pool-water interface (i.e. in the presence of a pool) to the mass transfer across the air-water interface (i.e. without the presence of the pool). As it is, the mass transfer coefficient between pool and water can be expressed as a function of the mass transfer coefficient between air and water (Hibbs and Gulliver, 1999):

$$k_w = \left(k_L\, u_w^{*}\right)\left(\frac{Sc_w}{Sc}\right)^{1/2} \tag{3.46}$$

where,

k_L = overall mass transfer coefficient for volatilisation on rivers and channels

Sc_w = Schmidt number of the chemical in water

u_w^{*} = friction velocity at the water surface (m/s)

u_w^{*} can be expressed in terms of the river mean current, u_c, by the following empirical relation extracted from data compiled by Fischer at al. (1979) and Fischer (1973):

$$u_w^{*} = u_c\left(5.4\times10^{-3}\right)^{0.5} \tag{3.47}$$

According to Ueda et al.’s (1977) study on eddy diffusivity in open channel flow, k_L, for rivers and channels can be estimated from the following equation, for Reynolds numbers ranging from 2.6 x 10^3 to 1.3 x 10^7:

$$k_L = 0.0626\, u_w^{*}\, Sc_w^{-2/3} \tag{3.48}$$

3.4.3.2 Dissolution on open and coastal waters

For spills on open sea, Dodge et al. (1983) developed an expression for k_w that accounts for the effect of waves:

$$k_w = 10 \frac{u_w^*}{\frac{\sigma \, Ln(\delta_+)}{\kappa} + \beta_w + 2.35} \tag{3.49}$$

$$\delta_+ = \frac{10 u_w^* \rho_w}{\mu_w} \tag{3.50}$$

$$\beta_w = \begin{cases} 12.5 Sc^{0.667} + \dfrac{\sigma \, Ln(Sc_w)}{\kappa} - 5.3 & u_{(z=10m)} \; < \; 5m/s \\ 0.55 h_w^{0.5}\left(Sc_w^{0.667} - 0.2\right) - \dfrac{\sigma \, Ln(Sc_w)}{\kappa} + 11.2\sigma & u_{(z=10m)} \; \geq \; 5m/s \end{cases} \tag{3.51}$$

$$h_w = 0.01384 \frac{u_{(z=10m)} \, u_w^* \rho_w}{\mu_w} \tag{3.52}$$

$$u_w^* \; = \; u_{(z=10m)} \left(\frac{\rho_a}{\rho_w}\right)^{1/2} \left(\frac{1}{2} C_f\right)^{1/2} \tag{3.53}$$

$$\frac{1}{2} C_f = \begin{cases} 1.98 \times 10^{-3} & u_{(z=10m)} < 0.1 m/s \\ 1.25 \times 10^{-3} \left[u_{(z=10m)}\right]^{-0.2} & 0.1 \; < \; u_{(z=10m)} < 3.06 m/s \\ \left[0.8 + 0.065 u_{(z=10m)}\right] \times 10^{-3} & 3.06 \; < \; u_{(z=10m)} < 22.3 m/s \\ 2.25 \times 10^{-3} & 22.3 m/s \; < \; u_{(z=10m)} \end{cases} \tag{3.54}$$

where,

δ_+ = height of the boundary layer formed between the pool and the water surface (m)

β_w = an empirical function dependent on the surface roughness

h_w = wave height (m)

C_f = friction coefficient at the water-pool interface (–)

$u_{(z=10m)}$ = wind speed measured at 10 m above the pool (m/s)

3.5 Heat transfer

In this section, the derivation of the equation used to calculate the variation of the pool temperature as a function of time is presented. This is followed by a description of the various heat transfer mechanisms for spills on land or water.

Figure 3.7 shows the various heat transfer mechanisms between the pool, surface and surroundings for spills on land or water.

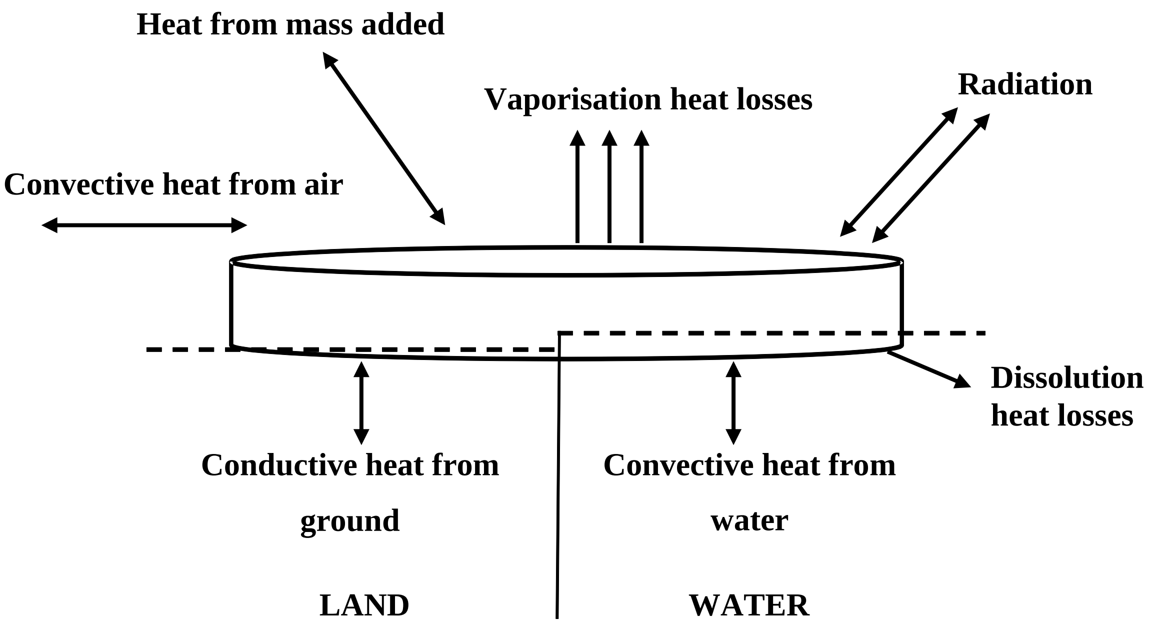

Figure 3.7. Diagram showing the heat transfer mechanisms between the pool and the surroundings (the dash lines in the diagram represent the land and water surfaces)

3.5.1 Energy balance

An energy balance which accounts for heat transferred by the various mechanisms shown in figure 3.7 is required to calculate the temperature of the pool at any given time. The rate of change in the total enthalpy of the pool is given by (Webber, 1989):

$$\frac{dH_L}{dt} = \pi r^2 \left(Q''_{in} - \dot{m}''_{vap} h_v(T_L) - \dot{m}''_{sol}\, h_{sol}(T_L)\right) + \dot{m}_{spill}\, h_l(T_{spill}) \tag{3.55}$$

where,

H_L = total enthalpy of the pool (J)

Q''_{in} = heat input to the pool per unit area (W/m^2)

$h_v\left(T_{pool}\right)$ = vapour enthalpy at the pool temperature (T_{pool}) (J)

$h_{sol}\left(T_{pool}\right)$ = liquid enthalpy of the chemical dissolved in water at the pool temperature (J)

$h_l\left(T_{spill}\right)$ = liquid enthalpy at the temperature of the spill (T_{spill}) (J)

T_{spill} = temperature of the spill (K)

For a pool containing a pure component, the enthalpy of the pool is given by:

$$H = \rho V h_l\left(T_{pool}\right) \tag{3.56}$$

where,

$h_l\left(T_{pool}\right)$ = liquid enthalpy at the pool temperature (J)

V = pool volume (m^3)

Taking the derivative of equation (3.56):

$$\frac{dH}{dt} = \frac{d}{dt}\left(\rho V h_l\left(T_{pool}\right)\right) \tag{3.57}$$

Assuming the density of the pool remains constant over each time interval, equation (3.57) becomes:

$$\frac{dH}{dt} = \rho\left[V\frac{dh_l\left(T_{pool}\right)}{dt} + h_l\left(T_{pool}\right)\frac{dV}{dt}\right] \tag{3.58}$$

A mass balance around the control volume of the pool gives:

$$\frac{dV}{dt} = -\frac{\pi r^2}{\rho}\left(\dot{m}''_{vap} + \dot{m}''_{sol}\right) + \frac{\dot{m}_{spill}}{\rho} \tag{3.59}$$

Substituting equation (3.59) into (3.58) gives:

$$\frac{dH}{dt} = \rho\left[\frac{dh_l\left(T_{pool}\right)}{dt} - \frac{\pi r^2}{\rho}\left(\dot{m}''_{vap} + \dot{m}''_{sol}\right) + \frac{\dot{m}_{spill}}{\rho}\right] \tag{3.60}$$

Substituting equation (3.60) into the energy balance (equation (3.55)) and rearranging gives:

$$\rho V \frac{dh_l(T_{pool})}{dt} = \pi r^2\left(Q''_{in} - \dot{m}''_{vap}H_{vap} - \dot{m}''_{sol}H_{sol}\right) + \dot{m}_{spill}\left(h_l\left(T_{spill}\right) - h_l\left(T_{pool}\right)\right) \tag{3.61}$$

where,

H_{vap} = heat of vaporisation at the pool temperature (J)

H_{sol} = heat of dissolution at the pool temperature (J)

Equation (3.61) may be formulated in terms of the pool temperature instead of the pool enthalpy. This presents the advantage of reducing the computational workload and improving the accuracy of the simulation, avoiding the numerical procedure to solve the above equation implicitly. Assuming the specific heat capacity at constant pressure, c_p, to be constant with temperature and defining the enthalpy of the liquid as $h_l = c_p\left(T - T_{ref}\right)$, the variation of the pool temperature over time is given by:

$$\frac{dT_{pool}}{dt} = \frac{1}{c_p \rho V}\left[\left(\pi r^2\right)\left(Q''_{in} - \dot{m}''_{vap}H_{vap} - \dot{m}''_{sol}H_{sol}\right) + \dot{m}_{spill}\, c_p\left(T_{spill} - T_{pool}\right)\right] \tag{3.62}$$

The heat transfer effects included under the term Q''_{in} in equation (3.62) are:

- Conduction from the ground
- Convection from water
- Convection from air
- Long wave radiation and solar incidence

3.5.2 Heat conduction from the ground

For pools spreading and vaporising on land, the heat transfer between the pool and the surface is modelled as a transient one-dimensional heat transfer process. The ground is assumed to be a semi-infinite solid in which the temperature will vary only in the vertical direction. Perfect thermal contact is assumed between the ground and pool.

The transient conduction problem in a semi-infinite solid is described by the following partial differential equation (Incropera and DeWitt, 1996):

$$\frac{1}{\alpha}\frac{\partial T}{\partial t} = \frac{\partial^2 T}{\partial z^2} \tag{3.63}$$

where,

α = thermal diffusivity of the solid (m^2/s)
z = distance in the vertical direction measured from the ground's surface (m)

Equation (3.63) is accompanied by the boundary conditions:

$$T = T_0 \text{ at } t = 0\,s \text{ and } z > 0 \tag{3.64}$$

$$T = T_0 \text{ at } z = \infty \text{ and } t > 0 \tag{3.65}$$

$$T = T_{pool} \text{ at } z = 0\,m \text{ and } t > 0 \tag{3.66}$$

where, T_0 is the initial temperature of the ground (K).

Perfect thermal contact between the pool and the ground's surface is implied in equation (3.66). The analytical solution of the problem for a pool of constant area gives the following expression for the heat flux (Shaw and Briscoe, 1980):

$$Q''_{cond} = \frac{k_s\left(T_0 - T_{pool}\right)}{\sqrt{\pi\alpha\, t}} \tag{3.67}$$

where, k_s is the thermal conductivity of the ground surface

When the pool is spreading, successive annular elements of the ground surface have been in contact with the pool for different times. Thus, the conductive heat flux becomes (Shaw and Briscoe, 1980):

$$Q''_{cond} = \frac{1}{\pi r^2}\left[\frac{k_s\left(T_0 - T_{pool}\right)}{\sqrt{\pi\alpha}}\int_0^{r(t)}\frac{2\pi r' dr'}{\sqrt{t-\tau}}\right] \tag{3.68}$$

where,

$r(t)$ = current radius of the pool (m)
t = current time (s)
$r^{'}$ = radius of the annular elements (m)
$\tau^{'}$ = time of arrival of the pool at radius r’ (s)

3.5.3 Water/pool convective heat transfer

For pools simultaneously spreading and vaporising on water, the heat transfer from the water surface to the pool is modelled as steady state convection. The heat flux per unit area is given by:

$$Q^{''}_{water} = h_w \left(T_w - T_{pool}\right) \tag{3.69}$$

where,

$Q^{''}_{water}$ = convective heat transfer from water to the pool (W/m^2)
h_w = average heat transfer coefficient (W/m^2.K)
T_w = temperature of the water surface (K)

The value of the average heat transfer coefficient has been experimentally determined to be 500 W/m^2.K for the vaporisation of n-butane on water (Reid and Smith, 1978). Due to lack of experimental data, this value is often used for most substances in Integral models (Ivings et al., 2009).

3.5.4 Ice/pool conduction heat transfer

For cryogenic spills where the pool temperature is significantly below the water freezing point, a thin layer of ice may form under the pool. A transient heat transfer model for a solid layer with a variable thickness is used to calculate the heat flux into the pool (Reid and Smith, 1978):

$$Q''_{ice} = \frac{\varepsilon}{\sqrt{t}} \tag{3.70}$$

$$\varepsilon = \frac{k_{ice}(T_{ice} - T_{pool})}{(\pi\,\alpha_{ice})^{1/2}\, erf\left[\dfrac{\kappa\,\beta}{2\sqrt{\alpha_{ice}}}\right]} \tag{3.71}$$

where,

Q''_{ice} = conductive heat transfer from the ice layer formed under the cryogenic pool (W/m^2)

k_{ice} = conductivity of the ice layer (W/m^2.K)

T_{ice} = ice temperature (water freezing point) (= 273.15 K)

α_{ice} = thermal diffusivity of the ice layer (m^2/s)

β = coefficient of volumetric expansion for water to ice (= 1.0907)

erf = error function

The parameter κ in equation (3.71) is calculated using (Reid and Smith, 1978):

$$\frac{(T_{ice} - T_{pool})k_{ice}\exp\left(-\dfrac{\beta^2\kappa^2}{4\alpha_{ice}}\right)}{(\pi\,\alpha_{ice})^{1/2}\, erf\left(\dfrac{\beta\kappa}{2\sqrt{\alpha_{ice}}}\right)} - \frac{(T_w(t=0) - T_{ice})k_w\exp\left(-\dfrac{\kappa^2}{4\alpha_w}\right)}{(\pi\,\alpha_w)^{1/2}\left\{1 - erf\left(\dfrac{\kappa}{2\sqrt{\alpha_w}}\right)\right\}} = \frac{1}{2}\Delta H^f{}_w(\rho_{ice})^{\beta\kappa} \tag{3.72}$$

where,

$T_w(t=0)$ = water temperature at the start of the release (K)

k_w = thermal conductivity of water (W/m^2.K)

α_w = thermal diffusivity of water (m^2/s)

$\Delta H^f{}_w$ = fusion heat of water (J)

ρ_{ice} = density of ice (kg/m^3)

3.5.5 Pool/air convective heat transfer

A steady state convection model is used to determine the heat flux between the pool and air. The correlation employed is for flat plate geometry under laminar or turbulent flow parallel to the pool surface (Fleischer, 1980):

$$Q''_{atm} = \frac{k_{air} N_u}{2r}\left(T_{atm} - T_{pool}\right) \tag{3.73}$$

where,

k_{air} = thermal conductivity of air (W/m^2.K)

N_u = Nusselt number $h_{air}(2r) / k_{air}$

h_{air} = heat transfer coefficient between air and the pool (W/m.K)

T_{atm} = atmospheric temperature (K)

The Nusselt number is evaluated at laminar or turbulent conditions with a critical Reynolds number of 320,000 (Fleischer, 1980):

$$N_u = \begin{cases} 0.664 P_r^{1/3} R_e^{1/2} & R_e < 320{,}000 \\ 0.037 P_r^{1/3}\left[R_e^{0.8} - 15200\right] & R_e \geq 320{,}000 \end{cases} \tag{3.74}$$

where,

P_r = Prandtl number $c_{pair}\mu_{air} / k_{air}$

R_e = Reynolds number $u_{z=10m}\rho_{air}L / \mu_{air}$

c_{pair} = heat capacity of air (J/kg.K)

μ_{air} = air dynamic viscosity (Pa.s)

Laminar flow is only present for pools with very small radii.

3.5.6 Long wave radiation and solar incidence

Long wave radiation follows Stefan-Boltzman law (Incropera and DeWitt, 1996):

$$Q''_{l-wave} = \varepsilon\sigma_{SB}(T^4_{atm} - T^4_{pool}) \tag{3.75}$$

where,

Q''_{l-wave} = heat flux from long wave radiation (W/m^2)

ε = emissivity of the pool (–)

σ_{SB} = Stefan-Boltzman constant (5.7x10^{-8} W/m^2.K^4)

Long wave radiation is important at high pool temperatures as experienced in pool fires.

The solar incidence is determined from the incident solar flux, S , which depends on the meteorological conditions.

The total radiation heat flux from long wave and solar incidence is given by:

$$Q''_{rad} = \varepsilon\sigma_{SB}\left((T_{atm})^4 - (T_{pool})^4\right) + S \qquad (3.76)$$

3.6 Concluding remarks

In this chapter, the assumptions made and the equations governing pool spreading and evaporation of cryogenic and volatile pools based on published literature were presented.

For pools spreading on water, a model describing three successive regimes, gravity-resistive, viscous-resistive and viscous-surface tension was reviewed. For the case of pool spreading on land, a rough surface was modelled as the surface of a golf ball, which holds-up an amount of liquid of height equivalent to the average roughness length of the surface. However, some uncertainty in the values selected for parameters, such as the empirical constants for spreading on water and the minimum thickness for spreading on land remains. This is partly due to the fact that these are based on the available experimental data which is mostly old and at small scale. New validation of the spreading model against experimental data published in recent years is presented in chapter 6, with the aim of resolving these uncertainties.

The energy balance was formulated in terms of the pool temperature instead of the pool enthalpy. The heat transfer mechanisms accounted for include conduction from the ground, forced convection from water and air, conduction from ice due to water freezing, long wave radiation and solar incidence.

The mass balance across the pool accounted for the mass added from a continuous spill, and the mass lost from the pool by vaporisation and dissolution. Pool vaporisation covered two distinctive cases: evaporation and boiling. For boiling pools, the liquid pool was assumed to be in equilibrium with the vapour above it. For evaporating pools, a general solution that can predict the evaporation rate at low and high mass transfer rates was shown. Pool dissolution was modelled for open sea and rivers or channels spill scenarios. However, the prediction of evaporation and dissolution of individual components in a mixture as well as the modelling of the mixture's boiling behaviour were not taken into account. These effects are incorporated to the model in chapter 4 of this thesis.

Finally, the need to simultaneously calculate the spreading, vaporisation and dissolution of the pool gives rise to a stiff a problem, due to the different time-scales of each phenomenon (Brambilla and Manca, 2008). Chapter 5 presents the implementation of a numerical algorithm (Hindmarsh and Radhakrishnan, 1993) to address stiff problems of ordinary differential equations, improving the convergence of the model solution and its computational efficiency.

CHAPTER 4. MULTI-COMPONENT POOL MODEL

4.1 Introduction

It is common practice in integral pool models to approximate the behaviour of a mixture as a pure or single component pool using the properties of the predominant component. Examples include models for pools formed from releases of crude oil, Liquefied Natural Gas (LNG) and Liquefied Petroleum Gas (LPG) (Hoult, 1972b; Reid and Wang, 1978; Fay, 1969 and 2003).

Previous authors (see for example, Valencia and Reid, 1979; Conrado and Vesovic, 2000) have investigated the impact of composition on the spreading and evaporation of cryogenic pools, specifically LNG and LPG spilled on water. Conrado and Vesovic (2000) found that treating LNG (composition: 90 mole% Methane and 10 mole% Ethane) as pure Methane results in underestimation of the total evaporation time of the order of 10% to 15%.

This chapter describes the extension of the pool spreading, vaporisation and dissolution model presented in the previous chapter to mixtures.

To account for the mixture behaviour, the multi-component model tracks the transient pool inventory at each step, and employs established mixing rules to estimate overall pool properties.

Two distinctive cases for pool vaporisation are studied: boiling and evaporation. While the pool is boiling, the liquid and vapour phases are assumed to be in equilibrium governed by Raoult’s Law. For evaporation, the pure component model presented in chapter 3 has been extended to account for the diffusion of multiple components into air. Additionally, the model makes continuous checks for transitions between boiling and evaporation by performing a bubble point calculation at each step of the simulation.

The dissolution of water-soluble chemicals present in the mixture is accounted in the present work. This is considered to be a novel feature as compared to existing multi-component pool models. Two mechanisms are proposed, one for dissolution on rivers or channels and another for spills on open sea water.

Additionally, the results and discussion of a comprehensive investigation on the effects of pool composition involving case studies for cryogenic, evaporating and water-soluble liquids, are presented in this chapter. Further assessment of the efficacy of the multi-component pool model, by comparison against a widely used simulation software for multi-component pools, LPOOL HGSYSTEM 3.0 (Post, 1994), and against published experimental data, is shown in chapters 5 and 6 of this thesis.

This chapter is divided into two main sections: the first describes the development of the multi-component pool model based on the premises presented in chapter 3. The second section presents the results of a series of case studies that investigate the impact of composition on pool spreading, evaporation and dissolution phenomena.

4.2 Model formulation

The multi-component pool model comprises the following set of equations:

- ☐ Spreading law to determine the variation of the pool radius as a function of time, as presented in chapter 3 of this thesis.
- ☐ Mass balance around the control volume of the pool for each component in the mixture.
- ☐ Energy balance around the control volume of the pool assuming the pool is shallow enough that the well-mixed assumption presented in chapter 3 applies.

4.2.1 Energy balance

The variation of enthalpy over time for a multi-component pool can be expressed as an extension of the energy balance for a single-component pool shown in equation (3.54), section 3.5.1, to mixtures:

$$\frac{d\left(M_{pool}\,h_L\left(T_L, X_{pool}{}^{i}\right)\right)}{dt} = \dot{m}_{spill}\,h_{spill}\left(T_{spill}, X_{spill}{}^{i}\right) + \pi r^2\left(Q_{in}{}'' - \dot{m}''{}_{vap}\sum_{i=1}^{n}\left(Y_{vap}{}^{i} h_V{}^{i}\left(T_L\right)\right) - \dot{m}''{}_{sol}\sum_{i=1}^{n}\left(X_{sol}{}^{i} h_{sol}{}^{i}\left(T_L\right)\right)\right) \tag{4.1}$$

where,

$h_L\left(T_L, X_{pool}{}^{i}\right)$ = specific liquid enthalpy at the temperature and composition of the pool (J/kg)

$X_{pool}{}^{i}$ = mass fraction of component i in the pool

$h_{spill}\left(T_{spill}, X_{spill}{}^{i}\right)$ = specific liquid enthalpy at the temperature and composition of the spill (J/kg)

$X_{spill}{}^{i}$ = mass fraction of component i in the spill rate

$Q''{}_{in}$ = total heat flux into the pool resulting from air convection, radiation and ground conduction or water convection (W/m^2)

$Y_{vap}{}^{i}$ = vapour mass fraction of component i in the evaporation flux

$h_V{}^{i}\left(T_L\right)$ = specific vapour enthalpy of component i at the pool temperature (J/kg)

$X_{sol}{}^{i}$ = mass fraction of component i in the dissolution flux

$h_{sol}{}^{i}\left(T_L\right)$ = specific liquid enthalpy of component i dissolved into water at the pool temperature (J/kg)

n = total number of components

The left hand side of equation (4.1) can be further expanded resulting in:

$$\frac{d\left(M_{pool}\,h_L\right)}{dt} = \frac{dM_{pool}}{dt}h_L + M_{pool}\left[\left(\frac{\partial h_L}{\partial T_L}\,\frac{dT_L}{dt}\right) + \sum_{i=1}^{n}\left(\frac{\partial h_L}{\partial X_{pool}{}^{i}}\,\frac{dX_{pool}{}^{i}}{dt}\right)\right] \tag{4.2}$$

The next steps show how equation (4.1) can be solved for the term $\frac{dT_L}{dt}$ in equation (4.2).

Assuming ideal mixing, the liquid enthalpy at the pool temperature and composition can be expressed as (Smith et al., 2005):

$$h_L = \sum_{i=1}^{n} X_{pool}{}^{i}\,c_p{}^{i}\left(T_L - T_{ref}\right) \tag{4.3}$$

where,

$c_p{}^i$ = specific heat capacity of the liquid at constant pressure for component i (J/kg K)

T_{ref} = reference temperature (K)

Similarly, the total liquid enthalpy at the spill temperature and composition can be written as:

$$h_{spill} = \sum_{i=1}^{n} X_{spill}{}^i \, c_p{}^i \left(T_{spill} - T_{ref}\right) \tag{4.4}$$

The partial derivatives of the pool liquid enthalpy with respect to composition and temperature are respectively given by:

$$\left(\frac{\partial h_L}{\partial T_L}\right)_{P, X_{poolI}} = \sum_{i=1}^{n} X_{pool}{}^i c_p{}^i \tag{4.5}$$

$$\left(\frac{\partial h_L}{\partial X_{pool}{}^i}\right)_{P, T_L} = c_p{}^i \left(T_L - T_{ref}\right) \qquad \forall \quad i = 1, \ldots, n \tag{4.6}$$

Substituting equations (4.3), (4.5) and (4.6) into equation (4.2) it is found that:

$$\frac{d\left(M_{pool} h_L\right)}{dt} = \frac{dM_{pool}}{dt} \sum_{i=1}^{n} X_{pool}{}^i \, c_p{}^i \left(T_L - T_{ref}\right) + \sum_{i=1}^{n} M_{pool} \left[X_{pool}{}^i c_p{}^i \, \frac{dT_L}{dt} + c_p{}^i \left(T_L - T_{ref}\right) \, \frac{dX_{pool}{}^i}{dt} \right] \tag{4.7}$$

The overall mass balance in the pool was given in the previous chapter by equation (3.23) and is reproduced here:

$$\frac{dM_{pool}}{dt} = \dot{m}_{spill} - \pi \, r^2 \left(\dot{m}''_{vap} + \dot{m}''_{sol}\right) \tag{3.23}$$

Alternatively, the pool mass balance for each component may be expressed as:

$$\frac{d\left(X_{pool}{}^{i} M_{pool}\right)}{dt} = X_{spill}{}^{i}\dot{m}_{spill} - \pi r^{2}\left(Y_{vap}{}^{i}\dot{m}''_{vap} + X_{sol}{}^{i}\dot{m}''_{sol}\right) \qquad \forall \quad i = 1,\ldots,n \tag{4.8}$$

Expanding equation (4.8) and applying the overall mass balance (equation (3.23)) results in:

$$M_{pool}\frac{dX_{pool}{}^{i}}{dt} = \dot{m}_{spill}\left(X_{spill}{}^{i} - X_{pool}{}^{i}\right) - \pi r^{2}\left[\left(Y_{vap}{}^{i} - X_{pool}{}^{i}\right)\dot{m}''_{vap} + \left(X_{sol}{}^{i} - X_{pool}{}^{i}\right)\dot{m}''_{sol}\right] \tag{4.9}$$

Substituting equations (4.9) and (3.23) into equation (4.7) and rearranging gives:

$$\begin{aligned}\frac{d\left(M_{pool}\,h_{L}\right)}{dt} = M_{pool}\frac{dT_{L}}{dt}\sum_{i=1}^{n} X_{pool}{}^{i}c_{p}{}^{i} + \\ \sum_{i=1}^{n} c_{p}{}^{i}\left(T_{L} - T_{ref}\right)\left[\dot{m}_{spill}X_{spill}{}^{i} - \pi r^{2}\left(Y_{vap}{}^{i}\dot{m}''_{vap} + X_{sol}{}^{i}\dot{m}''_{sol}\right)\right]\end{aligned} \tag{4.10}$$

Returning to the energy balance presented in equation (4.1), equations (4.10) and (4.4) are substituted into equation (4.1) to obtain:

$$\begin{aligned}M_{pool}\frac{dT_{L}}{dt}\sum_{i=1}^{n} X_{pool}{}^{i}c_{p}{}^{i} = \pi r^{2}Q''_{in} + \dot{m}_{spill}\sum_{i=1}^{n}\left[X_{spill}{}^{i}c_{p}{}^{i}\left(T_{spill} - T_{ref}\right) - X_{spill}{}^{i}\,c_{p}{}^{i}\left(T_{L} - T_{ref}\right)\right] \\ -\pi r^{2}\left[\sum_{i=1}^{n}\dot{m}''_{vap}\,Y_{vap}{}^{i}\left(h_{v}{}^{i}\left(T_{L}\right) - c_{p}{}^{i}\left(T_{L} - T_{ref}\right)\right) + \dot{m}''_{sol}\,X_{sol}{}^{i}\left(h_{sol}{}^{i}\left(T_{L}\right) - c_{p}{}^{i}\left(T_{L} - T_{ref}\right)\right)\right]\end{aligned} \tag{4.11}$$

The specific heats of vaporisation and dissolution for each component at the pool temperature are respectively defined as:

$$Y_{vap}{}^{i}\Delta H_{vap}{}^{i}\left(T_{L}\right) = Y_{vap}{}^{i}\left(h_{V}{}^{i}\left(T_{L}\right) - c_{p}{}^{i}\left(T_{L} - T_{ref}\right)\right) \qquad \forall \;\; i = 1,\ldots,n \tag{4.12}$$

$$X_{sol}{}^{i}\Delta H_{sol}{}^{i}\left(T_{L}\right) = X_{sol}{}^{i}\left(h_{sol}{}^{i}\left(T_{L}\right) - c_{p}{}^{i}\left(T_{L} - T_{ref}\right)\right) \qquad \forall \;\; i = 1,\ldots,n \tag{4.13}$$

where,

$\Delta H_{vap}^{\ i}(T_L)$ = specific heat of vaporisation for component i at the pool temperature (J/kg)

$\Delta H_{sol}^{\ i}(T_L)$ = specific heat of dissolution for component i at the pool temperature (J/kg)

Rewriting equation (4.11) by using the definitions given in equations (4.12) and (4.13) results in the equation for the variation of temperature with time in a multi-component pool:

$$\frac{dT_L}{dt} = \frac{\dot{m}_{spill} \sum_{i=1}^{n} \left[X_{spill}^{\ i} c_p^{\ i} \left(T_{spill} - T_L \right) \right] + \pi r^2 \left[Q''_{in} - \sum_{i=1}^{n} \left[\dot{m}''_{vap} \left(Y_{vap}^{\ i} \Delta H_{vap}^{\ i} (T_L) \right) - \dot{m}''_{sol} \left(X_{sol}^{\ i} \Delta H_{sol}^{\ i} (T_L) \right) \right] \right]}{M_{pool} \sum_{i=1}^{n} X_{pool}^{\ i} c_p^{\ i}} \tag{4.14}$$

4.2.2 Pool vaporisation

4.2.2.1 Boiling pools

The pool will boil when its temperature is at the bubble point, T_{bubble}, of the mixture. The bubble point temperature is determined from the following expression assuming Raoult’s Law (Walas, 1985):

$$\sum_{i=1}^{n} \left(\frac{P_v^{\ i}(T_{bubble})}{P_{atm}} x_{pool}^{\ i} \right) - 1 = 0 \tag{4.15}$$

where,

$P_v^{\ i}(T_{bubble})$ = vapour pressure of component i at T_{bubble}(Pa)

$x_{pool}^{\ i}$ = mole fraction of component i in the pool

The vapour molar fraction of each component in the evaporation flux, $y_{vap}^{\ i}$, is given by:

$$y_{vap}{}^{i} = \frac{P_v{}^{i}\left(T_{bubble}\right)}{P_{atm}} x_{pool}{}^{i} \qquad \forall \;\; i = 1,\ldots,n \tag{4.16}$$

The rate at which heat must be supplied to the pool for it to remain at the bubble point is defined as (Cavanaugh et al., 1994):

$$Q_{bubble} = M_{pool} \sum_{i=1}^{n} X_{pool}{}^{i} c_p{}^{i} \left(\frac{dT_{bubble}}{dt} \right) \tag{4.17}$$

where, Q_{bubble} is the rate of heat added to the pool (W).

The time derivative term in equation (4.17) is obtained by differentiating equation (4.15) with respect to time:

$$\sum_{i=1}^{n} \left(x_{pool}{}^{i} \left(\frac{dP_v{}^{i}\left(T_{bubble}\right)}{dT_{bubble}} \frac{dT_{bubble}}{dt} \right) + P_v{}^{i}\left(T_{bubble}\right) \frac{dx_{pool}{}^{i}}{dt} \right) = 0 \tag{4.18}$$

Solving for $\frac{dT_{bubble}}{dt}$ we obtain:

$$\frac{dT_{bubble}}{dt} = - \frac{\sum_{i=1}^{n} \left(P_v{}^{i}\left(T_{bubble}\right) \frac{dx_{pool}{}^{i}}{dt} \right)}{\sum_{i=1}^{n} \left(x_{pool}{}^{i} \frac{dP_v{}^{i}\left(T_{bubble}\right)}{dT_{bubble}} \right)} \tag{4.19}$$

As the total heat entering the pool is used in both the vaporisation of the liquid and in maintaining the pool at the bubble point (Q_{bubble}), the overall vaporisation rate from a boiling pool is determined from the energy balance as:

$$\dot{m}''_{vap} = \frac{Q''_{in} - \dot{m}''_{sol} \sum_{i=1}^{n} X_{sol}{}^{i} \Delta H_{sol}{}^{i}\left(T_{bubble}\right) + \frac{\left(\dot{m}_{spill}\, c_{p\,spill}\left(T_{spill} - T_{bubble}\right) - Q_{bubble}\right)}{\pi r^2}}{\sum_{i=1}^{n} Y_{vap}{}^{i} \Delta H_{vap}{}^{i}\left(T_{bubble}\right)} \tag{4.20}$$

The main heat contributor to a boiling pool is the incoming heat from the surface under the pool. If the pool is on water the heat transfer is modelled as a convection problem using equation (3.69) reproduced here for clarity:

$$Q''_{water} = h_w \left(T_w - T_{pool}\right) \tag{3.77}$$

In reality different pool boiling regimes may be experienced for different fluids depending on the temperature difference between the pool and the water surface. These can be nucleate, transition or film boiling (Roshenshow,), and the heat transfer between the pool and the surface will be different for each boiling regime. In the present simplified model the different boiling regimes are not modelled, but are taken into account in equation (3.69) under the parameter h_w. As an example, when modelling LNG spilled on water which will be boiling in the film boiling regime the reduced heat transfer through the vapour film between the pool and the surface will be accounted for by a reduced value of h_w.

4.2.2.2 Evaporating pools

The pool will evaporate when its temperature is below the bubble point of the mixture.

In order to extend the single-component evaporation equation to multi-component pools it is desirable to express the vaporisation flux in a general form as equation (3.26), reproduced here for clarity:

$$\dot{m}''_{vap} = C_s\, u_a^{*} \theta k_L \tag{3.26}$$

The vaporisation flux for a component, i in a mixture is thus written as:

$$\dot{m}''^{\,i}_{vap} = C_s^{\,i}\, u_a^{*} \theta^i\, k_L^{\,i} \qquad \forall\ i = 1,\ldots,n \tag{4.21}$$

where,

$\dot{m}^{i''}_{vap}$ = vaporisation flux of component i in the mixture (kg/m^2.s)

$C_s{}^i$ = vapour concentration of component i at the pool surface (kg/m^3)

θ^i = correction factor (dimensionless)

$k_L{}^i$ = mass transfer coefficient of component i (dimensionless)

Assuming there is no accumulation of vapour above the pool, the evaporated liquid may be considered to diffuse through a layer of pure air. Hence, the resistance to mass transfer of a component in the vapour phase, $k_L{}^i$, defined in equations (3.37) to (3.39) applies to both single and a multi-component pools.

The vapour concentration of each component in the mixture at the pool surface can be expressed as (Cavanaugh et al., 1994):

$$C_s{}^i = \frac{M_c{}^i x_{pool}{}^i P_v{}^i}{RT_L} \qquad \forall \ i = 1,\ldots,n \tag{4.22}$$

where, $M_c{}^i$ is the molecular of component i (kg/kmol)

The definition for the correction factor, θ^i (see equation 4.21), in a multi-component pool has been given by Leonelli et al. (1994):

$$\theta^i = \frac{P_{atm}}{x_{pool}{}^i P_v{}^i} \frac{\dot{N}''_{vap}{}^i}{\dot{N}''_{vap}} Ln\left(\frac{\dot{N}''_{vap}{}^i \big/ \dot{N}''_{vap}}{\dot{N}''_{vap}{}^i \big/ \dot{N}''_{vap} - \dfrac{x_{pool}{}^i P_v{}^i}{P_{atm}}} \right) \qquad \forall \ i = 1,\ldots,n \tag{4.23}$$

where,

$\dot{N}''_{vap}{}^i$ = molar flux of component i at the pool surface (mole/s.m^2)

$\dot{N}''_{vap}$ = overall molar flux at the pool surface (mole/s.m^2)

The molar flux of component i ($\dot{N}''_{vap}{}^i$) and of its sum over all the components in the pool ($\dot{N}''_{vap}$) in equation (4.23), can be respectively defined as:

$$\dot{N}''_{vap}{}^i = \frac{\left(x_{pool}{}^i P_v{}^i \right)}{RT_L} \dot{v}_{vap}{}^i \tag{4.24}$$

$$\dot{N}''_{vap} = \sum_{i=1}^{n} \left[\frac{\left(x_{pool}{}^{i} P_v{}^{i} \right)}{RT_L} \dot{v}_{vap}{}^{i} \right] \tag{4.25}$$

where, $\dot{v}''_{vap\ i}$ is the velocity at which the vapour of component i escapes the pool surface (m/s).

Assuming that while the pool is evaporating, the velocity, $\dot{v}''_{vap}{}^{i}$, at which each component escapes the pool is approximately the same ($\dot{v}''_{vap}{}^{1} \approx \dot{v}''_{vap}{}^{2} \approx .... \approx \dot{v}''_{vap}{}^{n}$), the ratio of $\frac{\dot{N}''_{vap}{}^{i}}{\dot{N}''_{vap}}$ reduces to:

$$\frac{\dot{N}''_{vap\ i}}{\dot{N}''_{vap}} = \frac{\left(x_{pool}{}^{i} P_v{}^{i} \right)}{\sum_{i=1}^{n} \left(x_{pool}{}^{i} P_v{}^{i} \right)} \tag{4.26}$$

Substituting equation (4.26) into equation (4.23), the following expression for the correction factor is obtained:

$$\theta^{i} = \frac{P_{atm}}{\sum_{i=1}^{n} \left(x_{pool}{}^{i} P_v{}^{i} \right)} Ln \left(\frac{P_{atm}}{P_{atm} - \sum_{i=1}^{n} \left(x_{pool}{}^{i} P_v{}^{i} \right)} \right) \tag{4.27}$$

The final expression for the total evaporation flux of the pool is found by summing over all the components in the mixture:

$$\dot{m}''_{vap} = \sum_{i=1}^{n} C_s{}^{i} \, u_a{}^{*} \theta^{i} \, k_L{}^{i} \tag{4.28}$$

4.2.2.3 Transition between boiling and evaporating pools

Transition from boiling to evaporating pools

The pool will stop boiling when the heat flux gained from the surroundings is less than the heat flux lost because of increase in bubble point temperature, Q_{bubble}, pool evaporation and dissolution. This condition is expressed as:

$$\sum_{i=1}^{n}\left(\dot{m}''_{vap}{}^{i}\Delta H_{vap}{}^{i} + \dot{m}''_{sol}{}^{i}\Delta H_{sol}{}^{i}\right) + \frac{Q_{bubble}}{\pi r^{2}} > Q''_{in} + \frac{\left(m_{spill}\, c_{p\,spill}\left(T_{spill} - T_{bubble}\right)\right)}{\pi\, r^{2}} \qquad (4.29)$$

Transition from evaporating to boiling pools

The pool will start boiling when both of the following conditions are met:

a) Enough heat is being provided by the surroundings to compensate the rise in the bubble point temperature and the heat losses by evaporation and dissolution. This can be written as:

$$Q''_{in} + \frac{\left(m_{spill}\, c_{p\,spill}\left(T_{spill} - T_{bubble}\right)\right)}{\pi\, r^{2}} \geq \sum_{i=1}^{n}\left(\dot{m}''_{vap}{}^{i}\Delta H_{vap}{}^{i} + \dot{m}''_{sol}{}^{i}\Delta H_{sol}{}^{i}\right) + \frac{Q_{bubble}}{\pi r^{2}} \qquad (4.30)$$

b) The temperature of the pool, T_{pool}, is greater or equal to the bubble point temperature, T_{bubble}.

4.2.3 Pool dissolution

The rate of mass lost by dissolution is expressed for mixtures as the sum of the individual contributions of each water-soluble component present in the pool:

$$\dot{m}''_{sol} = \sum_{i=1}^{n} k_{w}{}^{i} \rho_{w} Ln\left(\frac{1}{1 - w_{s}{}^{i}{}_{mix}}\right) \qquad (4.31)$$

where,

$k_w{}^i$ = mass transfer coefficient of each component (m/s)

$w_s{}^i{}_{mix}$ = contribution to molar solubility of each component in the mixture, given by:

$$w_s{}^i{}_{mix} = x^i{}_{pool}\ w_s{}^i \tag{4.32}$$

and,

$w_s{}^i$ = molar solubility of each component

Under the assumption that there is no accumulation of dissolved material under the pool, the liquid may be considered to diffuse through a layer of pure water. Hence, the resistance to mass transfer of a component in the soluble phase, $k_w{}^i$, defined in equations (3.46) and (3.47) (for rivers and channels) and in equations (3.48) to (3.53) (for open sea) applies to both single and a multi-component pools.

4.2.3.1 Dissolution on rivers and channels

The mass transfer coefficient for dissolution of water-soluble chemicals in multi-component spills on rivers or channels, $k_w{}^i$, is given by the extension of Dodge et al. (1983) single component model (equation (3.46)) to mixtures:

$$k_w{}^i = 0.0626\,u_w{}^*\ Sc^i{}_w{}^{-2/3}\left(\frac{Sc^i{}_w}{Sc}\right)^{1/2} \tag{4.33}$$

where,

$k_w{}^i$ = mass transfer coefficient for dissolution on rivers and channels for each component

$u_w{}^*$ = friction velocity at the water surface (m/s) defined as in equation (3.48)

$Sc^i{}_w$ = Schmidt number for each component, given by:

$$Sc^i{}_w = D^i{}_w \big/ \nu_w \tag{4.34}$$

and,

$D^i{}_w$ = diffusion coefficient on water of each component in the mixture (m^2/s)

4.2.3.2 Dissolution on open sea

The expression for the mass transfer coefficient for dissolution of water-soluble chemicals in multi-component spills on open waters is obtained from Dodge et al. (1983) single-component model extended here to mixtures:

$$k_w{}^i = 10\frac{u_w{}^*}{\frac{\sigma Ln(\delta_+)}{\kappa} + \beta^i{}_w + 2.35} \tag{4.35}$$

Where

$$\beta^i{}_w = \begin{cases} 12.5\left(Sc^i{}_w\right)^{0.667} + \frac{\sigma Ln\left(Sc^i{}_w\right)}{\kappa} - 5.3 & u_{(z=10m)} \quad < \quad 5m/s \\ 0.55 h_w{}^{0.5}\left(\left(Sc^i{}_w\right)^{0.667} - 0.2\right) - \frac{\sigma Ln(Sc^i{}_w)}{\kappa} + 11.2\sigma & u_{(z=10m)} \quad \geq \quad 5m/s \end{cases} \tag{4.36}$$

and

$k_w{}^i$ = mass transfer coefficient for dissolution on open sea for each component

δ_+ = height of the boundary layer formed between the pool and the water surface (m) defined by equation (3.51)

$\beta^i{}_w$ = an empirical function dependent on the surface roughness

$u_w{}^*$ = friction velocity at the water surface (m/s) defined as in equation (3.54)

h_w = wave height (m) defined as in equation (3.53)

σ = turbulent Schmidt number (= 0.8) (Tominaga, Stathopoulos, 2007)

4.2.4 Summary of the model

The following summarises the set of equations solved for the multi-component pool model:

1. Spreading law to determine the variation of the pool radius as a function of time, as presented in chapter 3 of this thesis. The assumptions taken in order to express the pool spreading law as it is in the present work are:
    - ❑ The spill source is located at the centre of the pool and the pool is considered to be axisymmetric
    - ❑ Fluid flow is considered only in the radial direction

- ❑ The height of the pool is uniform along its length. In reality, the pool will have a height profile depending on the topography of the surface (e.g., if the surface is inclined, rough or smooth). Except at early stages of spreading, the pool height is very small with respect to the pool radius, so the variation on the pool height is small with respect to the horizontal spreading distance.
- ❑ The pool is cylindrical in shape. This assumption is applied to unconfined pools spreading over flat surfaces such as flat ground or water basins and to confined pools spreading inside a bund. In the case of a confined pool, the maximum radius of the pool is equal to the radius of the bund. Once the pool has reached its maximum radius, variations in the volume of the pool due to evaporation and spill rate are accounted for by changing the height of the pool

2. Mass balance around the control volume of the pool for each component in the mixture. The main assumptions considered in deriving the mass balance in the pool and determining the amount of vapour produced were:

- ❑ That the vapour above the pool behaves as an ideal gas. This is a reasonable simplification given that the pool is subject to low pressures (1 atm), and
- ❑ The fluid properties of the pool including density, specific heat capacity and vapour pressure are assumed to be constant over the entire volume of the pool at each time step. This is the underlying assumption in all integral pool models which handle average properties across the pool volume

3. Energy balance around the control volume of the pool assuming the pool is shallow enough that the well-mixed assumption presented in chapter 3 applies. This assumption is based on the fact that the pool is assumed to be sufficiently thin so that its temperature is constant in the vertical direction. For volatile pools, a temperature gradient in the vertical direction exists if the ground and air above the pool are at different temperatures. However, some authors (see for example Leonelli et al., 1994) have reported little impact on the prediction of the vaporisation rate when accounting for a vertical temperature gradient in the pool. Experimental confirmation of this phenomenon is however not available

4. Cumulative mass vaporised

5. Cumulative mass dissolved

These can be written in matrix form as a system of ordinary differential equations (ODEs):

$$\frac{\partial \bar{Y}}{\partial t} = G(\bar{Y}, t) \tag{4.37}$$

where,

$$\bar{Y} = \begin{pmatrix} r \\ T_L \\ M_{pool}{}^{i} \\ M_{vap}{}^{i} \\ M_{sol}{}^{i} \end{pmatrix} \tag{4.38}$$

$$G = \left(\begin{array}{cl} \boldsymbol{f}\left(r, M_{pool}{}^{i}, T_L\right) & \\ \boldsymbol{g}\left(M_{pool}{}^{i}, T_L\right) + \pi r^2 \boldsymbol{h}\left(M_{pool}{}^{i}, T_L\right) & \\ \dot{m}_{spill}{}^{i} - \pi r^2 \left(\dot{m}''_{vap}{}^{i} + \dot{m}''_{sol}{}^{i}\right) & \forall\, i = 1, \ldots, n \\ \pi r^2 \dot{m}''_{vap}{}^{i} & \forall\, i = 1, \ldots, n \\ \pi r^2 \dot{m}''_{sol}{}^{i} & \forall\, i = 1, \ldots, n \end{array} \right) \tag{4.39}$$

and,

$$\boldsymbol{f}\left(r, M_{pool}{}^{i}, T_L\right) = \begin{cases} Pools\ on\ land = \left[2g \left(\dfrac{\sum_{i=1}^{n} M_{pool}{}^{i}}{\pi r^2 \rho_{pool}(T_L)} - h_{\min} \right) \right]^{0.5} \\ Pools\ on\ water = 0 \end{cases} \tag{4.40}$$

$$\boldsymbol{g}\left(M_{pool}{}^{i}, T_L\right) = \frac{\sum_{i=1}^{n} \dot{m}_{spill}{}^{i}\, c_p{}^{i}(T_L) \cdot \left(T_{spill} - T_L\right)}{\sum_{i=1}^{n} M_{pool}{}^{i}\, c_p{}^{i}(T_L)} \tag{4.41}$$

$$\boldsymbol{h}\left(M_{pool}{}^{i}, T_L\right) = \frac{Q''_{in} - \sum_{i=1}^{n} \dot{m}''_{vap}{}^{i} \Delta H_{vap}{}^{i}(T_L) - \sum_{i=1}^{n} \dot{m}''_{sol}{}^{i} \Delta H_{sol}{}^{i}(T_L)}{\sum_{i=1}^{n} M_{pool}{}^{i}\, c_p{}^{i}(T_L)} \tag{4.42}$$

where,

$M_{vap}{}^{i}$ = mass of component i vaporised

$M_{sol}{}^{i}$ = mass of component i dissolved

ρ_{pool} = density of the mixture at the pool composition

and the remaining symbols are as previously defined in this chapter and previous.

4.3 Case studies

The formulation of the multi-component pool evaporating model was presented above. The following section presents and discusses the results of a series of hypothetical case studies using the multi-component model in order to investigate the impact of the type of inventory on the pool spreading, evaporation and dissolution. Comparisons between the model's predictions for pure components and mixtures are shown. Different mixtures classified under cryogenic, evaporating and water-soluble liquids are investigated for both instantaneous and continuous releases on land and water surfaces.

The simulations presented in this chapter and the next were performed with an Intel 1.8 GHz processor with 2.6 Mb of RAM memory. They took on average a run time of 30 s to 2 mins.

4.3.1 Cryogenic liquids

Table 4.1 summarises the prevailing conditions and surface characteristics selected to showcase the results of the multi-component pool model presented in section 4.2.2 for cryogenic liquids. Pure Methane and an 85 wt% Methane and 15 wt% Ethane mixture, representative of the composition of LNG (Thyer, 2003), are released as saturated liquids.

The four case studies presented in this section include continuous spills on typical land and water surfaces.

Case studies A and B are pools formed from continuous spills on calm sea. The value of the heat transfer coefficient between the surface and the pool, in both cases, is assumed to be constant and equal to that for Methane film boiling (Vesovic, 2000; Hissong, 2007). For the mixture, the validity of the assumption of a constant heat transfer coefficient is uncertain as the variable composition and pool temperature affects the resistance to heat transfer from the surface. However, the theoretical work of Hissong (2007) demonstrated that an 83 wt% Methane, 7 wt% Ethane and 10 wt% heavier hydrocarbons mixture experiences film boiling until 70% of the mass initially released has vaporised. Thus, in this study, a constant heat transfer coefficient is assumed to hold for most of the vaporisation duration of the Methane/Ethane mixture.

Case studies C and D are pools formed from continuous spills on concrete. The values for thermal conductivity and diffusivity of the surface are taken from Cook and Woodward (1993).

The surface roughness length upwind from the pool is taken as 10^{-4} m for calm sea (CPR, 2005). For spills on concrete it is taken as 10^{-2} m to simulate an open field without obstacles (van den Bosch, C., 2005.).

Table 4.1. Prevailing conditions and surface characteristics for case studies A to D

		Case study			
		A	**B**	**C**	**D**
Release	Type of spill	Continuous	Continuous	Continuous	Continuous
	Spill rate (kg/s)	1	1	1	1
	Spill duration (h)	2	2	2	2
	Spill temperature (K)	111.7	111.7	111.7	111.7
	Spill composition				
	Methane (wt%)	85	100	100	85
	Ethane (wt%)	15	0	0	15
Ambient	Ambient temperature (K)	288	288	288	288
	Ambient pressure (Pa)	101,325	101,325	101,325	101,325
	Atmospheric stability (Pasquill class)	D-Neutral	D-Neutral	D-Neutral	D-Neutral
	Wind speed at 10 m height (m/s)	5	5	5	5
	Upwind surface roughness length (m)	10^{-4}	10^{-4}	10^{-2}	10^{-2}
	Solar incidence (W/m^{2}K)	0	0	0	0
Surface	Surface	Calm sea	Calm sea	Concrete	Concrete
	Bund diameter (m)	0	0	0	0
	Bund height (m)	0	0	0	0
	Surface temperature (K)	283	283	288	288
	Surface thermal conductivity (W/m K)	–	–	1.21	1.21
	Surface thermal diffusivity (10^7 m^2/s)	–	–	4.72	4.72
	Heat transfer coefficient (W/m^2 K)	155	155	–	–

4.3.1.2. Pools on water

The following figures present the simulation results of case studies A and B. The mass spill rate into the pool is 1 kg/s. The temperature of the sea surface is assumed to be 283 K.

Figure 4.1 shows the variation of the vaporisation rate with time for pure Methane (curve A) and an 85 wt% Methane and 15 wt% Ethane mixture (curves B to D). Curve B shows the overall vaporisation rate of the mixture, while curves C and D respectively show the vaporisation rates of Methane and Ethane in the mixture.

Curve A in figure 4.1 shows a continuous increase with time in the pure Methane vaporisation rate from zero to the maximum value of 1 kg/s achieved at the steady state (45 s after release). The pool reaches steady state when the mass accumulation term in equation (3.23) is zero. For a continuous spill at steady state the vaporisation and spill rates are equal if there is no dissolution. In curve B, showing the results for the mixture, the following successive stages may be identified. First, the pool vaporisation rate increases with time as the surface area available for evaporation increases due to pool spreading. The pool vaporisation rate then decreases in time up to an inflection point ca. 70 s where it recovers and reaches steady state at approximately 155 s.

Comparing curves A and B in figure 4.1 it is observed that the vaporisation rate of the Methane/Ethane mixture (curve B) initially coincides with the vaporisation rate of pure Methane (curve A). However, from around 15 to 155 s the vaporisation rate predicted for the mixture is up to 8% lower than for pure Methane. The shape of curve B in figure 4.1 may be explained with the help of the temperature vs. composition phase diagram for Methane and Ethane shown in figure 4.2.

Based on the formulation of the multi-component boiling model presented in section 4.2.2.1 the pool will boil at the bubble point of the mixture. This means that while the pool is boiling its temperature will follow the lower curve shown in figure 4.2. In this figure the bubble point temperature increases from the boiling point of methane (at ethane mass fraction = 0) to the boiling point of ethane (at ethane mass fraction = 1).

The composition of the vapour that escapes the pool is determined from the dew point curve at the pool temperature. In other words, the composition of the vapour at a given pool composition is found by moving horizontally from the bubble to the dew point curve, as indicated in figure 4.2.

While the Methane / Ethane mixture boils the pool temperature will follow the bubble point curve shown in figure 4.2, however the final temperature of the pool will be lower than the normal boiling point of Ethane. The initial composition of 85 % Methane and 15% Ethane is indicated by point A in figure 4.2. The final temperature of the pool is read from the dew point curve at the initial composition of the pool. As seen in figure 4.2 this temperature is lower than the normal boiling point of Ethane as pure component. The final fraction of Methane in the pool is indicated by point B in figure 4.2.

The bubble and dew point temperatures curves shown in figure 4.2 were obtained from the respective flash calculations using Raoult’s Law (Walas, 1985):

$$\boldsymbol{T_{bubble}}: \quad \sum_{i=1}^{n}\left(\frac{P_v^{\,i}\left(T_{bubble}\right)}{P_{atm}}x_{pool}^{\ \ i}\right)-1=0 \qquad (4.15)$$

$$\boldsymbol{T_{dew}}: \quad \sum_{i=1}^{n}\left(\frac{P_{atm}}{P_v^{\,i}\left(T_{bubble}\right)}y_{vap}^{\ \ i}\right)-1=0 \qquad (4.37)$$

The vapour pressures of Methane and Ethane were obtained from DIPPR® thermo-physical properties package (Design Institute for Physical Properties, 2012).

From figure 4.2 it can be seen that the slope of the dew point curve is steep at low Ethane fractions, while the bubble point slope is almost flat in the region from zero to ca. 0.85. Hence, even at Ethane liquid mass fractions of 0.7 and 0.8 the vapour phase is composed almost entirely of Methane. This explains the initial agreement of curves A and B in figure 4.1.

As the spill progresses the pool becomes richer in Ethane, indicated by moving to the right in figure 4.2, and the gradient of the bubble point curve increases. For a mixture that boils at constant pressure, the heat entering the system is spent in both the phase change and as sensible heat to keep the pool at the bubble point. When the gradient of the bubble point curve increases, the rate at which heat must be supplied to the pool for it to remain at the bubble point, Q_{bubble}, (see section 4.2.2.1) also increases. This leaves less energy in the pool to cause the phase change. Consequently, between 15 and 70 s after release the vaporisation rate of the mixture decreases with time as observed in curve B in figure 4.1.

Nonetheless, after approximately 70 s the vaporisation rate of the mixture shown in figure 4.1 starts increasing again. This new increment can be explained by a decrease on the heat of vaporisation of the mixture. The heat of vaporisation of the mixture is defined in the present model as the weighted sum of the vaporisation enthalpies of pure Methane and Ethane (see section 4.2.1). As the pool becomes richer in Ethane which has a lower heat of vaporisation ($\Delta H_{vap}(T_{sat}$, 1atm) = 16,030 J/mole) than Methane ($\Delta H_{vap}(T_{sat}$, 1atm) = 31,890 J/mole), the heat of vaporisation of the mixture decreases. That is, less energy per mole of mixture is required for the phase change. Hence, the vaporisation rate starts increasing up to the maximum value of 1 kg/s, given by the steady state condition. The values of the heat of vaporisation for Methane and Ethane at their respective normal boiling point given above were obtained from DIPPR® thermo-physical properties package (Design Institute for Physical Properties, 2012).

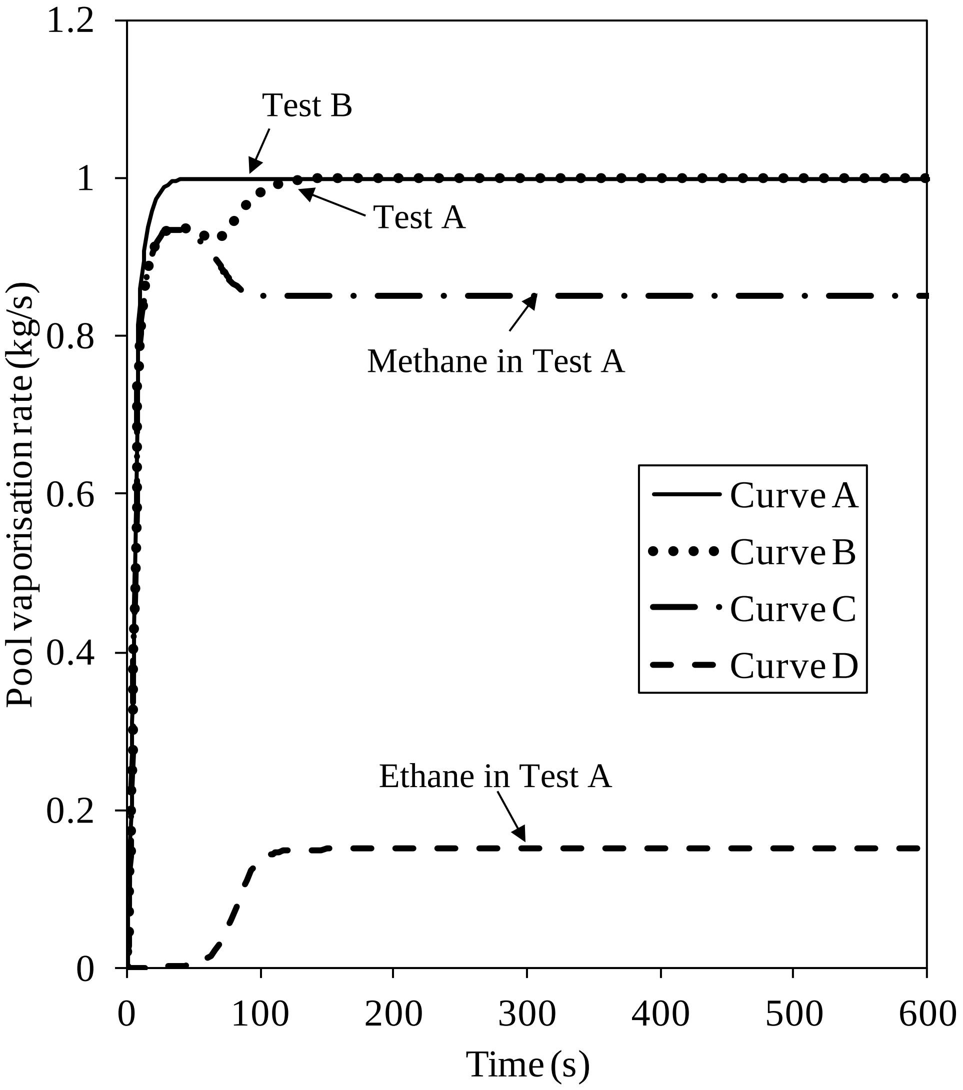

Figure 4.1. Variation of the pool vaporisation rate with time for continuous releases on calm sea at a temperature of 283 K and a wind speed of 5 m/s at 10 m height

Spill rate: 1 kg/s

Curve A: Test B, pure Methane

Curve B: Test A, mixture Methane/Ethane

Curve C: Test A, Methane in the mixture

Curve D: Test A, Ethane in the mixture

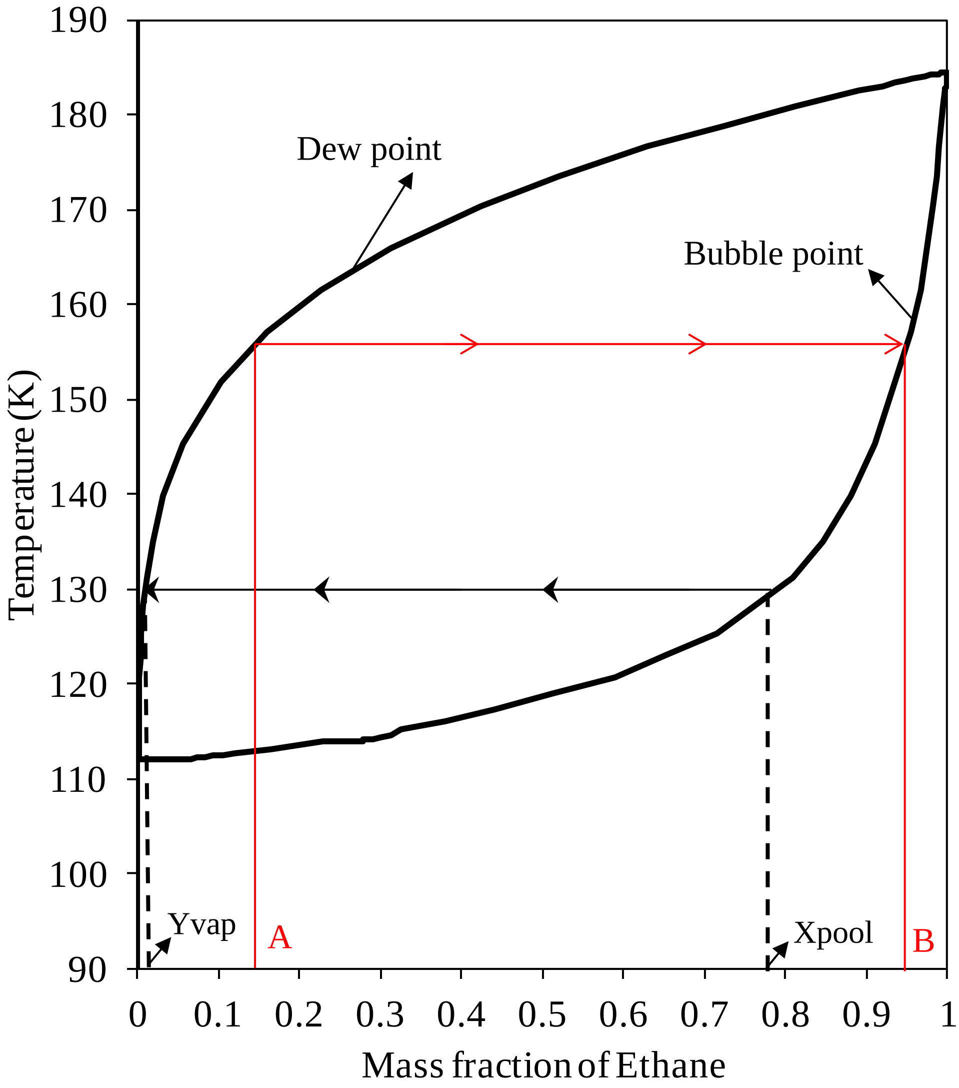

Figure 4.2. Phase envelope for a Methane and Ethane system

Figures 4.3 and 4.4 respectively show the variation of pool temperature and radius with time for the case studies described above.

Curve A in figure 4.3 shows the variation of the pool temperature with time for the mixture. Curve B are the results of the mixture's bubble point temperature. Curve C shows the variation of the pool temperature with time for the pure Methane release. Curve D represents the normal boiling point of Methane. The bubble point temperature of the mixture (curve B) was obtained from DIPPR® thermo-physical properties package (Design Institute for Physical Properties, 2012). Curves A and B start from

Methane’s boiling point and increase up to the bubble point temperature of an 85 wt% Methane and 15 wt% Ethane mixture.

Figure 4.4 shows the variation of the pool radius with time for the mixture (curve A) and pure Methane (curve B).

From figure 4.3, it can be observed that the pool remains at its bubble point in the time frame under consideration. This indicates that enough heat is being supplied by the surroundings for the pool to remain in the boiling regime. It is shown later (see next section) that this is not the case for cryogenic spills on land.

From figure 4.4, showing the variation of the pool radius with time, a difference of 15% between the maximum pool radius for the mixture (curve A) and the pure component (curve B) cases is observed. In the analysis of the variation of the pool vaporisation rate with time, shown in figure 4.1, it is found that the vaporisation rate of the mixture never exceeds the vaporisation rate of the pure component. As mass is added to the pool at the same rate in both cases, the pool accumulates more mass in the mixture case and therefore spreads to a larger radius.

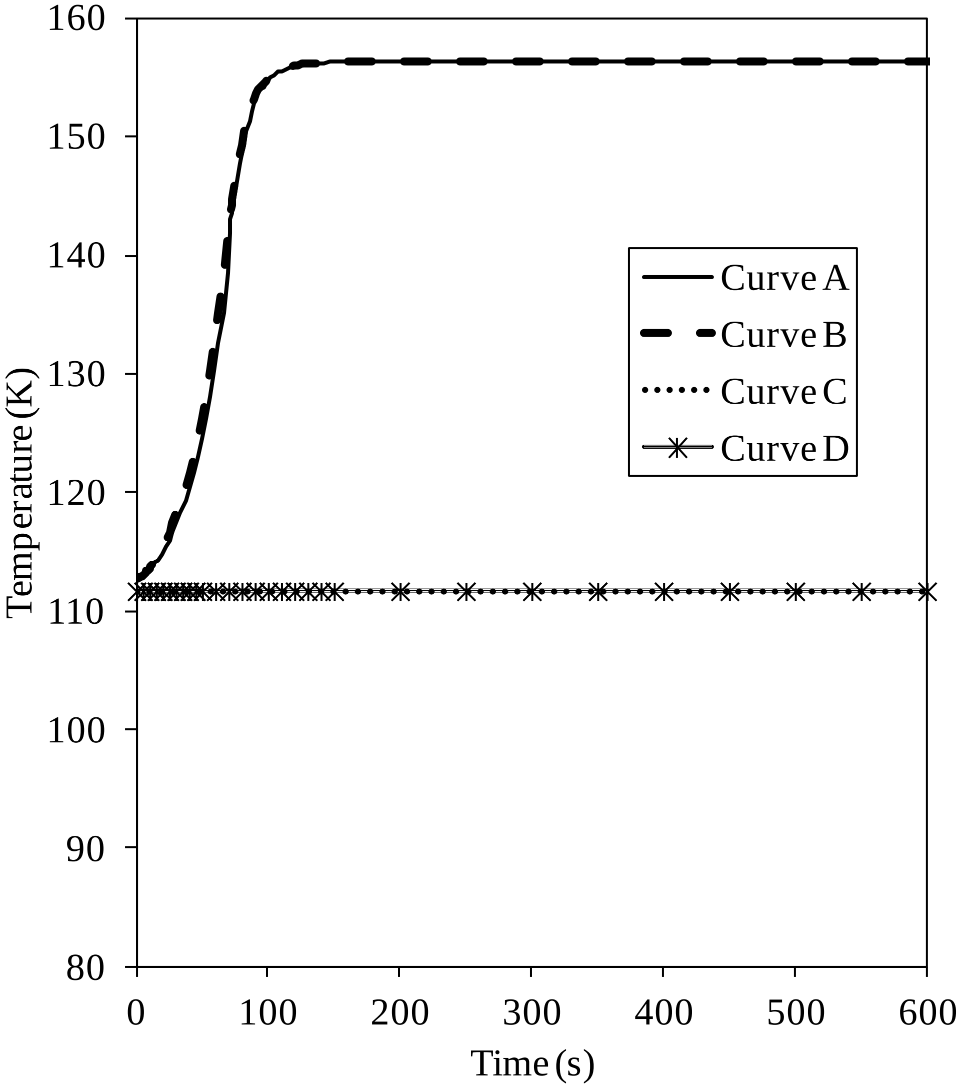

Figure 4.3. Variation of the pool and bubble point temperatures with time for continuous releases on calm sea at a temperature of 283 K and a wind speed of 5 m/s at 10 m height

Spill rate: 1 kg/s

Curve A: Test A, mixture Methane/Ethane: Pool temperature

Curve B: Test A, mixture Methane/Ethane: Bubble point temperature

Curve C: Test B, pure Methane: Pool temperature

Curve D: Test B, pure Methane: Normal boiling point

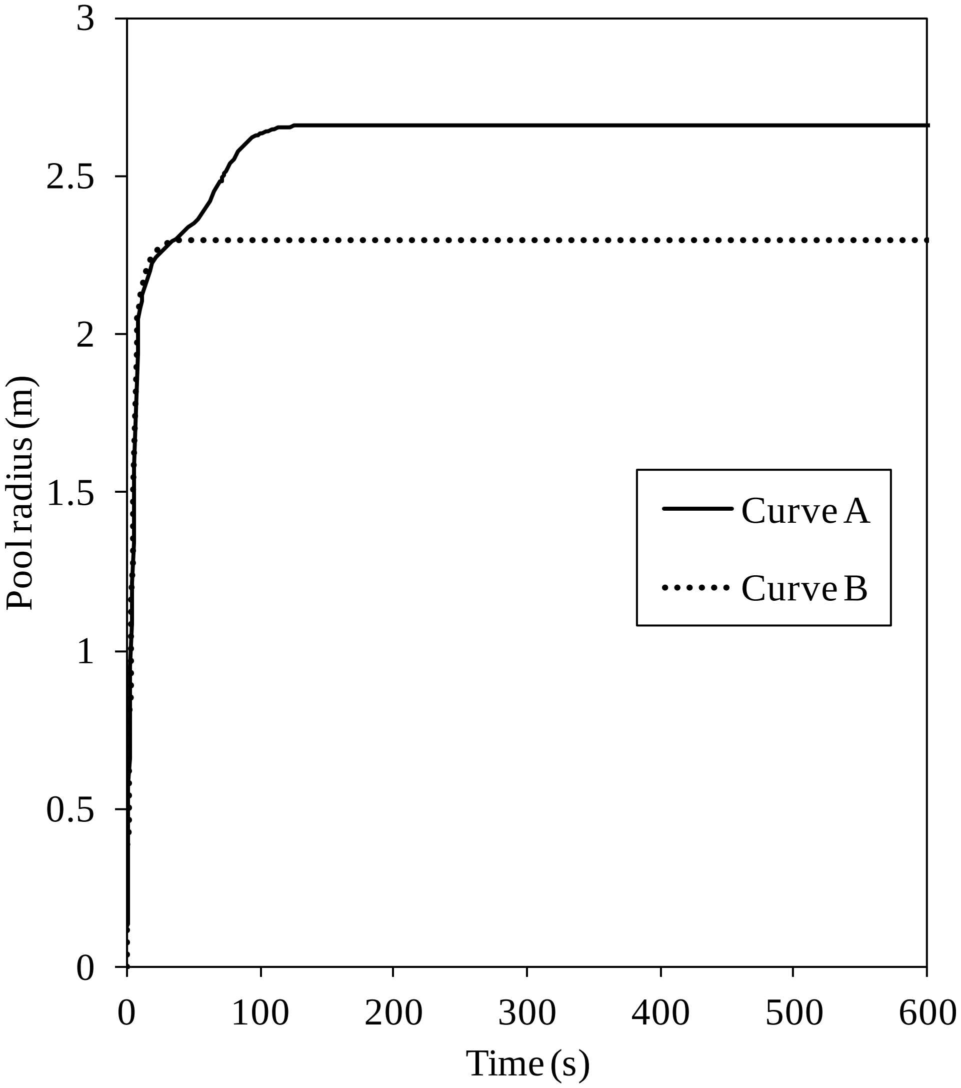

Figure 4.4. Variation of the pool radius with time for continuous releases on calm sea at a temperature of 283 K and a wind speed of 5 m/s at 10 m height

Spill rate: 1 kg/s

Curve A: Test A, mixture Methane/Ethane

Curve B: Test B, pure Methane

The above analysis showed the differences on the vaporisation and spreading rates between pure Methane and a Methane/Ethane mixture with a composition typical of LNG. The findings will impact the subsequent gas dispersion and pool fire characteristics.

Based on the comparison of the pool vaporisation rate with time shown in figure 4.1 it may be observed that it takes three times longer for the mixture to reach the maximum of 1 kg/s evaporation rate than for pure Methane. Such differences highlight the significant errors associated with approximating the mixture as a pure component. However, as the vaporisation rate predicted for pure Methane is greater than for the mixture, such approximation is conservative from the perspective of gas dispersion.

On the other hand, based on the comparison of the pool radius with time presented in figure 4.4, a difference of 15% between the maximum radii of the pool predicted in both scenarios was reported. Subsequently, the total area covered by the pool is under-predicted by 30% for pure Methane as compared to a typical LNG composition thus affecting the subsequent pool fire characteristics and safety separation distance estimations.

The following figure shows the comparison between the multi-component model results and the results of the previous work of Conrado and Vesovic (2000) on boiling of LNG pools on water. The example case is a 50,000 kg instantaneous spill of LNG (90 mole% Methane and 10 mole% Ethane) on water at a temperature of 295 K. The simulation runs for the multi-component pool model were carried out assuming a wind speed of 5 m/s at 10 m height.

From the figure it is observed that the results of the multi-component pool model follow the general trend of the previous results of Conrado and Vesovic (2000) for the case where wind blowing above the pool surface does not allow accumulation of vapour (Conrado_Vesovic_wind). Initially, there is good agreement between both models, although the multi-component pool model presented here reaches a maximum vaporisation rate at a value higher than predicted by Conrado and Vesovic (2000). However, after the vaporisation rate starts to decrease it can be observed that the present work predicts a much lower evaporation than Conrado and Vesovic (2000) model. This may be due to the pool spreading law used in both models. While the multi-component pool model described here assumes that the pool will continue to spread until it has reached a minimum thickness dependent of the surface, Conrado and Vesovic (2000) do not. By assuming a minimum thickness the pool stops spreading once the pool depth has reached this limit value, and as mass is constantly lost by evaporation the pool surface area would have to decrease in order to maintain the mass balance in the pool. This will effectively result in lower predictions of the pool vaporisation rate. The use of the minimum thickness factor in integral pool models is highly debatable as it leads to rather counter intuitive behaviour as just described. However, it is also expected that the pool will stop spreading at a certain point and reach its maximum area. A possibility could be to use the idea of minimum thickness but not as a fixed value dependent solely on the surface characteristics, but as a function of the pool and surface properties. This approach is followed in chapter 6 of the present work regarding the spreading of pools on smooth land surfaces.

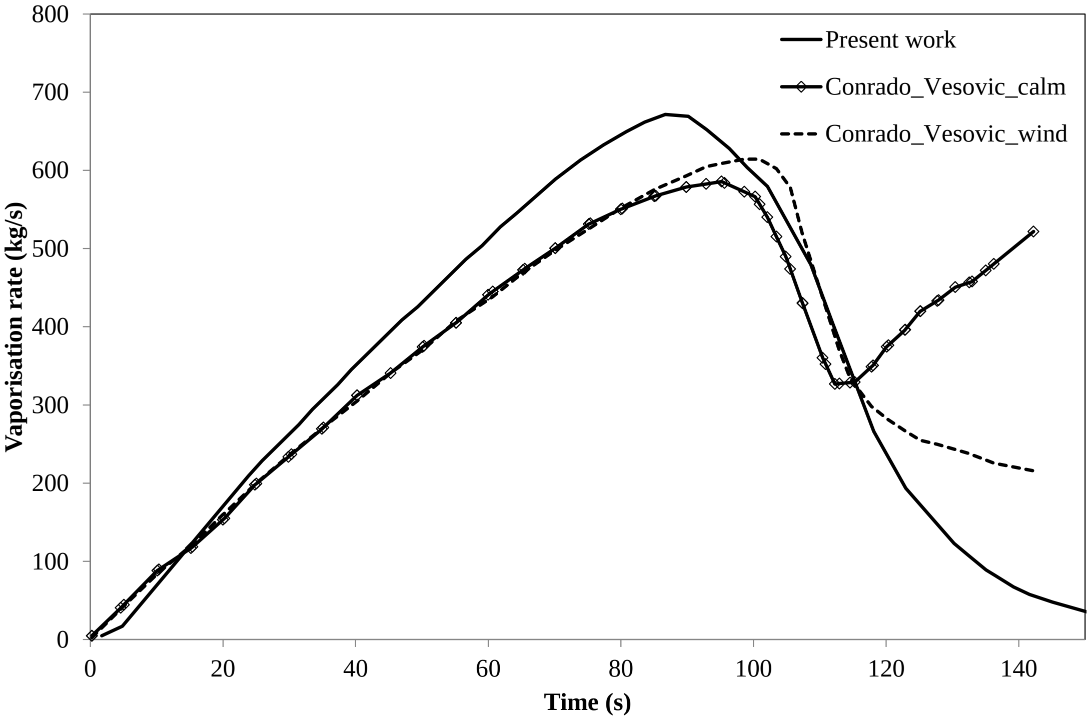

Figure 4.5. Comparison of the vaporisation rate predicted by the multi-component pool model with Conrado and Vesovic (2000) for an instantaneous release 50,000 kg of LNG (90% Methane and 10% Ethane) on water.

Wind speed: 5 m/s at 10 m height

Water temperature: 295 K

4.3.1.2. Pools on land

Figures 4.6 to 4.8 present the results of case studies C and D (see table 4.1) for continuous spills on land. The surface is assumed to be concrete at an initial temperature of 288 K. The mass spill rate is taken as 1 kg/s.

Figure 4.6 shows the variation of the vaporisation rate with time for the pure Methane release (curve A) and an 85 wt% Methane and 15 wt% Ethane mixture (curve B). Additionally, curves C and D respectively show the vaporisation rate of Methane and Ethane in the mixture.

Figure 4.7 shows the variation of the pool and bubble point temperatures with time for pure Methane and the Methane/Ethane mixture. Curve A presents the predicted bubble point curve for the mixture obtained from DIPPR® thermo-physical properties package (Design Institute for Physical Properties, 2012). Curves B and C respectively show the variation of the pool temperature for the Methane/Ethane mixture and pure Methane. Curve D represents the normal boiling point for Methane.

Figure 4.8 shows the variation of the pool radius with time for the mixture (curve A) and pure Methane (curve B).

From figure 4.6 it is observed that the progression of the vaporisation rate for spills on concrete reaches its maximum value after approximately 8 hrs for the Methane/Ethane mixture (curve B) and in 7 hrs for pure Methane (curve A). These times are significantly larger when compared to the case studies for pools on calm sea, where the vaporisation rate of pure Methane and the mixture reached the maximum in 45 and 155 s, respectively (see previous section).

The considerable difference in the time to reach steady state for the test cases on calm sea and concrete may be explained by analysing the surface/pool heat transfer characteristics in both scenarios. As was mentioned in chapter 3, calm sea is modelled as an isothermal flat surface, since it is assumed that the convection currents in the water are sufficient to keep the surface at constant temperature. On the other hand, a surface such as concrete is modelled as a semi-infinite solid with a time-variant temperature profile along the vertical axis. As the pool is at a lower temperature than the initial temperature of the surface, the time-variant model predicts a decrease on the heat flux from the surface to the pool due to the cooling effect. This is further evidenced when comparing the pool temperature profiles for water and land surfaces shown in figures 4.3 and 4.7, respectively.

Returning to figure 4.3, showing the variation of the pool temperature with time for a spill on calm sea, it is seen that the pool follows the bubble point curve for the Methane/Ethane mixture (curve A) and remains constant for the pure component at the normal boiling point of Methane (111.7 K) (curve C). In contrast, figure 4.7 shows a noticeable difference between the pool temperature of the Methane/Ethane mixture (curve B) and the bubble point curve (curve A) as well as a drop below 111.7 K in the pool temperature for pure Methane (curve C). This indicates that while the pool is observed to remain boiling on calm sea it undergoes a transition to evaporation on a concrete surface. The transition takes place at the point where the pool temperature drops below the bubble point or the normal boiling point as appropriate. As the rate of mass vaporised in the evaporation regime is lower than when the pool is boiling it takes longer for the pool evaporating on land to reach steady state conditions and the maximum vaporisation rate.

From figure 4.8, a 14% difference on the maximum pool radius between the pure component (curve B) and the mixture (curve A) may be observed. Similarly to the spreading of cryogenic liquids on water (see previous section), the pool accumulates more mass in the mixture case because of the lower vaporisation rates. Thus, it spreads to a larger radius in the case of the Methane/Ethane mixture as compared to pure Methane.

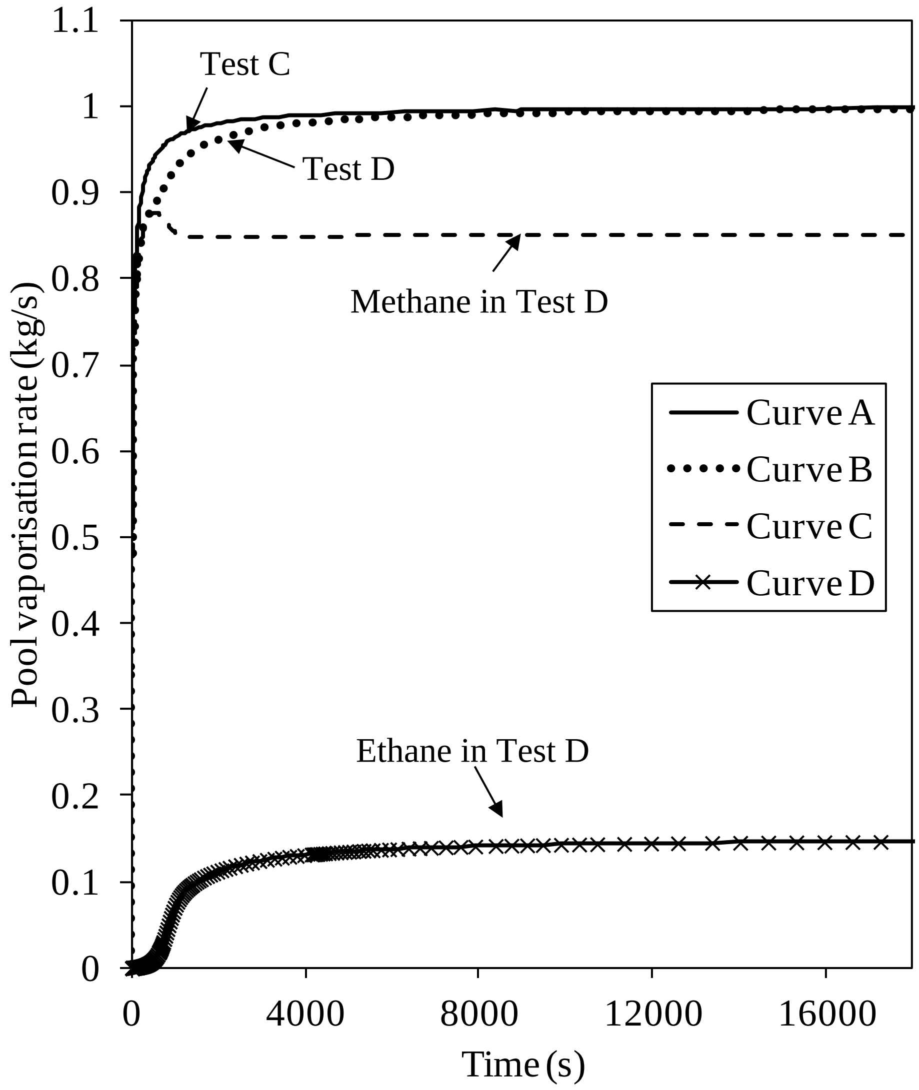

Figure 4.6. Variation of the pool vaporisation rate with time for continuous releases on concrete at a temperature of 288 K and a wind speed of 5 m/s at 10 m height

Spill rate: 1 kg/s

Curve A: Test C, pure Methane

Curve B: Test D, mixture Methane/Ethane

Curve C: Test D, Methane in the mixture

Curve D: Test D, Ethane in the mixture

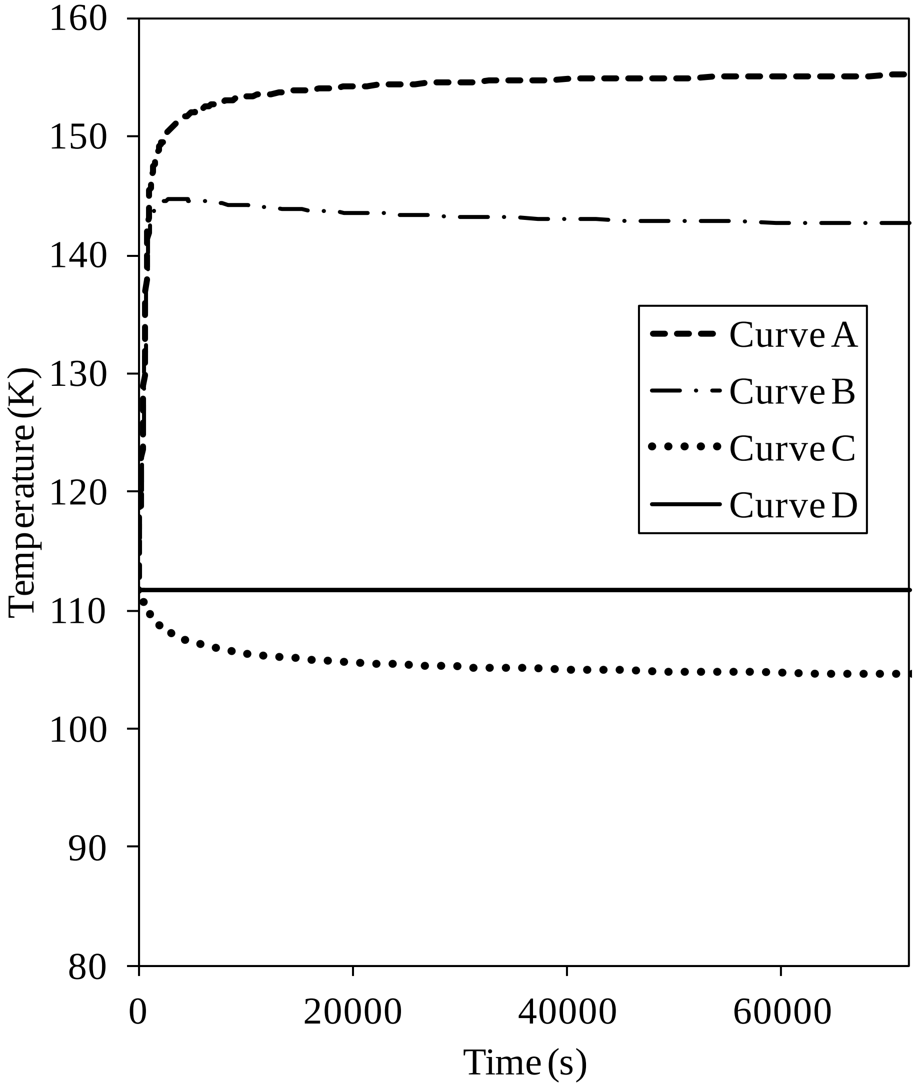

Figure 4.7. Variation of the pool temperature with time for continuous releases on concrete at a temperature of 288 K and a wind speed of 5 m/s at 10 m height

Spill rate: 1 kg/s

Curve A: Test D, mixture Methane/Ethane: Bubble point temperature

Curve B: Test D, mixture Methane/Ethane: Pool temperature

Curve C: Test C, pure Methane: Pool temperature

Curve D: Test C, pure Methane: Normal boiling point

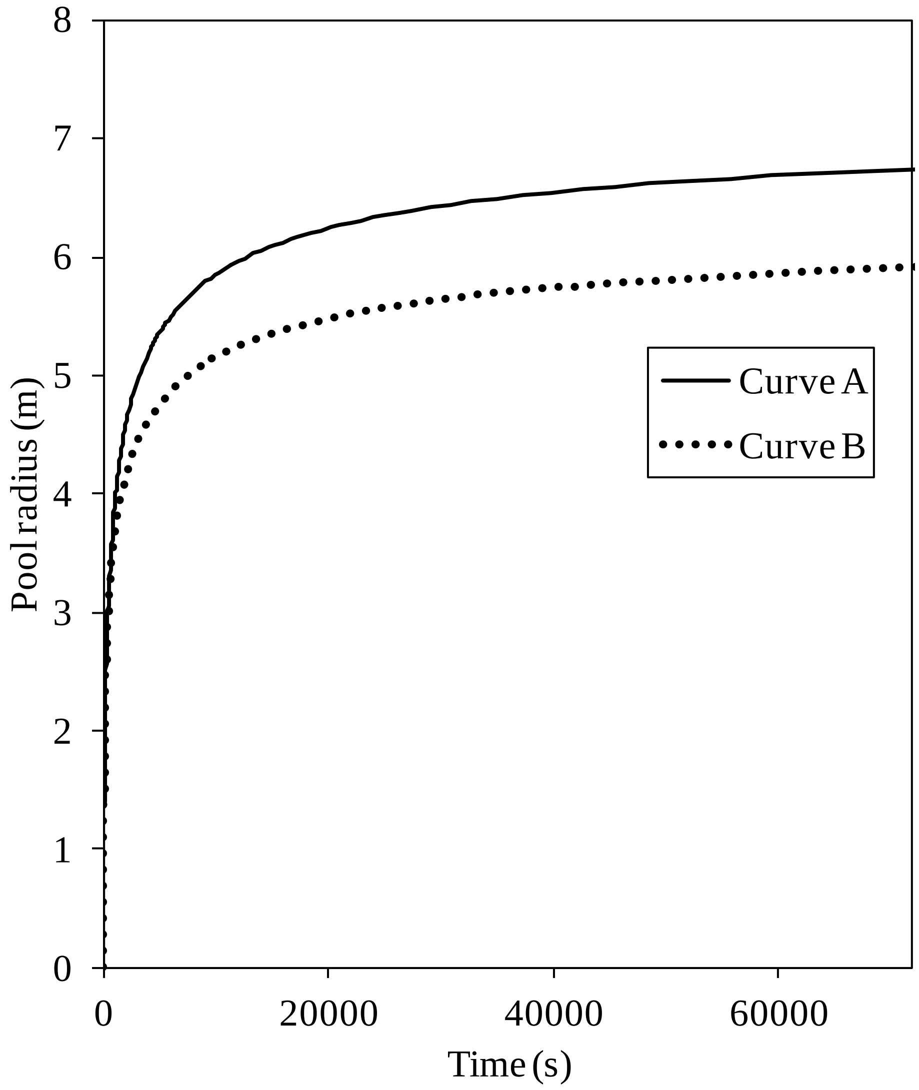

Figure 4.8. Variation of the pool radius with time for continuous releases on concrete at a temperature of 288 K and a wind speed of 5 m/s at 10 m height

Spill rate: 1 kg/s

Curve A: Test D, mixture Methane/Ethane

Curve B: Test C, pure Methane

Continuous spills at a constant spill rate after a certain time reach a steady state in which the pool has reached a maximum size. At this point there is no accumulation of mass in the pool and the vaporisation rate is equal to the spill rate. The pool will continue then to evaporate at a constant rate equal to the spill. This behaviour is the one observed in figure 4.6 for both the mixture and the pure Methane cases.

The above observations highlighted the differences in the vaporisation and spreading rates between pure Methane and a Methane/Ethane mixture released on a concrete surface. The findings will impact the characteristics of gas dispersion, pool fires and further consequence assessment. In line with the analysis presented in the previous section for continuous releases of cryogenic liquids on water, the results for pools on land also showed much longer times to reach the maximum vaporisation rate for the mixture than for the pure component. Consequently, the total amount of material vaporised from a pool is significantly over-predicted when a mixture is characterized as a pure component with the properties of the predominant material in the pool. For gas dispersion modelling the assumption that a mixture can be modelled as a pure component is conservative, but it may lead to overdesign of safety mitigation measures. Regarding the variation of the pool radius with time shown in figure 4.78 it was observed how the approximation of the Methane/Ethane mixture to pure Methane for continuous releases on land results in under predictions of the radius up to 15%. This observation is important for subsequent pool fire modelling and estimation of safe separation distances and hazard exclusion zones.

4.3.2 Evaporating liquids

The following presents the simulation results using the multi-component pool model presented in section 4.2.2.2 for selected case studies involving evaporating liquids. Table 4.2 lists the prevailing conditions and surface characteristics. The case studies include instantaneous and continuous spills on concrete. Simulation runs of instantaneous and continuous releases on water were also carried out. The results can be found in Appendix A.

Case studies E and F are pools formed from continuous spills on concrete. Mass is continuously added to the pool at a rate of 0.01 kg/s for 150,000 s.

Case studies G and H are pools formed from instantaneous spills on concrete with a bund of 4 m diameter. The total mass spilled is 1000 kg.

Similar to the studies on cryogenic liquids on land, the surface roughness length upwind from the pool is taken as 10^{-2} m. The atmospheric stability is categorised as neutral according to Pasquill's classification, indicating a minimal influence of vertical temperature gradients on the atmospheric turbulence. A wind speed of 5 m/s at 10 m above the pool and no solar incidence were chosen as conditions to simulate a cloudy day.

Table 4.2. Prevailing conditions and surface characteristics for case studies E to H

		Case study			
		E	**F**	**G**	**H**
Release	Type of spill	Continuous	Continuous	Instantaneous	Instantaneous
	Spill mass (kg)	–	–	1000	1000
	Spill rate (kg/s)	0.01	0.01	–	–
	Spill duration (h)	72	72	–	–
	Spill temperature (K)	293	293	293	293
	Spill composition (wt%)				
	n-Pentane	85	100	85	100
	n-Hexane	10	0	10	0
	m-Xylene	5	0	5	0
Ambient	Ambient temperature (K)	288	288	288	288
	Ambient pressure (Pa)	101,325	101,325	101,325	101,325
	Atmospheric stability (Pasquill class)	D-Neutral	D-Neutral	D-Neutral	D-Neutral
	Wind speed at 10 m height (m/s)	5	5	5	5
	Surface roughness length (m)	10^{-2}	10^{-2}	10^{-2}	10^{-2}
	Solar incidence ($W/m^2.K$)	0	0	0	0
Surface	Surface material	Concrete	Concrete	Concrete	Concrete
	Bund diameter (m)	0	0	4	4
	Bund height (m)	0	0	1	1
	Surface temperature (K)	288	288	288	288
	Surface thermal conductivity (W/m K)	1.21	1.21	1.21	1.21
	Surface thermal diffusivity (10^7 m^2/s)	4.72	4.72	4.72	4.72

4.3.2.1 Continuous spill

Figures 4.9 to 4.12 present the results of case studies E and F. The mass spill rate in both cases is 0.01 kg/s. The concrete surface is initially at 288 K.

Figure 4.9 shows the variation of the vaporisation rate with time for the pure n-Pentane release (curve A) and an 85 wt% n-Pentane, 10 wt% n-Hexane and 5 wt% m-Xylene mixture (curve B). Curves C, D and E respectively show the vaporisation rate of n-Pentane, n-Hexane and m-Xylene in the mixture.

From figure 4.9 it is observed that despite the differences in times for pure n-Pentane and the mixture to reach the maximum vaporisation rate, both cases predict very close values for the pool vaporisation rate. This contrasts with the case of cryogenic liquids analysed in the previous section, where noticeable differences between the mixture and the pure component were found. The reason for this may be due to the large dependence of the pool evaporation phenomena on ambient conditions. Examples include the wind speed, ambient temperature, solar radiation, etc. which are common to both the pure component and the mixture scenarios under study.

However, the differences in volatility of the mixture components are reflected in the composition of the vaporisation rate observed from curves C to E in figure 4.9. The volatility of a component in a mixture is dependent on its vapour pressure. Table 4.3 shows the vapour pressure and liquid specific heat capacity for n-Pentane, n-Hexane and m-Xylene at a temperature of 273 K predicted by DIPPR® thermo-physical properties package (Design Institute for Physical Properties, 2012).

Table 4.3. Vapour pressure and specific heat capacity at 273 K obtained from DIPPR® thermo-physical properties package (Design Institute for Physical Properties, 2012)

Component	Vapour pressure P_v^i (Pa)	Liquid specific heat capacity c_p^i (J/kg K)
n-Pentane	24,292	2245
n-Hexane	5,983	2182
m-Xylene	223	1647

Differences of orders of magnitude in the vapour pressure of n-Pentane, n-Hexane and m-Xylene can be seen in the table above. Returning to figure 4.9, it is observed that the vaporisation rate of n-Pentane is eight times greater than m-Xylene, due to the large differences in the vapour pressure of the components shown above.

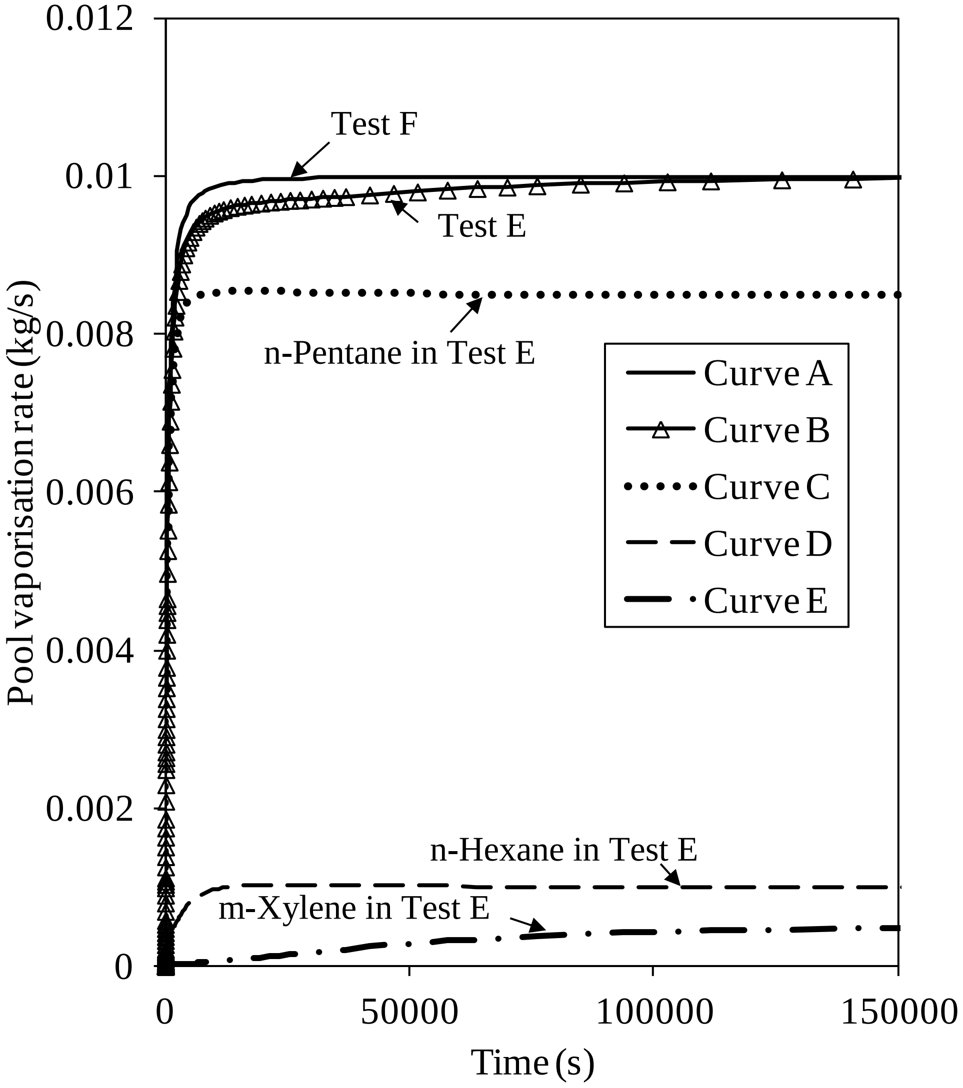

Figure 4.9. Variation of the pool vaporisation rate with time for continuous releases on concrete at a temperature of 288 K and a wind speed of 5 m/s at 10 m height

Spill rate: 0.01 kg/s

Curve A: Test F, pure n-Pentane

Curve B: Test E, mixture n-Pentane/n-Hexane/m-Xylene

Curve C: Test E, n-Pentane in the mixture

Curve D: Test E, n-Hexane in the mixture

Curve E: Test E, m-Xylene in the mixture

Figures 4.10 and 4.13 respectively show the variation of the pool temperature and radius with time for the pure component (curve B) and the mixture (curve A) cases.

From figure 4.10, an initial decrease on the pool temperature is observed for both pure n-Pentane and the mixture as the pool loses energy during evaporation. For the pure component the pool temperature continues to decrease, albeit at a lower rate, reaching steady state at a temperature of 255 K, some 33 K below the temperature of the surroundings. For the mixture on the other hand, after 5000 s approx., the pool temperature starts to increase attaining steady state at about 273 K, some 15 degrees below the ambient temperature. The differences between the results shown in curves A and B could be due to the differences in the specific heat capacity of the different components. These are shown in table 4.3 above as obtained from DIPPR® thermo-physical properties package (Design Institute for Physical Properties, 2012). From table 4.3 it is observed that n-Pentane has the highest specific heat and m-Xylene the lowest. As evaporation progresses the pool mass fraction of m-Xylene increases, due to the preferential vaporisation of the lighter components (n-Pentane and n-Hexane). The overall heat capacity of the mixture is thus reduced with time. Therefore, less heat is required to increase the pool temperature for the mixture than for the pure component.

Additionally, it was observed that the heat losses from the pool per unit area for the n-Pentane simulation were almost double that obtained for the mixture. This is shown in figure 4.11. In both scenarios, for the mixture and the pure component, the heat losses from evaporation are the largest contributor to the net heat variation in the pool, and would therefore determine the variation of the pool temperature with time. As such, the pool temperature would present a larger decrease for the pure n-Pentane case than for the mixture, after which the pool will reach a steady state where its conditions won’t vary with time. This is shown by the levelling of both curves in figure 4.10 after approx. 100,000 s.

Further verification of the variation of the pool temperature with time for pure n-Pentane in the current example is shown in figure 4.12. This figure shows the temperature profile of the pool in time for pure n-Pentane and for a binary mixture in which both components have the material properties of n-Pentane. It can be observed that both curves show the same profile for the pool temperature. This comparison serves as an additional verification of the results of the multi-component pool model.

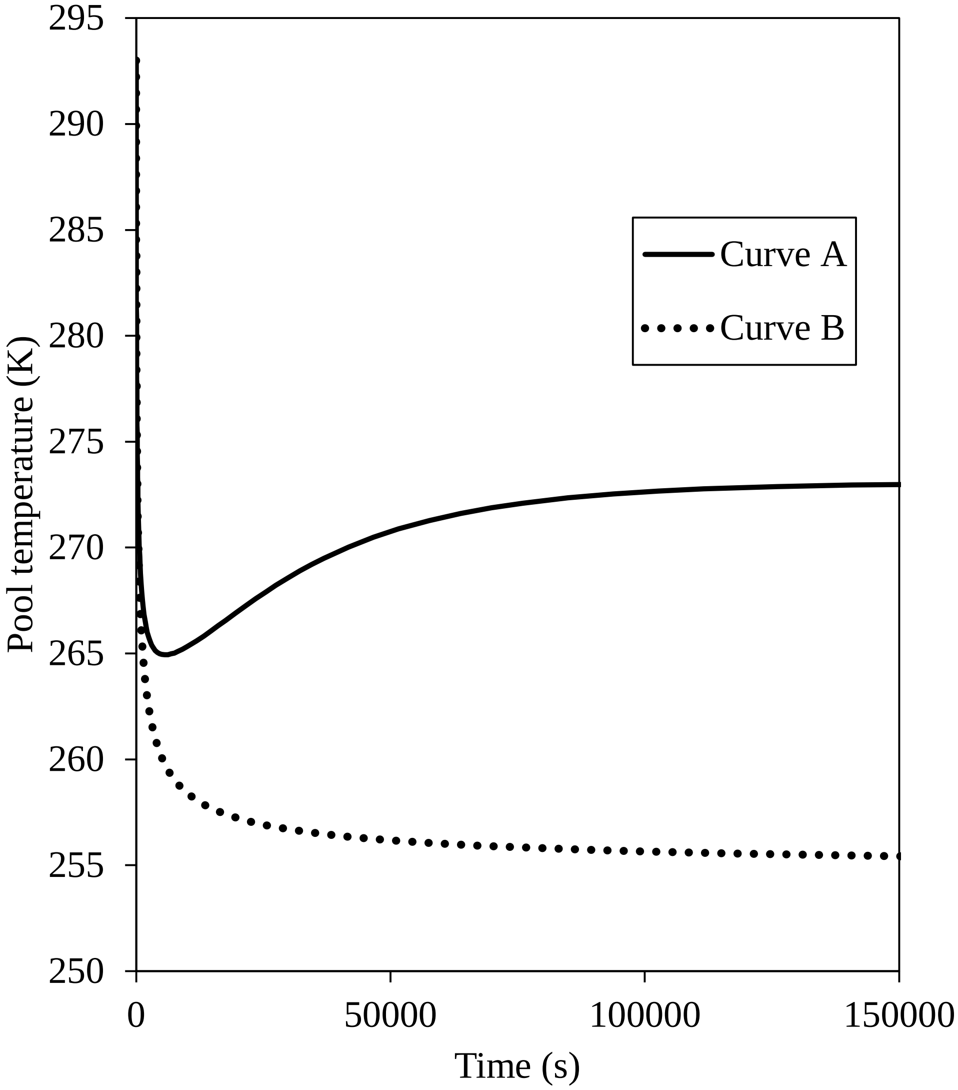

Figure 4.10. Variation of the pool temperature with time for continuous releases on concrete at a temperature of 288 K and a wind speed of 5 m/s at 10 m height

Spill rate: 0.01 kg/s

Curve A: Test E, mixture n-Pentane/n-Hexane/m-Xylene

Curve B: Test F, pure n-Pentane

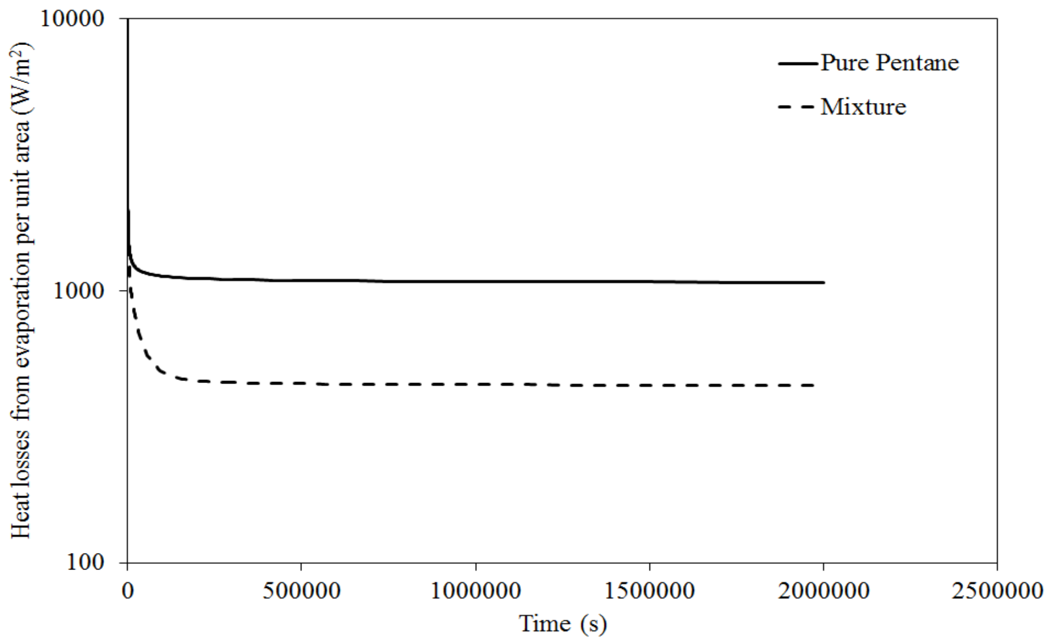

Figure 4.11. Variation of the heat of evaporation per unit area with time for the mixture and pure n-Pentane

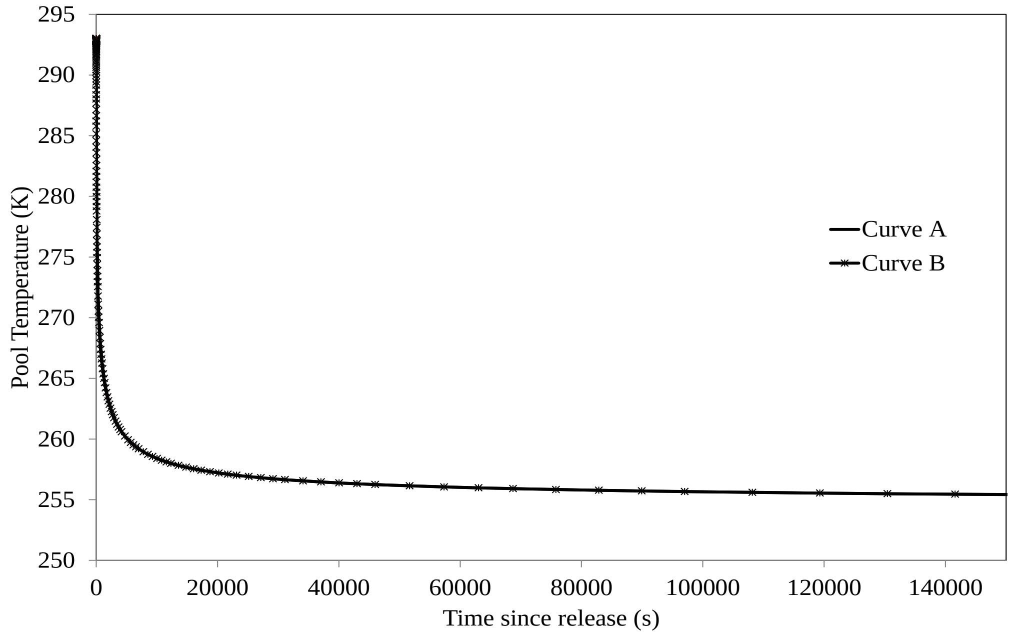

Figure 4.12. Variation of the pool vaporisation rate with time for continuous releases on concrete at a temperature of 288 K and a wind speed of 5 m/s at 10 m height

Spill rate: 0.01 kg/s

Curve A: Test F, pure n-Pentane

Curve B: Test E, a binary mixture where both components are n-Pentane

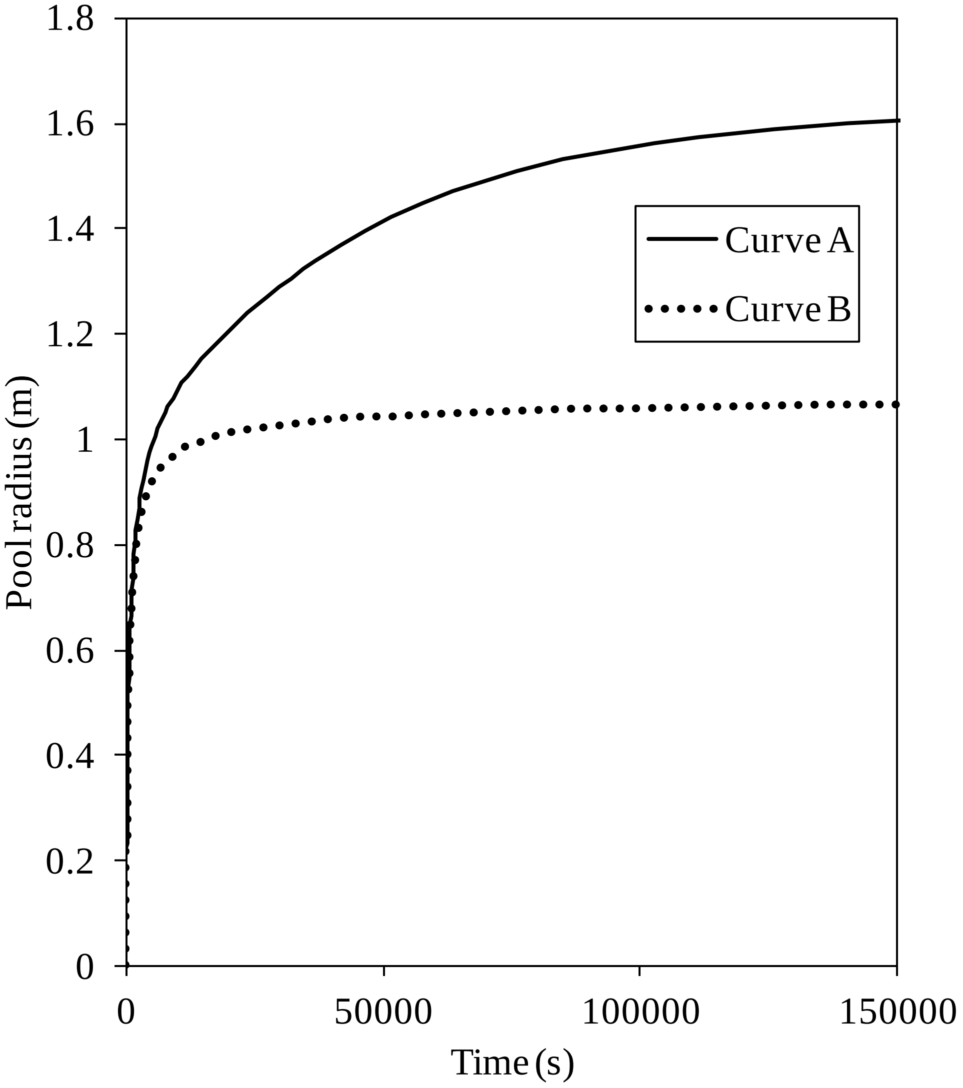

Figure 4.13. Variation of the pool radius with time for continuous releases on concrete at a temperature of 288 K and a wind speed of 5 m/s at 10 m height

Spill rate: 0.01 kg/s

Curve A: Test E, mixture n-Pentane/n-Hexane/m-Xylene

Curve B: Test F, pure n-Pentane

In figure 4.13 large differences in the prediction of the pool maximum radius can be observed between the pure component and the mixture. In this case study, the maximum radius of the pool would be under predicted by almost 40% if the mixture were approximated by pure n-Pentane. As was mentioned in the study for cryogenic liquids, the prediction of the maximum pool size also impacts the pool fire characteristics and the safe separation distances.

4.3.2.2. Instantaneous release

Figures 4.14 to 4.16 present the results of case studies G and H (see table 4.2). The total mass spilled is 1000 kg. The initial temperature of the surface is 288 K. The diameter of the bund is taken as 4 m.

The variation of the pool vaporisation rate with time for pure n-Pentane (curve A) and an 85 wt% n-Pentane, 10 wt% n-Hexane and 5 wt% m-Xylene mixture (curve B) are shown in figure 4.14.

Figure 4.15 show the vaporisation rate of n-Pentane (curve A), n-Hexane (curve B) and m-Xylene (curve C) in the mixture.

Figure 4.16 shows the variation of the pool temperature with time for both the pure component (curve A) and mixture (curve B).

From figure 4.14 it is observed that the vaporisation rate of the n-Pentane/n-Hexane/m-Xylene mixture and pure n-Pentane follow similar trends. In both cases the rate of evaporation shows an initial exponential decrease in time which levels off ca. 0.04 kg/s. This is followed by a further drop in the evaporation rate indicating that so much mass has been lost by the pool that it starts to shrink, effectively reducing the surface area available for evaporation. The results for the mixture presented in curve B show a smoother drop in the vaporisation rate than the pure component shown in curve A. The reason for this is the delayed vaporisation of the heavier components contained in the mixture. Additionally, comparing curves A and B it is observed that the results for the mixture indicate the pool will evaporate completely approx. 1200 s later than the pure component. In summary, it is observed that the pool composition has a limited impact on the pool vaporisation rate, although the presence of components with different volatilities in the mixture delays the disappearance of the pool.

A hand-calculation of the vaporisation rate for the pure n-Pentane case is shown here. From the energy balance the vaporisation rate from the pool in the first 10,000 s is determined from:

$$\dot{m}_{vap} = \frac{1}{\Delta H_{vap}} \left(Q_{cond} + Q_{conv} + Q_{rad} - M_{pool} c_{p\,pool} \frac{dT_{pool}}{dt} \right)$$

Remembering here the formulations of the heat of conduction, convection and radiation presented in chapter 3:

$$Q_{cond} = \frac{k\,(T_{surf} - T_{pool})\pi^{0.5} r^2}{(\alpha\, t)^{0.5}}$$

$$Q_{conv} = k_a Nu \frac{\pi\, r^2}{L} (T_{amb} - T_{pool})$$

$$Q_{rad} = \left[S + \varepsilon\, \sigma (T_{amb}^4 - T_{pool}^4)\right] \pi\, r^2$$

where,

ΔH_{vap} = n-Pentane heat of vaporisation = 400,000 J/kg

$c_{p\,pool}$ = n-Pentane specific heat capacity = 1,500 J/kg.K

k = Concrete thermal conductivity = 1.21 W/m.K

α = Concrete thermal diffusivity = 5.7 x 10^{-7} m^2/s

k_a = Air thermal conductivity = 0.0256 W/m.K

Nu = Nusselt number = 12,800

S = Solar incidence = 0 W/m^2

ε = Pool emissivity = 0.95

σ = Stefan-Boltzmann constant = 5.7 x 10^{-8} $W/m^2.K^4$

T_{amb} = ambient temperature = 288 K

T_{pool} = average pool temperature = 260 K

T_{surf} = surface temperature = 288 K

R = pool radius = 2 m

T = time = 10,000 s

M_{pool} = 500 kg

With the above values the heat of conduction, convection and radiation result in:

Q_{cond} = 3180 W; Q_{conv} = 8240 W; Q_{rad} = 1700 W

The average vaporisation rate in the first 10,000 s is calculated as:

$$\dot{m}_{vap} = \frac{1}{40{,}000 J/kg}\left(3180W + 8240W + 1700W - 500kg \cdot 1500J/kg.K\,\frac{(293K - 260K)}{10{,}000s}\right)$$

$$\dot{m}_{vap} = 0.00348 \text{ kg/s}$$

This is approximately equal to the value of 0.0378 kg/s result of the simulation.

In figure 4.15, showing the vaporisation rate of the individual components in the mixture, it is observed that n-Pentane (curve A) preferentially vaporises through most of the simulation. Only when the fraction of n-Pentane remaining in the pool is very small, the contributions of the other components, i.e. n-Hexane (curve B) and m-Xylene (curve C), become appreciable.

In figure 4.16 the variation of the pool temperature with time indicates marked differences between the mixture and the pure component. However, in the initial stages of the simulation both curves A and B show a decrease in the pool temperature due to the lower temperature of the surroundings and the cooling effects of evaporation. After approximately 1100 s the mixture temperature (curve A) starts recovering until it reaches thermal equilibrium with the surroundings at 288 K. On the other hand, the results of the pure component (curve B) show a larger drop and a deferred increase in the pool temperature (ca. 2700 s after release) up to a value close to 280 K. The differences observed between curves A and B can be attributed to differences in the specific heat capacity of n-Pentane, n-Hexane and m-Xylene also discussed in the analysis of evaporating continuous releases and shown in table 4.3. As the mixture becomes richer in the heavier components the heat capacity of the pool is reduced, becoming much lower than for pure n-Pentane, thus requiring less heat to increase its temperature.

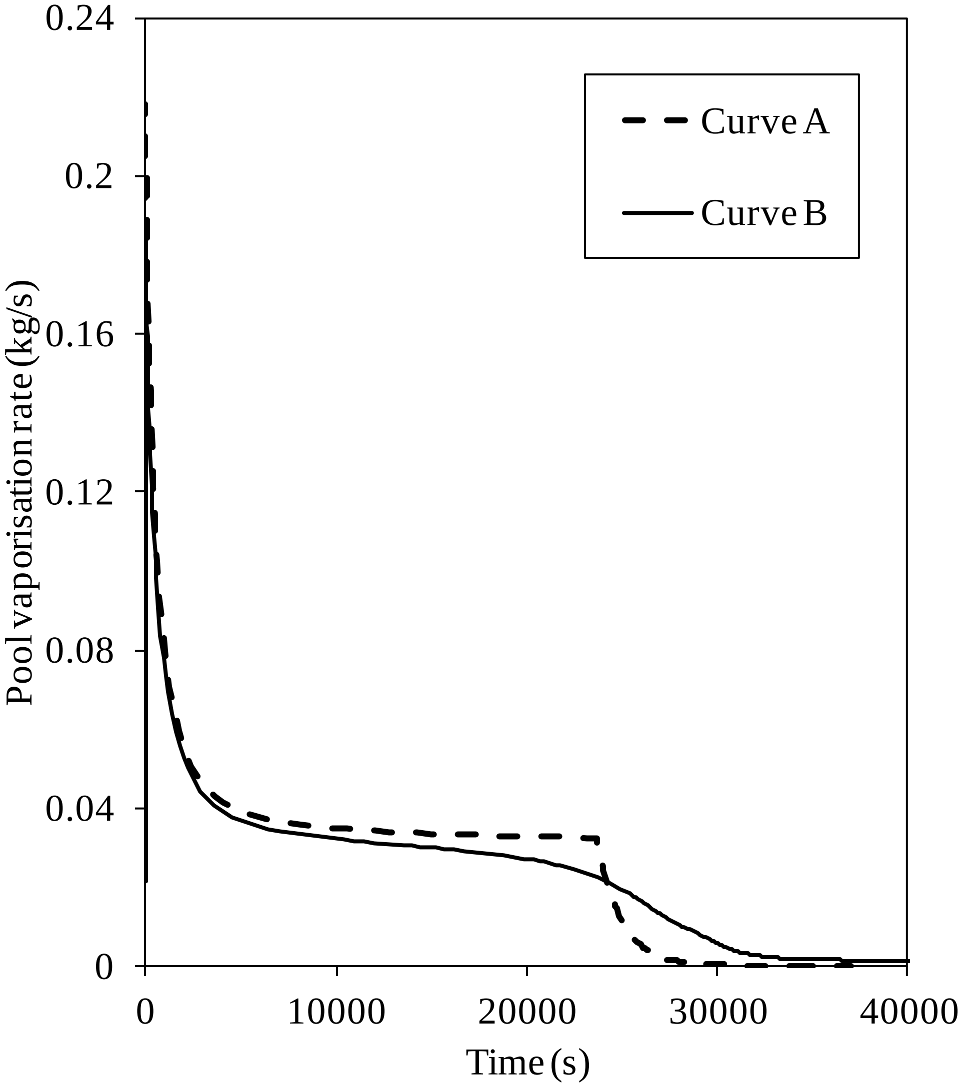

Figure 4.14. Variation of the pool vaporisation rate with time for instantaneous releases on concrete at a temperature of 288 K and a wind speed of 5 m/s at 10 m height

Spill mass: 1000 kg

Curve A: Test H, pure n-Pentane

Curve B: Test G, mixture n-Pentane/n-Hexane/m-Xylene

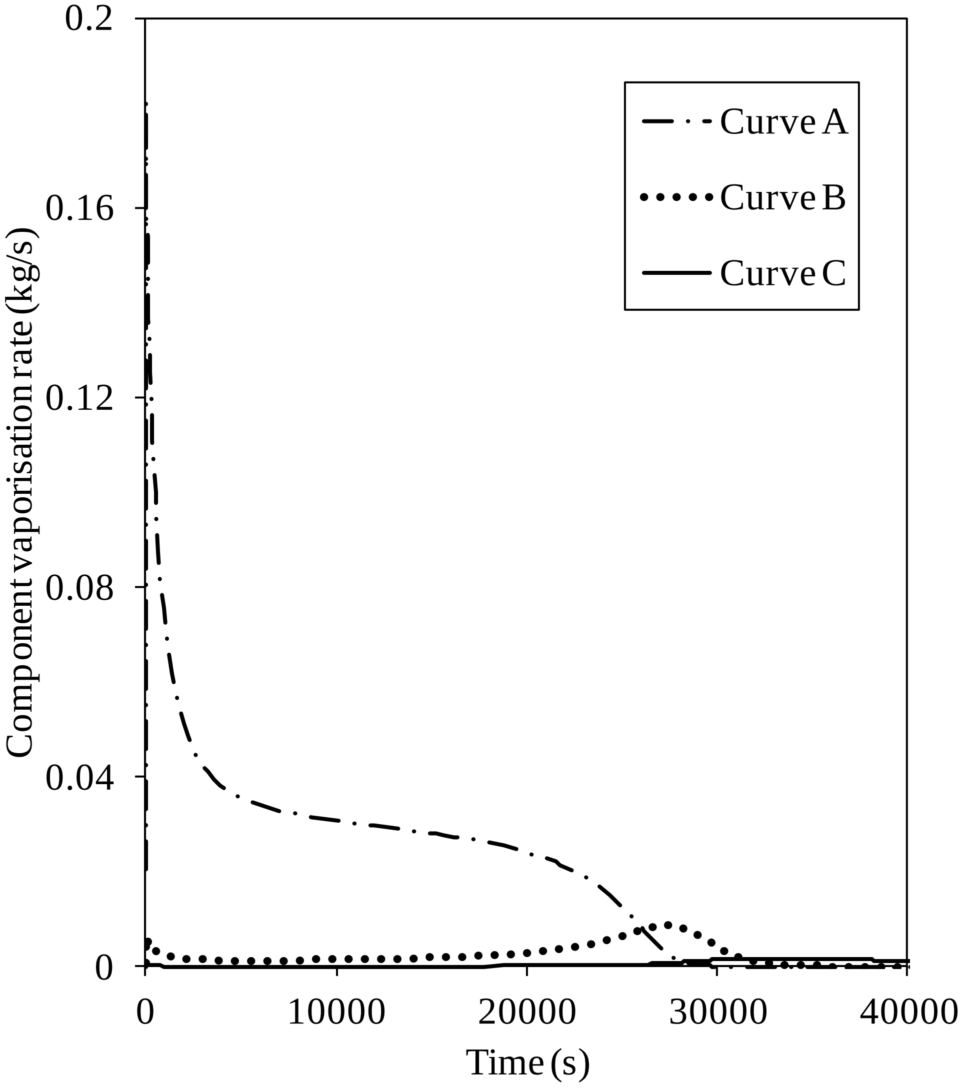

Figure 4.15. Variation of the component's pool vaporisation rate with time for instantaneous release on concrete of the mixture at a temperature of 288 K and a wind speed of 5 m/s at 10 m height

Spill mass: 1000 kg

Curve A: Test G, n-Pentane in the mixture

Curve B: Test G, n-Hexane in the mixture

Curve C: Test G, m-Xylene in the mixture

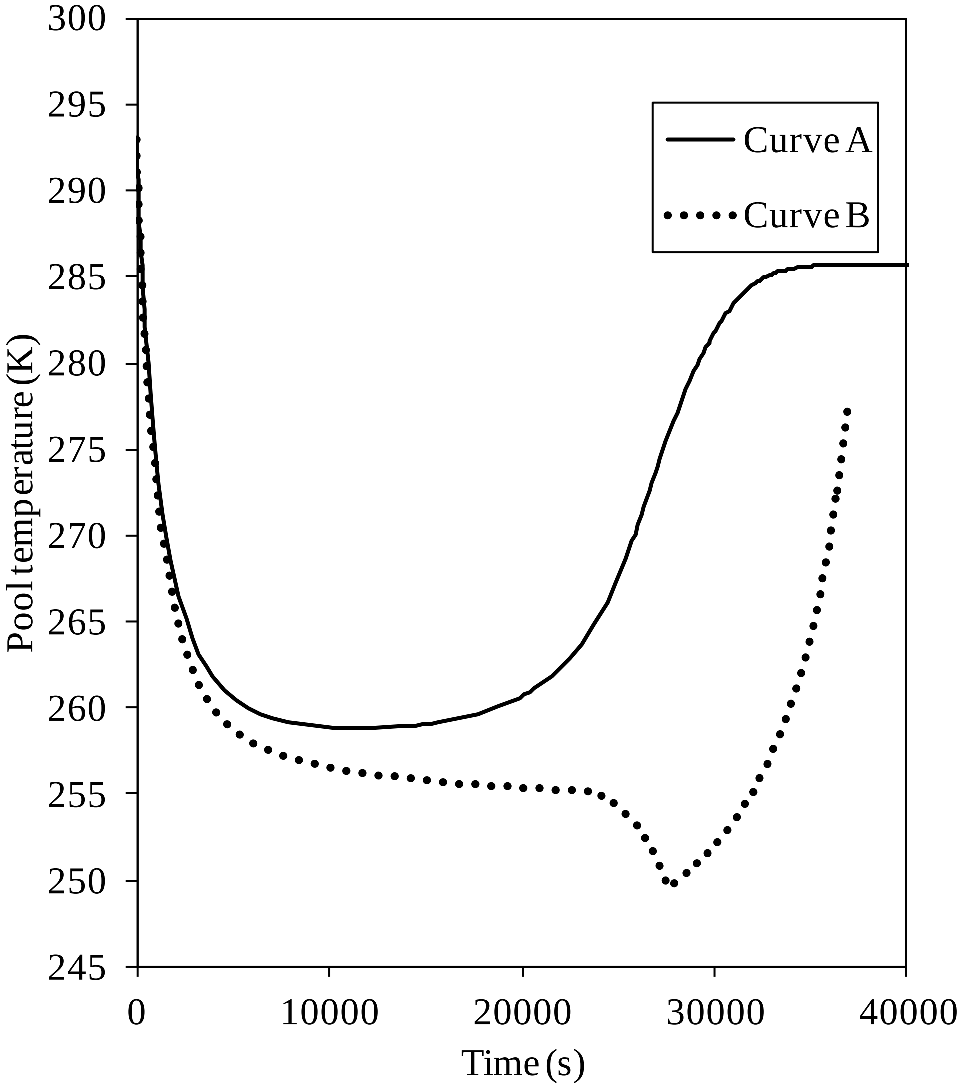

Figure 4.16. Variation of the pool temperature with time for instantaneous releases on concrete at a temperature of 288 K and a wind speed of 5 m/s at 10 m height

Spill mass: 1000 kg

Curve A: Test G, mixture n-Pentane/n-Hexane/m-Xylene

Curve B: Test H, pure n-Pentane

4.3.3 Water-soluble liquids

Table 4.4 presents the conditions and surface characteristics of the case studies selected to demonstrate the performance of the dissolution on water pool model presented in section 4.2.3.

The case studies are continuous releases on calm sea of pure Benzene and an 85 wt% Benzene and 15 wt% n-Hexane mixture. N-Hexane is insoluble in water and Benzene has a solubility of 1.8×10^{-3} kg/kg at 298 K (CAMEO Chemicals Database, 2011). A value of 500 W/m^2K for the heat transfer coefficient between the pool and the surface was selected based on experimental evidence for n-Butane spills on water (Reid and Smith, 1978).

Table 4.4. Prevailing conditions and surface characteristics for case studies I and J

		Case study	
		I	**J**
Release	Type of spill	Continuous	Continuous
	Spill rate (kg/s)	0.01	0.01
	Spill duration (s)	10,800	10,800
	Spill temperature (K)	298	298
	Spill composition (wt %)		
	Benzene	85	100
	n- Hexane	15	0
Ambient	Ambient temperature (K)	288	288
	Ambient pressure (Pa)	101,325	101,325
	Atmospheric stability (Pasquill class)	D-Neutral	D-Neutral
	Wind speed at 10 m height (m/s)	5	5
	Surface roughness length (m)	10^{-4}	10^{-4}
	Solar incidence (W/m^2K)	0	0
Surface	Surface	Calm sea	Calm sea
	Surface temperature (K)	283	283

The following figures present the simulation results for case studies I and J. The mass spill rate is 0.01 kg/s. The surface and ambient temperatures are 283 and 288 K respectively.

Figure 4.17 shows the variation of the pool vaporisation with time for the pure Benzene (curve B) release and an 85 wt% Benzene and 15 wt% n-Hexane mixture (curve A).

Figure 4.18 shows the results of the pool dissolution rate for the pure component (curve A) and the mixture (curve B).

From figure 4.17, it is observed that the vaporisation rate for the mixture (curve A) and the pure component (curve B) follow the same trend. Initially, the vaporisation rate of the mixture and the pure component increase with time up to a maximum value achieved at the steady state, approx. 4000 s after release. The maximum vaporisation rate observed for the mixture (curve A) is just 4% higher than for the pure component (curve B). This is in line with the observations made for evaporating liquids discussed in section 4.3.2, where it was concluded that the pool composition has a limited effect on the vaporisation rate.

On the other hand, the variation of the pool dissolution rate with time for the pure component (curve A) and the mixture (curve B) show differences of up to 20%, due to the differences in solubility between the mixture and the pure component cases. Such differences indicate significant errors in the prediction of toxicity levels in the water associated with approximating the mixture as a pure component. However, in this case study the results for pure Benzene are conservative as compared to the mixture.

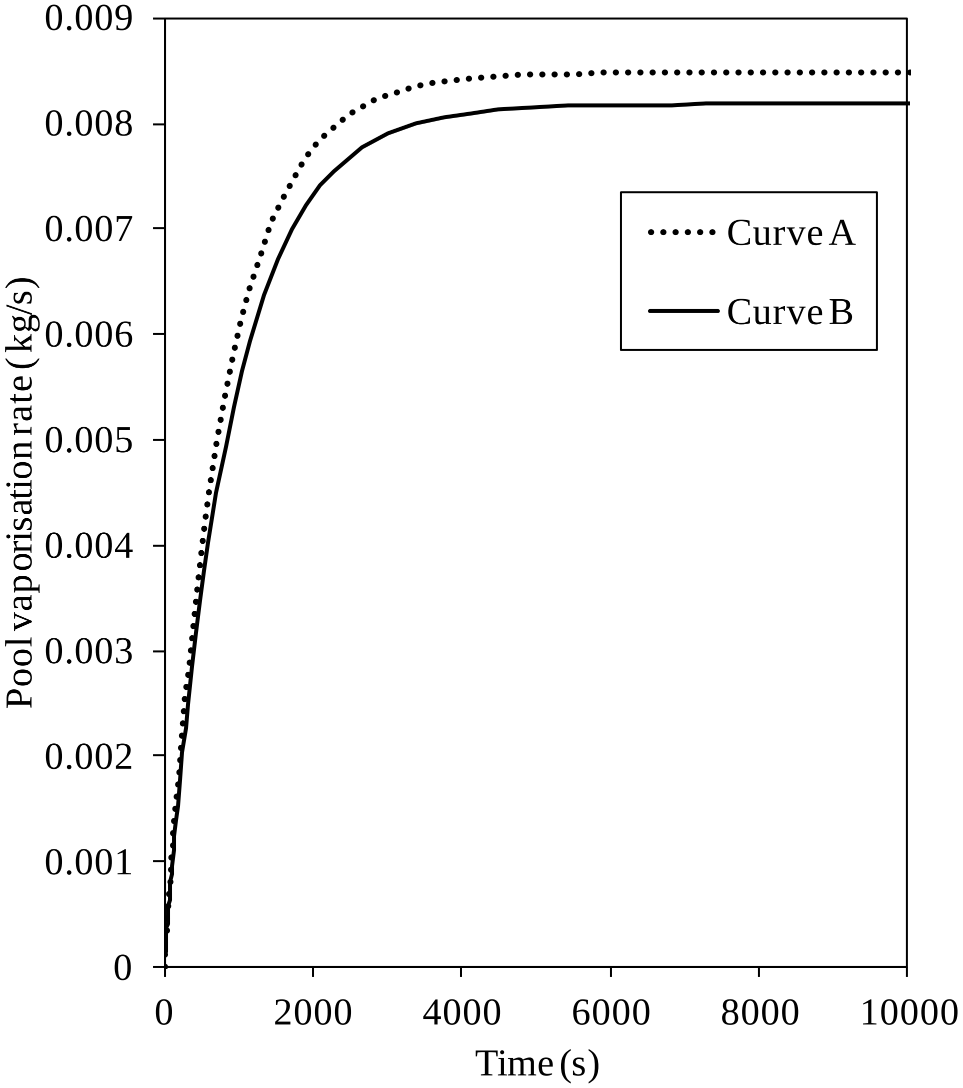

Figure 4.17. Variation of the pool vaporisation rate with time for continuous releases on calm sea at a temperature of 283 K and a wind speed of 5 m/s at 10 m height

Spill rate: 0.01 kg/s

Curve A: Test I, mixture Benzene/n-Hexane

Curve B: Test J, pure Benzene

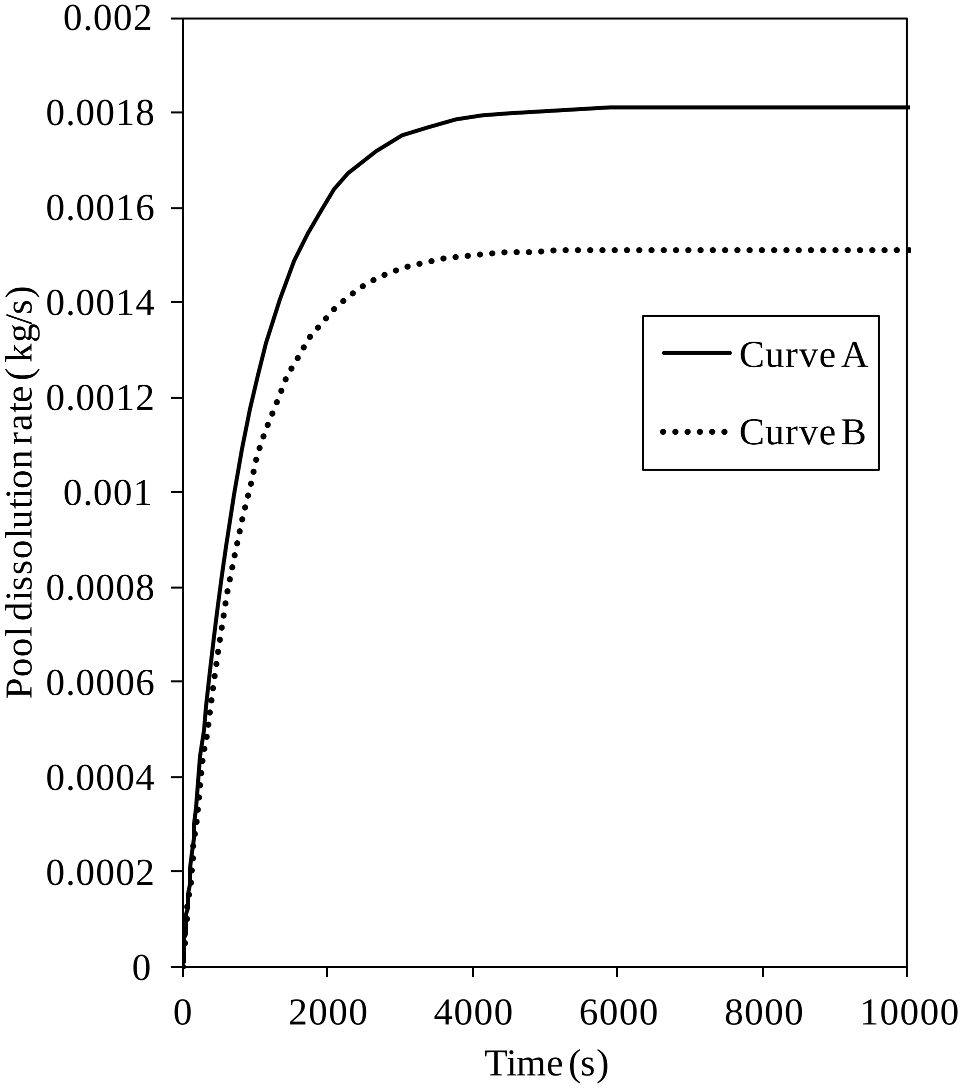

Figure 4.18. Variation of the pool dissolution rate with time for continuous releases on calm sea at a temperature of 283 K and a wind speed of 5 m/s at 10 m height
Spill rate: 0.01 kg/s
Curve A: Test J, pure Benzene
Curve B: Test I, Benzene/n-Hexane mixture

Figure 4.19 shows the variation of the pool radius with time for the Benzene/n-Hexane mixture (curve A) and for pure Benzene (curve B).

From figure 4.19 it is observed that the pool radius predicted for both the mixture and the pure component is very similar. The maximum pool radius obtained for the mixture (curve A) is only slightly higher by 2.5% than for pure Benzene (curve B).

Figure 4.20 shows the cumulative mass vaporised and dissolved for both pure Benzene and the Benzene/n-Hexane mixture scenarios. Curves A and B respectively show the cumulative mass vaporised for the Benzene/n-Hexane mixture and pure Benzene. The cumulative mass dissolved for the pure component and the mixture are respectively presented by curves D and E.

Comparing the cumulative mass vaporised for both scenarios, curves B and C, it is observed that when a water-soluble mixture is approximated by the soluble component in the mixture the mass vaporised from the pool is under predicted by 5%. Although the differences between both cases can point to this approximation being not conservative from the perspective of gas dispersion models a variation of only 5% is within the range of uncertainty of pool models predictions. From Curves D and E it is observed that differences between the cumulative mass dissolved for the mixture and the pure component can reach up to 20%. These differences will have major impact on the prediction of toxicity levels on water streams.

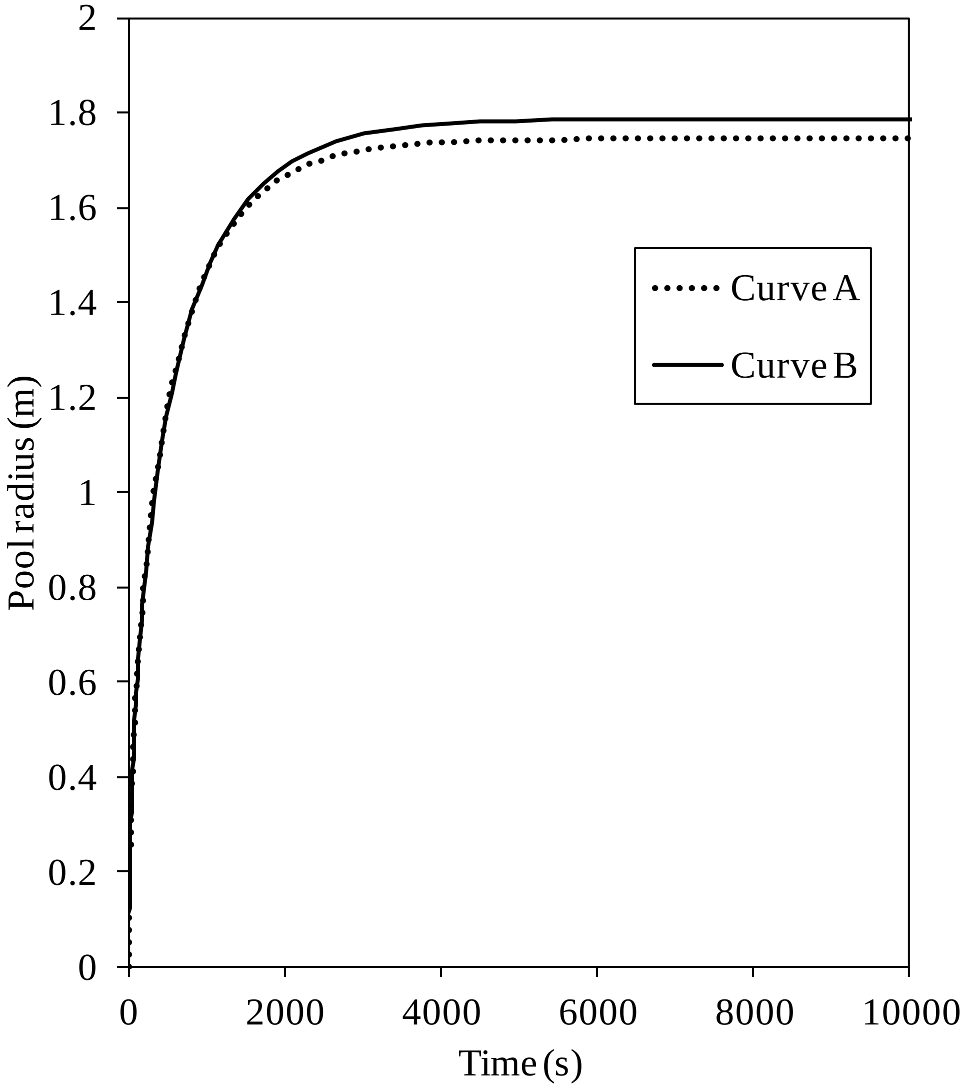

Figure 4.19. Variation of the pool radius with time for continuous releases on calm sea at a temperature of 283 K and a wind speed of 5 m/s at 10 m height.

Spill rate: 0.01 kg/s.

Curve A: Test I, Benzene/n-Hexane mixture

Curve B: Test J, pure Benzene

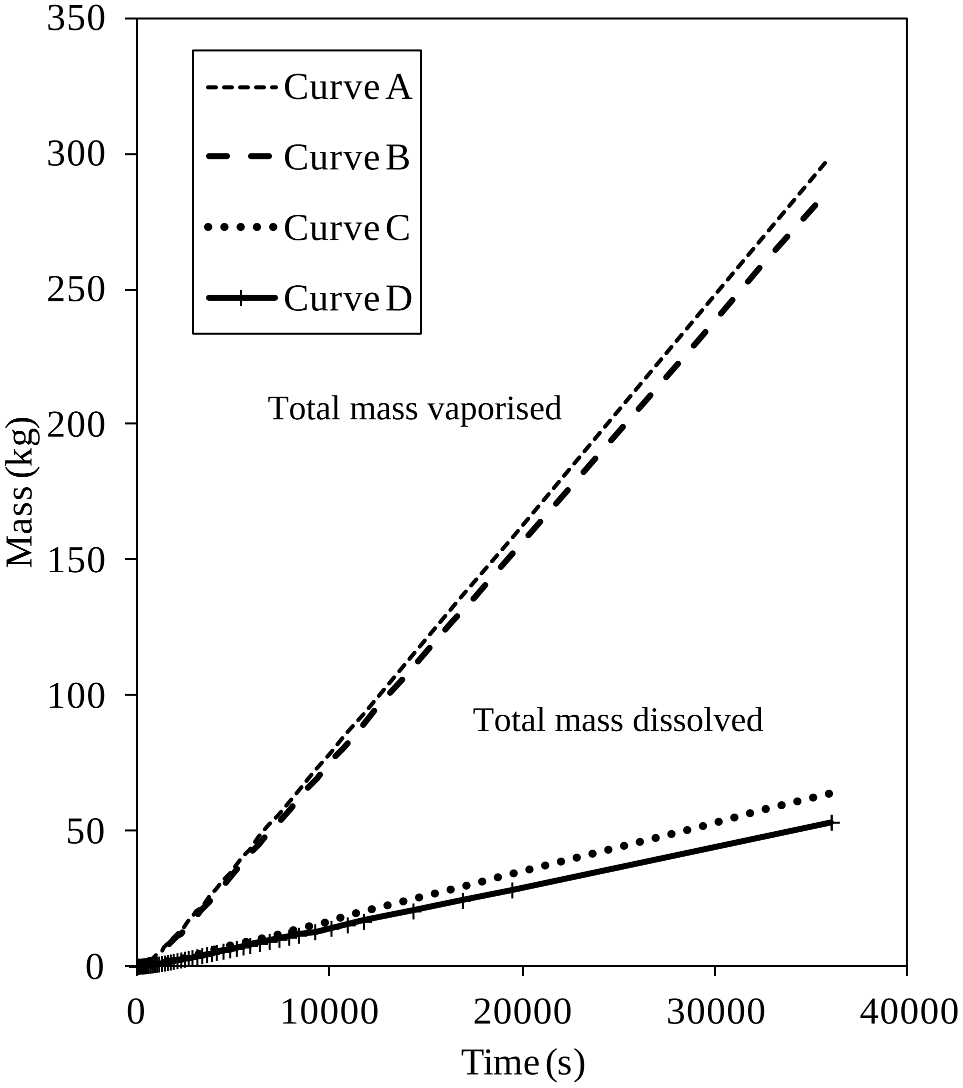

Figure 4.20. Cumulative mass vaporised and dissolved for continuous releases on calm sea at a temperature of 283 K and a wind speed of 5 m/s at 10 m above the surface.

Spill mass: 1000 kg.

Curve A: Test I, cumulative mass vaporised of the mixture Benzene /n-Hexane

Curve B: Test J, cumulative mass vaporised of pure Benzene

Curve C: Test I, cumulative mass dissolved of pure Benzene

Curve D: Test J, cumulative mass dissolved of the mixture Benzene /n-Hexane

4.4 Concluding remarks

This chapter presented the extension of the single-component pool spreading, vaporisation and dissolution model presented in chapter 3 to multi-component mixtures. The latter comprised cryogenic, evaporating and water-soluble liquids spilling on various surfaces including concrete, rivers or the sea.

Various hypothetical spill scenarios were then modelled in order to highlight the problems associated with approximating the evaporation of multi-component mixtures with single components. The important observations made based on the these investigations may be summarised as follows,

- ❑ For cryogenic liquids,
    - o The total amount of material vaporised from an 85 wt% Methane and 15 wt% Ethane mixture is significantly over-predicted when it is approximated with pure Methane. From the perspective of gas dispersion, this is conservative, but is not recommendable on the basis of mitigation overdesign
    - o The maximum pool radius for an 85 wt% Methane and 15 wt% Ethane mixture spreading on land or water is under-predicted assuming a pure Methane scenario. This is relevant for subsequent determinations of safe separation distances and hazard exclusion zones

- ❑ For evaporating liquids,
    - o The pool composition has an impact on the prediction of the pool radius. Modelling an 85 wt% n-Pentane, 10 wt% n-Hexane and 5 wt% m-Xylene mixture as pure n-Pentane will result in under-prediction of the maximum area covered by the pool in a continuous release and the time it takes for the pool to evaporate completely in an instantaneous case. This has implications for pool fires, safe separation distances and hazard exclusion zones calculations
    - o The pool composition has an impact on the predicted pool temperature. For both continuous and instantaneous releases modelling an 85 wt% n-Pentane, 10

    wt% n-Hexane and 5 wt% m-Xylene mixture as pure n-Pentane will result in under prediction of the pool temperature

    - The composition does not have a significant impact on the pool vaporisation rate for the range of mixtures and conditions tested

- ❑ For water-soluble liquids,
    - The pool composition has a small effect on the cumulative mass vaporised from the pool. When an 85 wt% Benzene and 15 wt% n-Hexane mixture is approximated by pure Benzene, the total mass vaporised from the pool is under predicted by 5%. However, this difference in within the expected accuracy of pool models, having a small impact on further gas dispersion modelling
    - The pool composition has a significant effect on the cumulative mass dissolved from the pool. When an 85 wt% Benzene and 15 wt% n-Hexane mixture is approximated by pure Benzene the total mass dissolved is over predicted by 20%. This approximation, though conservative, carries significant errors on the prediction of toxicity levels on water streams
    - The mixture composition does not have a significant impact on the pool vaporisation rate and radius within the range of mixtures and conditions tested

CHAPTER 5. IMPLEMENTATION AND VERIFICATION OF A NUMERICAL SOLUTION FOR THE MULTI-COMPONENT POOL MODEL

5.1 Introduction

In the preceding chapter, the formulation of a multi-component model based on the premises of Phast (Witlox, 2008) single-component pool model was presented. The application of the model to multi-component mixtures highlighted the drawbacks of approximating such systems by a single component evaporating pool.

Numerical stability and computational efficiency are qualities sought in accident modelling. Previous studies (Webber, 1989; Brambilla and Manca, 2009) on the numerical stability of single-component pool models have indicated that the involved phenomena develop on different time scales, making the problem stiff thus posing numerical complexity to the solution. Stiffness can be encountered when a numerical method is forced to use, in a certain interval, a step length which is excessively small in relation to the smoothness of the solution (Lambert, 1991); thus, increasing the computational demand in order to ensure a stable solution. In multi-component models stiffness is a greater concern than in single-component cases, as in the former the need to solve additional equations for each component (mass conservation, and cumulative mass evaporated and dissolved) increases the number of function evaluations per time step.

In order to overcome stiffness it is possible to change the model equations using quasi-steady state approximations for certain variables that change very slowly in time. This leads to sets of algebraic equations coupled to ordinary differential equations, which are then solved by a non-stiff method. The HGSYSTEM multi-component pool model LPOOL (Post, 1994) follows this approach. LPOOL is a later release of the LSM90 (Cavanaugh et al., 1994) model originally developed by Exxon and reviewed in chapter 2.

On the other hand, there are numerical methods available which are capable of handling stiff problems in an efficient manner with minimal loss of accuracy. The main advantage of such methods is that they do not require model approximations.
The present chapter describes the implementation of a numerical algorithm for stiff problems which uses a predictor-corrector method based on Backward Differentiation Formula (BDF) (Fatunla, 1988). This is followed by the results of a comparison between the numerical solver implemented in the present work and LPOOL (Post, 1994) for a series of hypothetical case studies.

Additionally, this chapter compares the results of the present work and LPOOL (Post, 1994) in terms of the range of application of both models, with particular emphasis on water-soluble mixtures.

Further validation of the multi-component pool model presented in this work against published experimental data is the focus of chapter 6.

5.2 Numerical solution of multi-component pool model by LSODE solver

This section discusses the numerical solution of the multi-component pool model using the public-domain solver Livermore Solver for Ordinary Differential Equations (LSODE) (Hindmarsh and Radhakrishnan, 1993).

The governing equations for the multi-component pool model presented in chapter 4 can be written in matrix form as a system of ordinary differential equations (ODEs):

$$\frac{\partial \bar{Y}}{\partial t} = G(\bar{Y}, t) \tag{5.43}$$

where,

$$\bar{Y} = \begin{pmatrix} r \\ T_L \\ M_{pool}{}^{i} \\ M_{vap}{}^{i} \\ M_{sol}{}^{i} \end{pmatrix} \tag{5.44}$$

$$G = \begin{pmatrix} \boldsymbol{f}\left(r, M_{pool}{}^{i}, T_L\right) & \\ \boldsymbol{g}\left(M_{pool}{}^{i}, T_L\right) + \pi r^2 \boldsymbol{h}\left(M_{pool}{}^{i}, T_L\right) & \\ \dot{m}_{spill}{}^{i} - \pi r^2 \left(\dot{m}''_{vap}{}^{i} + \dot{m}''_{sol}{}^{i}\right) & \forall\, i = 1, \ldots, n \\ \pi r^2 \dot{m}''_{vap}{}^{i} & \forall\, i = 1, \ldots, n \\ \pi r^2 \dot{m}''_{sol}{}^{i} & \forall\, i = 1, \ldots, n \end{pmatrix} \tag{5.45}$$

and,

$$\boldsymbol{f}\left(r, M_{pool}{}^{i}, T_L\right) = \begin{cases} Pools\ on\ land = \left[2g \left(\dfrac{\sum\limits_{i=1}^{n} M_{pool}{}^{i}}{\pi r^2\, \rho_{pool}\left(T_L\right)} - h_{\min} \right) \right]^{0.5} \\ Pools\ on\ water = 0 \end{cases} \tag{5.46}$$

$$\boldsymbol{g}\left(M_{pool}{}^{i}, T_L\right) = \frac{\sum\limits_{i=1}^{n} \dot{m}_{spill}{}^{i}\, c_p{}^{i}(T_L) \cdot \left(T_{spill} - T_L\right)}{\sum\limits_{i=1}^{n} M_{pool}{}^{i}\, c_p{}^{i}(T_L)} \tag{5.47}$$

$$\boldsymbol{h}\left(M_{pool}{}^{i}, T_L\right) = \frac{Q''_{in} - \sum\limits_{i=1}^{n} \dot{m}''_{vap}{}^{i} \Delta H_{vap}{}^{i}(T_L) - \sum\limits_{i=1}^{n} \dot{m}''_{sol}{}^{i} \Delta H_{sol}{}^{i}(T_L)}{\sum\limits_{i=1}^{n} M_{pool}{}^{i}\, c_p{}^{i}(T_L)} \tag{5.48}$$

where,

$M_{vap}{}^{i}$ = mass of component i vaporised

$M_{sol}{}^{i}$ = mass of component i dissolved

ρ_{pool} = density of the mixture at the pool composition

and the remaining symbols are as defined in chapters 3 and 4. It should be noted that for pools on land the dissolution equations do not need to be solved, since the dissolution rate per unit area of component i, $\dot{m}''^{\,i}_{sol}$, is zero.

For stiff problems, such as the one posed by the multi-component pool model, the Lawrence Livermore National Laboratory (LLNL) developed a new numerical solver, known as the Livermore Solver for Ordinary Differential Equations (LSODE; Hindmarsh and Radhakrishnan, 1993). This solver is based on the Backward Differentiation Formula (BDF) and adopts a linear multi-step predictor-corrector method. This method is further expanded in Appendix C. The predictor-corrector process for advancing the solution consists of first generating a predicted value, denoted by $\overline{Y}_n^{\,0}$, where the subscript *n* indicates the current time interval. This value is corrected by iterating over the corrector step until convergence is achieved.

The accuracy of the solution is assessed, after the convergence of the corrector step is achieved. The convergence of the corrector step refers to the stability of the method and tests whether or not the difference:

$$h_n\overline{Y}_n^{\,m} - h_n\overline{Y}_n^{\,m-1} \tag{5.49}$$

increases in successive steps. Here,

h_n = step length

m = superscript indicating the number of iterations in the convergence loop

On the other hand, the accuracy of the solution depends on the order of the method and refers to the smallest error possible introduced in a single step. For both tests, LSODE uses an error weight function which includes user-defined relative and absolute tolerances (Hindmarsh and Radhakrishnan, 1993).

The present work follows the algorithm shown next to calculate the pool variables at each time step:

1. The array $\bar{Y}$ is initialised using the initial values of the pool model variables shown in table 5.1
2. An initial estimate of the step size is given to the solver
3. The LSODE solver evaluates the right hand side of the ODEs, equation (5.45), to determine the pool variables at the desired time
4. The LSODE solver performs the convergence and accuracy tests using the input values for the tolerance, and adjusts the step length until convergence is attained
5. The calculated array $\bar{Y}$ is printed out

Table 5. 5. Initialisation of pool model variables

		Release	
Variable name	Symbol	Instantaneous	Continuous
Cumulative mass vaporised	$M_{vap\ i}$	0	0
Cumulative mass dissolved	$M_{sol\ i}$	0	0
Pool mass	$M_{pool\ i}$	$M_{spill\ i}$	$\dot{m}_{spill\ i}\ \Delta t$
Pool radius	r	0	$\left(\dfrac{\dot{m}_{spill\ i}\ \Delta t}{h_{\min}\pi\rho_{pool}}\right)^{0.5}$
Pool temperature	T_L	T_{spill}	T_{spill}

where the symbols above are as defined in chapters 3 and 4.

5.3 Verification

The previous section discussed the implementation of a numerical algorithm aimed at handling stiff problems in the multi-component pool model formulated in chapter 4. Here the robustness of the algorithm and its implementation is verified by comparison against a public-domain simulation software for multi-component pool spreading and evaporation, i.e. the HGSYSTEM 3.0 model LPOOL (Post, 1994), that has found wide used in industry and academia.

The LPOOL model is based on the previous model, LSM90, developed by Cavanaugh et al. (1994) and reviewed in chapter 2 of this thesis. It is applicable to ideal mixtures and accounts for pool spreading and vaporisation, but ignores the dissolution of water-soluble chemicals, which has been considered in the present work. It employs a first-order numerical explicit method with step control (see also section 2.8).

The following section shows the comparison of the performance of the numerical multi-step algorithm implemented in the present work and the numerical explicit method implemented in LPOOL. The models are assessed in terms of their numerical stability and range of application. The comparisons have been carried out for cryogenic, evaporating mixtures and water-soluble mixtures of two and three components.

5.3.1 Cryogenic mixtures

Table 5.2 presents the prevailing ambient conditions and surface characteristics selected for the verification of the present work for a mixture of 50 wt% Methane and 50 wt% Ethane released at the bubble point of 117.1 K.

The two case studies presented in this section are continuous spills on concrete and instantaneous spills on calm sea.

For continuous spills on concrete, mass is assumed to be added to the evaporating pool at a constant rate of 5 kg/s for 120 s. The surface roughness upwind to the pool is taken as 10^{-2} m assuming there are no major obstacles that could affect the wind profile (see also sections 4.3.1 and 4.3.2). The thermal conductivity and diffusivity of the surface are taken as the default values for concrete in the HGSYSTEM simulation package (see table 5.1).

Instantaneous spills on calm sea are simulated in a bund of 12 m diameter. The total mass spilled is 600 kg. The surface roughness length upwind from the pool is taken as 10^{-4} m (CRS, 2005) (see also sections 4.3.1 and 4.3.2).

A wind speed of 1 m/s at 10 m height, neutral atmosphere and no solar radiation are chosen as the prevailing ambient conditions in both studies. The surface and surrounding air are at 288 K.

Table 5.6. Prevailing conditions and surface characteristics for model verification with cryogenic mixtures

Release	Type of spill	**Continuous**	**Instantaneous**
	Spill rate (kg/s)	5	-
	Spill duration (s)	120	-
	Mass spilled (kg)	-	600
	Spill temperature (K)	117.1	117.1
	Spill composition (wt%)		
	Methane	50	50
	Ethane	50	50
Ambient	Ambient temperature (K)	288	288
	Ambient pressure (Pa)	101,325	101,325
	Atmospheric stability (Pasquill class)	D-Neutral	D-Neutral
	Wind speed at 10 m height (m/s)	1	1
	Surface roughness length (m)	10^{-2}	10^{-4}
	Solar incidence (W/m^2 K)	0	0
Surface	Surface material	Concrete	Calm sea
	Bund diameter (m)	0	12
	Bund height (m)	0	1
	Surface temperature (K)	288	288
	Surface thermal conductivity (W/m K)	0.94	-
	Surface thermal diffusivity (10^7 m^2/s)	7.90	-

5.3.1.1 Continuous spill on concrete

Figures 5.1 and 5.2 present the results of the comparison based on the present work using the adaptive solver for stiff problems and the LPOOL simulation for a pool formed from a continuous spill of a 50 wt% Methane and 50 wt% Ethane mixture on concrete.

Figure 5. shows the variation of the pool vaporisation rate with time obtained from the LPOOL simulation (curve A) and this work (curve B). From the figure it is observed that the variation of the pool vaporisation rate with time predicted by LPOOL (curve A) and by the present work (curve B) follow the same general trend. However, the results of the LPOOL simulation (curve A) present clear oscillations in the region between 5 and 30 s, while the results of the present work (curve B) follow a smooth curve. This demonstrates

the robustness of the present numerical method compared to the LPOOL numerical solver.

Figure 5.221 presents the variation of the Methane and Ethane vaporisation rates with time. The results for Methane obtained from the LPOOL simulation and the present work are respectively given by in curves A and B. The results for Ethane from the LPOOL simulation and this work are respectively given by curves C and D. The values shown on the vertical axis are given in logarithmic scale.

The results presented in figure 5.2 show a similar trend to the vaporisation rate of the mixture shown in figure 5.1. The results of the LPOOL simulation (curves A and C) oscillate in the region between 5 and 30 s, while this work's results (curves B and D) increase monotonically. Outside the instability region, the vaporisation rate of Methane predicted by LPOOL (curve A) and the present work (curve B) are in very good agreement. However, the vaporisation rate of Ethane predicted by both simulations show a difference of 6.5% outside the instability region. This deviation, although within the range of accuracy of pool models, may be attributed to differences in the thermo-physical properties packages used by LPOOL and the present work .

Comparisons of the predicted pool radius and temperature also indicated that the simulation results based on this work are numerically more stable than LPOOL. Additionally, good agreement (with average differences of 3%) between the two sets of simulations were observed outside the instability region. These results can be found in Appendix B.

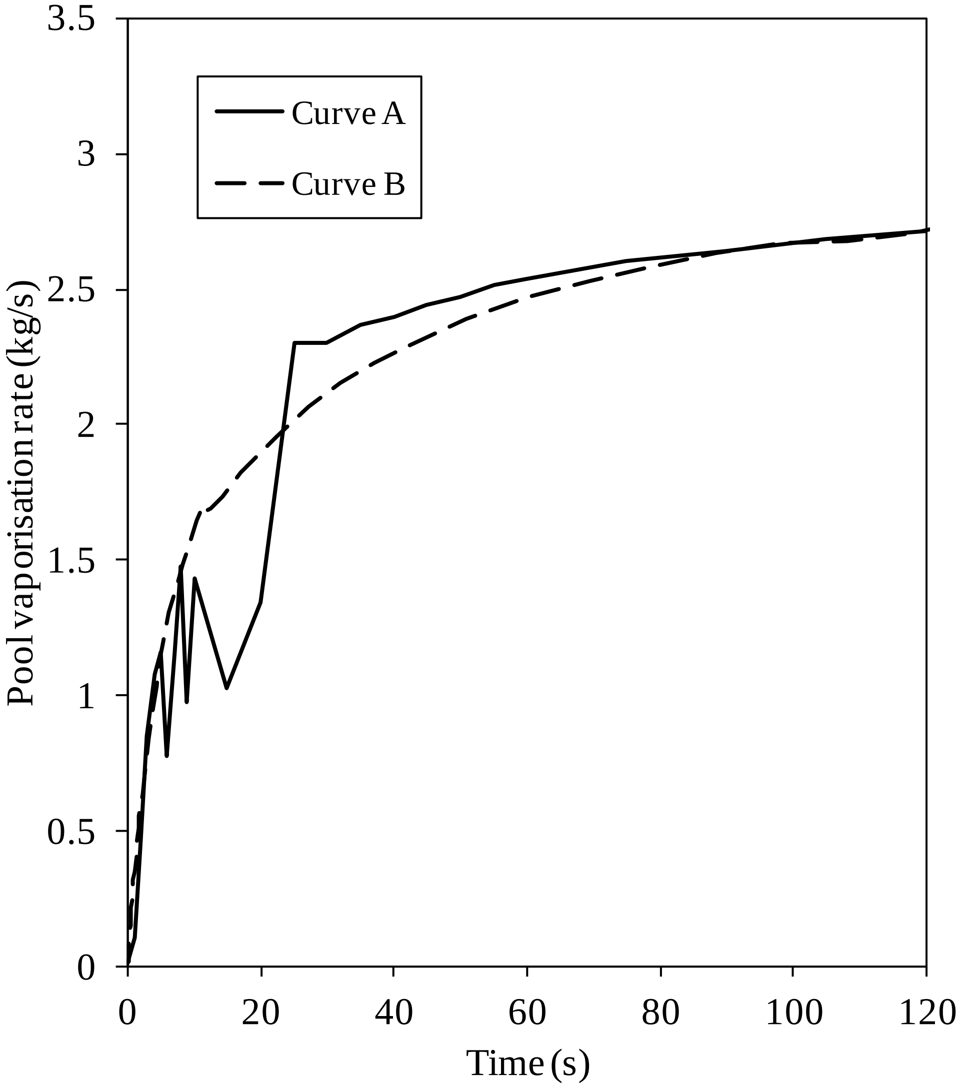

Figure 5.1. Variation of the pool vaporisation rate with time for a continuous Methane/Ethane spill on concrete at a temperature of 288 K and a wind speed of 1 m/s at 10 m above the surface

Spill rate: 5 kg/s

Curve A: LPOOL

Curve B: This work

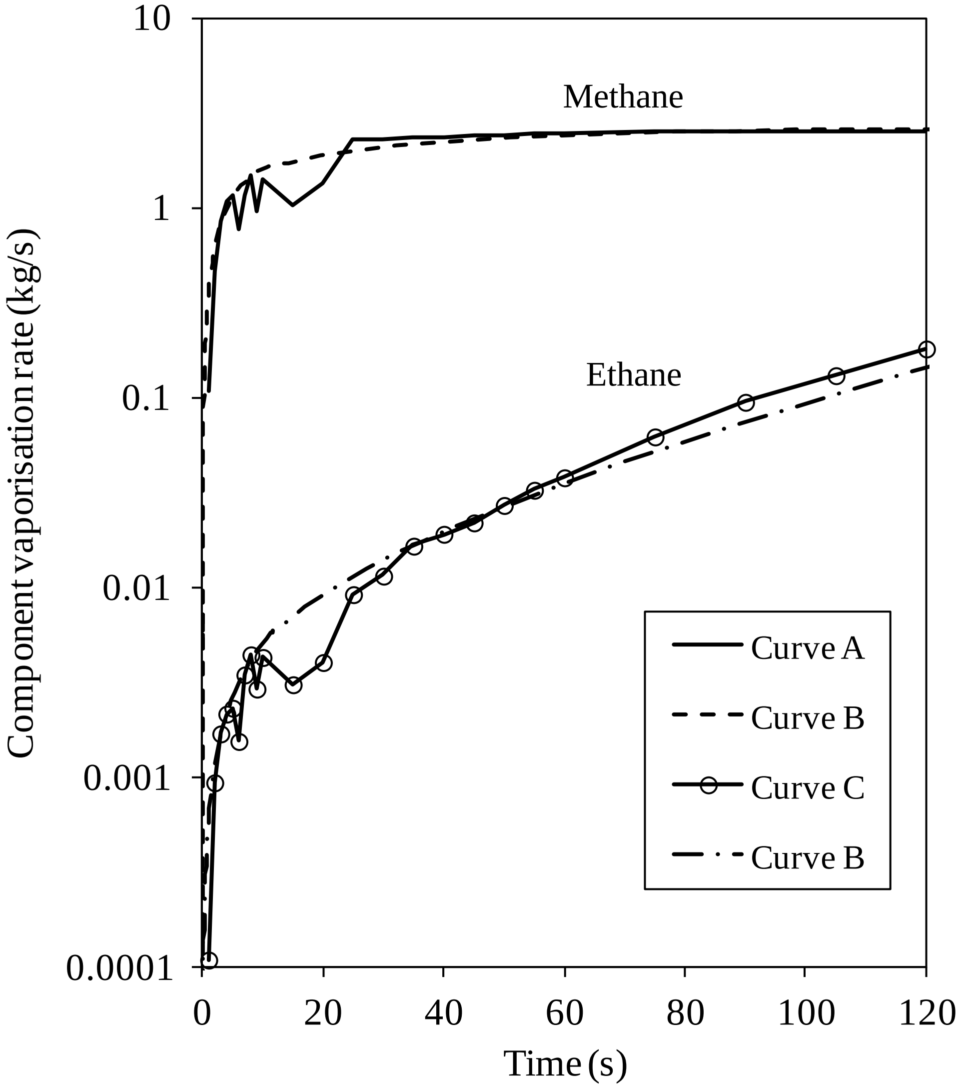

Figure 5.221. Variation of the Methane and Ethane vaporisation rates with time for a continuous spill on concrete at a temperature of 288 K and a wind speed of 1 m/s at 10 m above the surface

Spill rate: 5 kg/s

Curve A: LPOOL, Methane

Curve B: This work, Methane

Curve C: LPOOL, Ethane

Curve D: This work, Ethane

5.3.1.2 Instantaneous spill on calm sea

Figures 5.3 to 5.5 compare the results of the LPOOL (Post, 1994) simulation and the present work for various pools formed from an instantaneous spill of a 50 wt% Methane and 50 wt% Ethane mixture on calm sea.

Figure 5.322 shows the variation of the pool vaporisation rate with time for the LPOOL simulation (curve A) and this work (curve B).

Figure 5. shows the variation of vaporisation rates with time for each of the two components in the mixture. The results for Methane obtained from the LPOOL simulation and the present work are respectively shown in curves A and B. The results for Ethane from both the LPOOL simulation and this work are respectively presented in curves C and D.

From figure 5.3 it is observed that the predictions of LPOOL (curve A) and the present work (curve B) follow the same trend. The pool vaporisation rate initially increases up to a maximum value achieved at approximately 6 s after release, after which point it decreases indicating that the Methane inventory in the pool is rapidly depleting. A third stage shows a further increase in the pool vaporisation rate that corresponds to the onset of Ethane’s boiling. Between 30 and 50 s the Methane pool inventory is depleted and the pool is boiling with a constant area, given by the bund dimensions, and at constant temperature, equal to Ethane’s normal boiling point. Thus, the vaporisation rate does not change with time as observed in the figure. After approximately 60 s after release the vaporisation rate tails off indicating the ensuing disappearance of the pool. The differences between the results obtained from the LPOOL simulation (curve A) and the present work (curve B) are close to 8%. As in the example of continuous spills on concrete discussed in the above section, curve A in figure 5.3 presents oscillations up to 15 s after release, while curve B is smooth. This again demonstrates that the numerical solver implemented in the present work is numerically more robust than the LPOOL solver.

In figure 5.4 it is observed that the variation of the Methane and Ethane vaporisation rates with time show a similar trend to the variation of the pool vaporisation rate with time (figure 5.3). The results of the LPOOL simulation (curves A and C) oscillate approximately from 5 and 25 s after release, while this work's results (curves B and D) follow a smooth trend. In the first 5 s of the simulation, good agreement is observed between the vaporisation rate of Methane predicted by LPOOL (curve A) and the present work (curve B). The vaporisation rate of Ethane predicted by LPOOL (curve C) and by the present work (curve D) show differences of approx. 5% for times greater than 25 s. This deviation is in line with the previous observation made for continuous releases on land (see above section) and may be caused by the different properties packages used in LPOOL and the present work. Despite this, the differences between curves C and D are within the range of accuracy expected for pool models.

Figure 5.5 shows the variation of the pool temperature with time predicted by LPOOL (curve A) and this work (curve B). The pool temperature equals the bubble-point temperature of the boiling methane/ethane mixture. In the figure, the flat region between 0 s and 5 s corresponds to the interval in the Methane/Ethane phase diagram (see figure 4.2) where the slope of the bubble point curve is shallow. Following this, an increase in the pool temperature with time is observed up to the normal boiling point of Ethane (184.6 K). From 27 s after release, the pool contains pure Ethane and boils at constant temperature. In the figure it is observed that the LPOOL simulation and the results of the present work show differences of no more than 3%, which is considered to be an excellent agreement between the two models.

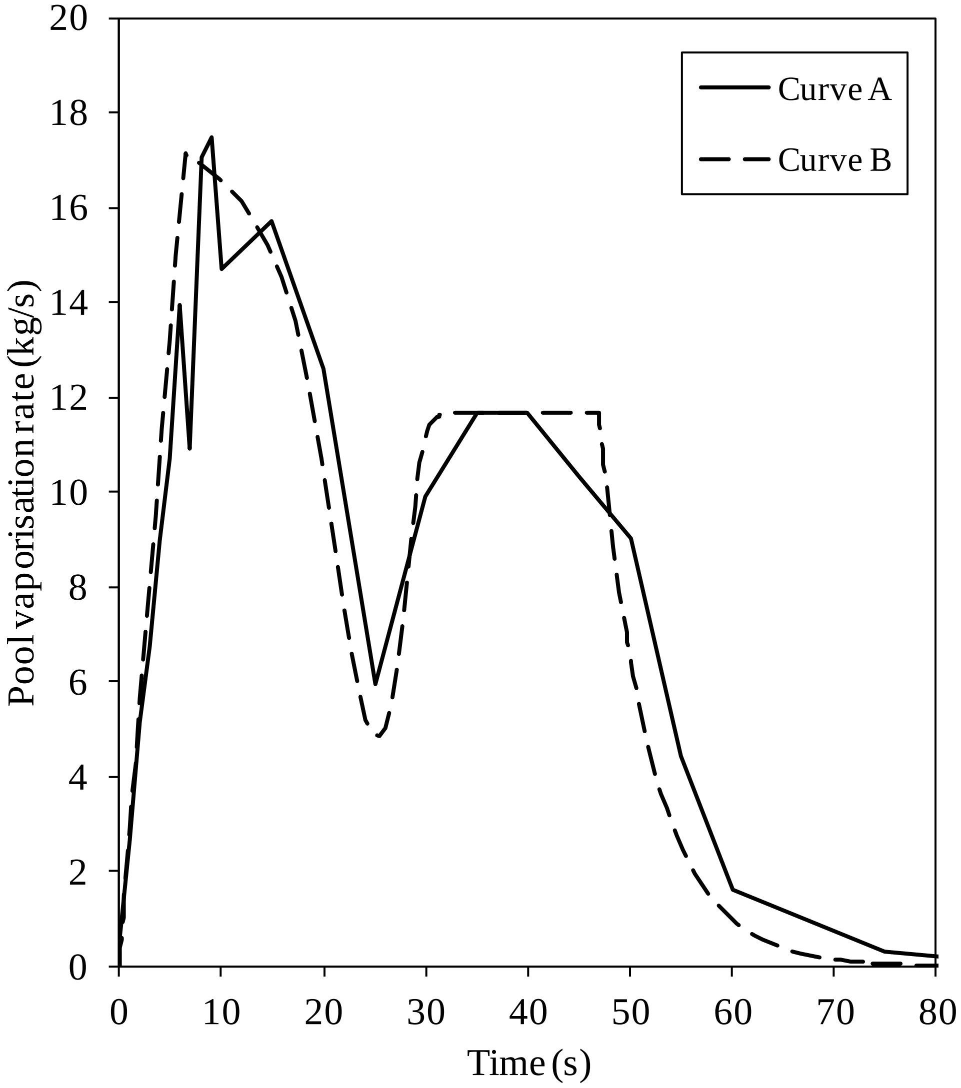

Figure 5.322. Variation of the pool vaporisation rate with time for an instantaneous Methane/Ethane spill on calm sea at a temperature of 288 K and a wind speed of 1 m/s at 10 m above the surface

Spill mass: 600 kg

Curve A: LPOOL

Curve B: This work

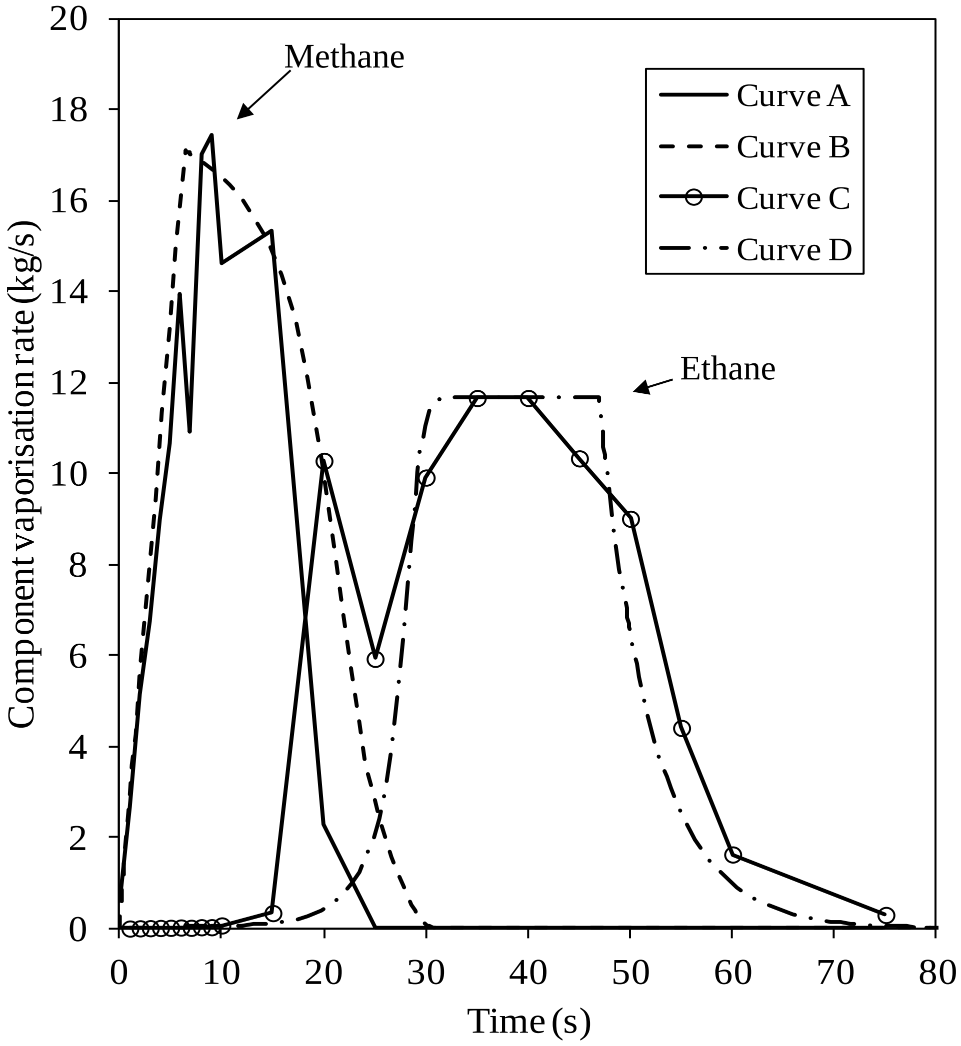

Figure 5.4. Variation of Methane and Ethane vaporisation rates with time for an instantaneous spill on calm sea at a temperature of 288 K and a wind speed of 1 m/s at 10 m above the surface

Spill mass: 600 kg

Curve A: LPOOL, Methane

Curve B: This work, Methane

Curve C: LPOOL, Ethane

Curve D: This work, Ethane

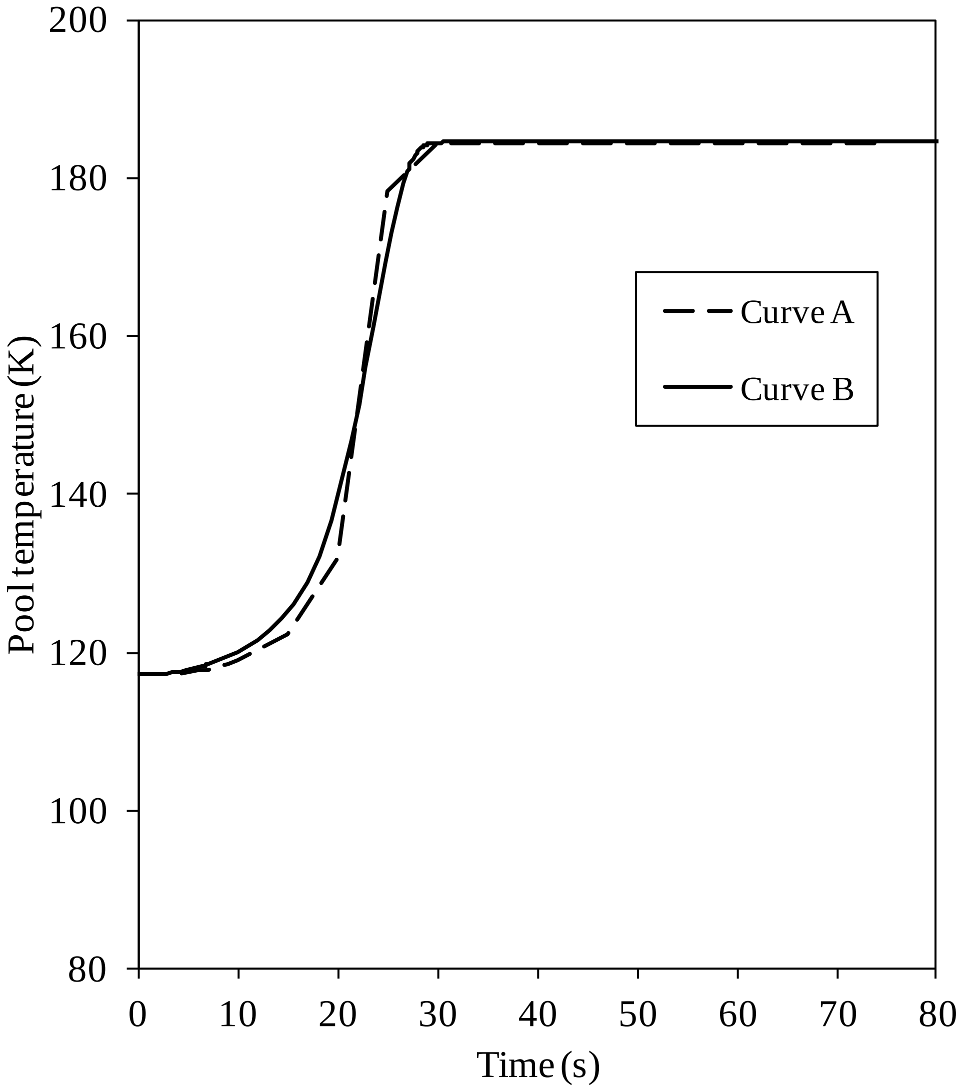

Figure 5.523. Variation of the pool temperature with time for an instantaneous Methane/Ethane spill on calm sea at a temperature of 288 K and a wind speed of 1 m/s at 10 m above the surface

Spill mass: 600 kg

Curve A: LPOOL

Curve B: This work

5.3.2 Evaporating mixtures

Table 5.3 shows the prevailing conditions and surface characteristics selected for the verification of this work against LPOOL for evaporating non-boiling mixtures. A mixture of 34 wt% n-Pentane, 33 wt% n-Hexane and 33 wt% n-Heptane continuously spilled on concrete is used in the simulations. A hypothetical instantaneous release on calm sea was also tested and its results can be found in Appendix B.

In this case study, mass is added to the pool at a constant rate of 5 kg/s for 3600 s. Similar to the studies on cryogenic liquids on land, the surface roughness upwind from the pool is taken as 10^{-2} m (see also section 5.3.1). The thermal conductivity and diffusivity of the surface are taken as the default values for concrete in LPOOL (Post, 1994). A wind speed of 5 m/s at 10 m height, neutral atmosphere and no solar radiation are the prevailing ambient conditions. The surface temperature is initially 293 K.

Table 5.7. Prevailing conditions and surface characteristics for model verification with evaporating mixtures

Release	Type of spill	**Continuous**
	Spill rate (kg/s)	5
	Spill duration (s)	3600
	Mass spilled (kg)	-
	Spill temperature (K)	298
	Spill composition (wt%)	
	n-Pentane	34
	n-Hexane	33
	n-Heptane	33
Ambient	Ambient temperature (K)	293
	Ambient pressure (Pa)	101,325
	Atmospheric stability (Pasquill class)	D-Neutral
	Wind speed at 10 m height (m/s)	5
	Surface roughness length (m)	10^{-2}
	Solar incidence ($W/m^2.K$)	0
Surface	Surface material	Concrete
	Bund diameter (m)	0
	Bund height (m)	0
	Surface temperature (K)	293
	Surface thermal conductivity (W/m K)	0.94
	Surface thermal diffusivity (10^7 m^2/s)	7.90

The following figures present the results of the comparison between the present work and LPOOL (Post, 1994) simulations.

Figure 5. shows the variation of the pool vaporisation rate with time obtained from the LPOOL simulation (curve A) and the present work (curve B).

Figure 5. compares the vaporisation rate of n-Pentane, n-Hexane and n-Heptane in the mixture. Curves A, C and E are the results of the LPOOL simulation for n-Pentane, n-Hexane and n-Heptane, respectively. Curves B, D and F show the results of the present work for the same components.

From figure 5.6 it is observed that the vaporisation rate predicted by the LPOOL simulation (curve A) and the present work (curve B) are in close agreement. The pool vaporisation rate obtained from LPOOL (curve A) and this work (curve B) increases with time as the pool spreads and covers a larger area. Although oscillations can be observed in the results obtained from LPOOL, the results obtained from the present work follow a smooth curve.

In figure 5.7, showing the variation of n-Pentane, n-Hexane and n-Heptane vaporisation rates with time, good agreement between both sets of simulations can be observed. In curve A, which shows the results of the LPOOL simulation for n-Pentane, oscillations are more noticeable than for the other components (curves C and E). On the other hand, the results of the present work increase monotonically with time for the three components.

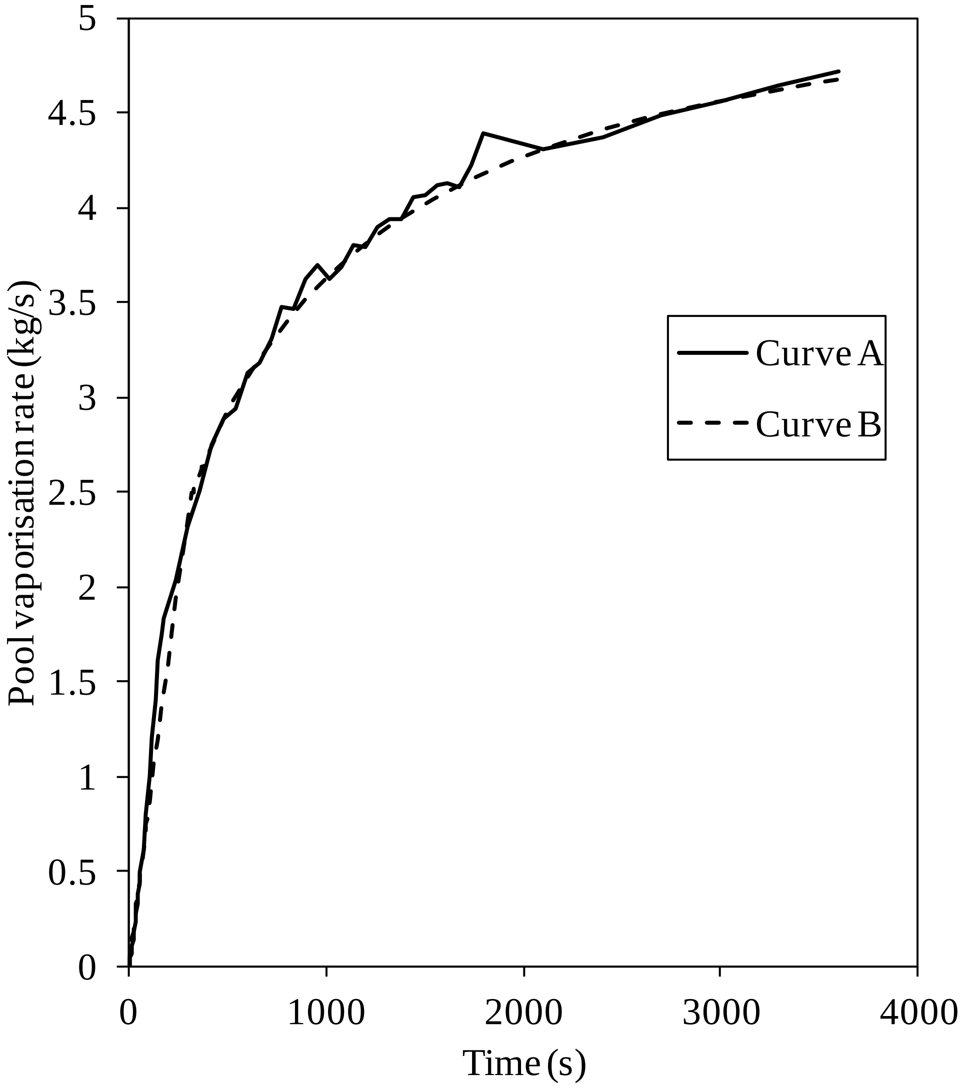

Figure 5.6. Variation of the pool vaporisation rate with time for a continuous n-Pentane/n-Hexane/n-Heptane spill on concrete at a temperature of 293 K and a wind speed of 1 m/s at 10 m above the surface

Spill rate: 5 kg/s

Curve A: LPOOL

Curve B: This work

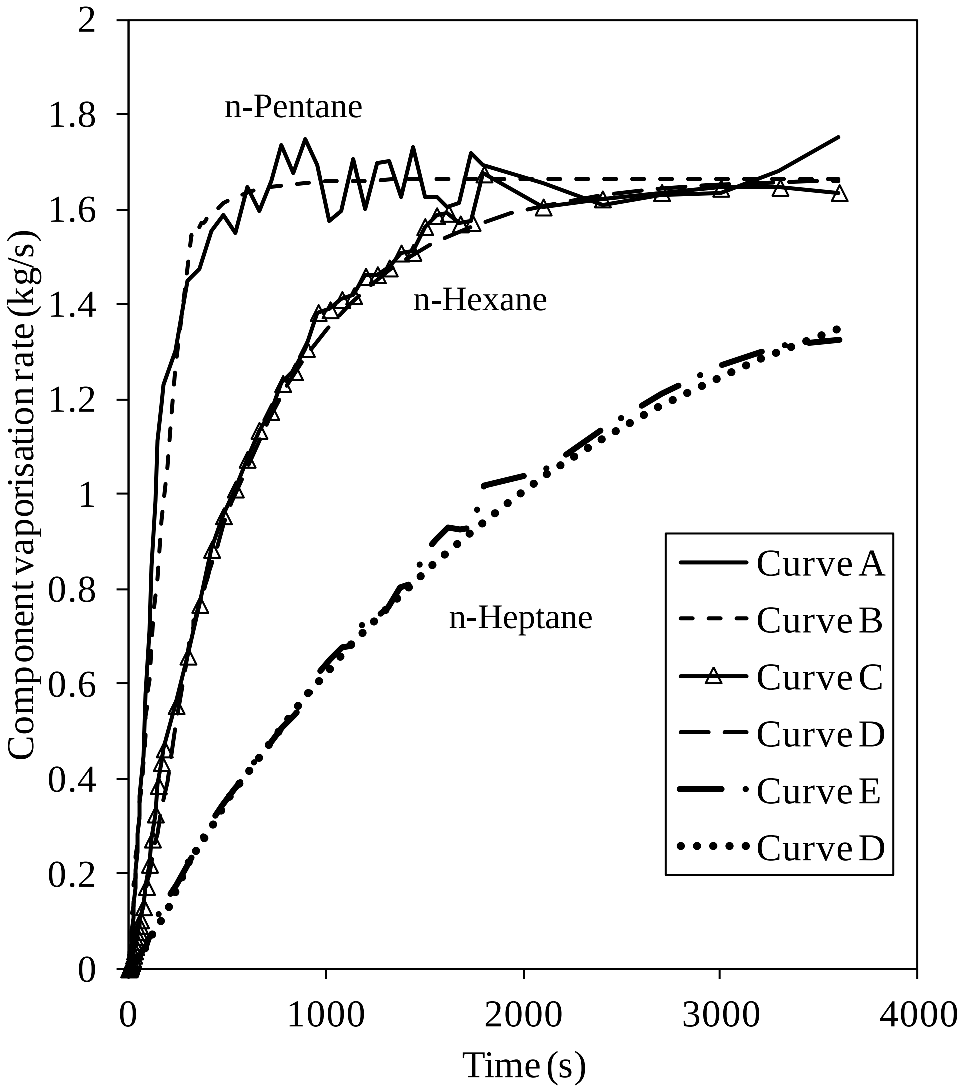

Figure 5.7. Variation of n-Pentane, n-Hexane and n-Heptane vaporisation rates with time for a continuous spill on concrete at a temperature of 293 K and a wind speed of 5 m/s at 10 m above the surface

Spill rate: 5 kg/s

Curve A: LPOOL, n-Pentane

Curve B: This work, n-Pentane

Curve C: LPOOL, n-Hexane

Curve D: This work, n-Hexane

Curve E: LPOOL, n-Heptane

Curve F: This work, n-Heptane

Figures 5.8 and 5.9 respectively show the progression of the pool temperature and radius with time based on LPOOL simulation (curve A) and this work (curve B).

From figure 5.8 good agreement between the results of the LPOOL simulation (curve A) and the present work (curve B) can be observed. Both curves show that the pool temperature initially decreases with time due to the cooling effect of the evaporation, the heat transfer from the warmer pool to the colder concrete surface, and the heat transfer from the warmer pool to the colder air (spill temperature of the spill is 5 K higher than ambient temperature; see table 5.3). After approximately 130 s both the LPOOL simulation (curve A) and the present work (curve B) predict a slow recovery in the pool temperature up to 292.5 K, close to the ambient temperature of 293 K. The results shown in curve A present some degree of oscillations while the present solution (curve B) shows marked improvements in the numerical stability. The maximum differences observed between curves A and B are less than 1%.

From figure 5.9 it may be observed that the prediction of the pool radius by the LPOOL simulation (curve A) and the present work (curve B) are in excellent agreement. The maximum differences observed between them are also less than 1%. Additionally, the results of the LPOOL simulation (curve B) present some degree of oscillations which are absent from the results of the present work (curve A).

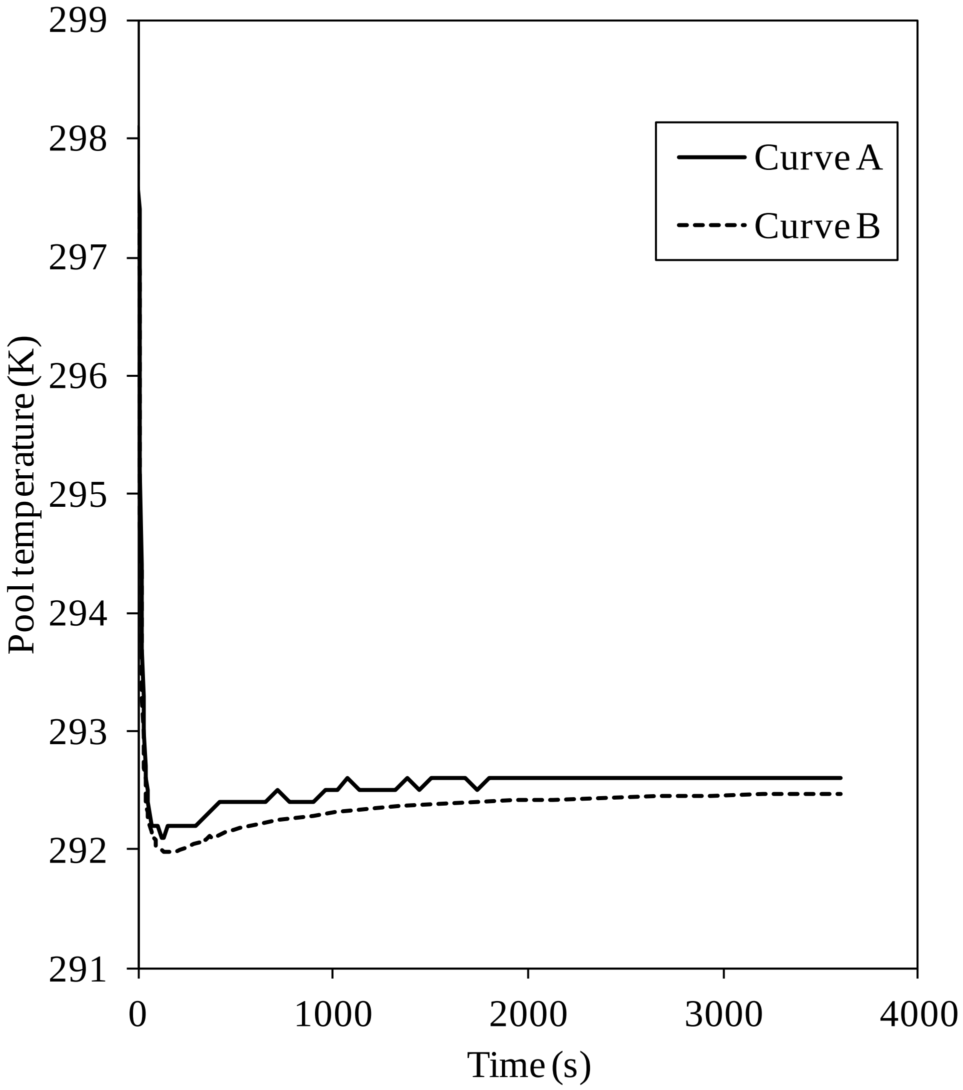

Figure 5.8. Variation of the pool temperature with time for a continuous n-Pentane/n-Hexane/n-Heptane spill on concrete at a temperature of 293 K and a wind speed of 5 m/s at 10 m above the surface

Spill rate: 5 kg/s

Curve A: LPOOL

Curve B: This work

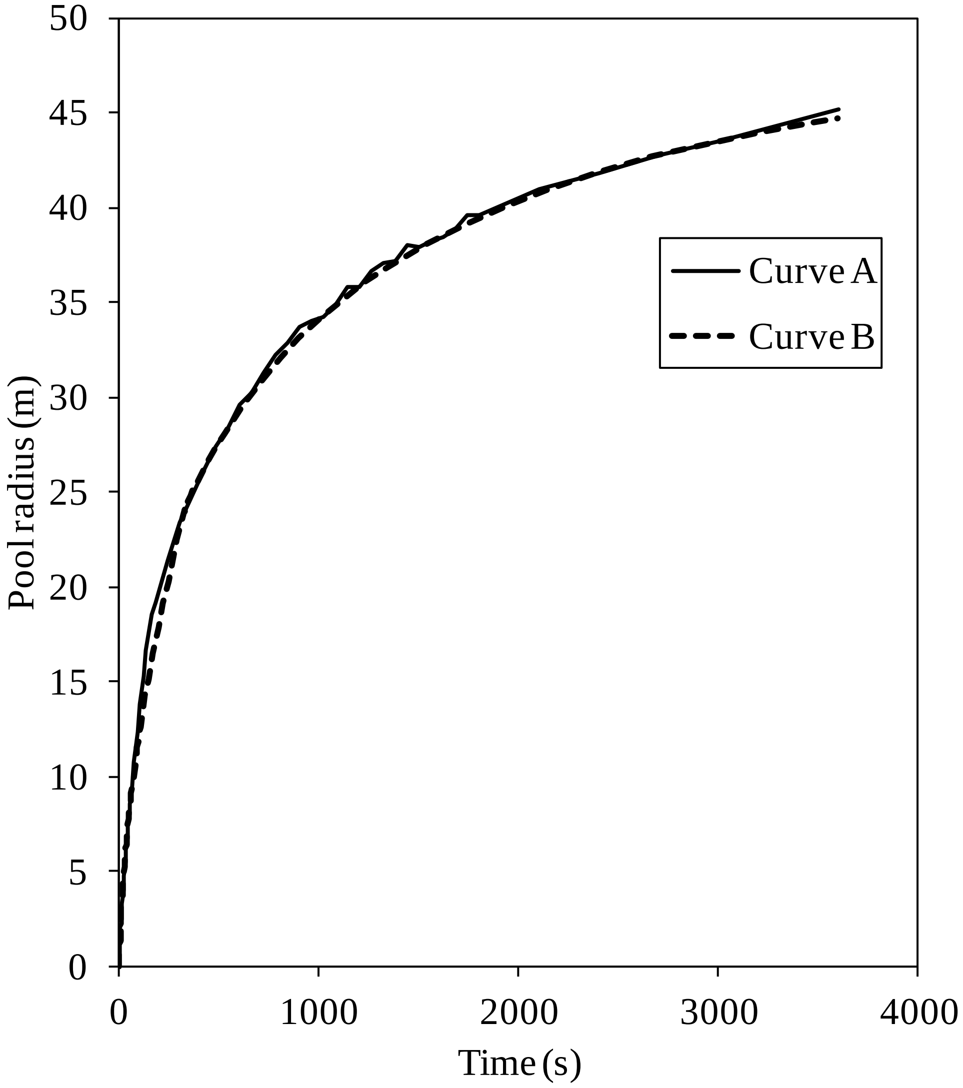

Figure 5.9. Variation of the pool radius with time for a continuous n-Pentane/n-Hexane/n-Heptane spill on concrete at a temperature of 293 K and a wind speed of 5 m/s at 10 m above the surface

Spill rate: 5 kg/s

Curve A: LPOOL

Curve B: This work

5.3.3 Water-soluble mixtures

Table 5.4 presents the conditions and surface characteristics of the case studies selected for the comparison of the performance of this work against the simulation software LPOOL (Post, 1994) for water-soluble mixtures. While this work accounts for the dissolution of water-soluble chemicals in river waters or in open sea, these effects have been ignored by previous multi-component pool models, such as LPOOL (Post, 1994). Here, a measure of the impact of dissolution on the pool characteristics is given.

This comparison between LPOOL and the present work seeks to highlight the impact of dissolution in the results of a multi-component pool. In order to assess this, an initial comparison between the results for pools evaporating on water without dissolution was carried out. The results of this can be found in Appendix B. Very good agreement between LPOOL and the present work was observed for evaporating pools on water without dissolution. Therefore, all conditions remaining the same, the differences observed between the results of LPOOL and the present work for the following set of cases are attributed to the dissolution model.

A pool inventory of 50 wt% Benzene and 50 wt% n-Hexane was chosen for this purpose. n-Hexane is insoluble on water and the mass solubility of Benzene at $25^{o}C$ is 1.8×10^{-3} kg Benzene/kg Water (CAMEO Chemicals Database, 2011). Also, a value of 500 $W/m^{2}K$ for the heat transfer coefficient between the pool and the surface was selected based on experimental observations of n-Butane spills (Reid and Smith, 1978).

Additionally, the effect of variation of the benzene solubility on the pool characteristics was studied by halving and doubling the base solubility value (1.8×10^{-3} kg/kg), using namely, 9×10^{-4} kg/kg and 3.6×10^{-3} kg/kg. The results of these simulations carried out with the present model are shown as part of the comparisons against the LPOOL model.

Table 5.8. Prevailing conditions and surface characteristic for study of water-soluble liquids

Release	Type of spill	Instantaneous
	Spill mass (kg)	1000
	Spill temperature (K)	293
	Spill composition (wt %)	
	n- Hexane	0.5
	Benzene	0.5
Ambient	Ambient temperature (K)	288
	Ambient pressure (Pa)	101,325
	Atmospheric stability (Pasquill class)	D-Neutral
	Wind speed at 10 m height (m/s)	5
	Surface roughness length (m)	10^{-4}
	Solar incidence (W/m^{2}K)	0
Surface	Surface	River or channel
	Bund diameter (m)	4
	Bund height (m)	1
	Surface temperature (K)	283
	Heat transfer coefficient (W/m^2 K)	500

The following figures show the results of the comparison between the present work and LPOOL simulations for an instantaneous release of a Benzene/n-Hexane mixture at the conditions given above.

Figure 5.10 shows the variation of the pool vaporisation rate with time obtained from the LPOOL simulation (curve A) and the present work (curves B to D) for benzene solubility values of 9 x 10^{-4} kg/kg, 1.8 x10^{-3} kg/kg and 3.6 x10^{-3} kg/kg.

Figure 5.11 shows the variation of the pool dissolution rate with time predicted by the present work (curves A to C) and LPOOL (curve D). Curves A to C are the results of the simulation using benzene solubility values of 3.6 x10^{-3} kg/kg, 1.8 x10^{-3} kg/kg and 9 x 10^{-4} kg/kg, respectively.

The progression of the pool radius with time as predicted by the present work (curves A to C) and LPOOL (curve D) is shown in figure 5.12. Curves A to C are the results of the simulation for benzene solubility values of 9 x 10^{-4} kg/kg, 1.8 x10^{-3} kg/kg and 3.6 x10^{-3} kg/kg, respectively.

From figure 5.10 it is observed that for curves A to D the pool vaporisation rate reaches a maximum value (between 0.045 and 0.055 kg/s) in the first few seconds of the simulation, followed by a sudden drop. Later, a gradual decrease in time is observed up to approximately 36,000 s where the vaporisation rate shows a more pronounced decline. The initial peak in the vaporisation rate corresponds to the instant where the pool has reached its maximum area given by the dimensions of the bund (see table 5.4). This is followed by a decrease caused by the drop in the pool temperature due to the cooling effect of the evaporation and heat losses to the ambient (note from table 5.4 that the spill temperature is some 10 degrees higher than the surface's). The gradual decrease in the vaporisation rate observed immediately after is related to the decrease of the pool composition of the more volatile component (n-Hexane). After approximately 10 hrs the pool has lost so much mass that the surface area and consequently the vaporisation rate decrease rapidly in time.

In figure 5.10 it is also observed that the LPOOL simulation (curve A) predicts a higher vaporisation rate than the present work (curves B to D) as the former assumes that the water-soluble chemical (Benzene) will only vaporise and not dissolve in water. The largest differences (approx. 10% to 12%) between the vaporisation rate predicted by the present work and LPOOL (curve A) correspond to the highest value of the benzene solubility (curve D). Comparing curves B to D for the different values of benzene solubility it can be observed that the pool vaporisation rate decreases with increasing solubility.

Additionally from the figure, it can be seen that although the numerical solution is stable for both models, the selection of the step size in the present work (curve B) produce a much smoother curve than the LPOOL simulation (curve A). This can be an indicative that the numerical method implemented in LPOOL may not converge to the real solution.

In figure 5.11 it may be observed that the dissolution rate predicted by the present work (curves A to C) increases with time up to the instant where the pool area starts reducing. As LPOOL does not account for dissolution, no such corresponding data can be presented. From the theory presented in chapter 4 (see section 4.2.3) it follows that the rate of dissolution is partly governed by the molar composition of the water-soluble chemical in the pool. And as was mentioned above, n-Hexane is the most volatile component in the mixture therefore, as time passes the fraction of Benzene in the pool increases and consequently the rate of dissolution increase with time. Comparing curves A to C in figure 5.11 it is observed that the pool dissolution rate increases with increasing values of benzene solubility.

In figure 5.12 it can be observed that the present work (curves A to C), which considers the effects of water dissolution, predicts that the pool vaporises completely at the same time as the LPOOL simulation (curve D). Thus it can be concluded that for the range of mixtures and conditions tested, the solubility of the mixture does not have a significant impact on the pool total evaporation time.

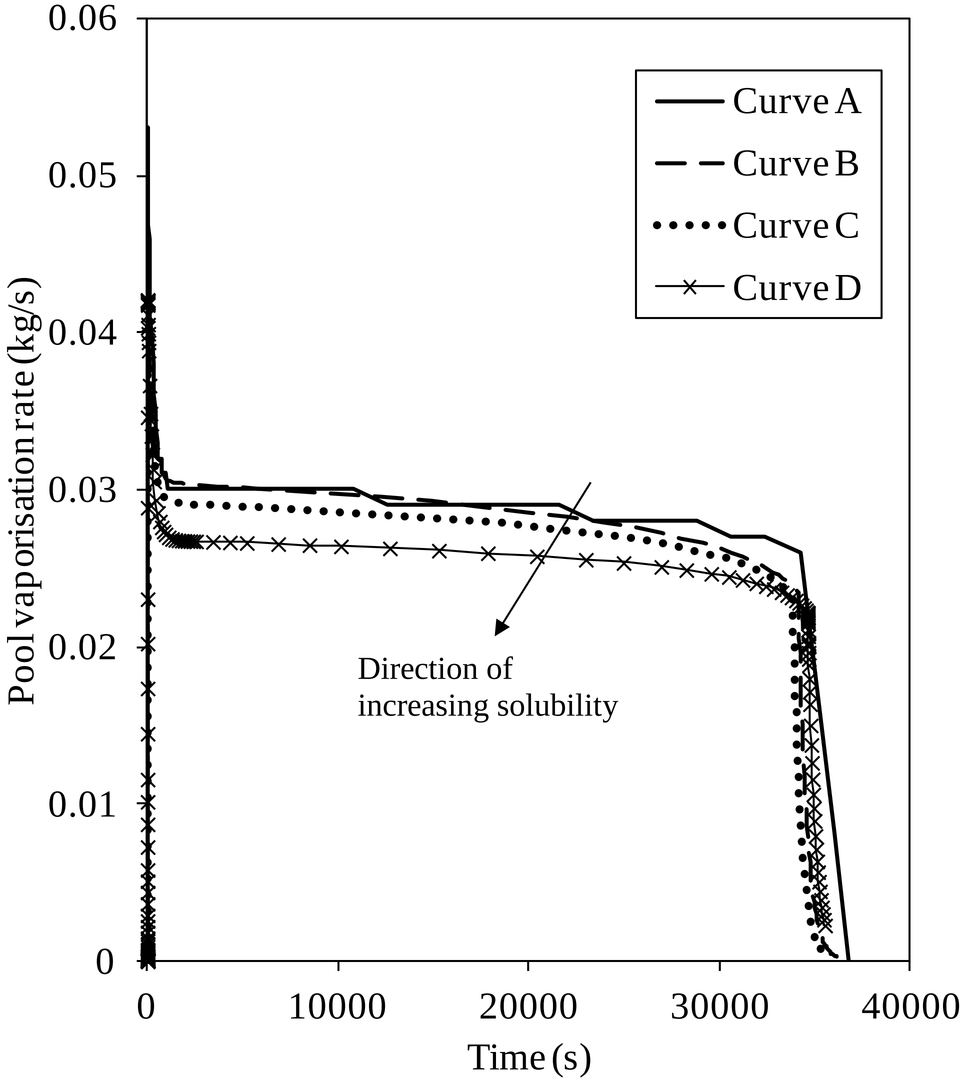

Figure 5.10. Variation of the pool vaporisation rate with time for an instantaneous Benzene/n-Hexane release on a river at a temperature of 283 K and a wind speed of 1 m/s at 10 m above the surface

Spill mass: 1000 kg

Curve A: LPOOL simulation

Curve B: This work: $9x10^{-4}$ kg/kg

Curve C: This work: 1.8 $x10^{-3}$ kg/kg (base case)

Curve D: This work: $3.6x10^{-3}$ kg/kg

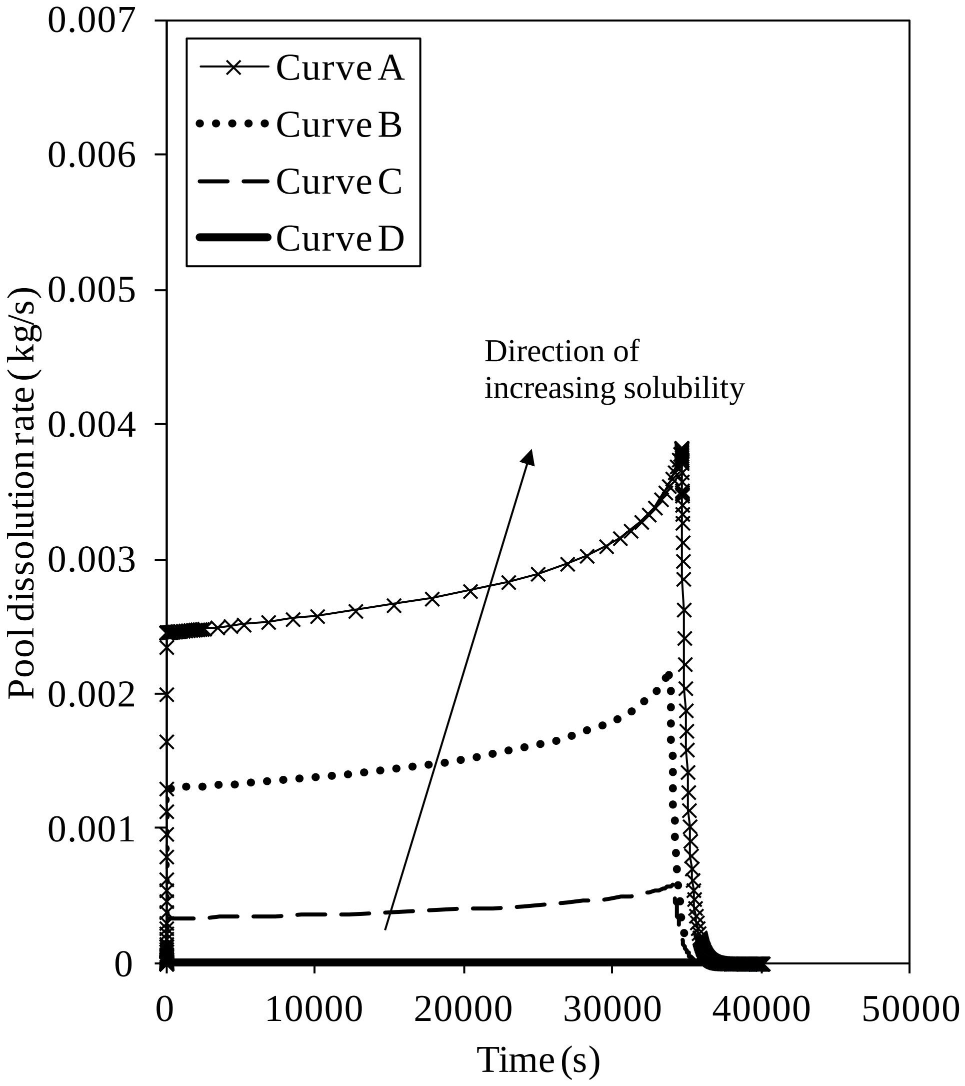

Figure 5.11. Variation of the pool dissolution rate with time for an instantaneous Benzene/n-Hexane release on a river at a temperature of 283 K and a wind speed of 1 m/s at 10 m above the surface

Spill mass: 1000 kg

Curve A: This work: 3.6×10^{-3} kg/kg

Curve B: This work: 1.8×10^{-3} kg/kg (base case)

Curve C: This work: 9×10^{-4} kg/kg

Curve D: LPOOL simulation

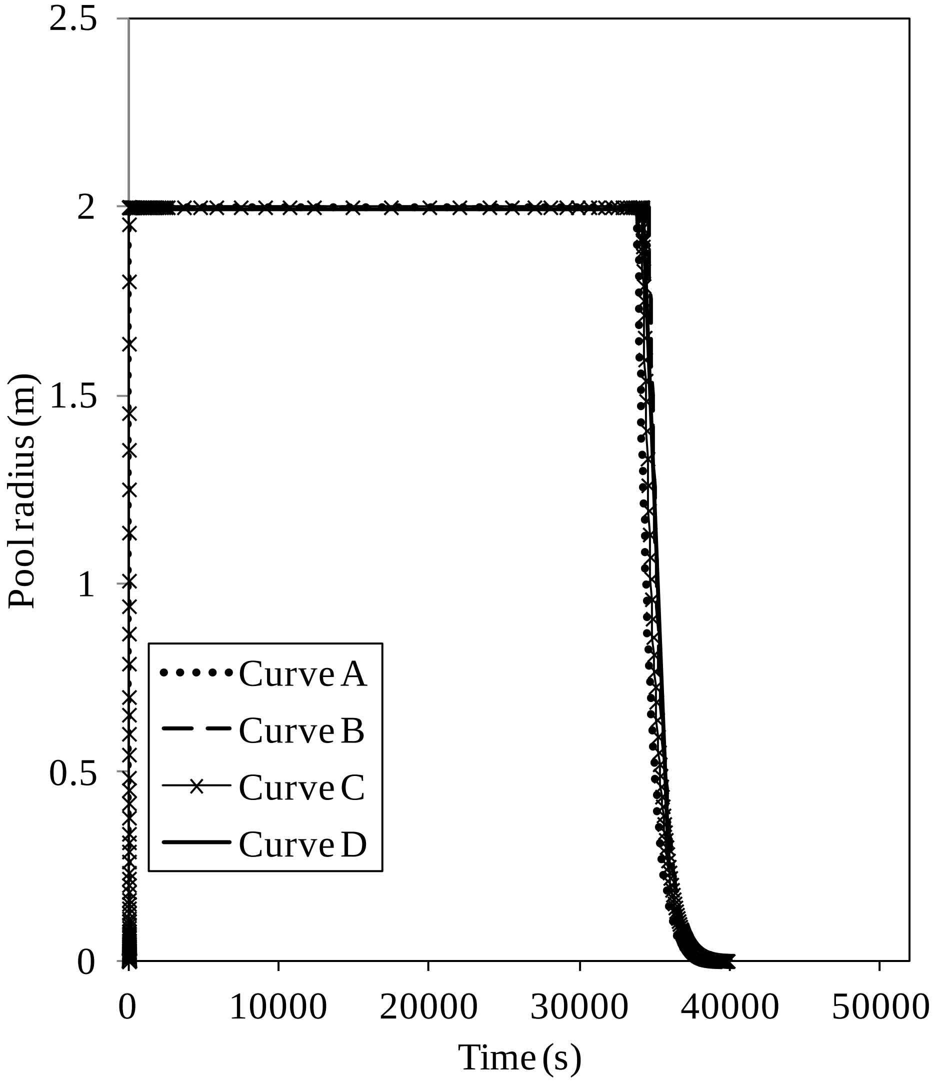

Figure 5.12. Variation of the pool radius with time for an instantaneous Benzene/n-Hexane release on a river at a temperature of 283 K and a wind speed of 1 m/s at 10 m above the surface

Spill mass: 1000 kg

Curve A: This work: 1.8 x10^{-3} kg/kg (base case)

Curve B: This work: 9x10^{-4} kg/kg

Curve C: This work: 3.6x10^{-3} kg/kg

Curve D: LPOOL simulation

5.4 Concluding remarks

This chapter presented the implementation of a public-domain solver for stiff problems in the multi-component pool model formulated in chapter 4 of this thesis. The numerical method used is based on Backward Differentiation Formula (BDF); a linear multi-step predictor-corrector method.

The results of the present work were verified against a widely-used public-domain simulation software for multi-component pools, LPOOL (Post, 1994). LPOOL employs a first-order numerical explicit method with step control to solve a system of algebraic and ordinary differential equations. The robustness of the numerical solution implemented in the present work was assessed for a series of hypothetical case studies involving continuous and instantaneous spills of cryogenic, evaporating and water-soluble mixtures on land and water surfaces. Both models were also compared in terms of their range of application, particularly in the case of water-soluble chemicals.

From the model verification it was found that the solver implemented in this work was numerically robust when solving a stiff problem. Also, the present implementation showed improved numerical stability as compared to the numerical algorithm in LPOOL. The maximum deviations between their results were within the range of accuracy expected of such pool models.

In terms of the range of application, it was found that the LPOOL simulation leads to an overestimation of 10% on average of the total vaporisation rate from water soluble mixtures, for the range of mixtures and conditions tested. A clear trend for the variation of the pool vaporisation and dissolution rates with respect to the solubility of benzene was found. The pool vaporisation rate was found to decrease with increasing solubility while the dissolution rate showed an increase with respect to the same parameter, within the range of mixtures and conditions tested.

Overall, it could be concluded that the LPOOL model with its present numerical approach is not suitable to simulate the behaviour of multi-component pools in the boiling regime as the rate at which the pool temperature varies with time is very much lower than the rate of pool spreading making the simultaneous solution of ODEs a stiff problem. On the other hand, for the case of non-boiling pools LPOOL was found to perform better, although the selection of time step is still not the optimal to guarantee a stable solution. By employing a more rigorous numerical solution as the one described in this chapter the problem of stiffness in the multi-component pool model is overcome and the results were numerically stable across the solution space.

CHAPTER 6. MODEL VALIDATION

6.1 Introduction

In the preceding chapters, the governing theory and numerical algorithm describing a mathematical model for the simulation of pool spreading, vaporisation and dissolution of a mixture was presented. The results of a series of hypothetical cases were shown in order to verify the robustness and numerical accuracy of the model in predicting the behaviour of a multi-component pool against a pure component approximation and the existing HGSYSTEM pool model, LPOOL (Post, 1994).

In this chapter, the model developed is validated against experimental published data. The results of the validation tests are then used to determine the accuracy and the range of applicability of the multi-component pool model.

The validation tests comprise a total of seven sets of experiments, five to validate the performance of pools on land surfaces and the remaining two on water surfaces. Table 6.1 provides a summary of the validation experiments. These were selected on the basis of covering a range of inventories (pure components and mixtures), different surfaces (soil, concrete, water) in the presence or absence of bunds, and instantaneous and continuous releases.

This chapter is divided into the 4 sections:

- ☐ Section 6.2 presents the validation of the spreading model
- ☐ Section 6.3 presents the validation of the boiling pool model
- ☐ Section 6.4 presents the validation of the evaporating pool model
- ☐ Section 6.5 presents the conclusions of the chapter

Table 6.1 Summary of the experiments used for validation

Experiment	Number of runs compared	Surface	Indoors/ Outdoors	Spill	Substance(s) tested	Scale	Model validated
Belore and McBean (1986)	8	Plywood	Indoors	Continuous	Water	Large	Spreading of pools on land
Dodge et al. (1983)	2	Water	Outdoors	Instantaneous /Continuous	n-Pentane/ n-Octane	Large	Spreading of pools on water
Reid and Wang (1978)	2	Soil/ Concrete	Indoors	Instantaneous	LNG	Medium	Boiling of pools on land
Burgess et al. (1972)	18	Water	Indoors	Instantaneous	Methane / LNG	Small	Boiling of pools on water
Kawamura and MacKay (1987)	4	Sand	Outdoors	Continuous	n-Pentane/ n-Hexane / Toluene	Medium	Evaporation model
Reijnhart and Rose (1980)	16	Insulated surface	Indoors	Instantaneous	Toluene/ n-Pentane	Small	Evaporation model
Okamoto et al. (2009)	3	Insulated surface	Indoors	Instantaneous	n-Pentane/ n-Hexane/ n-Heptane mixtures	Small	Evaporation model

6.2 Validation of the spreading model

The following section presents the validation of the spreading model against real data for spills on land and water. The experiments selected for the model validation involve chemicals of low volatility and solubility, in order to separate the spreading from the evaporation and dissolution phenomena. The validation of the spreading on land model is presented first, followed by comparisons for pools spreading on water.

6.2.1 Spreading of pools on land

In this section, the performance of the pool spreading model on land is validated against experimental data compiled by Belore and McBean (1986) (see table 6.1). Two representative tests namely Tests 1 and 2 are selected for this exercise.

The tests were performed spilling water continuously over a square plywood surface 3 x 3 m. The source of the spill was located at the centre of the plywood surface and the appropriate spill rate was set by adjusting the area of discharge opening. Flow depth markers were located at regular distances. The spreading rate of the pool was determined by timing the arrival of the pool front at each of the flow depth markers. The spill rates used in tests 1 and 2 were 1.19 kg/s and 1.69 kg/s respectively. Belore and McBean (1986) repeated each test four times on average in order to verify the reproducibility of their experimental results.

Values quoted for thermal conductivity and diffusivity of plywood at 300 K were taken from Incropera and DeWitt (1996). Table 6.2 presents a summary of the input data used to simulate the two tests.

The roughness length of the plywood surface was not reported by Belore and McBean (1986) and values for the pool minimum depth (see chapter 3, section 3.3.2) cannot be accurately estimated. In the present model the pool minimum depth is only dependent on the roughness of the surface the pool spreads over. As it is, the pool minimum depth relative to the surface roughness is taken as 10^{-3} and $5\cdot10^{-3}$ m to simulate a smooth surface (van den Bosch, 2005).

Table 6.2. Summary of test conditions for Belore and McBean (1980) experiments

Test number	**1**	**2**
Chemical	Water	Water
Spill rate (kg/s)	1.19	1.69
Spill duration (s)	60	60
Spill temperature (K)	295	295
Air temperature (K)	295	295
Type of surface	Plywood	Plywood
Surface temperature (K)	295	295
Thermal conductivity (W/m K)	0.087	0.087
Thermal diffusivity (10^{-7} m^2/s)	1.563	1.563
Test duration (s)	60	60

Figures 6.1 and 6.2 show the variation of the predicted and experimental pool radius with time for tests 1 and 2, respectively. Curves A and C corresponds to the predicted data for pool minimum depths of 10^{-3} and $5\cdot10^{-3}$ m, while curve D presents the experimental results. From the figures it can be seen that the experimental data lies between curves A and C.

Although, it is observed that the model gives a conservative estimate of the pool radius for the lowest value of the pool minimum depth (10^{-3} m), the accuracy of the model can yet be improved. When the pool has spread to an area such that its depth is close to the value of the surface roughness length, it can be assumed that the forces acting upon the pool are mainly gravity and surface tension. Under this assumption the depth of the pool would be equal to the capillary length, h_{cap}, given by (Webber, 1990):

$$h_{cap} = \sqrt{\frac{\sigma_L}{g\,\rho_L}} \tag{6.1}$$

where, σ_L is the surface tension of the pool

For water at 20 °C the capillary depth is $2.7\cdot10^{-3}$ m (properties obtained with DIPPR® thermo-physical properties package (Design Institute for Physical Properties, 2012)). Curve B in figures 1 and 2 shows the variation of the predicted pool radius against time for tests 1 and 2 using a value of the minimum pool depth equal to the capillary depth.

From the figures improved agreement between modelled and real data can be observed when setting the pool minimum depth equal to the capillary depth for a smooth surface such as plywood. However, as many of the surfaces over which spillages take place in real scenarios will have larger roughness lengths than this example, it is proposed to implement an algorithm capable of selecting the appropriate pool minimum depth, according to the surface roughness and capillary depth of the pool.

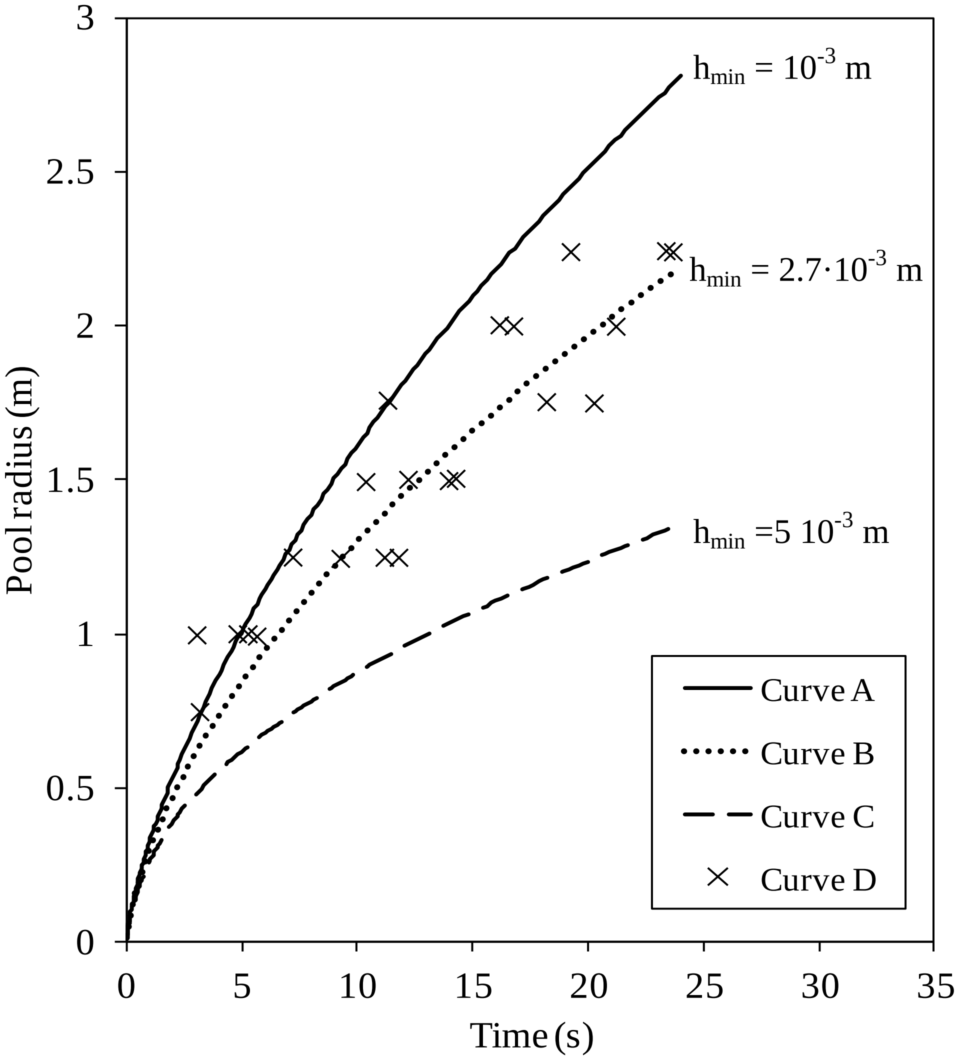

Figure 6.1. Variation of the pool radius with time for water continuously spilled on plywood. Spill rate = 1.19 kg/s

Curve A: Predicted data. Pool minimum depth = 10^{-3} m

Curve B: Predicted data. Pool minimum depth = $2.7\cdot10^{-3}$ m

Curve C: Predicted data. Pool minimum depth = $5\cdot10^{-3}$ m

Curve D: Experimental data (Belore and McBean, 1980)

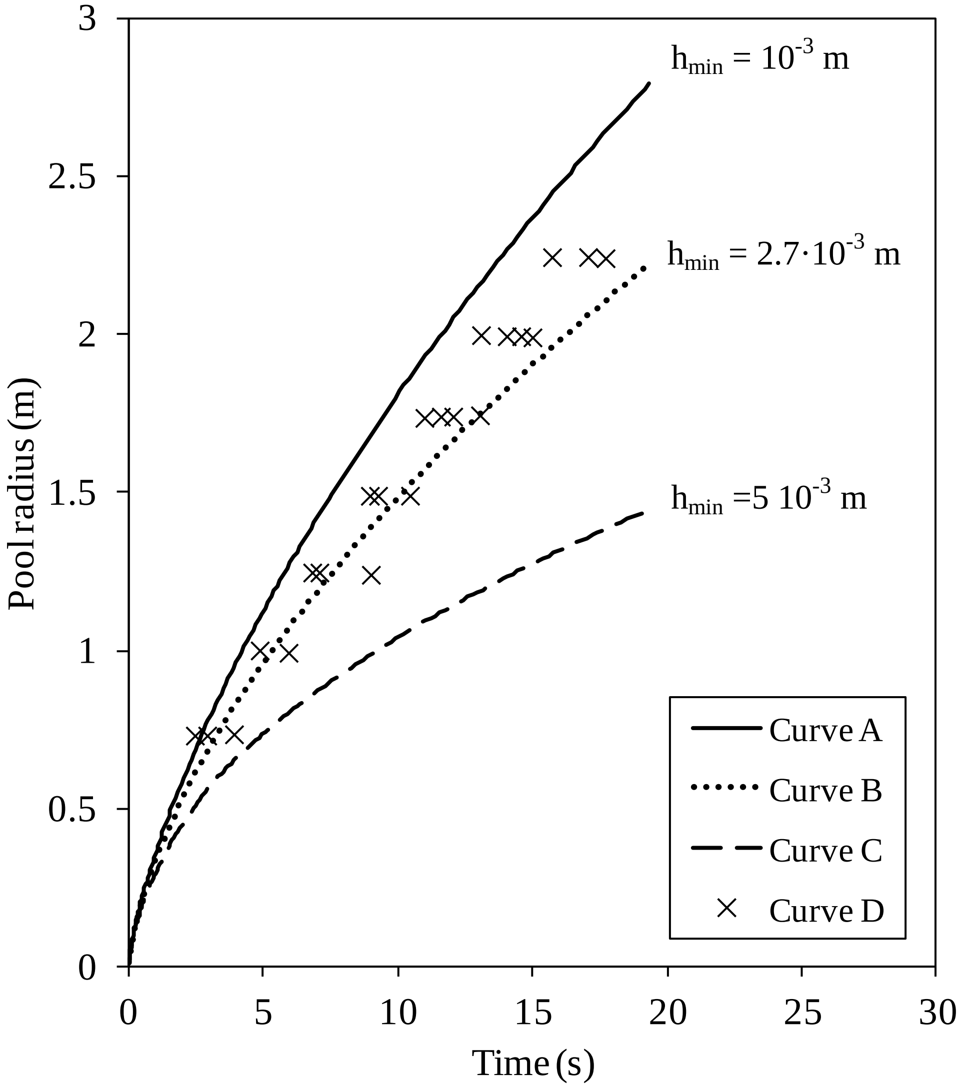

Figure 6.2. Variation of the pool radius with time for water continuously spilled on plywood. Spill rate = 1.69 kg/s

Curve A: Predicted data. Pool minimum depth = 10^{-3} m

Curve B: Predicted data. Pool minimum depth = $2.7 \cdot 10^{-3}$ m

Curve C: Predicted data. Pool minimum depth = $5 \cdot 10^{-3}$ m

Curve D: Experimental data (Belore and McBean, 1980)

The impact of the variation of the minimum thickness parameter on the pool results was further investigated in the following example of a continuous spill of 5 kg/s of n-Butane on a concrete surface at an initial temperature of 283 K. In this study the minimum thickness parameter was varied between 5 (a typical value for concrete) and 20 mm (a value used for rough terrain such as grassland or rough sandy terrain). Figure 6.3 shows the variation of the pool vaporisation rate with time at different values of the minimum thickness.

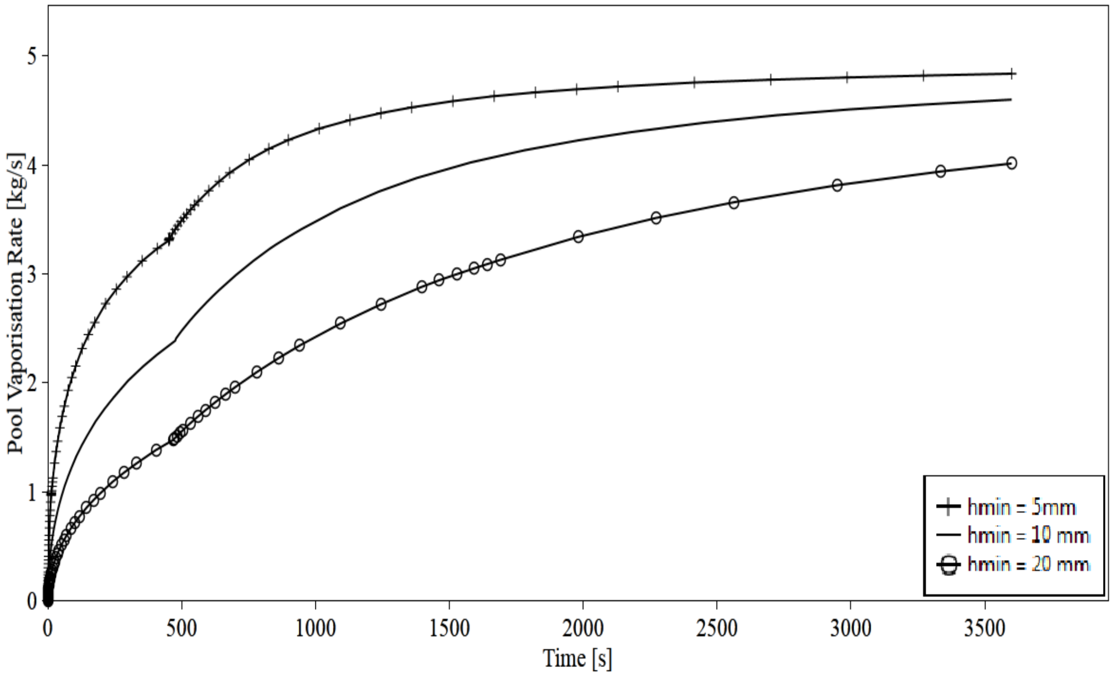

Figure 6.3. Variation of the pool vaporisation rate with time for a continuous n-butane spill on concrete at different values of the minimum thickness.

Spill rate = 5 kg/s

Spill temperature = 272.15 K

Initial surface temperature = 283 K

From figure 6.3 it can be observed that the variation of the pool minimum thickness has a visible impact on the variation of the pool vaporisation rate predicted by the model. In the present example, if using a minimum thickness of 5 mm it is observed that the vaporisation rate reaches the maximum value of 5 kg/s at 3600 s after release. On the other hand, using higher values of the minimum thickness results in lower vaporisation rates, up to 40%, observed at 3600 s after release.

Regarding further experimental evidence on pool spreading, Moorhouse and Carpenter in 1986 (Thyer, 1996) measured pool radius variation from large scale LNG spills on concrete and soil. No further indication of the type of soil used on the experiments, whether farmland or rough sand, is given. In the review presented by Thyer (1996) predicted and experimental results are compared for the Moorhouse and Carpenter (1986) tests. The predicted data was obtained by Moorhouse and Carpenter (1986) using the spreading equation presented by Shaw and Briscoe (1980) and also used in the present work. Different values for the minimum pool thickness were compared against the field data. For the concrete surface the experimental data show apparent better agreement with the predicted results for a minimum thickness of 10 mm. For the soil surface the majority of the field data points lay between the predicted pool radii using 20 and 10mm of minimum pool thickness. These values for the minimum thickness obtained from the experiments are much higher than typically quoted values for concrete or soil surfaces (Napier and Roopchand, 1986) (van den Bosch, 2005).

This shows that there is inconsistency on the values found in the literature for pool's minimum thickness as a function of the type of substrate solely. And it is thus recommended to follow an approach as suggested in the present work which takes into account the surface tension of the fluid.

6.2.2 Spreading of pools on water

In this section the performance of the pool spreading model on water for continuous and instantaneous releases is validated against the experimental data compiled by Dodge et al. (1983) for various hydrocarbons on a water basin. Tests I 1-2 and II 1-4, for which the chemical of interest was n-Octane, were chosen for the model validation.

The tests were conducted on a square 18.3 m x 18.3 m water basin of 0.3 m depth. In test II 1-4, a centrifugal pump was used to provide a constant spill rate of 0.89 kg/s throughout the experiment. The n-Octane was discharged vertically through a pipe at a height of 6.4 mm above the water surface to minimise the vertical momentum of the fluid.

In test I 1-2 an open cylindrical tank without a bottom lid was descended onto the surface of the water and filled with 7.3 kg of n-Octane. The tank was rapidly raised, instantaneously releasing the contents into the water. A set of 15 pegs connected to a galvanometer were placed along the diagonals of the basin at intervals of 0.3 m and 0.6 m from the spill source in order to time the arrival of the pool front. Table 6.3 presents a summary of the input data used in the simulations.

Table 6. 3. Summary of test conditions for Dodge et al. (1983) experiments

Test number	**I 1-2**	**II 1-4**
Chemical	n-Octane	n-Octane
Spill rate (kg/s)	-	0.89
Spill mass (kg)	7.3	-
Spill duration (s)	-	60
Spill temperature (K)	293	293
Air temperature (K)	293	293
Type of surface	Calm sea	Calm sea
Surface temperature (K)	293	293
Test duration (s)	60	60

Figure 6.4 shows the comparison between the predicted and experimental pool radius for tests I 1-2 and II 1-4 (see table 4.1). From the figure it can be seen that better agreement between the predicted and experimental data is obtained for the instantaneous spill

(curve A) as compared to the continuous (curve B) case. It is also observed that the results of the model shown in curve B increasingly over predict the experimental data. This may be due to the assumption of constant pool mass implicit in the derivation of the spreading on water equations (see section 3.3.1.1). Instantaneously released pools spread faster than pools that are continuously fed. As such, an instantaneous pool may reach its maximum area before any mass lost due to vaporisation becomes significant with respect to the total mass spilled. This is not the case for continuous pools where pool growth is slower and vaporisation effects may be relevant during spreading.

The average % deviation of the model is -9.7%. The 95% confidence interval is between 0.4 and -19.8 % error with respect to the experimental data.

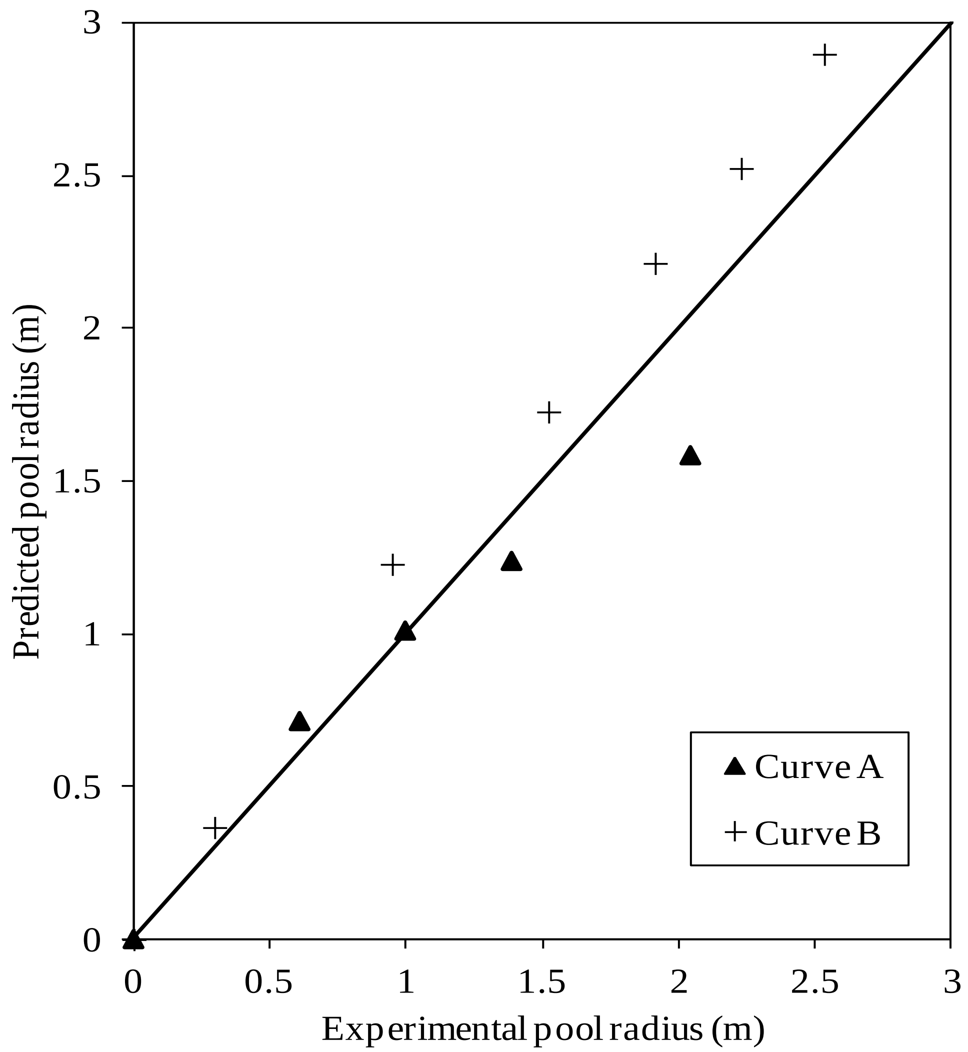

Figure 6.4. Predicted against experimental (Dodge et al., 1983) pool radius for n-Octane spilled on water

Curve A: Instantaneous spill. Spill mass = 7.03 kg

Curve B: Continuous spill. Spill rate = 0.89 kg/s. Duration of the spill = 60 s

The spreading on water model used in the present work consists of a series of equations for the pool radius as a function of time, pool mass and an empirical coefficient. The formulation for a continuous spill on calm water was presented in chapter 3 of this thesis and it is reproduced here for the purposes of clarity:

$$r = 1.24\left(g\Delta \frac{\dot{m}_{spill}}{\rho} \right)^{1/4} t^{3/4} \tag{3.8}$$

The impact of the variation of the empirical coefficient (K1 = 1.24) on the pool results is investigated next. For this purpose an example of a continuous spill of 2 kg/s acrylonitrile on calm water at 288 K is chosen. The following figure shows the variation of the pool radius with time for values of the empirical constant of 0.80, 1.24 and 1.60.

From figure 6.5 it is observed that the variation of the empirical coefficient in the spreading on water model has reduced impact on the variation of the pool radius with time for the conditions studied. The differences are only observed at the early stages of the spill and the variability of the coefficient does not have a visible effect on the prediction of the final pool radius. From this it can be concluded that the uncertainty in the estimation of the empirical coefficient for the spreading on water model will have a minimal effect on the prediction of the variation of the pool radius with time for the range of conditions tested.

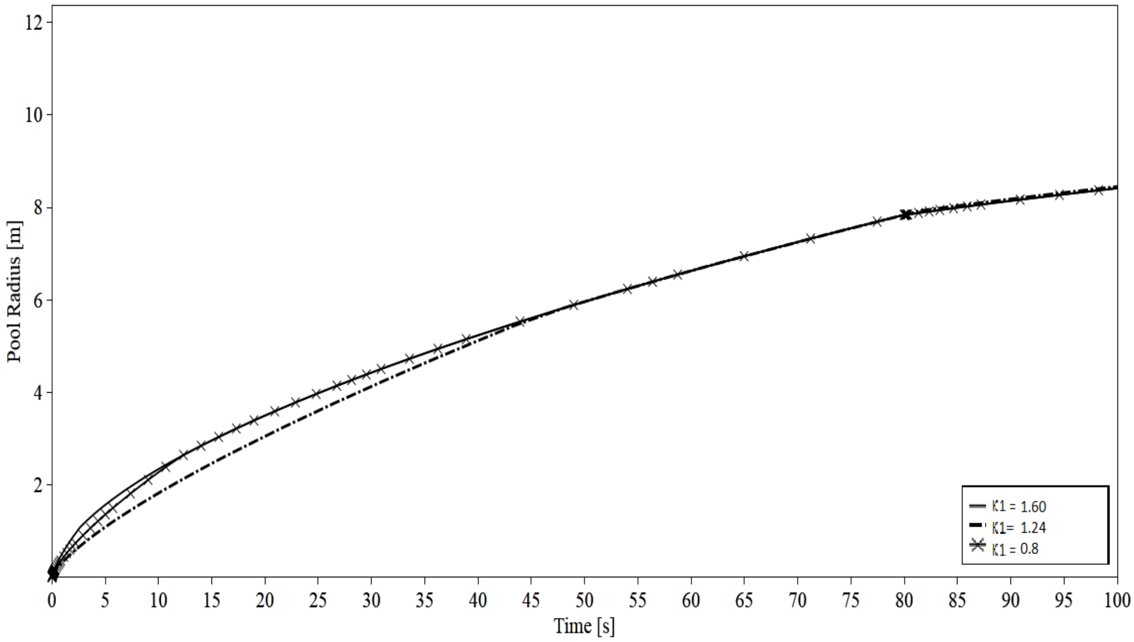

Figure 6.5. Variation of the pool radius with time for a continuous acrylonitrile spill of 2 kg/s on calm sea for different values of the empirical constant for spreading on water.

6.3 Validation of the pool boiling model

The following section presents the validation of the pool boiling model against real data available in the published literature. The set of experiments selected for the model validation comprises spills of constant area carried out under controlled indoors conditions in order to better characterize the phenomena. As pool boiling is mainly driven by the rate of heat transfer from the surface to the pool, the selection of the experiments also took into account the absence of wind to minimise the rate of convective heat transfer. The validation of the model for pools on soil and concrete is presented first (section 6.3.1), followed by comparisons against experiments performed over water surfaces (section 6.3.2).

6.3.1 Pools boiling on land

In this section, the model for pool boiling on land is validated against experimental data compiled by Reid and Wang (1978). These experiments were carried out in the Massachusetts Institute LNG Research Centre where LNG was spilled onto different dike floor materials, insulated concrete, soil, sand, polyurethane and corrugated aluminium. For the purposes of this study, two of the tests, tests 47 and 70, performed on soil and concrete, respectively, are used to validate the pool boiling model.

Test 70 was carried out on a 1 m^2 rectangular concrete surface. Test 47, on the other hand, was carried out on a Styrofoam box of the same area filled initially with soil. The thermal properties of the concrete and soil used in the tests are given in table 6.4.

Table 6.4. Thermal properties of concrete and soil in Reid and Wang (1978) experiments

	Surface	
Material properties	**Soil**	**Concrete**
Thermal conductivity (W/m K)	6	1.21
Thermal diffusivity (m^2/s)	$3.41 \cdot 10^{-5}$	$5.72 \cdot 10^{-7}$

The edges of the surfaces in both tests were insulated to avoid heat losses. A Styrofoam top cover was also used to minimize any convective heat transfer from the air.

The composition of the Liquefied Natural Gas (LNG) used in the tests was not reported by Reid and Wang (1978). Consequently, the simulations were performed using an 85 wt% Methane and 15 wt% Ethane mixture, which is a composition typically used for modelling LNG (Thyer, 2003).

The vaporisation rate of the LNG was determined from weight readings of a load cell placed under the test surfaces at 1 s interval. The total mass spilled for tests 47 and 70 were 0.645 kg and 3.5 kg respectively. Table 6.5 presents a summary of the input data used in the simulations.

Table 6.5. Summary of test conditions for Reid and Wang (1978) experiments

Test number	**47**	**70**
Chemical	LNG	LNG
Spill mass (kg)	0.645	3.5
Spill temperature (K)	112	112
Air temperature (K)	293	293
Type of surface	Soil	Concrete
Surface temperature (K)	280	280
Test duration (s)	60	60

Figure 6.6 shows a comparison of the predicted and experimental percentage of mass vaporised to total mass spilled for an instantaneous release of LNG on soil and concrete.

From figure 6.6, it can be seen that good agreement is obtained between the predicted and experimental data for the vaporisation of LNG from concrete (curve A). Additionally, good agreement is obtained for the vaporisation of LNG from soil (curve B) up to the point where Reid and Wang (1978) observed percolation of the LNG into the soil (> 70% percentage of mass vaporised to total mass spilled – indicated on figure). At this point boiling of LNG took place beneath the soil.

The average % deviation of the model is 0.2%. The confidence interval of the model is between 4.8 and -4.4% difference with respect to the experimental data.

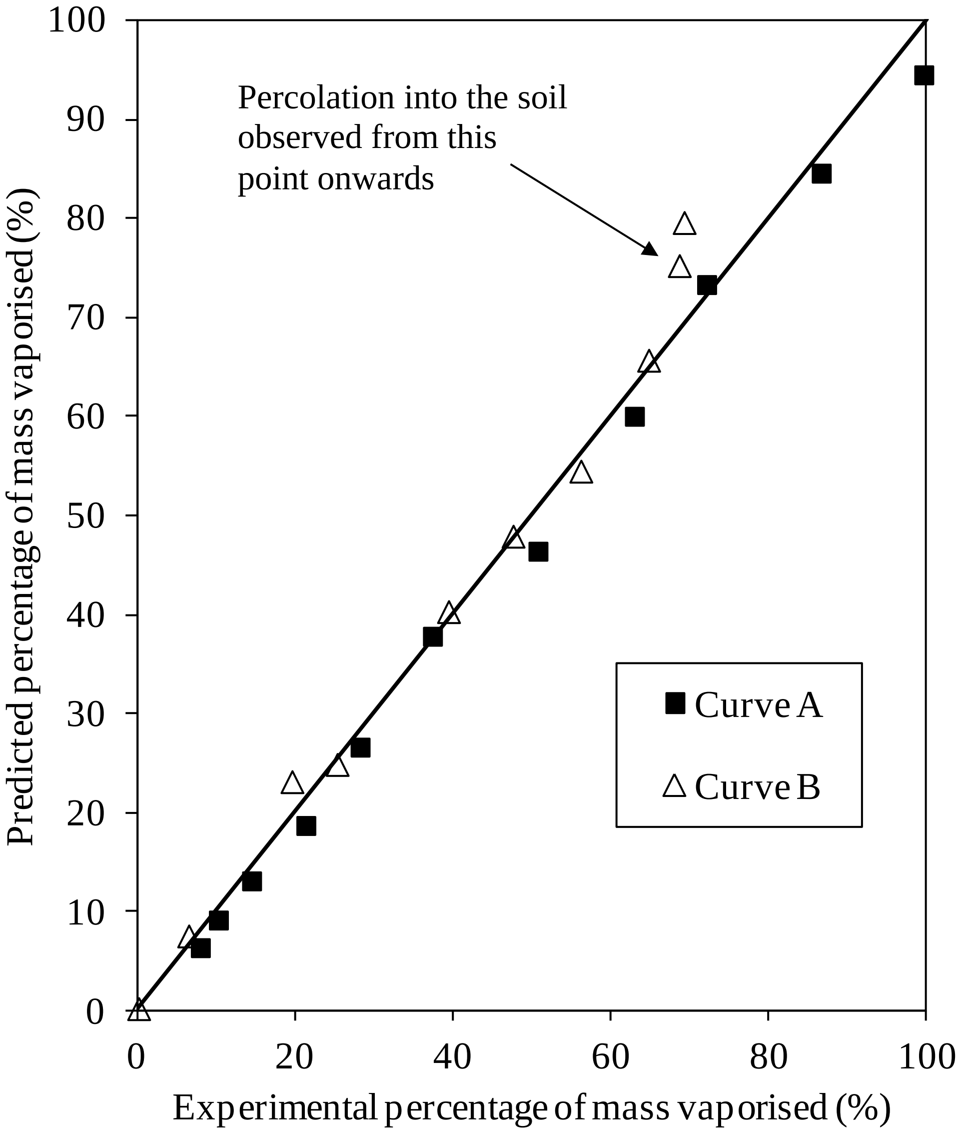

Figure 6.6. Predicted against experimental (Reid and Wang, 1978) percentage of mass vaporised for an instantaneous LNG spill. Spill area = 1 m^2

Curve A: LNG spilled on concrete

Curve B: LNG spilled on soil

6.3.2 Pools boiling on water

In this section, the model for pool boiling on water is validated against the experimental data compiled by Burgess et al. (1972). Burgess et al. (1972) carried out a series of LNG tests on water for the US Bureau of Mines. Experiments were also performed with Methane and Nitrogen. A set of 4 different tests for which the chemicals of interest were LNG and liquefied Methane were chosen for the model validation. Each test was repeated a certain number of times to attest the reproducibility of the experimental results. The total number of runs was 18 as indicated in table 6.6.

The tests were carried out on a 0.074 m^2 water reservoir, resting on a balance which automatically recorded the weight loss at 50 g intervals. The chemical was spilt instantaneously from a tilting container onto the water reservoir from a height of 0.1 and 0.3 m. The volume of chemical spilled in each test ranged from 0.002 to 0.0045 m^3. The rate of mass vaporised with time was determined from the balance readings. The input data used in the model simulations is presented in table 6.6.

Table 6.6. Test conditions for Burgess et al. (1972) experiments

Test number	**18 to 24**	**44 to 49**	**56 and 57**	**58 to 60**
Chemical	LNG	Methane	Methane	Methane
Spill mass (kg)	0.55	0.846	1.270	1.904
Spill temperature (K)	112	111.7	111.7	111.7
Type of surface	Water	Water	Water	Water
Surface temperature (K)	278.15	278.15	278.15	278.15
LNG composition (% v/v):				
Methane	94.74%			
Ethane	5.20%			
Propane	0.04%			
Butane	0.02%			

Figure 6.7 shows the variation of the total mass vaporised with time for the instantaneous release of LNG on water. Curves A and B respectively show the predicted results for a pure Methane and LNG simulation, while curve C shows the data measured by Burgess et al. (1972).

From figure 6.7 it can be observed that the predicted results (curves A and B) closely match the measured data (curve C) up to 30 s after release. During this time the mass vaporised is mostly composed of Methane leading to the excellent agreement initially evidenced between the predicted results for Methane (curve A) and the experimental data (curve C). After 30 s, lower vaporisation is reported by the experiments (curve C) as compared to the predicted values for Methane (curve A). This would indicate a decrease in the real inventory of Methane in the pool which results in an increase on the bubble point temperature and in the pool sensible heat, thus reducing the amount of energy available for vaporisation (see also chapter 4, section 4.3.1). The results of the simulation for LNG (curve B) follow the experimental trend for times greater than 40 s, but predict slightly higher values of the total mass vaporised, which can be simply attributed to mass losses during the experiment. Despite this, good agreement is observed between curves B (LNG predicted data) and C (measured data) with an average deviation of 5%. The results of the Methane simulation (curve A) are less accurate, although conservative, with maximum differences of 10% with respect to the experimental data.

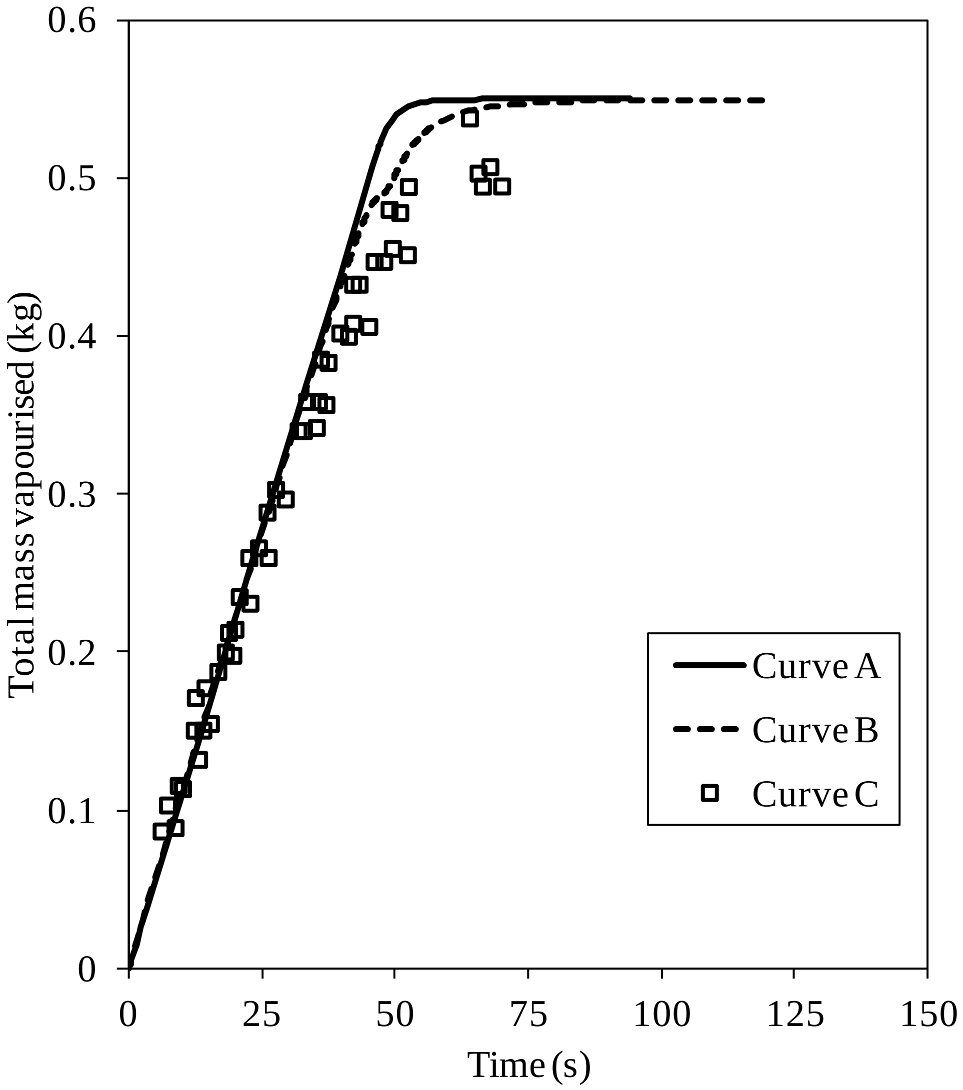

Figure 6.7. Variation of the mass vaporised with time for LNG instantaneously spilled on water

Curve A: Predicted data for pure Methane

Curve B: Predicted data for LNG

Curve C: Experimental data for LNG (Burgess et al., 1972)

Figure 6.8 shows the cumulative mass vaporised with time for the instantaneous release of liquefied Methane on water. From the figure it may be observed that the model is in good agreement with the experimental data. The average % deviation of the model is 1%. And the confidence interval of the model is between 6.5 and -4.6% deviation from the experimental data.

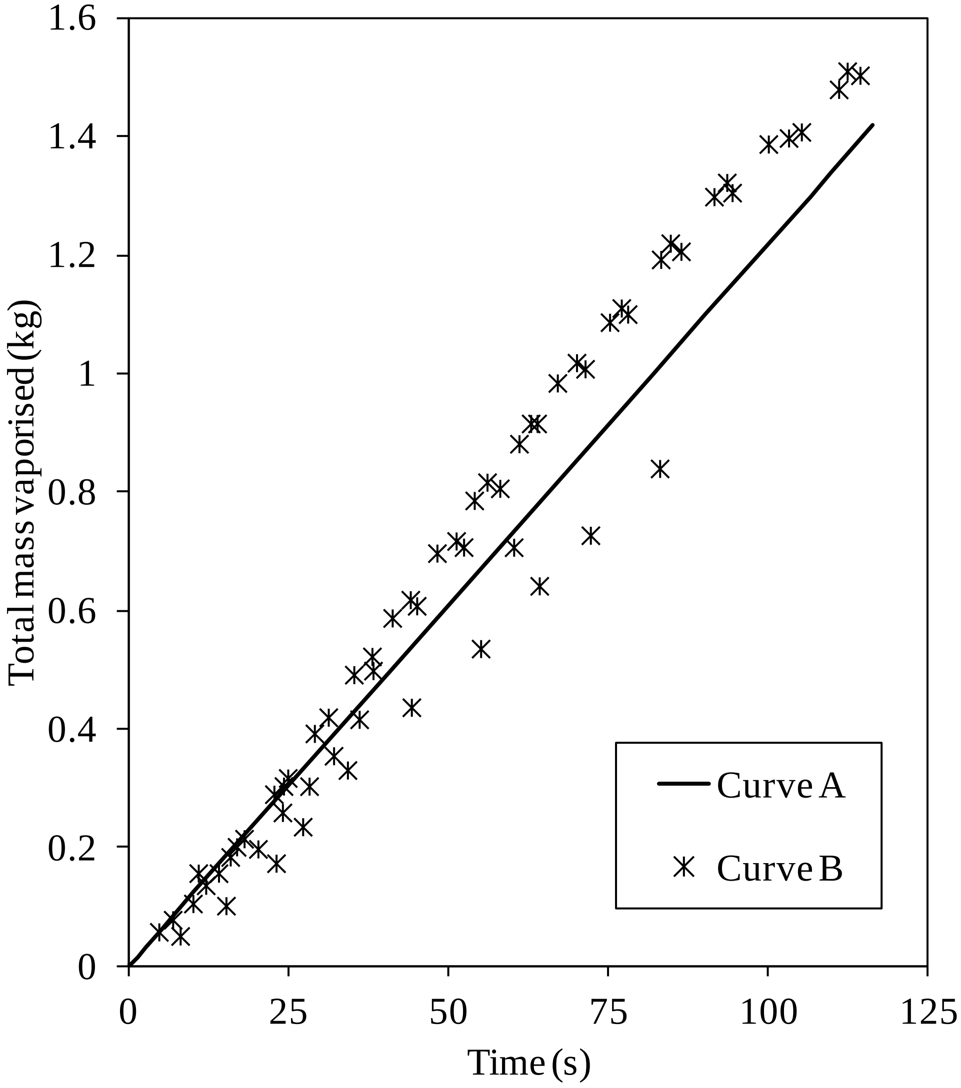

Figure 6.8. Variation of the mass vaporised with time for liquefied Methane instantaneously spilled on water

Curve A: Predicted data

Curve B: Experimental

6.4 Validation of the pool evaporation model

This section presents the validation of the pool evaporation model against three sets of experimental data: Kawamura and MacKay (1987), Reijnhart and Rose (1980) and Okamoto et al. (2009) (see table 6.1). The first two sets of experimental data comprise tests carried out for pure chemicals, while the third set includes binary and ternary mixtures. The tests selected for the purposes of validation included constant area pools and the chemicals studied do not boil at ambient conditions.

6.4.1 Pure components

6.4.1.1 Kawamura and MacKay (1987)

Kawamura and MacKay (1987) measured the evaporation rate of seven volatile chemicals from a circular pan under known meteorological conditions. The experiments were conducted at the Environment Canada Atmospheric Environment Services experimental site in Woodbridge, Ontario. All experiments were conducted during daylight.

The tests used to validate the evaporation model namely Tests 18, 20, 21 and 22 were carried out on an evaporation pan of dimensions of inner diameter of 0.46 m and a depth of 0.102 m. The chemicals tested were n-Pentane, Toluene and n-Hexane. The evaporation pan was initially filled to a depth of 0.05 m with sand and was subsequently partially buried in the ground, to avoid distortion of the wind profile against the border of the pan. The pan was then filled with the chemical tested and allowed to evaporate in the presence of wind and sun. The test was carried out until either the level of chemical remaining in the pan was less than 0.01 m or the experimental duration became excessively long. The evaporation rate was determined by measuring the volume of chemical remaining in the pan after the termination of the experiment. Table 6.7 gives the test conditions for the four tests.

Table 6.7. Test conditions of Kawamura and MacKay (1987) evaporation experiments

Test number	**18**	**20**	**21**	**22**
Chemical	Toluene	Hexane	Pentane	Pentane
Spill duration	Instantaneous	Instantaneous	Instantaneous	Instantaneous
Spill mass (kg)	3.46	2.62	4.37	2.49
Spill temperature (K)	298.15	300.15	296.15	298.15
Pan diameter (m)	0.46	0.46	0.46	0.46
Surface roughness length (m)	10^{-2}	10^{-2}	10^{-2}	10^{-2}
Wind speed at 10 m (m/s)	2.65	1.59	4.94	5.42
Atmospheric stability (Pasquill class)	Unstable-A	Unstable-A	Unstable-A	Slightly unstable-B
Duration of the experiment (s)	1260	540	385	209
Solar radiation (W/m^2)	872	728	647	861
Atmospheric temperature (K)	298	300	296	298
Surface temperature (K)	296	296	295	295
Sand thermal conductivity (W/m.K)	2.08	2.08	2.08	2.08
Thermal diffusivity of sand (m^2/s)	$7\cdot10^{-7}$	$7\cdot10^{-7}$	$7\cdot10^{-7}$	$7\cdot10^{-7}$

Table 6.8 shows the comparison of the predicted and experimental evaporation rates for the tests conducted by Kawamura and MacKay (1987). The average evaporation rate, $\overline{\dot{m}}_{vap}$, given in table 4.8 is calculated using:

$$\overline{\dot{m}}_{vap} = \frac{\sum_{j=1}^{m} \dot{m}_{vap} \Delta t}{t} \tag{6.2}$$

where,

$\dot{m}_{vap}$ = evaporation rate at the time interval Δt

Δt = time interval

t = total simulation time

j = sub-index indicating the number of time steps

m = total number of time steps in the simulation

Table 6.8. Comparison of the predicted and experimental (Kawamura and MacKay, 1987) average evaporation rates for tests 18, 20, 21 and 22

Test number	**18**	**20**	**21**	**22**
Chemical	Toluene	Hexane	Pentane	Pentane
Temperature of the spill (K)	298.15	300.15	296.15	298.15
Average experimental evaporation rate (kg/m^2 h)	3.9	7.28	23	27.1
Average predicted evaporation rate (kg/m^2 h)	4.42	10.31	27.08	33.79
Deviation between model and experimental data (%)	**-13%**	**-42%**	**-18%**	**-25%**

From the table above it is observed that the average predicted-measured deviation of the four tests is 24.5 %. The best agreement between predicted and measured data is obtained at low vapour pressures and moderate wind speeds (test KM18). However the model is found to be too conservative at low wind speeds (test KM20). At low wind speeds it is possible that vapour accumulates above the pool surface, effectively impeding the mass diffusion through the boundary layer. For simplicity the model assumes the vapour diffuses through a layer of pure air, thus this observation may explain the differences found.

The upper and lower limits of the confidence interval are respectively, 35.4 and -52.9%. The wide spread between the upper and lower limits of the confidence interval points to limitations on the model to accurately predict the evaporation rate. However, it is difficult to draw a definitive conclusion on the model's performance due to the small number of the data points for the tests (only 4).

6.4.1.2 Reijnhart and Rose (1980)

Reijnhart and Rose (1980) carried out a series of experiments using pure hydrocarbons with low (Toluene) and high (n-Pentane) volatilities in order to measure the rates of evaporation from free surfaces as a function of wind velocity, wind tunnel surface roughness and liquid temperature.

The tests were carried out in a 10 m long, square section of 1 m x 1 m wind tunnel. The chemicals tested were allowed to freely evaporate from a square pan of dimensions 0.25 m x 0.25 m and height = 0.05 m, placed 7 m from the entrance to the tunnel. Figure 6.9 shows the experimental set-up.

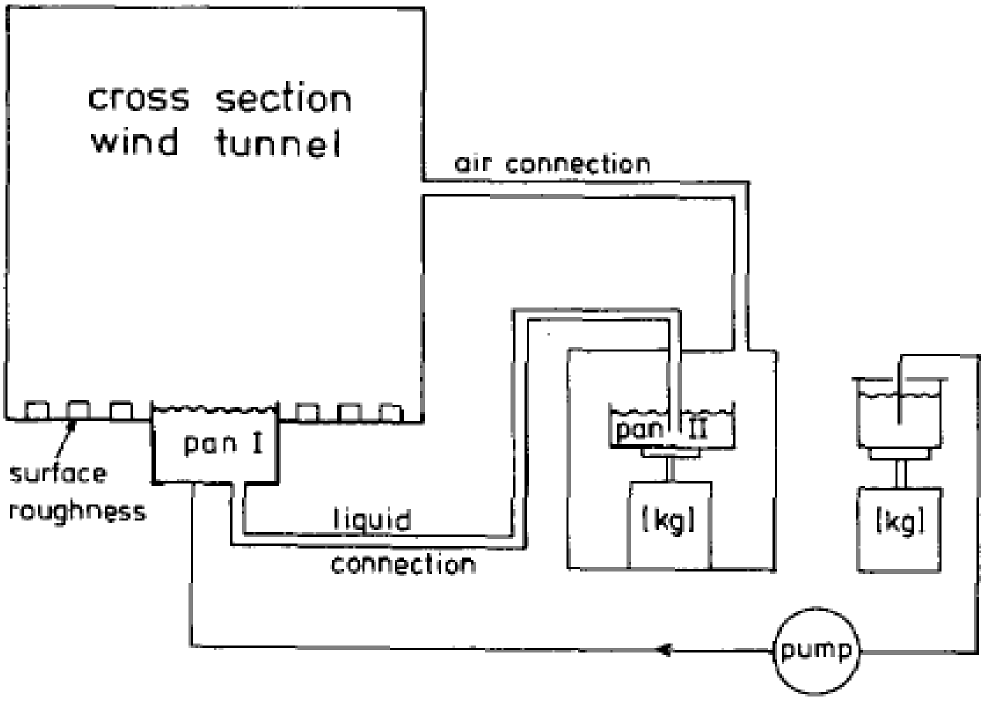

Figure 6.9. Experimental set-up for wind tunnel tests (Reijnhart and Rose, 1980)

In order to simulate land surface roughness, Lego blocks of different heights were placed on the wind tunnel floor. The wind velocity in the tunnel was measured at various heights using either, laser-Doppler anemometry or a Pitot tube. The temperature of the pool was maintained constant at 298 K throughout the experiments using a heating element and a temperature controller. Due to pressure fluctuations in the tunnel and waves in the liquid surface, it was not possible to measure directly the rate at which mass was lost from the evaporation pan (pan I). Instead, the evaporation rate was measured indirectly from the weight loss in an interconnected pan (pan II) of the same area, maintained at the wind tunnel pressure, and from the pumping rate from the reservoir to pan I. A summary of the test conditions for Reijnhart and Rose (1980) experiments are shown in table 6.9.

Table 6.9. Test conditions for Reijnhart and Rose (1980) experiments

Test number	**1**	**2**	**3**	**4**
Chemical	Toluene	Toluene	Toluene	n-Pentane
Spill mass (kg)	10	10	10	10
Spill temperature (K)	298	298	298	298
Surface roughness length (m)	$2.5\cdot10^{-3}$	$2.5\cdot10^{-3}$	$2.5\cdot10^{-3}$	$2.5\cdot10^{-3}$
Average wind speed (m/s)	3.83	5.02	5.93	3.15
Atmospheric stability	Neutral	Neutral	Neutral	Neutral

Test number	**5**	**6**	**7**	**8**
Chemical	n-Pentane	n-Pentane	Toluene	Toluene
Spill mass (kg)	10	10	10	10
Spill temperature (K)	298	298	298	298
Surface roughness length (m)	$2.5\cdot10^{-3}$	$2.5\cdot10^{-3}$	10^{-4}	10^{-4}
Average wind speed (m/s)	4.10	5.11	3.56	4.14
Atmospheric stability	Neutral	Neutral	Neutral	Neutral

Test number	**9**	**10**	**11**	**12**
Chemical	Toluene	Toluene	Toluene	Toluene
Spill mass (kg)	10	10	10	10
Spill temperature (K)	298	298	298	298
Surface roughness length (m)	10^{-4}	10^{-4}	10^{-4}	$2.2\cdot10^{-5}$
Average wind speed (m/s)	5.01	5.90	7.46	2.38
Atmospheric stability	Neutral	Neutral	Neutral	Neutral

Test number	**13**	**14**	**15**	**16**
Chemical	Toluene	Toluene	Toluene	Toluene
Spill mass (kg)	10	10	10	10
Spill temperature (K)	298	298	298	298
Surface roughness length (m)	$2.2\cdot10^{-5}$	$2.2\cdot10^{-5}$	$2.2\cdot10^{-5}$	$2.2\cdot10^{-5}$
Average wind speed (m/s)	3.22	3.99	5.33	6.56
Atmospheric stability	Neutral	Neutral	Neutral	Neutral

Figures 6.10 and 6.11 respectively show the comparison of the predicted and experimental reduced evaporation rate with average wind speed across the boundary layer for Toluene and n-Pentane.

From figure 6.10, it can be seen that good agreement is obtained between the predicted and experimental evaporation rate for Toluene. On the other hand, in figure 6.11, it can be seen that the evaporation model consistently over predicts the evaporation rate of n-Pentane. Despite the small number of experimental data points (3), the observed trend highlights the limitation of the model in accurately predicting the evaporation rates of more volatile chemicals. Additional investigations are required to fully understand these limitations.

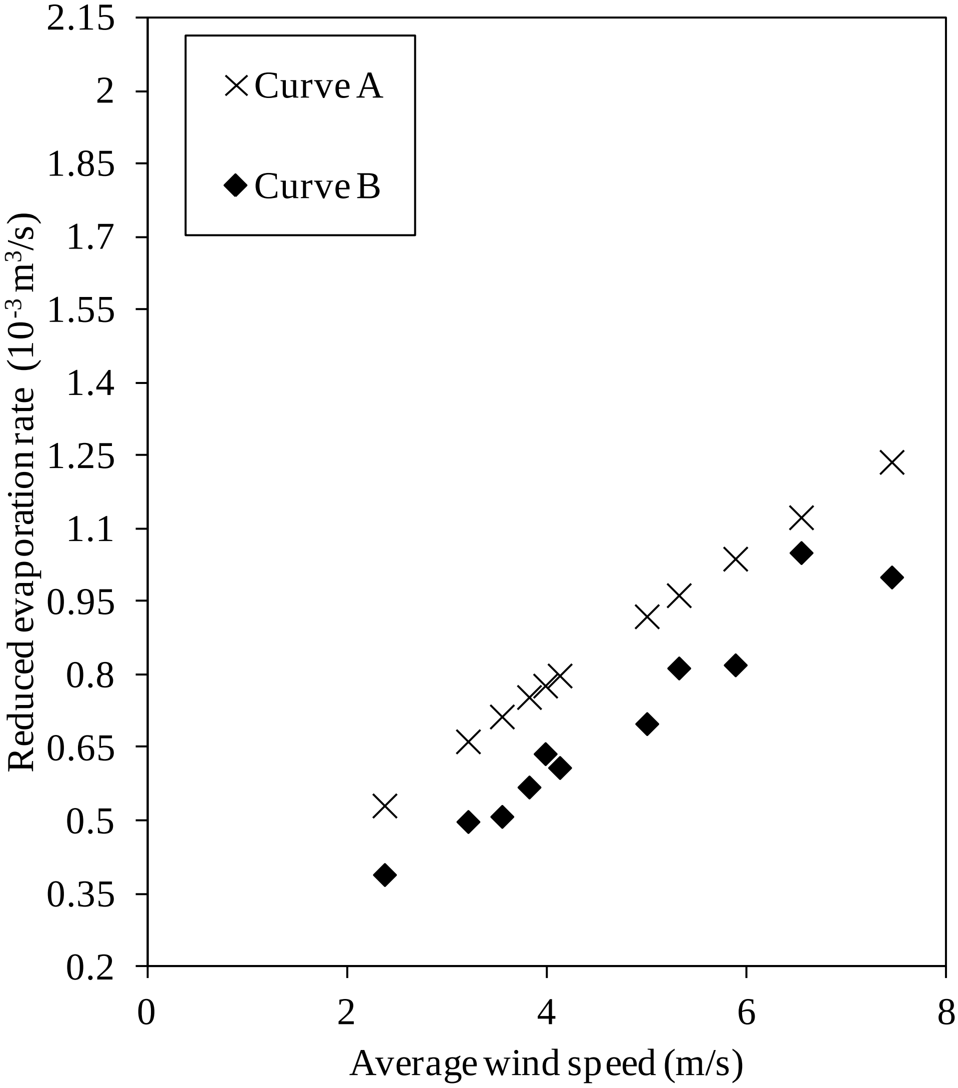

Figure 6.10. Variation of reduced evaporation rate with average wind speed for Toluene at 298.15 K

The reduced evaporation rate is given by: $E_{vap} = \frac{\dot{m}_{vap} \cdot R \cdot T_{pool}}{P_v \cdot M}$

Curve A: Predicted data

Curve B: Experimental data (Reijnhart and Rose, 1980)

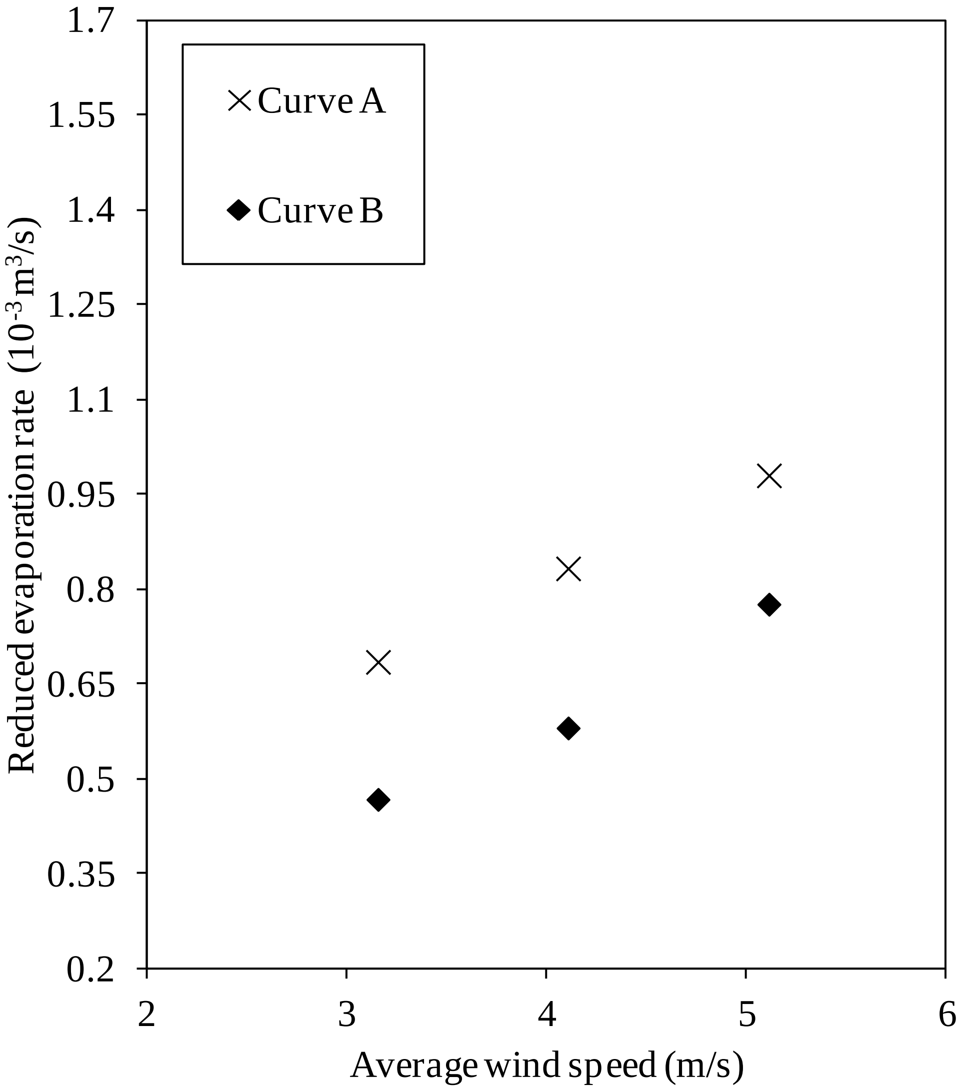

Figure 6.11. Variation of reduced evaporation rate with average wind speed for n-Pentane at 298.15 K

The reduced evaporation rate is given by: $E_{vap} = \dfrac{\dot{m}_{vap} \cdot R \cdot T_{pool}}{P_v \cdot M}$

Curve A: Predicted data

Curve B: Experimental data (Reijnhart and Rose, 1980)

6.4.2 Mixtures

Okamoto et al. (2009) carried out a series of laboratory scale experiments to study the evaporation patterns of binary and ternary mixtures of n-Pentane, n-Hexane, n-Heptane, Toluene and p-Xylene at various compositions.

The evaporation rate was determined from the measured weight loss read from an electronic balance of accuracy ±0.01 g. A square insulated pan of area 0.1 m^2 was loaded on the balance, and the mixture under study was instantaneously poured into the tray. The weight losses were recorded every 10 s until the weight loss fraction reached 0.7. The weight loss fraction is given by:

$$a = \frac{w_0 - w}{w_0} \tag{6.3}$$

where,

a = weight loss fraction

w_0 = initial mass in the pool

w = current mass in the pool

The measurements were conducted under a fume hood. The fume hood fan was not operated, and the liquid sample was degraded under no wind condition. It should be noted that in the absence of wind the prevailing mass transfer mechanism between the pool and the air above it is natural convection. This poses a difficulty for the purpose of validation as the model assumes forced convection through a turbulent boundary layer. However, Okamoto et al. (2009) carried out measurements of the mass transfer coefficients for pure components under the same conditions as the mixture studies. The mass transfer coefficients for pure components were determined from measurements of the evaporation rate and vapour pressures. Table 6.10 shows the experimental values obtained for n-Pentane, n-Hexane and n-Heptane.

Table 6.10. Experimental values for the mass transfer coefficients of hydrocarbon solvents (Okamoto et al., 2009)

Solvent	Mass transfer coefficient (10^{-4} m/s)
n-Pentane	3.64
n-Hexane	2.70
n-Heptane	2.63

The tests were carried out with different values of spilled mass corresponding to initial pool depths of 0.001, 0.0015 and 0.002 m. The temperature of the pool was recorded with a thermometer located at the base of the pan.

Tests carried out for binary and ternary mixtures of n-Pentane, n-Hexane and n-Heptane were selected for the purposes of comparison against the model. The conditions of the three tests selected are shown in table 6.11.

Table 6.11. Test conditions for Okamoto et al. (2009) experiments

Test number	**1**	**2**	**3**
Spill temperature (K)	273	273	273
Air temperature (K)	273	273	273
Initial pool depth (m)	0.0015	0.0015	0.002
Type of surface	Insulated	Insulated	Insulated
Spill composition (% mol/mol)			
n-Pentane	50	50	33.4
n-Hexane	50	0	33.3
n-Heptane	0	50	33.3

Figures 6.12 to 6.14 show the predicted (curve A) and measured (curve B) pool evaporation rate against the weight loss fraction for binary and ternary mixtures of n-Pentane, n-Hexane and n-Heptane.

From the figures it is observed that the predicted and experimental data follow the same general trend. The model over-predicts the measured pool evaporation rate for weight loss fractions greater than 0.1, although it fails to account for the initially high rates of mass vaporised observed in the experiments. It should be noted that the experiments were carried out in the absence of wind, as Okamoto et al. (2009) reported the fume hood fan was shut down while the mixtures were tested. In the absence of wind, it is likely that vapour will build up above the pool surface, increasing the concentration of the chemicals in the air and impeding the mass transfer from the liquid to the vapour phase. Thus, it is expected that measured evaporation rates will be lower than the predicted data as it is evidenced in the figures.

Despite this, the average error between predicted and experimental data is 3.9% and the confidence interval of the model lies between -4.1% and 11.9% deviation from the measured data.

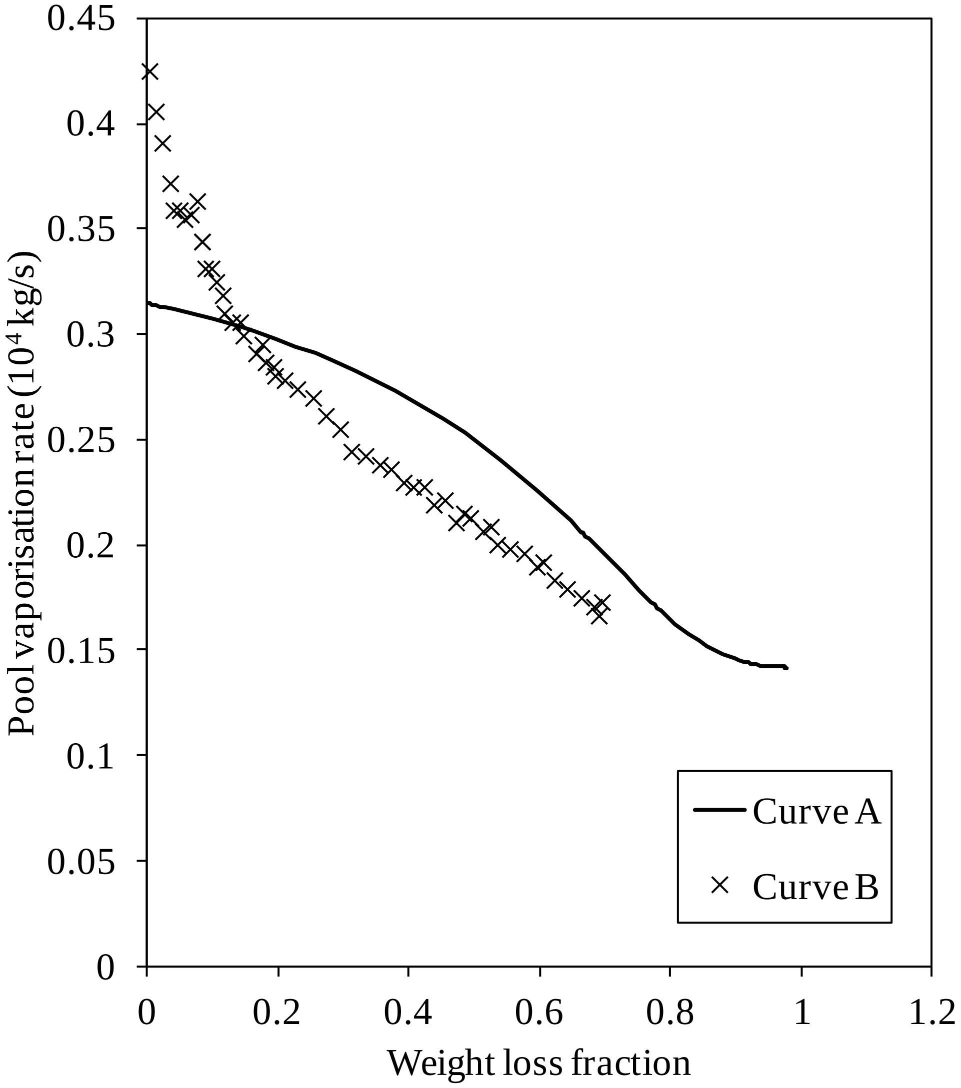

Figure 6.12. Variation of the pool evaporation rate against the weight loss fraction for an n-Pentane/ n-Hexane instantaneous spill

Curve A: Predicted data

Curve B: Experimental data (Okamoto et al., 2009)

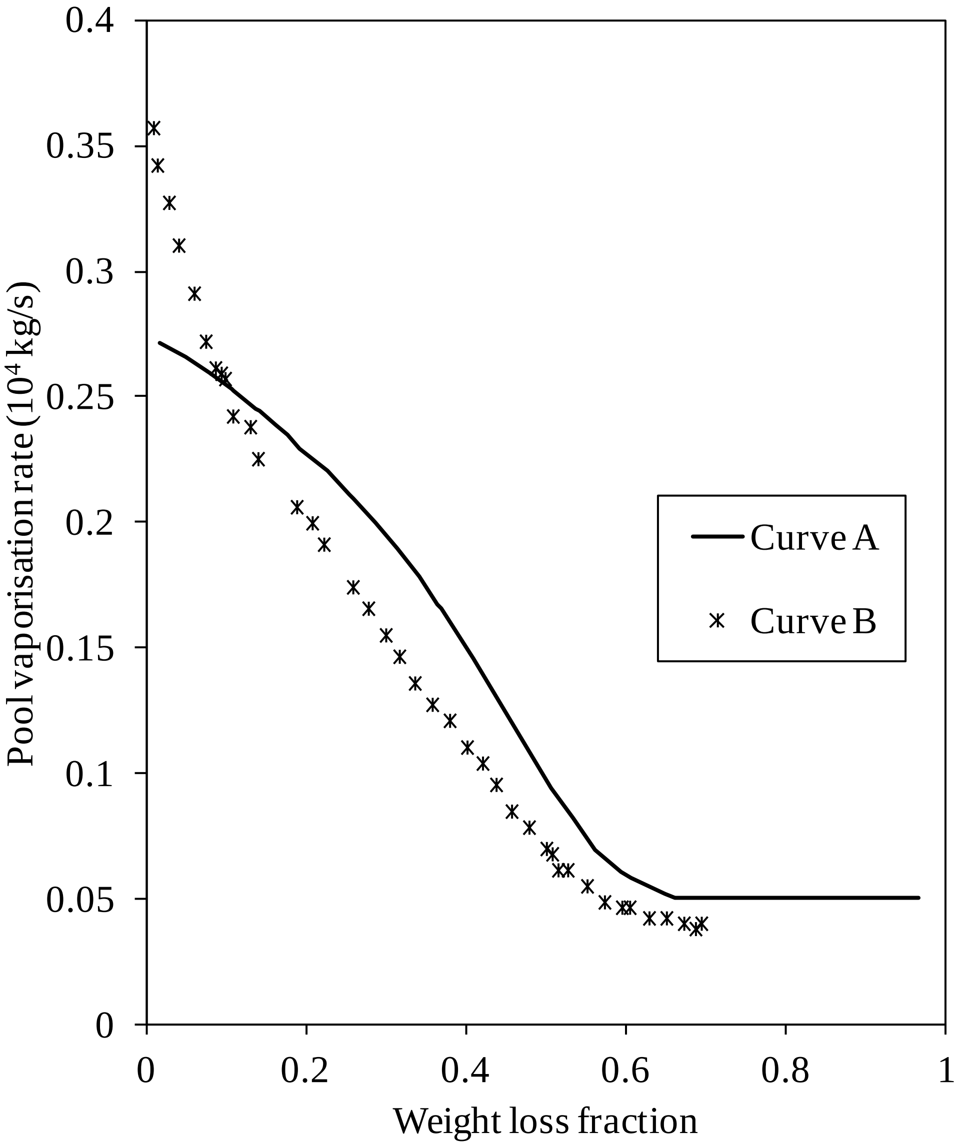

Figure 6.13. Variation of the pool evaporation rate against the weight loss fraction for an n-Pentane/ n-Heptane instantaneous spill

Curve A: Predicted data

Curve B: Experimental data (Okamoto et al., 2009)

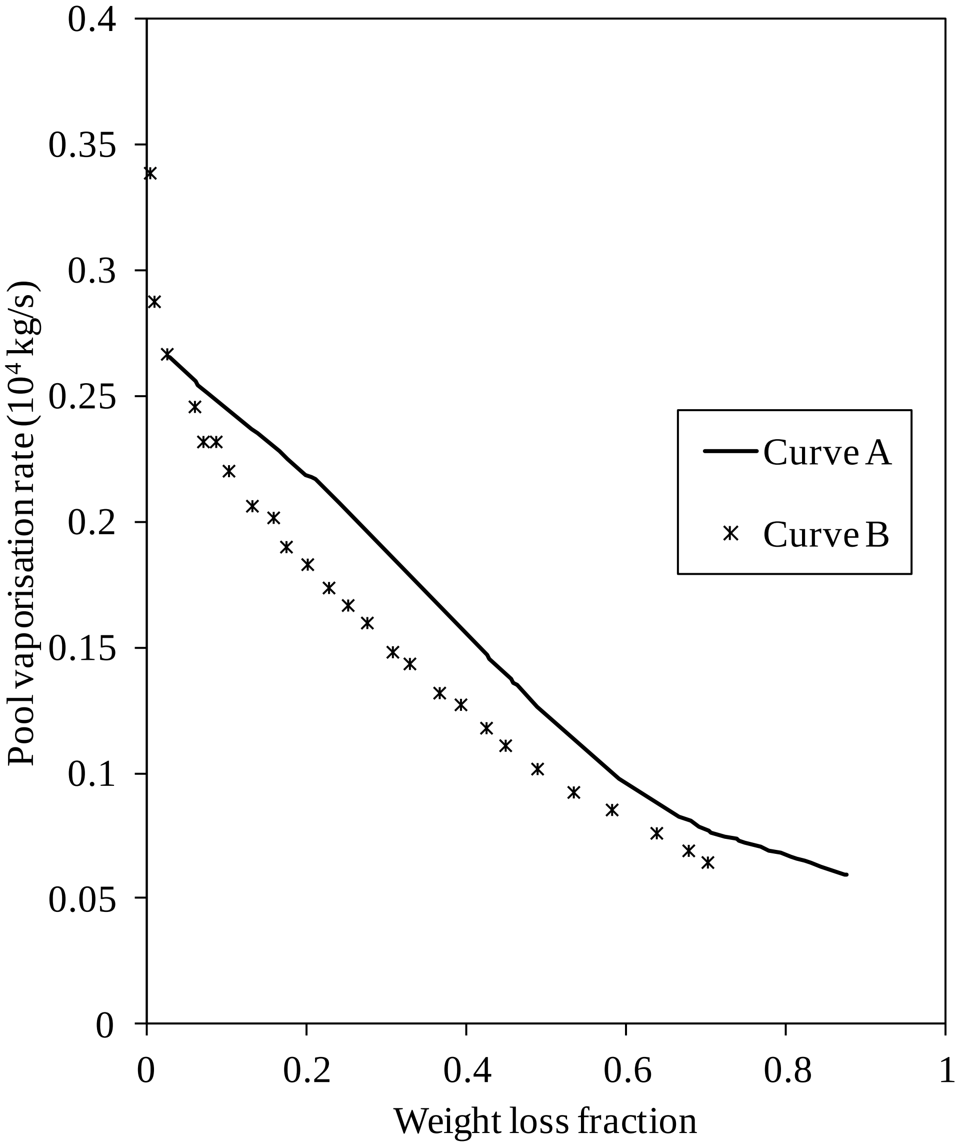

Figure 6.14. Variation of the pool evaporation rate against the weight loss fraction for an n-Pentane/ n-Hexane/ n-Heptane instantaneous spill

Curve A: Predicted data

Curve B: Experimental data (Okamoto et al., 2009)

6.5 Concluding remarks

The important observations made from the validation conducted in this chapter can be summarised as follows:

- ☐ The model for spreading on land has been validated against experiments by Belore and McBean (1980) for spreading of water on plywood. The model is found to predict the pool radius with higher accuracy when taking the pool minimum depth equal to the capillary depth for the case of a smooth surface. An improved algorithm which selects the appropriate pool minimum depth, according to the surface roughness and capillary depth of the liquid is suggested

- ☐ From a sensitivity analysis studying the effect of the variation of the pool minimum thickness on the evaporation rate from a boiling pool on land it was found that the first has a visible impact on the pool results. This also highlights the need to establish an improved method for calculating the pool minimum thickness which takes into account the physical phenomena of surface tension

- ☐ The model for spreading on water model has been validated against experiments by Dodge et al. (1983) for n-Octane on water. The model is found to produce accurate predictions for n-octane spills, with a slightly higher accuracy for smaller times for instantaneous spills than for continuous spills. This is attributed to the assumption of negligible vaporisation losses in the model, which is less applicable to continuous spills

- ☐ From a sensitivity analysis carried out on the effect of the variation of the empirical constant for pool spreading on water it was found that the former has a reduced effect on the final radius of the pool. Therefore uncertainty on the value of this constant won't have a significant effect on the pool results

- ☐ The model for pool boiling on land has been validated against experiments by Reid and Wang (1978) for LNG spills on concrete and soil. The model is found to be in excellent agreement, i.e. the confidence interval is between 4.8 and -4.4% error from the experimental data

- ❑ The model for pool boiling on water has been validated against experiments by Burgess et. al. (1972) for LNG on water. The model performs well against the experimental data for a pure component (liquefied Methane) and a mixture (LNG). The confidence interval of the model is between 6.5 and -4.6% error with respect to the experimental data

- ❑ The model for evaporating pools has been validated against experiments with pools of constant area carried out by
    - Kawamura and MacKay (1987): Pentane, Toluene and n-Hexane spills on sand; with wind
    - Reijnhart and Rose (1980): Toluene and n-Pentane spills on insulated substrate; with wind
    - Okamoto et al. (2009): n-Pentane/n-Hexane/n-Heptane mixture spills on insulated surfaces; no wind

  It was concluded that:

    - For pure components with low volatility (e.g. Toluene), the evaporation model was found to be in good agreement with the experimental data
    - For pure components with relatively high volatility (e.g. n-Pentane), the evaporation model was found to over predict the experimental data. Additional investigations are required to fully understand these limitations
    - For mixtures, the evaporation model was found to be in good agreement with the experimental data. The average deviation between predicted and experimental data is 3.9%

CHAPTER 7. CONCLUSIONS AND FUTURE WORK

7.1 Conclusions

The main contributions of this work were:

- ☐ Review of the state of the art in integral pool models
- ☐ Development, testing and validation of a pool model for the prediction of spreading, vaporisation and dissolution of hydrocarbon mixtures
- ☐ Improvement of the numerical stability of the multi-component pool model by the implementation of a robust numerical algorithm

The following summarises the main conclusions reached:

In chapter 2, a state of the art review showed that there is still significant room for improving pool spreading and vaporisation models reported in the literature. For example, some empirical parameters used in integral pool spreading and evaporation models present some degree of uncertainty as they are based on the available experimental data which is mostly old and at small scale. The review also showed that while current multi-component pool models are able to predict spreading and vaporisation in different types of surfaces they fail to account for the dissolution of water-soluble chemicals in spills on rivers, bays or in open sea.

In chapter 3, the assumptions made and the equations governing pool spreading and evaporation of cryogenic and volatile pools based on published literature were presented. For pools spreading on water, a model based on three successive regimes, gravity-resistive, viscous-resistive and viscous-surface tension was reviewed. Pool vaporisation considers two limiting cases: evaporation and boiling. The energy balance was formulated in terms of the pool temperature instead of the pool enthalpy to reduce the computational workload and improve the accuracy of the simulation. The heat transfer mechanisms accounted for include conduction from the ground, convection from water and air, conduction from ice due to water freezing, long wave radiation and solar incidence.

In chapter 4, the extension of the pool spreading, vaporisation and dissolution model presented in chapter 3 to multi-component pools was shown. To account for the mixture behaviour, the multi-component pool model keeps track of the transient pool inventory applying mass balances for each component. Nevertheless, it is assumed the pool is well mixed for which a single energy balance over the pool volume needs to be solved. Additionally, a series of theoretical cases comparing mixtures and pure components were presented to highlight the possible inaccuracies associated with approximating the evaporation of multi-component mixtures by single components. The conclusions reached from these comparisons are summarised here:

- For a cryogenic mixture of 85 wt% Methane and 15 wt% Ethane, the total amount of material vaporised was over-predicted when approximated by pure Methane, and the maximum pool radius and temperature were under estimated.

- For an 85 wt% n-Pentane, 10 wt% n-Hexane and 5 wt% m-Xylene evaporating mixture, the maximum pool radius and temperature were under-predicted when approximated by pure n-Pentane. However, for the range of conditions tested the pool composition was not found to have a significant impact on the vaporisation rate

- For a water-soluble mixture of 85 wt% Benzene and 15 wt% n-Hexane, the cumulative mass vaporised was slightly under-predicted (by 5%) when approximated by pure Benzene and the dissolution rate was over-predicted. Additionally, for the range of conditions tested the pool composition was not found to have a significant impact on the pool radius

Chapter 5 presented the implementation of a public-domain solver for stiff problems in the multi-component pool model formulated in chapter 4 of this thesis. The numerical method used is based on Backward Differentiation Formula (BDF), a linear multi-step predictor-corrector method. The results of the present work were verified against a widely-used public-domain simulation software for multi-component pools, LPOOL (Post, 1994). Both models were also compared in terms of their range of application, particularly in the case of water-soluble chemicals. From the model verification it was found that the solver implemented in this work was numerically robust when solving a stiff problem and showed improved stability as compared to the numerical algorithm in LPOOL. In terms of the range of application, it was found that the LPOOL simulation leads to a conservative estimate of the total vaporisation rate from water soluble mixtures but to an underestimation of the total time it takes the pool to evaporate completely, with maximum differences of 12%. The pool vaporisation rate was found to decrease with increasing solubility while the dissolution rate showed an increase with respect to the same parameter, within the range of mixtures and conditions tested.

The important observations made from the validation conducted in chapter 6 can be summarised as follows:

- ☐ For smooth surfaces such as plywood, the spreading on land model is found to predict the pool radius with higher accuracy when taking the pool minimum depth equal to the capillary depth of the liquid. It is suggested to implement an improved algorithm which selects the appropriate pool minimum depth, according to the surface and liquid properties

- ☐ The model for spreading on water is found to produce accurate predictions for n-Octane spills, with a slightly higher accuracy for smaller times for instantaneous spills than for continuous spills. This is attributed to the assumption of negligible vaporisation losses implicit in the model equations, which is less applicable to continuous spills

- ☐ The model for pool boiling on land is found to be in excellent agreement, i.e. the confidence interval is between 4.8 and -4.4% error from the experimental data

- ☐ The model for pool boiling on water performs well against the experimental data for a pure component (liquefied Methane) and a mixture (LNG). The confidence interval of the model is between 6.5 and -4.6% error with respect to the experimental data

- ❑ With respect to the model for evaporating pools:
  - For pure components with low volatility (e.g. Toluene), the evaporation model was found to be in good agreement with the experimental data
  - For pure components with relatively high volatility (e.g. n-Pentane), the evaporation model was found to over predict the experimental data. Additional investigations are required to fully understand these limitations
  - For mixtures, the evaporation model was found to be in good agreement with the experimental data. The average deviation between predicted and experimental data is 3.9%

7.2 Suggestions for future work

Extension to non-ideal mixtures

The multi-component pool model developed and validated in this work assumes ideal liquid behaviour and vapour-liquid equilibrium governed by Raoult's Law. An extension to the present model can account for non-ideal liquid phase introducing activity coefficients to represent the interactions between the components in a mixture. Additionally, the implementation of a property system to estimate fugacities by an appropriate equation of state can extend the present work to mixtures containing polar chemicals.

Stratified pool model

The validity of the well-mixed assumption in the multi-component pool model has been found to be less applicable to evaporating pool scenarios than to boiling pools, as the validation presented in chapter 6 showed. To account for a concentration and temperature gradient along the pool depth, the spill can be modelled as a well-mixed bulk whose composition and temperature may differ from that of an infinitesimally thin layer above it. Separate mass and energy balances would be carried out for the two segments of the pool, and the mass and heat transfer mechanisms through the interface would be described in terms of diffusion models.

Modelling first-order chemical reactions

Many chemicals present in solvents and hydrocarbon mixtures react with water producing gases or liquids compounds which can be toxic and/or flammable. In order to model the formation of products from hydrolysis, first order kinetics can be incorporated to the multi-component pool model. The reaction would be assumed to proceed until equilibrium is reached and the pool composition remains constant with time. If the products are liquid it would be assumed they mix with the pool, and if they are in gaseous phase they would be part of the pool vaporisation rate.

Effect of turbulence from plunging jets

The elevation of the release point and the velocity of the mass discharged into the pool can have a significant effect on the pool characteristics, more so for spills on water surfaces. The turbulence mixing product of a plunging jet can enhance the heat transfer between the pool and the water body and increase the rate at which water-soluble chemicals dissolve.

REFERENCES

Bird, R., Steward, W., and Lightfoot, E. (1971). *Transport Phenomena.* New York: John Wiley and Sons.

Blokker, P. C. (1964). Spreading and evaporation of petroleum products on water. *4th International Harbour Conference*. 911-919. Antwerp.

Boyle, G., and Kneebone, A. (1973). *A laboratory investigation into the characteristics of LNG spills on water.* Shell Research Limited.

Brambilla, S., and Manca, D. (2009). Accidents involving liquids: A step ahead in modelling pool spreading, evaporation and burning. *J. Hazard. Mater., 161* (2-3), 1265-1280.

Brighton, P. (1985). Evaporation from a plane liquid surface into a turbulent layer. *J. Fluid Mech., 159,* 323-345.

Brighton, P. (1990). Further verification of a theory for mass and heat transfer from evaporating pools. *J. Hazard. Mater., 23,* 215-234.

Brown, P.N.; Byrne, G.D.; Hindmarsh, A.C. (1989). VODE: A variable coefficient ODE solver. *SIAM, J. Sci. Stat. Comput, 10*, 1038-1051.

Burgess, D., Biordi, J., and Murphy, J. (1972). *Hazards of spillage of LNG into water.* U.S. Bureau of Mines.

Burgess, D., Murphy, J., and Zabetakis, M. (1970). *Hazards of LNG spillage in marine transporation.* U.S. Bureau of Mines.

CAMEO Chemicals Database (2011), Retrieved February 2011 from: http://cameochemicals.noaa.gov/

Cavanaugh II, T., Siegell, J., and Steinberg, K. (1994). Simulation of Vapor Emissions from Liquid Spills. *J. Hazard. Mater., 38* (1), 41-63.

Chang, H.R. and Reid, R.C. (1982). Spreading-boiling model for instantaneous spills of Liquefied Petroleum Gas (LPG) on water. *J. Hazard. Mater., 7*, 19-35.

Conrado, C., and Vesovic, V. (2000). The influence of chemical composition on vaporisation of LNG and LPG on unconfined water surfaces. *Chem. Eng. Sci.*, *55* (20), 4549-4562.

Control of Major Accident Hazard (COMAH) - Safety Reports (2010). Retrieved on September 2010, from: http://www.hse.gov.uk/comah/srag.htm

Control of Major Accident Hazard (2010). Retrieved on September 2010, from: http://www.hse.gov.uk/comah/index.htm

Cook, J., & Woodward, J. (1993). A new unified model for jet, dense, passive, and buoyant dispersion including droplet evaporation and pool modeling. *Intern. Conf. and Exhibition on Safety Health & Loss Prevention in the Oil, Chemical and Process Industries AIChE*. Singapore.

CPR (2005). *Guidelines for quantitative risk assessment (TNO Purple Book)*. 4.11. The Hague: Ministerie van VROM.

Cronin, P.S. and Evans, J.A. (2002) *A series of experiments to study the spreading of liquid pools with different bund arrangements.* Advantica Technologies Limited, for HSE under contract. Report: 405/2002

Design Institute for Physical Properties, American Institute of Chemical Engineers (2012). Retrieved 16-01-2012, from: http://www.aiche.org/dippr/products/801.aspx

Dodge, F., Park, J., Buckingham, J., and Magott, R. (1985). *Revision and experimental verification of the hazard assesment computer system models for spreading, movement, dissolution, and dissipation of insoluble chemicals spilled onto water.* Report: CG-D-35-83. Washington.

Drivas, P. (1982). Calculation of evaporative emissions from multicomponent liquid spills. *Environ. Sci. Technol., 16* (10), 726-728.

European Comission (2012). Chemical Accidents (Seveso II) – Prevention, Preparedness and Response. Latest update on April 2012. Retrieved on May 2012, from: http://ec.europa.eu/environment/seveso/index.htm

Fatunla, S. (1988). *Numerical methods for initial value problems in ordinary differential equations.* Boston: Academic Press.

Fay, J. (1969). *Oil on the sea.* New York: Plenum.

Fay, J. (1971). Physical processes in the spread of oil on a water surface. *Proceedings at Joint Conference and Control of Oil Spills.* Washington D.C. June 15-17.

Fay, J. (1973). Unusual fire hazard of LNG tanker spills. *Comb. Sci. Tech*., *7,* 47-49.

Fay, J. (2003). Model of spills and fires from LNG and oil tankers. *J. Hazard. Mater*., *96* (2-3), 171-188.

Fay, J. (2007). Spread of large LNG pools on the sea. *J. Hazard. Mater*., *140* (3), 541-551.

Feldbauer, G.F., Heigl J.J., McQueen, W., Whip, R.H., May, W.G. (1972). *Spills of L.N.G. on water—Vaporization and downwind drift of combustible mixtures*. Esso Research and Engineering Company, Report: EE61E-72.

Fischer, H.B, List, E. J., Koh, R. C. Y., Imberger, J. and Brooks, N. H. (1979). *Mixing in inland and coastal waters*. New York: Academic Press.

Fischer, H.B. (1973). Longitudinal dispersion and turbulent mixing in open-channel flow. *Annu. Rev. Fluid. Mech*., *5,* 59-78.

Fleischer, F. (1980). *SPILLS: An evaporation/air dispersion model for chemical spills on land.* Houston, Texas: Shell Westhollow Research Centre.

French, D.P and Isaji, T. (2004). Evaluation of the consequences of chemical spills using modelling: chemicals used in deepwater oil and gas operations. *Environ. Modell. Softw.*, *19*, 629-644.

French, D.P., Whittier, N., Ward, M. and Santos, C. (2006). Spill hazard evaluation for chemicals shipped in bulk using modelling. *Environ. Modell. Softw., 21,* 156-169.

Gear, C. (1971). *Numerical initial value problems in ordinary differential equation.* Hemel Hempsted: Prentice Hall.

Goldwire, H., Rodean, H., Cederwall, R., Kansa, E., Koopman, R., McClure, J. (1983). *Coyote Series Data Report LLNL/NWC 1981 LNG spill tests dispersion, vapor burn, and rapid phase transition.*

Hakinson, G., and Murphy, D. (1987). *Personal comunication to P.W.M. Brighton,.* British Gas Midlands Research Station.

Herbs, S.E., Southworth, G.R. and Allen, C.P. (1983). Rates of dissolution of constituent organic contaminants from coal liquefaction oil films into water. *Water. Res., 17*(11), 1639-1646.

Hibbs, D.E. and Gulliver, J.S. (1999). Dissolution rate coeffcients for surface slicks on rivers. *Water. Res., 33*(8), 1811-1816.

Hindmarsh, A., and Radhakrishnan, K. (1993). *Description and use of LSODE, the Livermore Solver for Ordinary Differential Equations.* California: Lawrence Livermore Laboratory Report.

Hissong, D.W. (2007). Keys to modelling LNG spills on water. *J. Hazard. Mater. 140,* 465-477.

Hoult, D. (1972a). Oil spreading on the sea. *Annu. Rev. Fluid Mech., 4,* 341-368.

Hoult, D. P. (1972b). The fire hazard of LNG spilled on water. *Proc. Conference on LNG Importation and Safety*, 87. Boston, Mass.

Incropera, F., and DeWitt, D. (1996). *Fundamentals of heat and mass transfer* (4th ed.). New York: Wiley.

Ivings, M. and Webber, D.M. (2007). Modelling bund overtopping using a shallow water CFD model. *J. Loss Prevent. Proc., 20* (1), 38-44.

Ivings, M., Webber, D. M., Gant, S. and Jagger, S. (2009). *LNG source terms models and hazard analysis: a review of the state-of-the-art and approach to model assessment.* Quincy, Massachusets, USA: The Fire Protection Research Foundation.

Kawamura, P., and MacKay, D. (1987). The evaporation of volatile liquids. *J. Hazard. Mater.*, 343-364.

Klimenko, V. (1981). Film boiling on a horizontal plate - new correlation. *Int. J. Heat Mass Transfer, 24,* 69–79.

Koopman, R.P., Cederwall, R.T., Ermak, D.L., Goldwire, H.C., Hogan, W.J., McClure, J.W., McRae, T.G., Morgan, .D.L., Rodean, H.C. and Shinn, J.H. (1982). Analysis of Burro series 40m^3 LNG spill experiments. *J. Hazard. Mater.,* 6, 43-83.

Kunsch, J. (1998). Two-layer integral model for calculating the evaporation rate from a liquid surface. *J. Hazard. Mater., 59,* 167-187.

Lees, R. (1996). Chapter 15: Emission and dispersion. *Loss Prevention in the Process Industries.* 15/56-15/68; S. Mannan Ed.; Elsevier.

Leonelli, P., Stramigioli, C., and Spadoni, G. (1994). The modelling of pool vaporization. *J. Loss Prevent. Proc.*, *7* (6), 443-450.

Liang, L.S. (1971). *Spreading of oil on calm water: Inertial phase.* M.S. thesis. MIT, Department of Mechanical Engineering.

Lind, C. (1974). *Explosion hazards associated with spills of large quantities of hazardous materials.* Phase I, U.S. Coast Guard Report No. NTIS AD-A001242.

MacKay, D. and Leinonen, P.J. (1977). *Mathematical model of the behaviour of oil spills on water with natural and chemical dispersion*. Report EPS-3-EC-77-19.

MacKay, D., and Matsugu, R. (1973). Evaporation rates of liquid hydrocarbon spills on land and water. *Can. J. Chem. Eng., 51,* 434.

Matsugu, R.S (1973). *M.S. Thesis.* Department of Chemical Engineering and Applied Chemistry. University of Toronto, Canada.

McNutt, M., Camili, R., Guthrie, G., Hsieh, P., Labson, V., Lehr, B., McLay, D., Ratzel, A. and Sogge, M. (2011). *Assessment of Flow Rate Estimates for the Deepwater Horizon / Macondo Well Oil Spill.* Report to National Incident Command, Interagency Solutions Group, Flow Rate Technical Group. Retrieved on February 2012, from: http://www.doi.gov/deepwaterhorizon/loader.cfm?csModule=security/getfile&PageID=237763

Mikesell, J., Buckland, A., Diaz, V. and Kives, J.J. (1991). *Proceedings of the International Conference and Workshop on Modelling and Mitigating the Consequences of Accidental Releases of Hazardous Materials*. New Orleans, Lousiana.

Moorhouse, J., and Carpenter, R. (1986). Factors affecting water evolution rates from liquefied gas spills. *I. Chem.E. North Western Branch Papers*, No. 1.

Napier, D., and Roopchand, D. (1986). An approach to hazard analysis of LNG spills. *J. Occup. Accid., 7*, 251-272.

Office of Public Sector Information (2008). *The Buncefield Incident 11 December 2005. The final report of the Major Incident Investigation Board. Volume 1.* Kew, Richmond. Retrieved on October 2011, from: http://www.buncefieldinvestigation.gov.uk/reports/volume1.pdf

Opschoor, G. (1979). *Methods for the calculation of the physical effects of the escape of dangerous material.* “Yellow Book” TNO.

Parker, R., Pope, J., Davidson, J., Simpson, W. (1975). *The Flixborough Disaster: Report of the Court of Inquiry*. Report to the Department of Employment.

Pasquill, F. (1943). Evaporation from a Plane, Free-Liquid Surface into a Turbulent Air Stream. *P. Roy. Soc. Lond. A. Mat., A182*, 75.

Ponchaut, N.F., Chernovsky, M., Gavelli, F., and Kytömaa, H.K. (2009). Modeling the spreading of large LNG spills on water. AIChE Spring Meeting, April 2009. *9th Topical Conference on Natural Gas Utilization, Tampa, Florida*.

Post, L. (editor) (1994). *HGSYSTEM 3.0 Technical Reference Manual*. Report No. TNER.94.059, Shell Research Limited, Thornton Research Centre. Chester, England.

Raj, P., and Kalelkar, A. (1974). *Assessment models in support of the hazard assessment handbook.* Cambridge, Massachusets: Arthur D. Little, Inc. for the Department of Transportation U.S.

Reid, R., and Smith, K. (1978). Behaviour of LNG on water. *Hydrocarb. Process., 57* (4), 117-121.

Reid, R., and Wang, R. (1978). The boiling rates of typical dike floor materials. *Cryogenics, 18* (7), 401-404.

Reinjhart, R., and Rose, R. (1980). Vapour Cloud Dispersion and Evaporation of Volatile Liquids in Atmospheric Wind Fields - II Wind Tunnel Experiments. *Atmos. Environ., 14* (7), 759-762.

Sambeth, J. (1983). The Seveso Accident. *Chemosphere, 12* (4/5), 681-686.

Shaw, P., and Briscoe, F. (1980). Spread and evaporation of liquid. *Prog. Energ. Combust., 6* (2), 127-140.

Skinner, S.K. and Reilly, W.K. (1989). *The Exxon Valdez Oil Spill*. Report prepared by the National Response Team. Retrieved on August 2011, from: http://docs.lib.noaa.gov/noaa_documents/NOAA_related_docs/oil_spills/ExxonValdez_NRT_1989_report_to_president.pdf

Smith, J.M., van Ness, H.C. and Abbott, M.M. (2005). *Introduction to chemical engineering thermodynamics*. Boston, Mass: McGraw Hill.

Socolofsky, S., and Jirka, G. (2004). *Environmental fluid mechanics 1: mixing and transport processes in the environment. Engineering lectures.* Texas A&M University.

Sutton, O. G. (1934). Wind structure and evaporation in a turbulent atmosphere. *P. Roy. Soc. Lond. A. Mat., A*, 701-722.

Thyer, A.M. (2003). A review of data on spreading and vaporisation of cryogenic liquid spills. *J. Hazard. Mater., A99,*31-40.

Ueda, H., Moller, R., Komori, S., and Mizushina, T. (1977). Eddy diffusivity near the free surface of open channel flow. *Int. J. Heat Mass Transfer, 20*, 1127-1136.

US Energy Information Administration. EIA (2011). *International Energy Outlook 2011*. Report: DOE/EIA-0484(2011). Retrieved on December 2011, from: http://205.254.135.7/forecasts/ieo/pdf/0484%282011%29.pdf

Valencia-Chavez, J.A. and Reid, R.C. (1979). The effect of composition onthe boiling rates of liquefied natural gas for confined spills on water. *Int. J. Heat Mass Transfer, 22* 831-838.

van den Bosch, C. (2005). Pool evaporation. In C. van den Bosch, and R. Weterings, *Methods for the calculation of physical effects (TNO Yellow Book)*. 3.1-3.128. The Hague: Ministerie van VROM.

van Ulden, A., and Holstag, A. (1985). Estimation of atmospheric boundary laye rparameters for diffusion applications. *J. Climate Appl. Meteorol., 24*, 1196-1207.

Walas, S.M. (1985). *Phase equilibria in chemical engineering.*Newton: Butterworth-Heinemann.

Webber, D. (1989). Evaporation of Liquid Pools - a Unified Treatment. *Mathematics in Major Accident Risk Assesment*, 131-144.

Webber, D. (1990). *A model for pool spreading and vaporisation and its implementation in the computer code GASP*. UKAEA Report Safety and Reliability Directorate.

Webber, D., and Jones, S. (1987). A model of spreading vaporising pools. *International Conference on Vapour Cloud Modelling.* 226-250. Boston: AIChE Journal.

Witlox, H. (2008). *PVAP- Theory document.* London: DNV Technica (Phast Technical Reference).

Appendix A. Comparisons between single and multi-component releases of evaporating liquids on calm sea

The following figures present the results of the case studies comparing the behaviour of a pure n-Pentane pool and an 85 wt% n-Pentane, 10 wt% n-Hexane and 5 wt% m-Xylene on calm sea. Table A.1 gives the release and prevailing ambient conditions selected for the studies.

Table A 1. Release and prevailing ambient conditions

Release	Type of spill	**Continuous**	**Continuous**	**Instantaneous**	**Instantaneous**
	Spill mass (kg)	–	–	1000	1000
	Spill rate (kg/s)	0.01	0.01	–	–
	Spill duration (hrs)	72	72	–	–
	Spill temperature (K)	293	293	293	293
	Spill composition (wt%)				
	n-Pentane	85	100	85	100
	n-Hexane	10	0	10	0
	m-Xylene	5	0	5	0
Ambient	Ambient temperature (K)	283	283	283	283
	Ambient pressure (Pa)	101,325	101,325	101,325	101,325
	Atmospheric stability (Pasquill class)	D-Neutral	D-Neutral	D-Neutral	D-Neutral
	Wind speed at 10 m height (m/s)	5	5	5	5
	Surface roughness length (m)	10^{-4}	10^{-4}	10^{-4}	10^{-4}
	Solar incidence ($W/m^2.K$)	0	0	0	0
Surface	Surface material	Calm sea	Calm sea	Calm sea	Calm sea
	Bund diameter (m)	no bund	no bund	no bund	no bund
	Surface temperature (K)	283	283	283	283
	Heat transfer coefficient (W/m^2 K)	500	500	500	500

A.1. Continuous releases

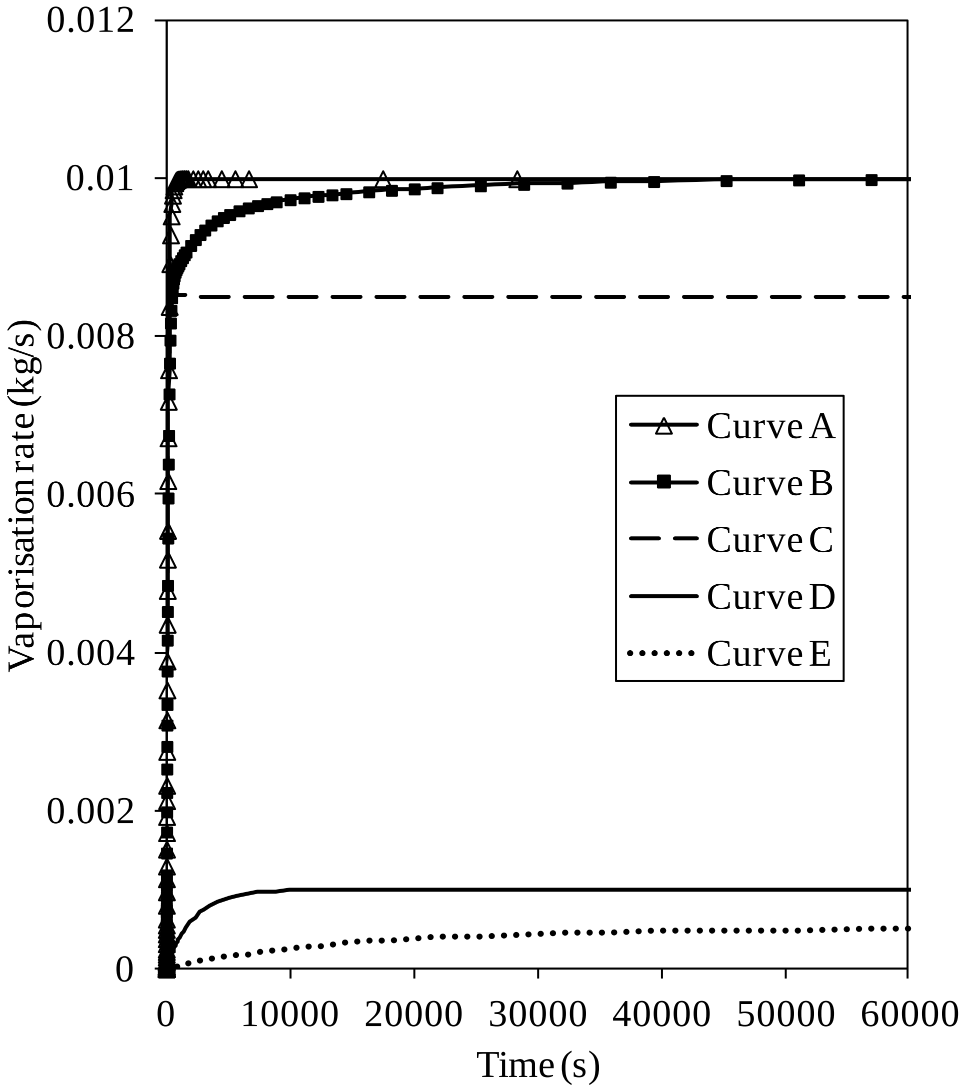

Figure A. 1. Variation of the pool vaporisation rate with time for continuous releases on calm sea at a temperature of 283 K and a wind speed of 5 m/s at 10 m above the surface. Spill rate: 0.01 kg/s. Curve A: pure n-Pentane. Curve B: n-Pentane/n-Hexane/m-Xylene. Curve C: n-Pentane. Curve D: n-Hexane. Curve E: m-Xylene.

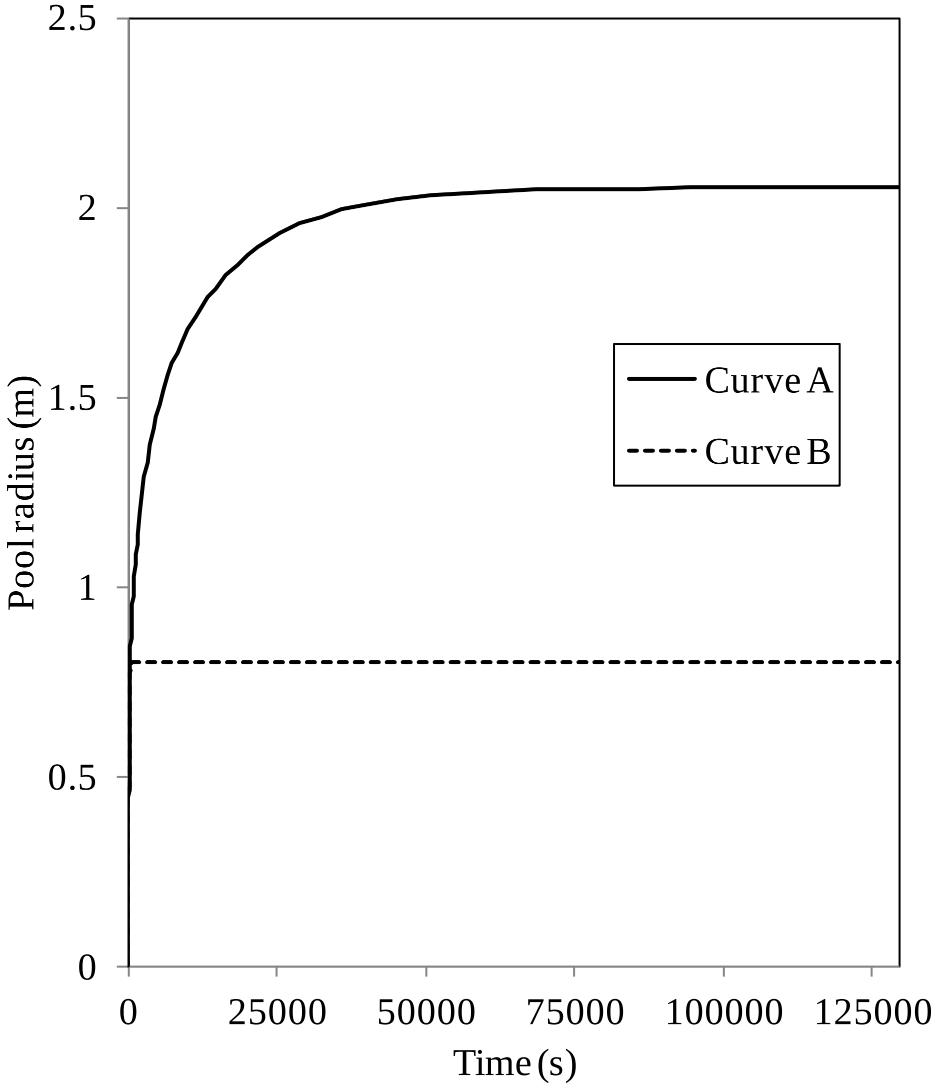

Figure A. 2. Variation of the pool radius with time for continuous releases on calm sea at a temperature of 283 K and a wind speed of 5 m/s at 10 m above the surface. Spill rate: 0.01 kg/s. Curve A: n-Pentane/n-Hexane/m-Xylene. Curve B: pure n-Pentane.

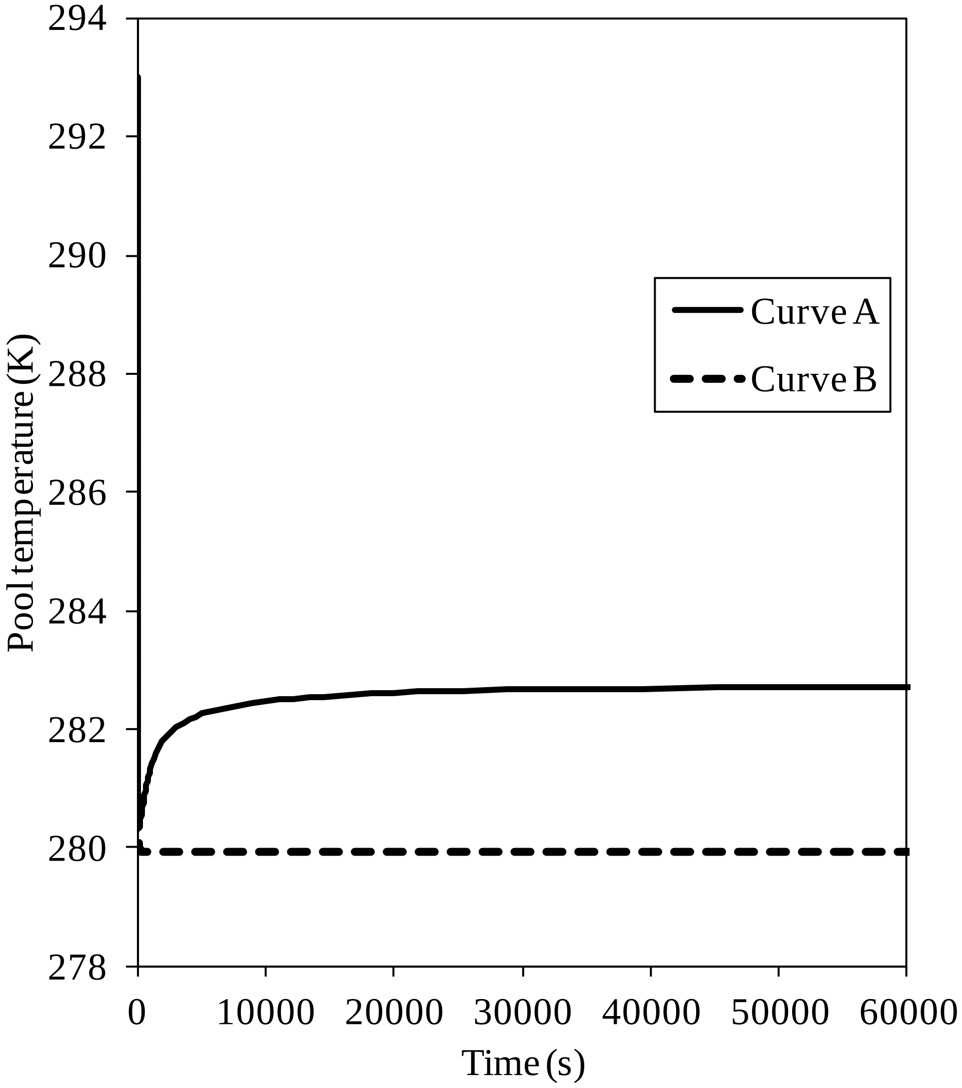

Figure A. 3. Variation of the pool temperature with time for continuous releases on calm sea at a temperature of 283 K and a wind speed of 5 m/s at 10 m above the surface. Spill rate: 0.01 kg/s. Curve A: n-Pentane/n-Hexane/m-Xylene. Curve B: pure n-Pentane.

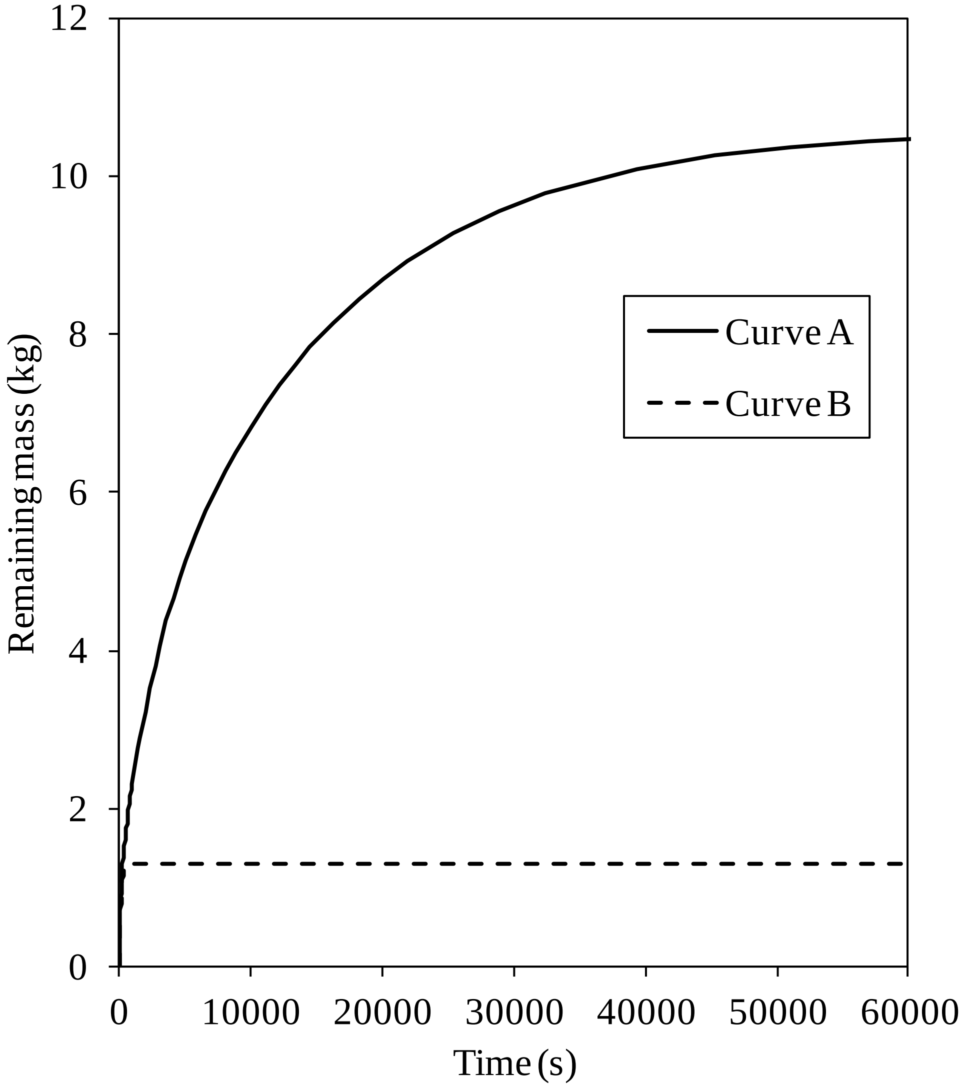

Figure A. 4. Variation of the remaining mass in the pool with time for continuous releases on calm sea at a temperature of 283 K and a wind speed of 5 m/s at 10 m above the surface. Spill rate: 0.01 kg/s. Curve A: n-Pentane/n-Hexane/m-Xylene. Curve B: pure n-Pentane.

A.2. Instantaneous releases

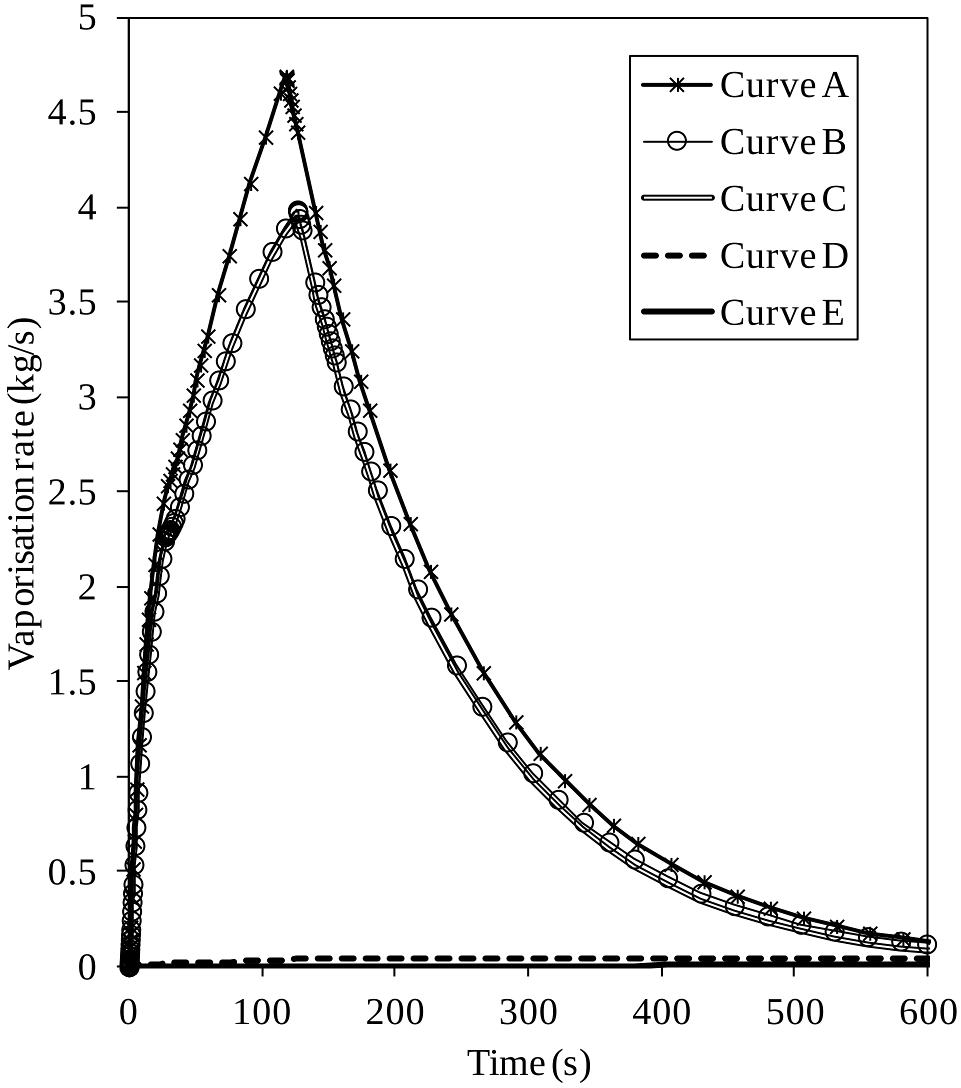

Figure A. 5. Variation of the pool vaporisation rate with time for instantaneous releases on calm sea at a temperature of 283 K and a wind speed of 5 m/s at 10 m above the surface. Spill mass: 1000 kg. Curve A: pure n-Pentane. Curve B: n-Pentane/n-Hexane/m-Xylene. Curve C: n-Pentane. Curve D: n-Hexane. Curve E: m-Xylene.

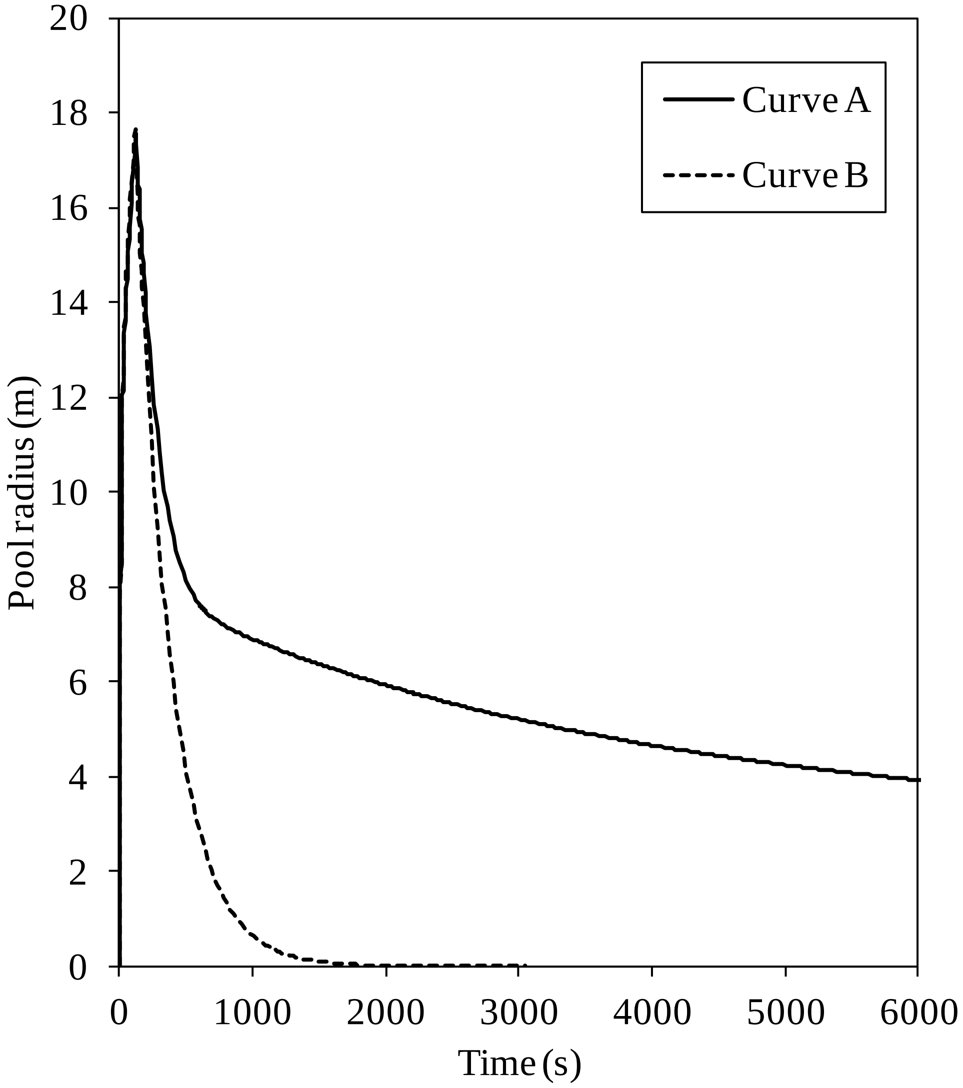

Figure A. 6. Variation of the pool radius with time for instantaneous releases on calm sea at a temperature of 283 K and a wind speed of 5 m/s at 10 m above the surface. Spill mass: 1000 kg. Curve A: n-Pentane/n-Hexane/m-Xylene. Curve B: pure n-Pentane.

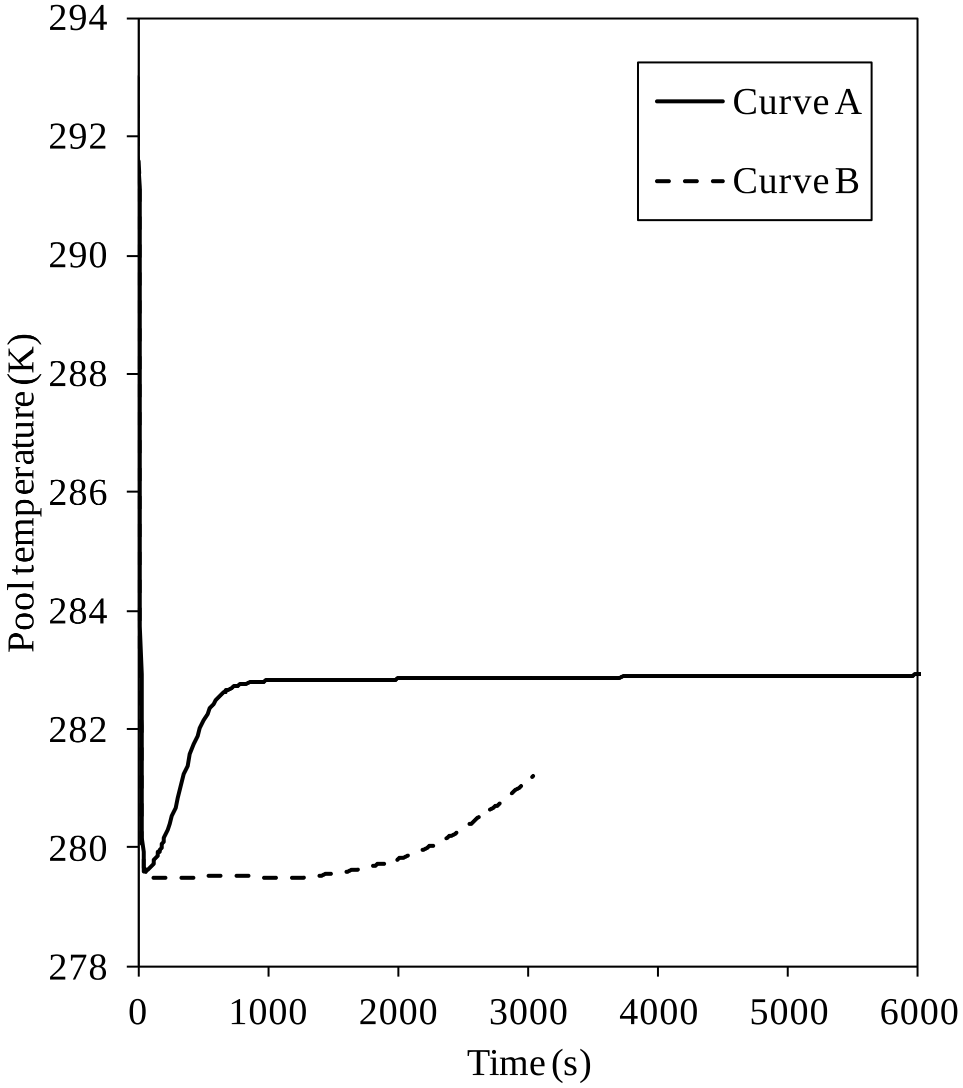

Figure A. 7. Variation of the pool temperature with time for instantaneous releases on calm sea at a temperature of 283 K and a wind speed of 5 m/s at 10 m above the surface. Spill mass: 1000 kg. Curve A: n-Pentane/n-Hexane/m-Xylene. Curve B: pure n-Pentane.

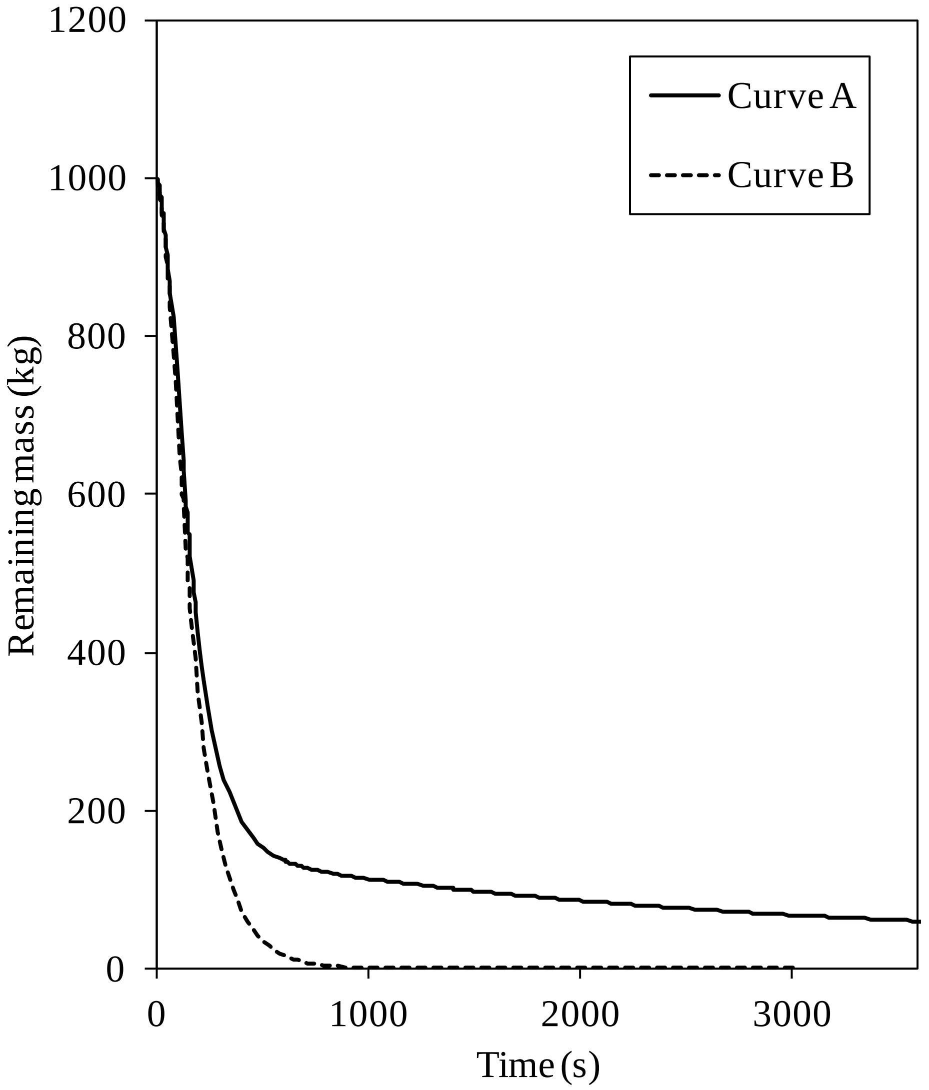

Figure A. 8. Variation of the remaining mass in the pool with time for instantaneous releases on calm sea at a temperature of 283 K and a wind speed of 5 m/s at 10 m above the surface. Spill mass: 1000 kg. Curve A: n-Pentane/n-Hexane/m-Xylene. Curve B: pure n-Pentane.

Appendix B. Comparison between LPOOL and the present multi-component pool model

The following figures show the comparison between the present work and LPOOL (Post, 1994) for two hypothetical cases of cryogenic and evaporating mixtures releases on concrete and calm sea surfaces. Table B.1 shows the release and prevailing ambient conditions.

Table B. 1. Release and prevailing ambient conditions

	Type of spill	**Continuous**	**Instantaneous**
Release	Spill mass (kg)	–	1000
	Spill rate (kg/s)	5	–
	Spill duration (hrs)	120	–
	Spill temperature (K)	117.1	293
	Spill composition (wt%)		
	Methane	50	–
	Ethane	50	–
	n-Pentane	–	34
	n-Hexane	–	33
	m-Heptane	–	33
Ambient	Ambient temperature (K)	288	293
	Ambient pressure (Pa)	101,325	101,325
	Atmospheric stability (Pasquill class)	D-Neutral	D-Neutral
	Wind speed at 10 m height (m/s)	1	5
	Surface roughness length (m)	10^{-2}	10^{-4}
	Solar incidence ($W/m^2.K$)	0	0
Surface	Surface material	Concrete	Calm sea
	Bund diameter (m)	no bund	18
	Bund height (m)	–	1
	Surface temperature (K)	288	288
	Heat transfer coefficient (W/m^2 K)	–	500
	Surface thermal conductivity (W/m K)	0.94	–
	Surface thermal diffusivity (10^7 m^2/s)	7.90	–

B.1. Continuous release on concrete

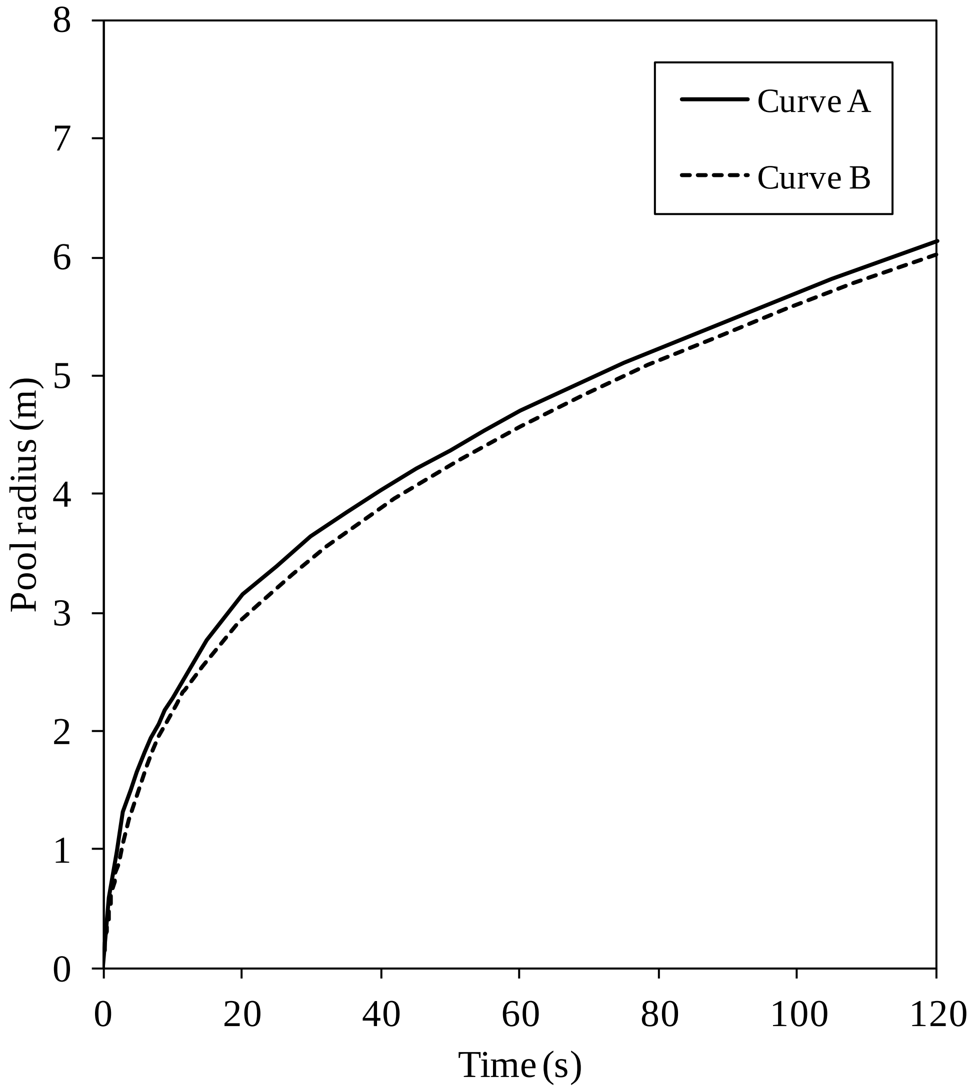

Figure B. 1. Variation of the pool radius with time for a continuous release of a 50 wt% Methane and 50 wt% Ethane mixture on concrete at a temperature of 288 K and a wind speed of 1 m/s at 10 m above the surface. Spill rate: 5 kg/s.

Curve A: LPOOL simulation. Curve B: Present multi-component model

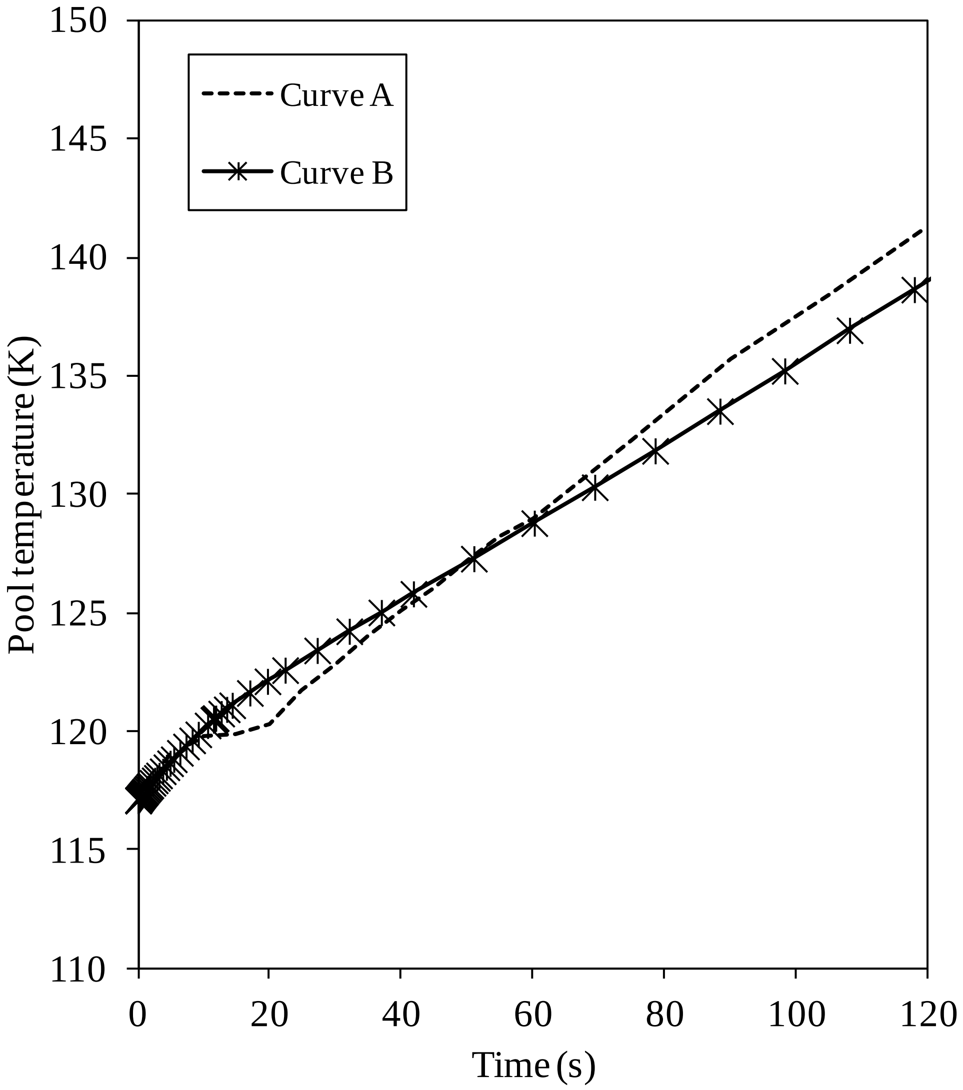

Figure B. 2. Variation of the pool temperature with time for a continuous release of a 50 wt% Methane and 50 wt% Ethane mixture on concrete at a temperature of 288 K and a wind speed of 1 m/s at 10 m above the surface. Spill rate: 5 kg/s.

Curve A: LPOOL. Curve B: Present multi-component model

B.2. Instantaneous release on calm sea

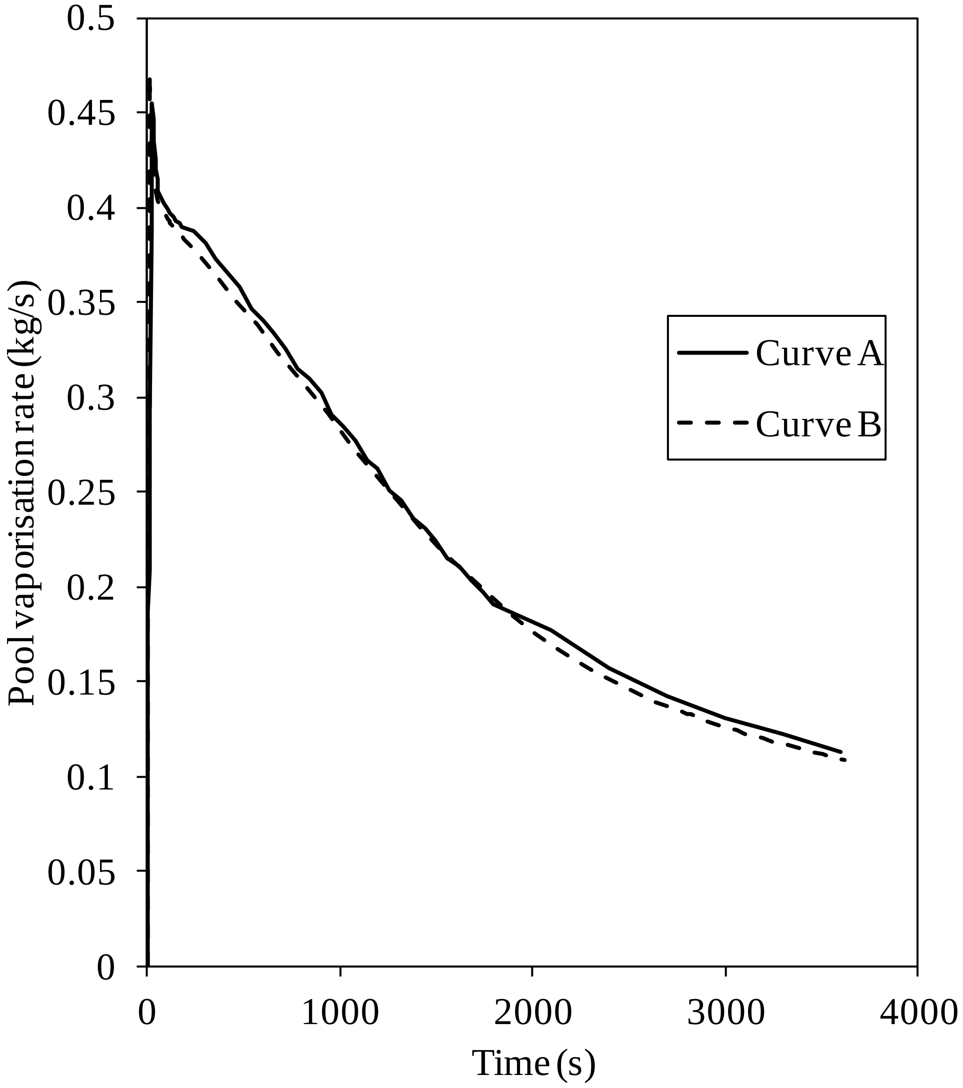

Figure B. 3. Variation of the pool vaporisation rate with time for an instantaneous n-Pentane/n-Hexane/n-Heptane spill on calm sea at a temperature of 288 K and a wind speed of 5 m/s at 10 m above the surface. Spill mass: 1000 kg.

Curve A: LPOOL. Curve B: Present multi-component model

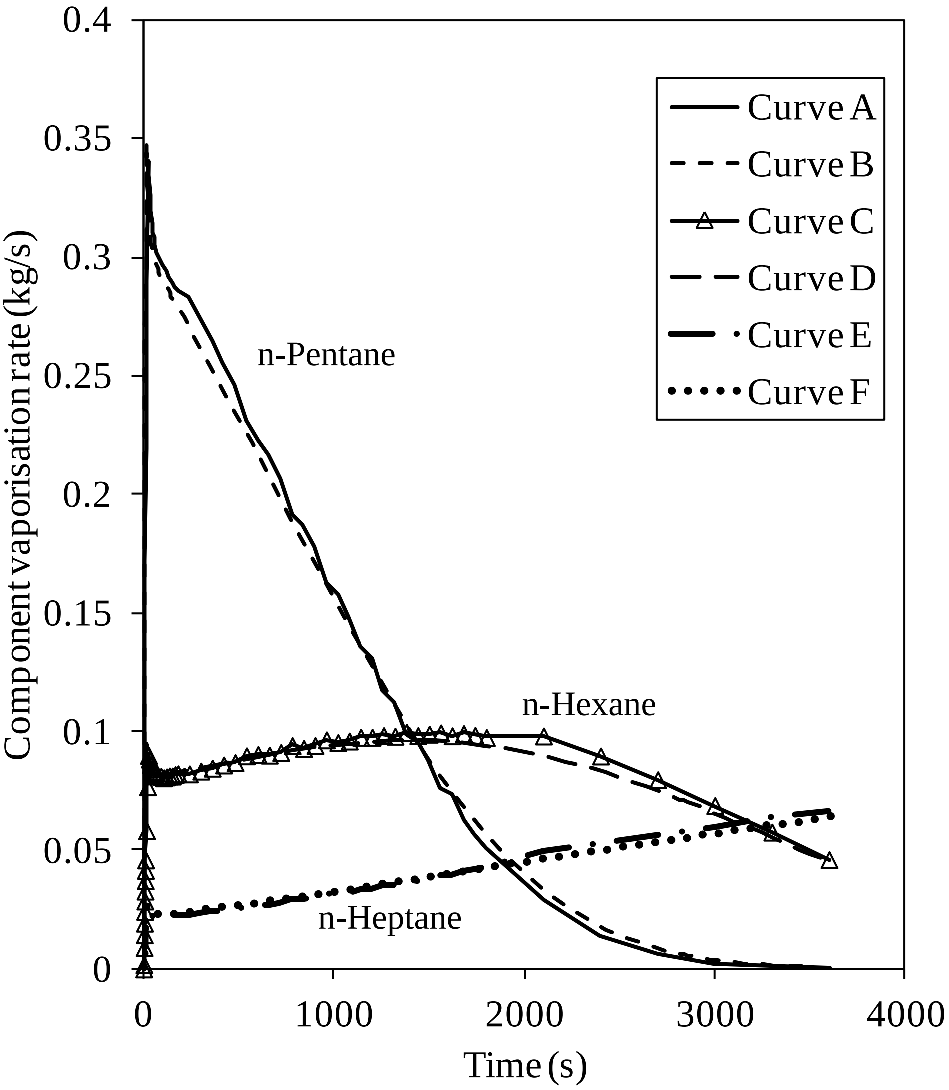

Figure B. 4. Variation of n-Pentane, n-Hexane and n-Heptane vaporisation rates with time for an instantaneous spill on calm sea at a temperature of 288 K and a wind speed of 5 m/s at 10 m above the surface. Spill mass: 1000 kg.

Curve A: LPOOL, n-Pentane. Curve B: Present multi-component model, n-Pentane. Curve C: LPOOL, n-Hexane. Curve D: Present multi-component model, n-Hexane. Curve E: LPOOL, n-Heptane. Curve F: Present multi-component model, n-Heptane

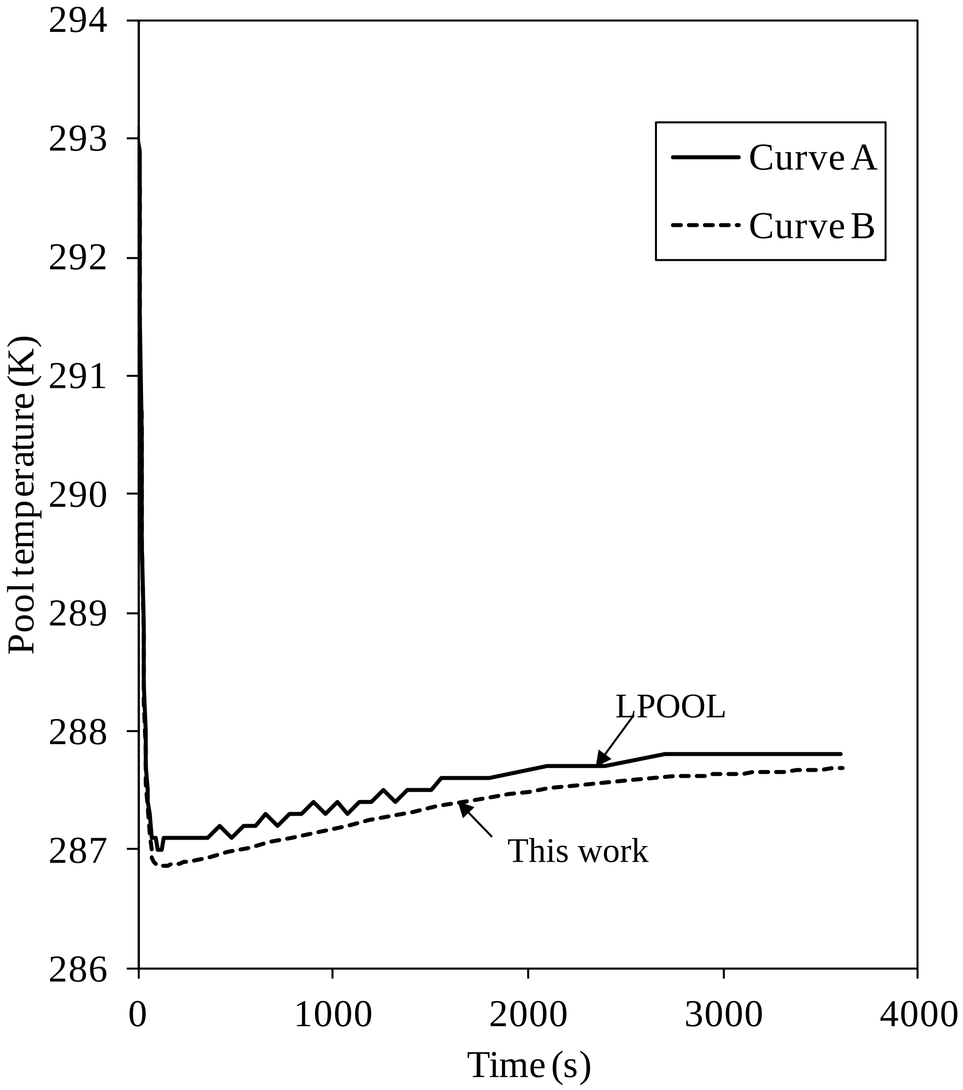

Figure B. 5. Variation of the pool temperature with time for an instantaneous n-Pentane/n-Hexane/n-Heptane spill on calm sea at a temperature of 288 K and a wind speed of 5 m/s at 10 m above the surface. Spill mass: 1000 kg.

Curve A: LPOOL Curve B: Present multi-component model

Appendix C. Linear Multi-Step Method: Backward Differentiation Formula

The following section describes the numerical method used in the solution of the system of ODE's presented in Chapter 5 of this thesis. The numerical method chosen uses the Backward Differentiation Formula.

The Backward Differentiation Formula in essence approximates the value of the derivative of the function at the current time step by an interpolation of the previous values of the function. Considering first a simple case of a single continuous function and a first order interpolation, the Backwards Difference Approximation will estimate the gradient of the function at x_n by the difference of the function evaluated at x_n and x_{n-1}:

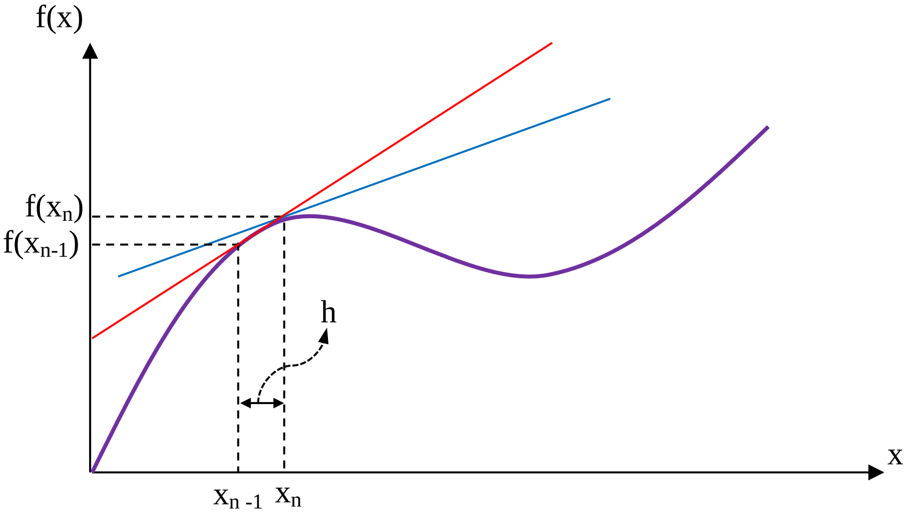

Figure C.1 Schematic representation of Backwards Difference Approximation

In the figure above the derivative of the function at x_n shown by the blue line is approximated to the slope of the red line such that:

$$y(x_n) = f'(x_n) = \frac{f(x_n) - f(x_{n-1})}{(x_n - x_{n-1})} = \frac{f(x_n) - f(x_{n-1})}{h} \tag{C.1}$$

The general form of this method for any order, k, is given by (Lambert, 1991):

$$\sum_{i=0}^{k} \delta_i \nabla^i f(x_{n+k}) = h\, y(x_{n+k}) \tag{C.2}$$

where,

δ_i is given by: $\begin{cases} \delta_0 = 0 \\ \delta_i = \dfrac{1}{i} \qquad i = 1,2,... \end{cases}$

and ∇ is the backward difference operator:

$\nabla f(x_n) = f(x_n) - f(x_n - 1)$

$\nabla^2 f(x_n) = \nabla f(x_n) - \nabla f(x_n - 1) = f(x_n) - 2f(x_n - 1) + f(x_n - 2)$

$\vdots$